# Synthesis and Fabrication of Plasmon Resonance-Tuned Silver Nanoparticle Films

**Róisín Mooney**

**1324701**

A thesis submitted to Auckland University of Technology in fulfilment of the requirements for the degree of Doctor of Philosophy

Dr Marcus Jones

Dr Taniela Lolohea


Auckland University of Technology

Faculty of Health and Environmental Science

School of Science

Department of Chemistry

2024

## Abstract

This thesis presents a series of optimisation experiments aimed at synthesising and fabricating plasmon resonance-tuned silver nanoparticle films. The initial focus of this work is to refine a wet chemical synthetic method that produces reproducible nanoparticle suspensions with tunable plasmonic properties. By effectively varying the synthetic reagents, we were able to control the size and shape of the resulting nanostructures, thereby tuning the surface plasmon resonance of these suspensions. The insights gained from the synthesis optimisation experiments were crucial for developing an efficient immobilisation process to attach these nanoparticles onto glass substrates. Ultimately, successfully fabricating a monolayer nanoparticle film with tunable plasmon resonance. Subsequently, these films were overlaid with rubrene to explore the impact of the plasmonic sublayer on the steady-state and time-resolved fluorescence in solid-state rubrene films. The findings and optimised protocols detailed in this thesis will serve as a strategic foundation for advancing future work on efficient up-conversion devices.

## Acknowledgements

First and foremost, I would like to thank my academic supervisors, Dr Marcus Jones and Dr Taniela Lolohea, for their invaluable assistance with my doctoral research.

I also want to extend my appreciation to all the dedicated academics and technical staff in the AUT School of Science Chemistry Department. Your constant encouragement and assistance have been a beacon of support during this endeavor. A special shoutout goes to Yan Wang, Iana Gritcan, Adrian Owens, and Tim Layt, who have always been there to tackle my seemingly endless technical challenges with creative solutions. This journey would not have been possible without the generous VC PhD scholarship funding provided by AUT.

My sincere thanks go to the MacDiarmid Institute for the wonderful support and countless development opportunities over the years. I cherish the encouragement from the MESA committee members and friends who have walked alongside me during my PhD, and I'm filled with excitement for what the future holds for our generation of emerging scientists.

I owe a tremendous debt of gratitude to Dr. Bronte Carr, Jess Fredericksen, and Olivia Matich. Our early mornings and late nights in the lab always felt more manageable with your companionship and laughter by my side.

Words cannot express my gratitude to Jessica Gregg, Kate Fagan, Cendrine Pfister and Casey Wakelin. From the very beginning of my academic journey, your love and friendship have been my steadfast pillars of strength, especially during the tough times.

Finally, I would like to thank my family.

To Dr. Ronan Mooney, becoming the second Dr. R. Mooney in the family is much easier knowing I have you as my big brother. Thank you for always being there for me and for everything you've done to support me.

To Liam Mooney, I wish you could have been by my side this past year. However, I will always be grateful for our debrief sessions and your song recommendations. I can not wait to celebrate graduating with you both in Chicago!

To my beloved parents, Helen and Martin Mooney, your unwavering belief in me has carried me through every challenge. Thank you for your endless love and for everything you have done to help me reach this milestone.

Finally, to Nick Coxon, thank you for filling my heart with excitement for the future and for all the happiness and horses that our life together will bring.

I love you all so dearly and appreciate you more than words can ever express.

## Attestation of Authorship

"I hereby declare that this submission is my own work and that, to the best of my knowledge and belief, it contains no material previously published or written by another person (except where explicitly defined in the acknowledgements), nor used artificial intelligence tools or generative artificial intelligence tools (unless it is clearly stated, and referenced, along with the purpose of use), nor material which to a substantial extent has been submitted for the award of any other degree or diploma of a university or other institution of higher learning."

Róisín Mooney

# Contents

# List of Figures

# List of Tables

# 1 Chapter 1 - Literature Review

| Abbreviations | |
|---|---|
| NIR | Near Infrared |
| SPR | Surface Plasmon Resonance |
| SPP | Surface Plasmon Polaritons |
| SP | Surface Plasmons |
| LSPR | Longitudinal Surface Plasmon Resonance |
| TSPR | Transverse Surface Plasmon Resonance |
| EBL | Electron Beam Lithography |
| SERS | Surface Enhanced Raman Spectroscopy |
| NMR | Nuclear Magnetic Resonance |
| EM | Electron Microscopy |
| XRD | X-ray Diffraction |
| MEF | Metal Enhanced Fluorescence |
| MEA | Metal Enhanced Absorption |
| RDE | Radiative Decay Engineering |
| HR-TEM | High-resolution Transmission Electron Microscopy |
| TTA | Triplet-triplet Annihilation |
| ISC | Inter System Crossing |
| UCNPs | Up-converting Nanoparticles |
| nm | Nanometre |
| eV | Electronvolt |
| mM | Millimole |

## 1.1 Introduction

The foundation of this research lies in the optical properties of noble metal nanoparticles and their ability to modulate light-induced processes within molecular systems. The primary aim of this project is to explore photon up-conversion in polycyclic aromatic hydrocarbons, with a particular focus on 5,6,11,12-tetraphenylnaphthacene (Rubrene). To this end, the project aims to develop a solid-state thin-film device to further investigate the plasmon-enhanced up-conversion mechanism. Figure 1 presents a schematic of the proposed device. The core objective of this work is to optimise the optical characteristics of the plasmonic layer to enhance metal-enhanced fluorescence within the system. This will be accomplished through the optimisation of robust synthetic methods for the production of silver nanoparticles and the effective development of thin-film fabrication protocols.

Photon up-conversion is a photophysical process that transforms two low-energy photons into a single high-energy photon. This phenomenon holds considerable promise for applications in biological imaging, data storage, and improved light harvesting in solar cells. However, current up-conversion techniques often face low efficiency, primarily

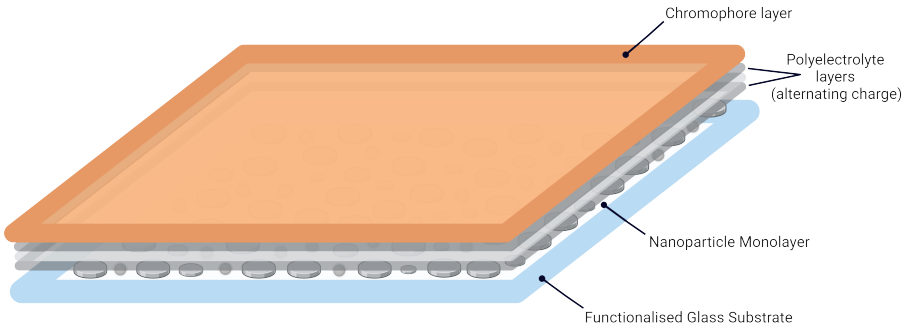


*Figure 1: Schematic of the proposed thin film plasmon enhanced up-conversion device*

due to the limited range of known sensitiser and emitter combinations. Additionally, achieving up-conversion in solid-state materials is more challenging due to the complexities associated with thin film fabrication. Nevertheless, recent studies have revealed the potential of an innovative approach driven by the substantial electric fields generated by plasmon resonances in illuminated noble metal nanoparticles.

Plasmons are collective oscillations of optically excited electrons observed across all metals. Notably, the resonant frequency of plasmons in noble metal nanoparticles can be finely tuned across the visible and into the near-infrared (NIR) spectrum through variations in nanoparticle morphology. Various wet chemical methods will be optimised to synthesise silver nanoparticles that exhibit a diverse range of resonant frequencies. This will facilitate the investigation of plasmon-driven light-matter interactions across a broad wavelength spectrum.

These synthesised nanoparticles will be immobilised onto functionalised glass substrates. The objective is to ensure that the tunable plasmon resonance observed in the nanoparticle suspension is effectively reproduced in the optical properties of the resulting nanoparticle layer. The meticulous fine-tuning and precise control over the optical properties of the nanoparticle sublayer are imperative for establishing a reliable correlation between the observed plasmon-enhanced excited state dynamics and their corresponding plasmon resonances. This research seeks to clarify the potential mechanisms behind solid-state metal-enhanced absorption and fluorescence in Rubrene. Previous studies have indicated that the efficiency of plasmon-enhanced up-conversion is closely linked to the effectiveness of metal-enhanced fluorescence within the system. By enhancing our understanding of the dynamics and efficiency of solid-state metal-enhanced fluorescence in Rubrene, we can outline strategic pathways for developing more efficient up-conversion devices.

## 1.2 Nanoplasmonics

Noble metal nanoparticles have been the subject of extensive research for several decades due to their intriguing optical and physical properties. The chemical and physical characteristics of bulk noble metals differ significantly from those of their nanoparticle counterparts.[1] Even inert metals such as gold, renowned for their non-reactivity, are considered for catalyst applications when utilised on a nanoscale.[2] The substantial extinction coefficients and high surface-to-volume ratios of noble metal nanoparticles render them a pivotal material for advancing applications in biological imaging,[3] optoelectronics,[4] and photovoltaics.[5]

The optical properties of nanoparticles can be tailored for specific purposes, thereby endowing these particles with a broad range of potential applications.[6–8] The remarkable optical properties encompass a wide range of the electromagnetic spectrum.[7] The surface plasmon resonance (SPR) bands of these particles can be adjusted from the visible to the infrared region.[9–12] This tunability can be achieved by modifying the particles' size, shape, and material composition, as these factors significantly influence the physical properties of the particles.[1] Consequently, solutions with a narrow size distribution and homogeneous shape are imperative for this investigation.

Gold spherical nanoparticles exhibit a vibrant red hue in colloidal solutions, whereas silver spherical nanoparticle colloidal solutions appear yellow.[2] This vivid colouration represents a prominent spectroscopic feature arising from plasmonic effects. An example of a range of possible suspension colours is presented in Figure 2. This image shows a series of gold core-silver nanorod solutions, increasing in length from right to left.

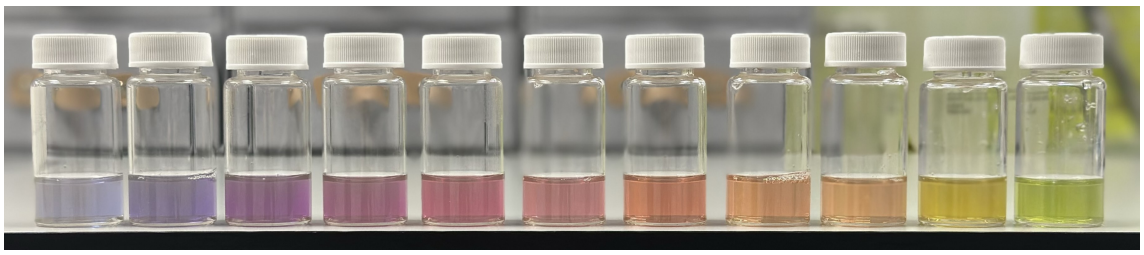

*Figure 2: Colloidal suspensions of gold-core silver nanoparticles of increasing length*

Surface plasmons (SP) are collective oscillations of delocalised electrons that exist near the surface. Surface plasmon polaritons (SPP) are electromagnetic surface waves involving a combined excitation of a surface plasmon and a photon. In a thin film of bulk metal, SPP will propagate parallel to the planar material-dielectric interface until all the energy is dissipated. This dissipation occurs through a combination of energy absorption by the

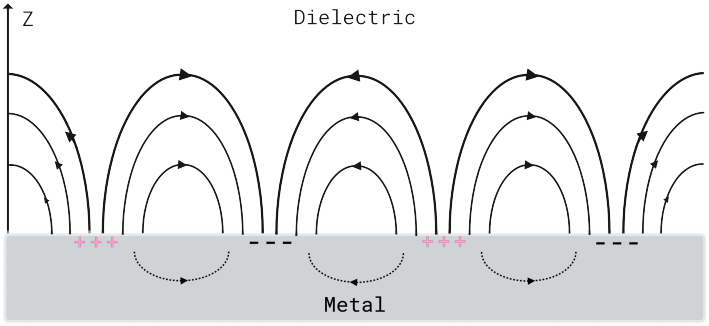


*Figure 3: Schematic of surface plasmon polaritons (SPP) in a bulk metal.*[14]

metallic surface and scattering.[13] A schematic of SPP in a bulk metal is presented in Figure 3. SPR refers to the excitation of SPP in a resonant manner by applying an incident light beam at the resonance frequency.

The optical properties of metal nanoparticles differ significantly from those of thin metal films due to the formation of localised SP. Localised SP are non-propagating excitations of conduction electron oscillations coupled to an electromagnetic field.[13] A schematic of localised SP is presented in Figure 4. The correlated oscillations of conduction electrons result in a collective displacement of the electron cloud relative to the nuclei, creating a restorative force that causes the oscillation of the electron cloud. Consequently, these electron cloud oscillations lead to the development of a dipolar electric field, which is responsible for the observed enhancements in the absorption and scattering capabilities of the nanoparticles. The near-field amplitude at the resonance wavelength is highly localised and decays rapidly with increased distance from the dielectric interface. However, far-field scattering capabilities are also enhanced at the resonance

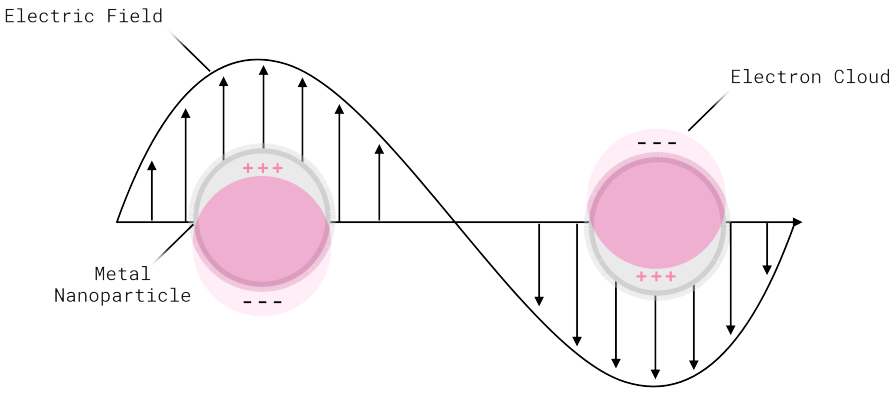


*Figure 4: Schematic of localised surface plasmon resonance (SPR) in noble metal nanoparticles.*[14]

wavelength and can be modulated to enhance phenomena at far-field distances.[13]

The resonance frequency of metal nanoparticles is intricately influenced by their geometric shape, size, and material composition.[1] For small spherical particles, a singular localised SPR is typically observed.[15] The theoretical extinction spectra for 30 nm gold and silver spherical nanoparticles are illustrated in Figure 5. The maximum resonance frequencies for these nanoparticles are situated within the visible spectrum, approximately at 540 nm for gold and 406 nm for silver.[16] The notable difference in the maximum wavelengths of these SPR peaks underscores the significant impact of the material composition on optical properties. Additionally, this resonance peak is expected to exhibit further redshifting and broadening as the diameter of the particles increases due to an increase in the number of plasmon modes.[1]

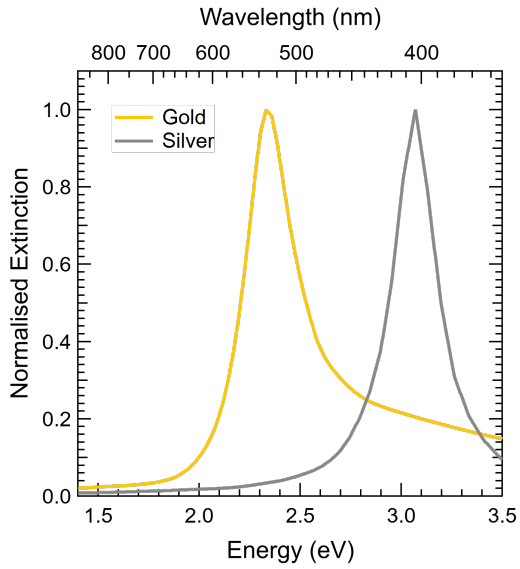


*Figure 5: Normalised theoretical extinction spectra of gold and silver 30 nm nanospheres.*[16]

The size and shape distribution within a nanoparticle suspension significantly influence the spectral profile of the excitation spectrum.[13] In highly monodisperse solutions, the spectral profile aligns closely with the extinction of the suspended particles. The spectral characteristics of spheres, triangular nanoplates, nanorods, and other complex morphologies exhibit distinct differences. An illustration of the difference in the optical properties of various silver nanoparticle shapes is reproduced from a review by Xia et al. in Figure 6 below. All these spectra were calculated with silver as the metal and for nanoparticles 40 nm in size, illustrating the significant shift in the SPR peaks observed when the shape of the nanoparticle is altered.[8]

Two prominent modes are observed in the extinction spectra of anisotropic nanoparticles.[10] The first peak, typically found at shorter wavelengths, corresponds to the trans-

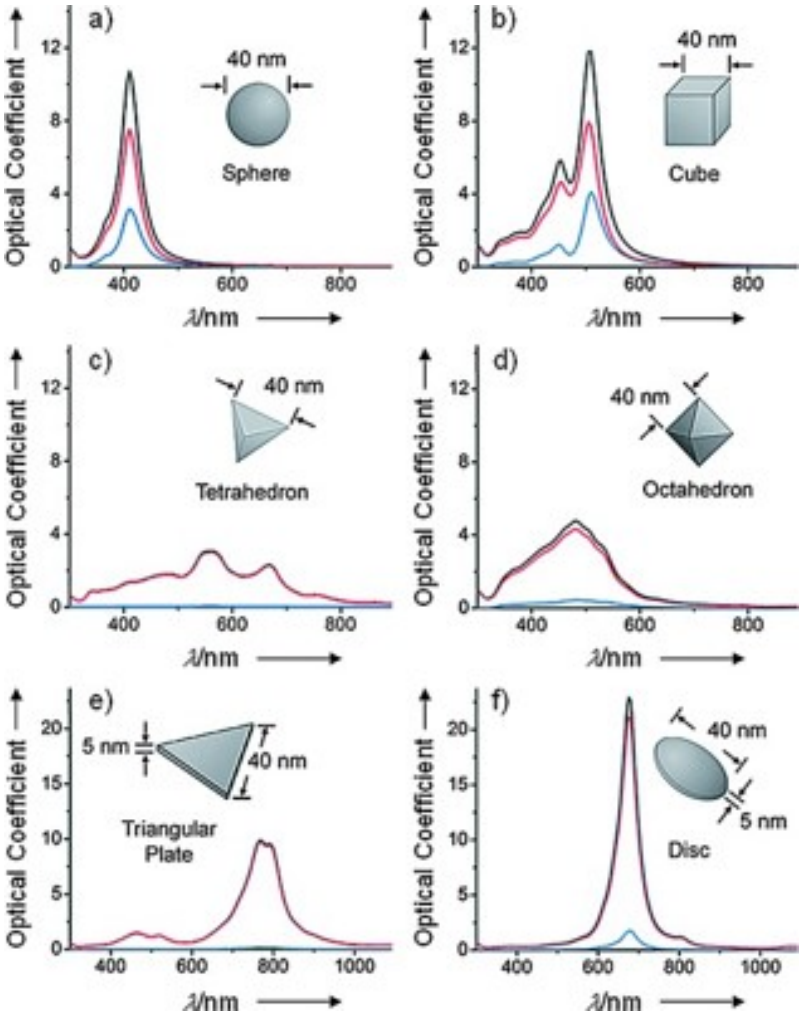


*Figure 6: Calculated extinction (black), absorption (red), and scattering spectra (blue) of silver nanocrystals. Comparing the optical properties of a a) sphere, b) cube, c) tetrahedron, d) octahedron, e) triangular plate, and f) circular plate. As reported by Xia et al.*[8]

verse surface plasmon resonance (TSPR). The second peak, often the most intense, signifies the longitudinal surface plasmon resonance (LSPR). Notably, the TSPR for rod-shaped particles exhibits only a slight shift with increasing particle size. In contrast, the LSPR can shift dramatically from the visible spectrum into the infrared region. As the rods increase in length, additional less intense resonance peaks may emerge, attributed to the less pronounced longitudinal modes.[17]

When various particles of differing sizes and shapes coexist in a suspension, attributing the resonance peaks to the structural characteristics of individual particles can become challenging. The resonance frequencies of each particle shape can be overshadowed by the spectral features of the most dominant morphology. This highlights the necessity for synthetic methods that yield a high production of monodisperse particles of a single type. A clear understanding of the resonance frequencies is essential for the ac-

curate design of plasmonic devices. This is primarily due to the crucial role that spectral overlap plays in many plasmonic enhancement mechanisms.

## 1.3 Noble Metal Nanoparticle Synthesis

The synthesis of spherical gold nanoparticles has been extensively documented in the literature, primarily due to the relatively straightforward and reproducible chemical reduction method.[18–21] While gold nanoparticles have demonstrated optical and electronic enhancement, there has been a growing preference for the use of silver nanoparticles.[22]

Silver nanoparticles have been shown to exhibit stronger optical responses and increased scattering capabilities.[12] Consequently, there has been a surge in the exploration of synthetic methods for producing silver nanoparticles owing to their diverse application potential.[6] However, due to the oxidative nature of silver, synthesising complex morphologies with high yield and monodispersity remains challenging.[23] Numerous studies have concluded that control over size and shape distribution can be achieved by modifying the parameters of the synthetic method.[7]

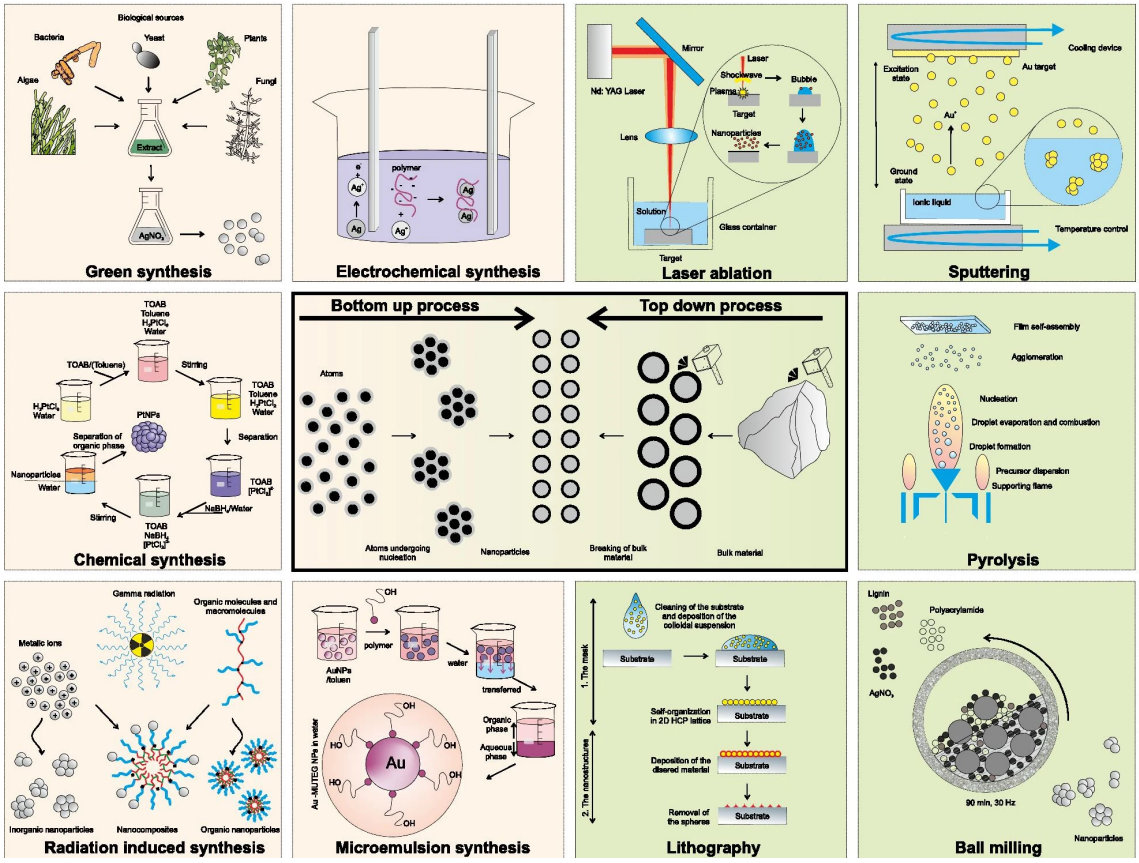


*Figure 7: Schematic representation of the bottom-up (yellow background) and top-down (green background) approaches of nanoparticle synthesis.*[24]

A reproduced image summarising the current nanoparticle synthesis routes in sim-

plified schematics is presented in Figure 7.[24] The synthesis methods for nanoparticles are generally classified into two main categories. The first category is methods involving a top-down process, which involves reducing bulk materials through chemical, physical, or mechanical processes to create nanoparticles.[7] The second category involves methods that employ a bottom-up process, starting with molecules, atoms, or ions to produce nanoparticles.[24] Numerous protocols for both approaches have been developed over the past few decades.[25–28] However, challenges remain regarding the monodispersity of nanoparticle solutions, as many of these protocols often lead to the formation of undesired shapes.[24]

The three primary routes for synthesising silver nanoparticles are physical, chemical, and biological.[29] The choice of a synthetic approach should align with specific application requirements and the desired dielectric conditions. These considerations have led to the expansion of approaches for metal nanoparticle synthesis, for example, synthesis in organic solvents, as aqueous solutions often present challenges in various application areas.[30] Physical methods such as laser ablation,[31] evaporation-condensation,[32] and gamma radiation[33] are renowned for their consistency in producing particles with a narrow size distribution. However, these methods are considered unconventional and expensive due to their high energy consumption for minimal output.[29] In contrast, wet chemical methods for particle synthesis are considered more conventional. Various synthetic routes are known, including chemical reduction,[18] seed-mediated growth,[34] and polyol reactions,[35] among others.[25,36]

### 1.3.1 Chemical Reduction

The chemical reduction method is commonly used to produce spherical nanoparticles, as well as triangular and circular nanoplates. The size, surface chemistry, and distribution of these nanoparticles can be controlled and tuned through the kinetics of the reaction.[37] The chemical reduction method typically involves using a silver salt precursor, commonly silver nitrate, which is reduced using a strong or weak reducing agent, such as sodium borohydride or ascorbic acid.[29] The reduction rate can be controlled through various reaction conditions, including overall reaction temperature, reagent temperature, reagent addition rates, and the precursor-to-reducing agent ratio. Additionally, a capping or stabilising reagent is required to ensure the stability of the particles in a colloidal solution.[7]

Trisodium citrate (TSC) is utilised as a stabilising reagent in many reported synthe-

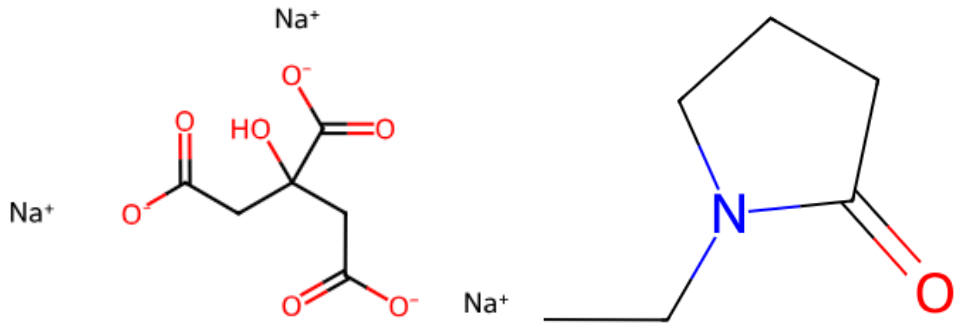


*(a) TSC* *(b) PVP*

*Figure 8: Chemical structures of TSC and PVP, commonly used capping agents in the synthesis of silver nanoparticles.*[38,39]

ses.[40] The chemical structure of TSC is depicted in Figure 8. TSC effectively stabilises the colloidal solution; however, in the case of synthesising small particles (<20 nm), there is a tendency for the particles to aggregate or coalesce into larger clusters over time. Additional surfactants and polymers are commonly employed to enhance stability and impede aggregation and sedimentation.[7]

The list of possible stabilising reagents continues to grow, with more recent studies branching out to investigate the potential of bio-surfactants for nanoparticle stability.[41] Polymers like polyvinylpyrrolidone (PVP) are commonly used reagents, and the repeating monomer for PVP is shown in Figure 8. Previous studies have shown that modifying the polymer chain length directly influences the success of the synthesis and the resulting particle size and shape.[42]

Adding a second stabilising agent is crucial when employing the chemical reduction method for synthesising triangular nanoparticles.[12] Incorporating polymers like PVP in the synthesis augments the initiation rate and reaction time, providing greater control over particle size distribution. Additionally, PVP exhibits a preferential binding to the {111} crystal facet, facilitating growth in the <100> direction. The selectivity of this capping agent is crucial for the anisotropic growth and selective etching required for uniform nanoplate production, leading to highly tunable localised surface plasmon resonance.[37]

Two additional factors that contribute to the successful synthesis of triangular nanoplates are the initial concentration of $H_2O_2$ and the crystal structure of the initial seed particle.[12] The formation of twinned or other defect planes during the nucleation stage is essential for breaking the symmetry of isotropic crystals, thereby assisting the required anisotropic growth.[37] It has been suggested that this critical step highly depends on the initial $H_2O_2$ concentration. Consequently, minor alterations to this concentration

can drastically affect the resulting particles. The initial concentration of $H_2O_2$ must be adequate to remove non-defective particles and induce the formation of planar twinned seeds, but not so high that the reaction is shifted out of dynamic equilibrium.[12]

While the initial concentration of $H_2O_2$ controls the success rate and yield of nanoplates, the concentration of sodium borohydride ($NaBH_4$) is the critical variable for controlling the aspect ratio of the produced particles. Previous work by Zhang et al. demonstrated that increasing the initial concentration increases the average edge length, resulting in a red-shift of the LSPR.[12]

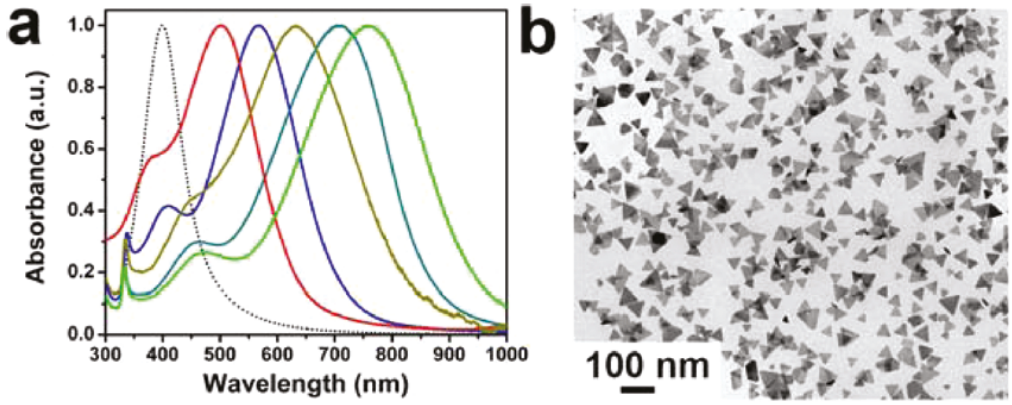


*Figure 9: Normalised extinction spectrum of silver triangular nanoplate suspensions with increasing final $NaBH_4$ concentrations. As reported by Zhang et al.*[12]

Figure 9 above illustrates the significant effectiveness of $NaBH_4$ as the tunable reagent in this synthesis. It provides insight into how increasing the initial concentration of $NaBH_4$ in the reaction promotes a higher yield of triangular plates and increases the average edge length of the plates. The extinction spectra highlight how increasing the edge length of the plates caused a significant red-shift in the LSPR wavelength. A proportionally smaller red-shift was also observed for the transverse mode resonance.[12]

Triangular nanoplates are a preferred morphology in many plasmonic applications due to their enhanced scattering capabilities, which are directly associated with the sharpness of the plate tips. A significant concern in this synthesis is the noticeable truncation at the tips of the plates. This is attributed to the thermodynamically unfavourable high surface energy at the tips, which readily truncates to decrease the overall surface energy.[43]

### 1.3.2 Seed Mediated Growth

Further development and understanding of the seed-mediated growth synthetic pathway has led to the synthesis of more complex morphologies, such as nanorods,[10,34,44] nanostars,[45,46] and chiral nanoparticles.[47] The reagents involved in the seed-mediated growth method are similar to most chemical reduction methods.[29] However, the synthesis occurs stepwise, with the nucleation reaction occurring first to form seeds or sub-10 nm spherical nanoparticles. These seeds are then introduced to a growth solution containing more silver salt precursor and a weaker reducing agent, typically ascorbic acid. This stepwise method ensures homogeneous nucleation and eliminates the possibility of new nucleation during the growth stage.[44] The growth solution usually contains a surfactant, typically cetyltrimethylammonium bromide (CTAB) or cetyltrimethylammonium chloride (CTAC), that acts as a directing agent.[48] The chemical structures of CTAB and CTAC are presented in Figure 10.

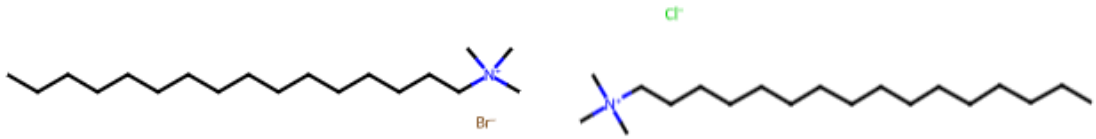


*(a) CTAB* *(b) CTAC*

*Figure 10: Chemical structures of CTAB and CTAC, commonly used shape-directing surfactants in the synthesis of silver nanoparticles.*[49,50]

In some methods, a combination of both surfactants is utilised, with the choice of surfactant being dependent on the desired size and shape of the particles. These surfactants are necessary to facilitate the anisotropic growth of complex morphologies.[37]

Control over these parameters is crucial for the CTAB-directed syntheses of nanorods, as optimised parameters are essential to achieve high rod-to-sphere yields.[44] Other variables that impact the particle size and shape in a seed-mediated growth method include the volume of the seed solution introduced to the growth solution and the concentration of the silver salt. Increasing the volume of the seed solution added to the growth solution has been previously reported to decrease the aspect ratio, whereas reducing the volume has been shown to increase the aspect ratio.[51] Alternatively, increasing the concentration of the silver salt precursor in the growth solution has been shown to increase the aspect ratio and decreasing the concentration will reduce it.[34]

### 1.3.3 Polyol

The polyol method has been hailed as a practical synthetic route for producing uniform silver nanoparticles, especially short silver nanorods.[52,53] Similar to the seed-mediated growth method, this method achieves uniform growth. However, it requires high temperatures, usually 100-200 °C, and more complex reagents than other wet chemical methods.[54] In polyol synthesis, the silver salt precursor is suspended in a glycol solvent at elevated temperatures for a specified duration. In most reported methods, silver trifluoroacetate (AgTFA) is the preferred silver salt precursor over the commonly used silver nitrate ($AgNO_3$) due to the decomposition of the nitrate group at elevated temperatures. The temperature required for the reaction ranges from 80-180°C, and this decomposition renders the reaction unpredictable and challenging to predict. Temperature is a critical variable in this synthesis, as even slight changes can significantly impact the resulting particle solutions due to alterations in the reduction rate.[52]

In contrast to other wet chemical methods that utilise $NaBH_4$ as the reducing agent, the polyol synthesis induces the reduction by the glycol solvent, which occurs only at specific temperatures depending on the chosen glycol solvent. While ethylene glycol is the most commonly employed polyol solvent, various methods utilise other glycol solvents such as 1,2-propylene glycol and 1,5-pentanediol.[55] Polyol synthesis also involves the addition of reagent additives to steer the reaction toward a specific shape.[43] For instance, the synthesis of nanocubes in the polyol method includes the addition of sodium sulfide ($Na_2S$) or sodium hydrosulfide (NaHS), which is not included in the synthesis of nanorods.[56] In contrast, additives like hydrochloric acid (HCl) and tannic acid (TA) are added to control pH and aid in preferential etching to synthesise silver nanorods.[53]

Apart from the high-temperature requirements, another drawback of the method is the challenge of tuning through adjustments in reagent concentrations. The most significant tuning parameter for the synthesis of nanorods via the polyol method is time.[52] If the reaction is conducted for too short a duration, only very short rods will be produced. Increasing the time allows these rods to grow longer, with an upper limit to this growth due to the complete use of the remaining silver precursor. This method yields short nanorods with high yield and low size distribution. Few studies into the tuning of these rods have been published without the need for a gold core stabiliser.[53] The synthesis of gold nanorods has also been reported. However, they do not process the same size and shape control as previous seed-mediated growth synthetic methods.[57,58]

### 1.3.4 Complimentary Core-Shell Methods

The synthesis of more complex nanoparticle morphologies often necessitates advanced methods, particularly for achieving aspect ratios that correspond to localised SPR in the 800-1000 nm range. While gold nanorods can be synthesised in high yield with precise control over aspect ratios, allowing for an extensive range of lengths, silver nanorods have presented challenges in achieving similar yields.[44] Previous polyol methods that utilised only silver have succeeded in producing a high yield of both short nanorods, approximately 100 nm in length, and long wires, reaching up to 1 µm in length.[53] However, the glycol solvent associated with this synthetic approach can complicate purification, thereby hindering the further application of these nanoparticles in fabrication processes.

Consequently, alternative techniques, including incorporating a secondary metal, have been explored to yield these more intricate shapes.[9,52] A notable example is the synthesis of silver nanorods with a gold core. Numerous studies have documented methods for fabricating silver nanorods with tunable aspect ratios by overgrowing silver on gold bi-pyramidal or other shaped cores.[11,59] These synthesis strategies emphasise the importance of starting with a uniform foundation when producing complex anisotropic particles; many reports indicate success in achieving a monodisperse solution of silver nanorods when extra purification steps are taken and when beginning with a monodisperse solution of gold core particles.

While this technique enables the synthesis of a high yield of nanorods, the inclusion of the secondary material that makes up the core can impact the resulting plasmon resonance. However, previous studies have shown that the core does not influence the plasmonic properties of nanorods when the shell thickness exceeds 5 nm.[60]

### 1.3.5 Influence of PVP in Nanoparticle Synthesis

PVP is a common additive in nanoparticle synthesis and acts as a dispersant, capping agent, or mild reducing agent, depending on the synthetic conditions. The stabilisation of nanoparticles in a colloidal solution relies on either steric repulsion or electrostatic stabilisation mechanisms.[61] Steric repulsion involves incorporating polymers, such as PVP, into the system, where they adsorb onto the particle surfaces, preventing contact with other nanoparticles in the suspension. To maintain steric repulsion, a sufficiently high polymer concentration is required to form a suitable coating on the particles, preserving repulsion between the hydrophobic carbon chains in the polymer layers. This differs from the mechanism employed in CTAB-capped particle solutions, which rely on the

distribution of charged species in the system to sustain electrostatic stabilisation.[62] Additionally, PVP's ability to achieve elongated inter-particle distances makes it an attractive dispersing agent.

Like most polymers, PVP is commercially available in various chain lengths. Previous studies, such as the one conducted by Xia et al., have shown that modifying the chain length can directly influence the size of the nanostructures formed. In the study, reducing the chain length from 55K to 10K while keeping all other reagents and concentrations constant significantly increased the final nanocube edge from 80 to 130 nm. The researchers attributed this change to the more efficient packing achieved by the shorter PVP chain, facilitating effective minimisation of surface free energy and promoting further growth along the {111} facet. They supported their theory with surface coverage calculations, which revealed that the coverage for the 10K PVP was reduced to 30 repeating units per $nm^2$ compared to 140 units for the 55K PVP.[64]

A study by Tsuji et al. has shown that altering the PVP chain length during synthesis can influence the shape of the resultant particles. Tsuji and co-workers observed that increasing the PVP length from 10 to 40 and 360K significantly influenced the preferred particle morphology. Specifically, when the shortest chain (10K) was used, the polyol synthesis yielded a high yield of nanoplates and sheets. In comparison, an increase in

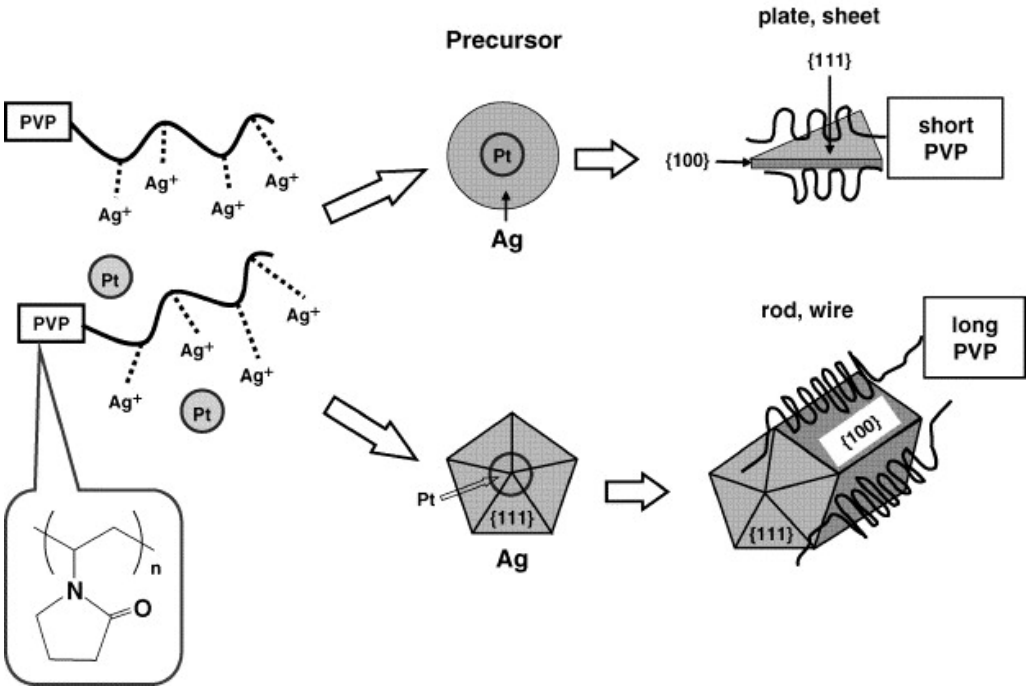


*Figure 11: A reproduced schematic of the proposed formation mechanism for different silver nanostructures under microwave irradiation for short-chain (10k) and long-chain (40k and 360k) PVP. As reported by Tsuji et al.*[63]

chain length to 40 or 360K resulted in a shift to nanorods and wires as the preferred morphology.[63]

The researchers attributed this phenomenon to the influence of chain length on the growth rate between the {100} and {111} directions. A reproduced schematic of their proposed formation mechanism is presented in Figure 11 above. This figure shows that the shorter 10K PVP chain was predominantly adsorbed onto the {111} facet, leading to an increased growth rate in the {100} direction and a higher yield of nanoplates. Conversely, for longer chain lengths, the PVP was preferentially adsorbed onto the {100} facet over the {111} facet, facilitating an increased growth rate in the {111} direction. The authors hypothesised that the adsorption selectivity occurs within the 10K to 40K molecular weight range, as no significant change in the particles produced was observed when the chain length was increased from 40K to 360K. This suggested a limitation to the influence of the chain length.[63]

## 1.4 Nanoparticle Immobilisation and Plasmon-Plasmon Coupling

The immobilisation of nanoparticles has garnered considerable attention in the field of nanoplasmonics.[65–67] Numerous studies are focused on utilising a fabricated nanoparticle layer as the foundational element of plasmon enhancement devices.[68,69] Immobilising nanoparticles onto functionalised substrates offers a practical approach to investigating potential plasmonic enhancement in the solid state. However, the practicality of the wet chemical fabrication of these nanoparticle layers poses notable challenges, including the degradation of nanoparticles during the immobilisation process and reduced control over critical design parameters, such as inter-particle distance, which can be more easily managed through engineered fabrication techniques.[70,71]

The immobilisation of nanoparticles with a controlled inter-particle distance enables the exploitation of a phenomenon known as plasmon-plasmon coupling.[72] This coupling, relevant in plasmonics and nanophotonics, serves as an effective tool for tailoring light-matter interactions on a nanoscale.[68] It arises from the interactions between the near-field electromagnetic fields of individual plasmons in close proximity, resulting in the creation of new hybridised plasmonic modes through the redistribution of electromagnetic energy. Consequently, plasmon-plasmon coupling can significantly influence the optical properties of a plasmonic system, leading to considerable variations in the spectral signature of nanoparticles immobilised in an array compared to when they are in suspension.[72]

Numerous factors, including the material, shape, size, and proximity of the particles, can influence the strength of the plasmon-plasmon coupling and the resulting modes.[70–72] Although effective control over the starting size, shape, and material compositions of the particles in these arrays can be achieved during nanoparticle synthesis, controlling factors such as particle proximity proves to be more challenging when employing wet chemical fabrication methods. It has been observed that the enhancement is maximised when particles are within a sub-2 nm proximity. Consequently, the majority of plasmon-plasmon coupling investigations resort to engineering techniques, such as electron beam lithography, for array fabrication.[73]

Electron beam lithography (EBL) is widely recognised as an effective technique for fabricating metal nanoparticle arrays, as it produces reproducible samples with uniform particle sizes and controlled inter-particle distances.[71] However, this method is associated with high energy and material costs. Additionally, existing methods currently offer a limited range of possible morphologies, which ultimately constrains the options available for tuning the optical properties of the arrays.[70] Research utilising EBL has demonstrated that plasmon coupling is polarisation-dependent. When the inter-particle axis and the polarisation direction of the incident light are parallel, the SPR is red-shifted compared to a single particle. Conversely, when the polarisation direction of the incident light is orthogonal to the inter-particle axis, a blue-shift is observed. However, this shift is significantly smaller than the parallel polarisation red-shift.[72]

Many wet-chemical fabrication processes utilise polymers as substrates, as the material can be manipulated to modulate the inter-particle distance.[66] A prior study by Yu et al. showcased an efficient approach for the wet chemical fabrication of silver nanosphere films using the Langmuir-Blodgett technique. In this study, Yu and co-workers successfully created high-density nanosphere substrates on temperature responsive polymer membranes. The use of polymers as substrates introduced the potential to manipulate inter-particle distances within the arrays, as these polymers shrink to varying extents when exposed to increased temperatures. This systematic adjustment of distances between nanoparticles clearly illustrates the shift in optical properties that can occur when the plasmon-plasmon coupling strength is altered. As the temperature rose and the polymer contracted more significantly, the number of nanoparticles in near-field proximity increased, leading to a red-shift of up to 110 nm in the plasmon resonance of the film.[74]

## 1.5 Plasmon-Enhanced Light-Matter Interactions

Various computational and experimental investigations have been conducted over the past few decades to validate plasmon-enhanced light-matter interaction processes.[6,75–78] The plasmonic effect has the potential to significantly enhance processes such as Raman scattering, fluorescence, photocatalysis, heat generation, and solar energy conversion by orders of magnitude due to its ability to enhance the local electric field. These observed enhancements offer substantial improvements in efficiency and signal quality for their respective applications.[6]

### 1.5.1 Surface Enhanced Raman Spectroscopy

The integration of silver nanoparticles has shown promise in enhancing surface-enhanced Raman spectroscopy (SERS), a vibrational spectroscopy technique with extremely high cross-section, making it practically applicable to single molecules. SERS, as a near-field enhancement technique, provides sensitive fingerprint structural information for single molecules and can be combined with other techniques, such as nuclear magnetic resonance (NMR), electron microscopy (EM), and X-ray diffraction (XRD), for comprehensive system analysis.[77]

The nanoparticle arrays fabricated on temperature-controlled polymer substrates, as described in the study by Hu et al., served as SERS substrates for Rhodamine 6G. The work by Hu and colleagues showcased the potential for optimising the signal enhancement factor by finely tuning the parameters of the nanoparticle substrate, which in turn influences the plasmon resonance of the nanoparticle array. They reported an enhancement factor increase of up to 100 times for specific bands, clearly illustrating the significance of spectral overlap in plasmonic systems.[74] The theoretical and experimental development of SERS systems is still evolving, and future advancements will depend on enhancing the reproducibility of SERS substrates that utilise nanoparticles with more intricate morphologies and broader spectral ranges.

### 1.5.2 Metal-Enhanced Fluorescence

Another significant application of plasmon-enhanced light-matter interactions is metal-enhanced fluorescence (MEF) and metal-enhanced absorption (MEA). Metal-enhanced fluorescence has been the subject of extensive research over the past few decades as a promising advancement in fluorescence spectroscopy.[6,75,76,79] This phenomenon has been developed through various techniques, ultimately resulting in the favourable modifica-

tion of the brightness and photostability of fluorophores in the near field of plasmonic materials. Incorporating noble metal nanoparticles and thin metallic films into systems has been a common approach to achieve this plasmonic enhancement. Figure 12 below illustrates a reproduced schematic of metal-enhanced fluorescence emission.[6] Figure 12 illustrates how the three mechanisms of localised SPR (a), plasmon-coupling (b) and radiative decay engineering (RDE) contribute to the overall fluorescence enhancement observed in MEF.[80]

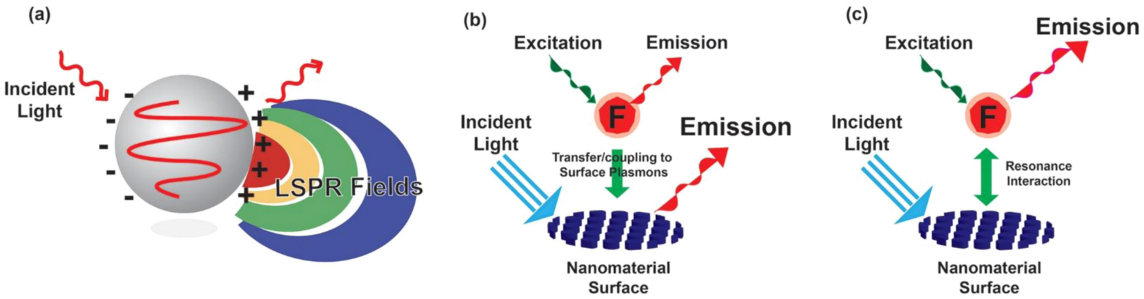


*Figure 12: Schematic of the mechanisms, localised SPR (a), plasmon-coupling (b) and radiative decay engineering (c), involved in metal enhanced fluorescence. As reported by Jeoug et al.*[80]

The LSPR mechanism involves the interaction of incident light with metal nanostructures. The light excites the free electrons in the metal, causing them to oscillate collectively. This oscillation creates a concentrated electric field around the metal surface. When fluorophores are positioned within the near-field, at a distance of less than 10 nm from the plasmonic material, they exhibit an increase in fluorescence intensity and a decrease in fluorescence lifetime. The enhanced electromagnetic field generated by the localised surface plasmon resonance around the metal nanostructure leads to a higher excitation rate and stronger fluorescence emission in the nearby fluorophores.[80]

The plasmon-coupling mechanism is the efficient coupling between the generated electromagnetic field and the nearby fluorophore. The non-radiative energy transfer resulting from this coupling enhances the excitation and emission rates of the fluorophore, leading to brighter fluorescence. The efficiency of this energy transfer depends on the distance between the metal and the fluorophore; optimising this distance allows for dominant energy transfer. The enhancement efficiency also depends on the spectral overlap between the SPR of the nanoparticles and the absorption spectrum of the fluorophore. The physical properties of the nanostructures also impact the degree of enhancement. Nanoparticles with sharp corners or defined edges exhibit a confined intensification of the electromagnetic field, effectively acting as an antenna to further enhance the fluorescence intensity of nearby fluorophores.[80]

The third mechanism, radiative decay engineering (RDE), involves modifying the radiative and non-radiative decay rates of the fluorophore to achieve an effective emission enhancement. The fluorophores in the near field, in an excited state, interact with the plasmons generated by the metal surface. These interactions alter the decay rates of the fluorophore, leading to more efficient emission and a shorter fluorescence lifetime. As a result, the fluorophore undergoes more excitation-emission cycles before photobleaching, leading to enhanced brightness and photostability.[80]

Han et al. investigated the metal-enhanced fluorescence of rubrene through the development of a series of core-shell Ag-rubrene nanoparticles to explore the potential enhancement when the organic light-emitting molecule was physically attached to metal nanoparticles.[81] The absorption and photoluminescence spectra for these core-shell nanoparticles can be found in Figure 13 below.

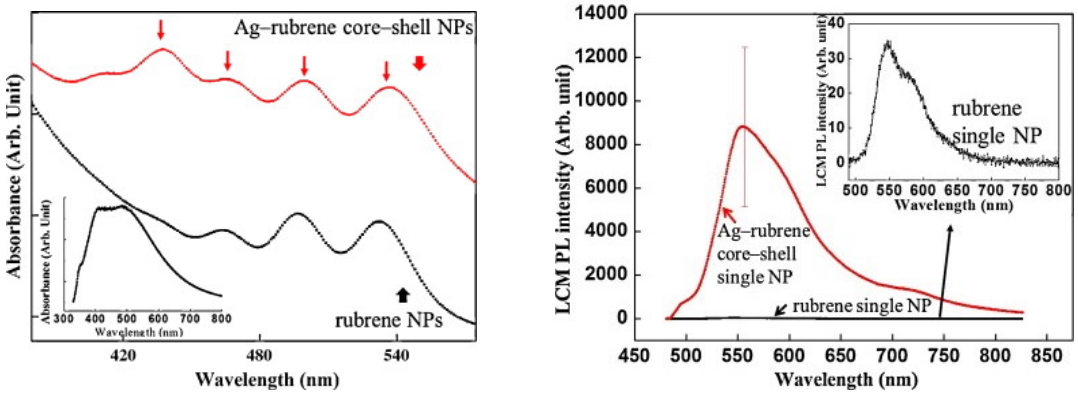


*(a) Absorbance* *(b) Photoluminescence*

*Figure 13: Absorbance and photoluminescence spectra comparing the intensity of core-shell Ag-rubrene and rubrene-only nanoparticles. Inset 1: UV/vis absorption spectrum of Ag NPs. Inset 2: Magnified LCM PL spectrum of rubrene single NPs. As reported by Han et al.*[81]

Han and colleagues confirmed the presence of both silver and rubrene in the core-shell nanoparticles through changes in the spectral profile. The absorbance spectrum of the isolated silver nanoparticles exhibited a single broad peak at 410-490 nm. Further analysis using spectrum and high-resolution transmission electron microscopy (HR-TEM) images revealed that the nanoparticles were polydisperse, with predominantly polyhedron-shaped particles having an average diameter of 72 nm. The absorbance spectrum of the rubrene nanoparticles exhibited the anticipated three peaks corresponding to the vibrational band transitions of rubrene at 463, 497, and 533 nm. In contrast, the absorbance spectrum of the core-shell nanoparticles showed the characteristic peaks of the rubrene and silver nanoparticles.[81] A high-resolution laser confocal microscope was employed to assess the photoluminescence intensities of the core-shell nanoparticles. The

average photoluminescence spectrum of the core-shell nanoparticles exhibited a 300-fold increase in intensity compared to the rubrene-only particles. The authors proposed that this heightened intensity resulted from the potential surface plasmon coupling enabled by the spectral overlap between the silver nanoparticles and rubrene.[81]

### 1.5.3 Photon Up-Conversion

Photon up-conversion is a photophysical phenomenon that has garnered considerable attention in research in recent decades.[82–86] It involves the absorption of two low-frequency photons to produce one higher-frequency photon.[82] This phenomenon has potential applications in biological imaging and solar energy.[83] Figure 14 below illustrates a typical schematic for the up-conversion phenomenon via triplet-triplet annihilation (TTA). In this process, the sensitiser molecule absorbs the low-energy photon, which then undergoes rapid intersystem crossing (ISC) to its triplet state. The energy of the sensitiser triplet is transferred to the triplet state of the emitter molecule. Through TTA, the energy from the two triplets can combine to form a singlet state of higher energy, which results in the emission of the higher energy photon from the emitter.[82]

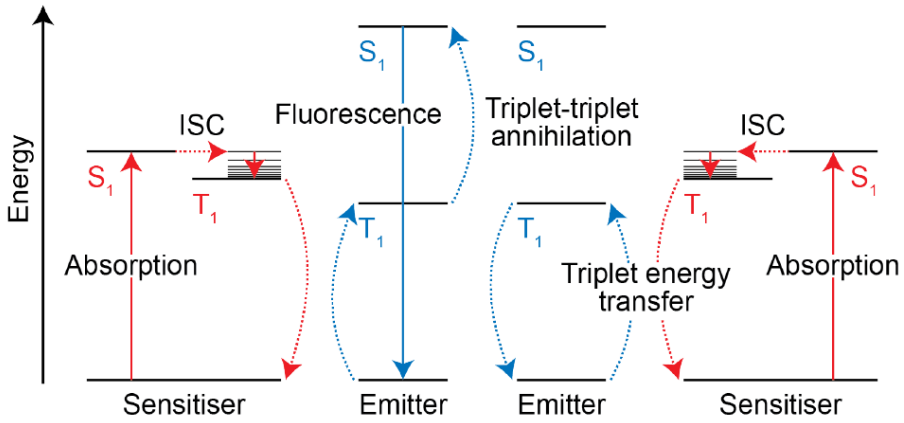


*Figure 14: Schematic of the upconversion phenomenon via TTA*

Numerous studies have investigated the phenomenon of up-conversion in polycyclic aromatic hydrocarbons.[85,87,88] Many of these inquiries have relied on semiconductor nanocrystals or quantum dots to facilitate the necessary energy transfer. Studies completed by Huang et al. demonstrated up-conversion through energy transfer from a lead selenide (PbSe) nanocrystal to the triplet state of rubrene. TTA followed this energy transfer to generate a higher energy singlet state, which, upon relaxation, emitted an up-converted photon. The proposed schematic for this process is illustrated in Figure 15. Notably, the ligands attached to the nanocrystal are electronically inert, precluding

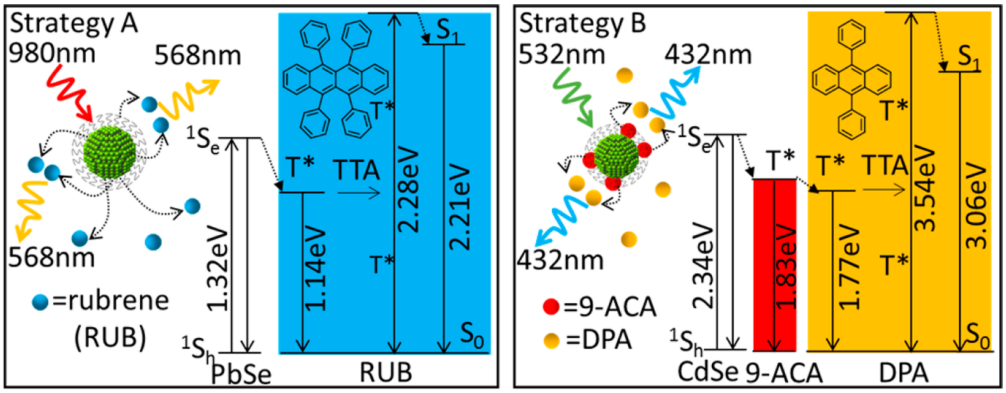


*Figure 15: Reproduced schematic of the nanocrystal up-conversion strategy. As reported by Huang et al.*[85]

the observation of an energy cascade.[85]

The study was conducted in the liquid phase and demonstrated the potential for up-conversion in polycyclic aromatic hydrocarbons. The research shows that this mechanism offers great flexibility by utilising various combinations of nanocrystals and emitters. The wide range of potential combinations also allows for the tunability of excitation and emission wavelengths.[85]

Many systems described in the literature utilise up-converting nanoparticles (UCNPs). UCNPs are usually comprised of semiconductor materials, either doped with rare earth elements or capped with sensitiser and emitter molecules.[82] While up-conversion systems that involve organic material are constrained by the relatively low photostability of organic compounds, UCNPs are significantly more photostable and are considered a favourable alternative in up-conversion systems. However, UCNPs have a relatively low quantum yield due to the small absorption cross-section and the surface quenching effect. Various optimisation techniques have been explored to enhance the quantum yield of UCNPs, including adjusting the concentration and type of rare earth ions, developing core-shell structures, and integrating plasmon nanoantennas.[82]

Research conducted by Zhou et al. involved the design of a composite film comprising a silver spherical nanoparticle layer on a glass substrate, layered with a zinc oxide (ZnO) spacer, and topped with a layer of UCNPs. This study revealed that the incorporation of the silver nanoparticle layer and the consequential plasmonic effect significantly improved the observed up-conversion efficiency in the UCNPs. They attributed this observed efficiency to the ability of the tailored nanoparticle structure to act as nanoantennas. The study also found that the thickness of the ZnO spacer layer significantly impacted the up-conversion intensity.[84]

Recent studies have highlighted the need for a transition to solid-state up-conversion investigations, as liquid-phase up-conversion systems are not considered suitable for device applications. However, these studies reveal several significant challenges that must be addressed to develop effective solid-state up-conversion devices. One of the primary challenges is optimising the sensitiser-to-emitter ratio. The concentrations of these two components must be carefully managed, and the fabrication processes for solid-state devices complicate consistent control of this parameter. If this ratio is not effectively regulated, the efficiency of the up-conversion system may be compromised. The potential applications of solid-state up-conversion systems represent a significant advancement in the pursuit of enhancing the overall efficiency of light harvesting.[89] This drives ongoing research into novel up-conversion systems.

## 1.6 Rationale and Design of the Study

More recently, plasmonic enhancement studies have shifted focus to applications in photovoltaics, aiming to improve the efficiency of solar cells.[90] Incorporating plasmonic nanoparticles into solar cells has shown potential for increasing light harvesting efficiency and improving photovoltaic performance by broadening the absorption cross-section across the electromagnetic spectra. Additionally, the increased scattering effects of plasmonic nanoparticles can enhance the optical path lengths of incident photons, contributing to increased absorption efficiency and photovoltaic conversion performance.[68] The careful design of plasmonic devices through alterations in morphologies, concentrations, and geometric positioning is crucial for achieving these enhancements in absorption efficiency and photovoltaic conversion performance.[6]

Ultimately, this project aims to develop a solid-state up-conversion device. The initial schematic of the device design is presented in Figure 1. However, previous research has highlighted the necessity of reproducibility and control over the design parameters of such solid-state devices.[89] Solid-state up-conversion has been previously demonstrated in Rubrene.[85,88] However, several critical limitations must be addressed to enhance its applicability. The foremost challenge is the low efficiency observed in current systems, which primarily stems from the intricate fabrication challenges inherent to solid-state devices.[89] Consequently, a significant portion of this research has concentrated on optimising the fabrication protocols associated with essential design parameters. We hypothesised that the efficacy of a plasmon-enhanced up-conversion system required an initial optimisation of the plasmonic layer.

Previous studies have shown that a thorough understanding of the efficiency of plasmon-enhanced up-conversion systems begins with an exploration of the mechanism underlying metal-enhanced fluorescence.[91] Below, Figure 16 presents a reproduced schematic of the plasmon-enhanced TTA up-conversion mechanism as proposed by Honda et al. This figure highlights two key aspects of the mechanism that are directly influenced by the plasmonic component of the system. The first aspect is the enhancement of photoexcitation by the plasmonic electromagnetic near-field effect, which leads to increased singlet production in the sensitiser. The second aspect concerns the increase of the radiative decay process in the emitter. However, it has been theorised that this enhancement contributes less significantly to the overall increase in up-conversion efficiency.[91]

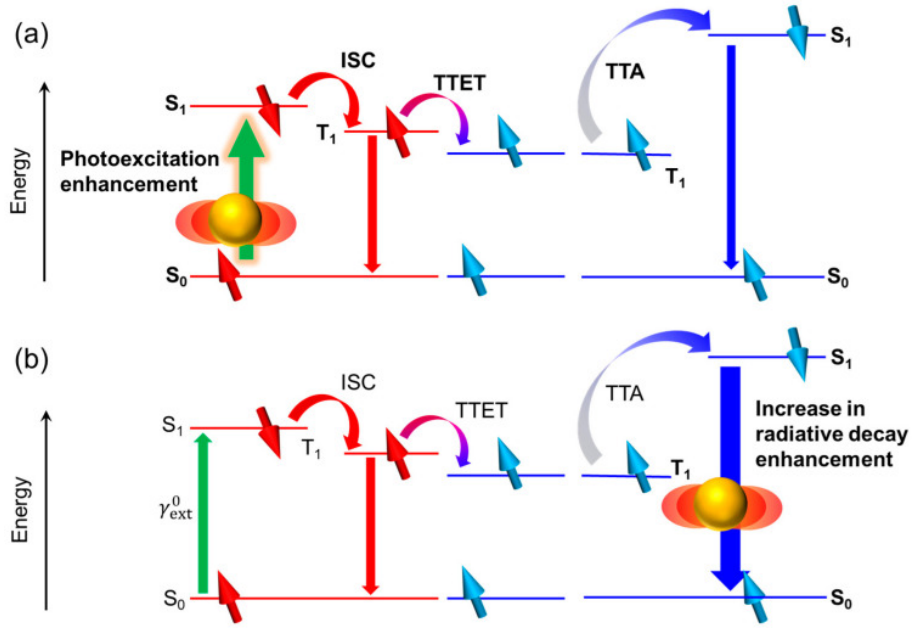


*Figure 16: Plasmon-enhanced photon up-conversion triplet-triplet annihilation mechanism as reported by Honda et al.*[91]

The energy level diagram of Rubrene, illustrated in Figure 17, depicts the pivotal energy levels within this system, most notably the first excited singlet state at 2.2 eV and the triplet state at 1.14 eV.[92]

This study aimed to investigate the dynamics of solid-state plasmonic enhancement in Rubrene thin films by incorporating a resonance-tuned nanoparticle sublayer into the device. The primary objective was to optimise potential metal-enhanced absorption and emission through the fine-tuning of the resonance frequencies of the plasmonic element. Specifically, we aimed to establish robust nanoparticle synthesis methods and film fabrication protocols to create a series of nanoparticle sublayer films. A key design parameter

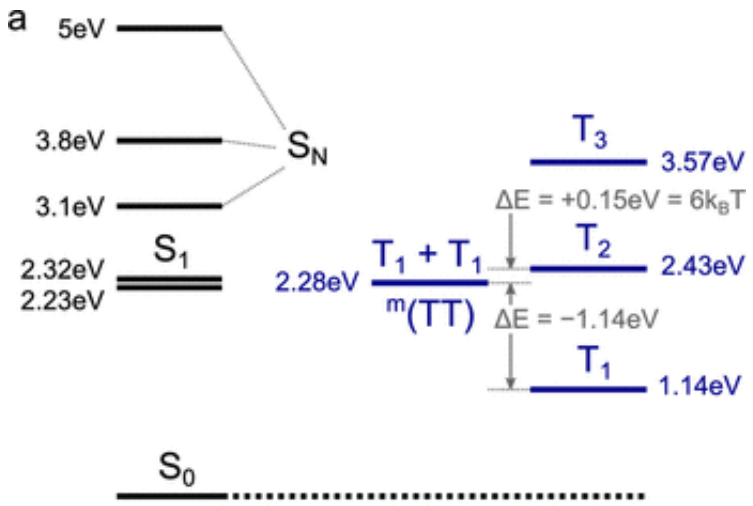


*Figure 17: Excited state energy diagram of Rubrene.*[92]

for these sublayers was the ability to adjust the SPR frequency across the electromagnetic spectrum. Our goal was to observe how the metal-enhanced fluorescence efficiency would vary with spectral overlap as the resonance frequency of the nanoparticle sublayer was systematically shifted towards the T1 triplet state at 1.14 eV. To achieve this, we planned to design the extinction properties of the plasmonic nanostructures in suspension so that they peaked across a wavelength range of 400-1000 nm. This broad range of plasmon resonance peaks was crucial for examining the effects of plasmon-plasmon coupling when these nanoparticles were immobilised on a glass substrate.

This available range enabled tuning the optical properties of the nanoparticle sublayers across the electromagnetic spectrum to align with the T1 triplet energy state. Previous studies have demonstrated that the strength of plasmon-plasmon coupling, and consequently the resultant shift in plasmon resonance, is influenced by the density of nanoparticles in the array and the number of particles in near-field proximity.[74] Therefore, we focused on optimising the immobilisation protocols to control these critical features of the nanoparticle array. Several post-synthetic treatments were also investigated to ensure the nanoparticles were highly stable and did not change shape during the immobilisation process. Once the immobilisation protocol was optimised, a thin film of Rubrene was overlaid onto the plasmonic sublayer.

We anticipated that thin films created from a rubrene solution in toluene, at maximum solubility (11 mM), would exhibit a sufficient molecular density for two Rubrene molecules in the excited T1 triplet states to engage in TTA. Consequently, this concentration was used to fabricate all Rubrene thin films in this study. Instead of the commonly used thermal evaporation method, we employed a spin coating technique for fabrica-

tion. A correlation was established between the spin coater rotation rate and the thickness of the rubrene films. Finally, we utilised steady-state and time-resolved fluorescence techniques to investigate the excited-state dynamics and any plasmonic enhancement observed within the system with each variation in the plasmonic sublayer.

# 2 Chapter 2 - Experimental Methods and Data Processing

## 2.1 Materials

Cetyltrimethylammonium Bromide (CTAB, 98%), Cetyltrimethylammonium Chloride (CTAC, 25 wt% $H_2O$), (3-Aminopropyl)trimethoxysilane (APTES, 97%), (3- Mercaptopropyl)trimethoxysilane (MPTMS, 95%), 5,6,11,12-tetraphenyl tetracene (Rubrene, 99.99%), Sodium Borohydride ($NaBH_4$, 99%), Chloroform (analytical standard), Poly(sodium 4-styrenesulfonate) (PSS, Mw=70000), Polyvinylpyrrolidone (29K PVP, Mw=29,000), Polyvinylpyrrolidone (10K PVP, Mw=10,000), Methanol (reagent standard), Acetone (reagent standard) and Toluene (Anhydrous, 99.8%) were all purchased from Merck (Sigma-Aldrich). L-Ascorbic Acid (AA, analytical standard), Hydrogen Peroxide ($H_2O_2$, 30%), Nitric Acid ($HNO_3$, 70%), Hydrochloric Acid (HCl, 26%), and Sulfuric Acid ($H_2SO_4$, 95%) were all purchased from ThermoFisher Scientific. Trisodium Citrate (TSC, 99%), Polyvinylpyrrolidone (44K PVP, Mw=44,000) and Silver Nitrate ($AgNO_3$) were all purchased from Avantor. All chemicals were used as received, with no additional purification performed.

## 2.2 Nanoparticle Synthesis

### 2.2.1 Aqua Regia Cleaning

All glassware used to synthesise, characterise, or store nanoparticles was cleaned for 5 minutes with a 3:1 HCl:$H_2NO_4$ concentrated aqua regia solution. The glassware was rinsed thoroughly with Type I water and dried under a stream of compressed air before use.

### 2.2.2 Silver Nanorod Synthesis

Silver nanorods were synthesised using a seed-mediated growth method. This synthesis was a variation of a previously reported method by Rekha et al.[51]

In the reported seed synthesis ice-cold, freshly prepared $NaBH_4$ (10 mM, 600 µL) was quickly injected into an aqueous solution of CTAB (100 mM, 80 µL) and $AgNO_3$ (20 mM, 500 µL) in 19.92 mL of Type I water, under vigorous stirring. Upon addition, the solution changed from colourless to pale yellow, and after a few minutes, the solution turned bright yellow.

A growth solution of $AgNO_3$ (20 mM, 250 µL) and AA (100 mM, 500 µL) was added to an aqueous solution of CTAB (10 mM, 10 mL) under vigorous stirring. The required volume of silver nanoseeds was then added. Upon addition, stirring was stopped, and

the final reagent NaOH (1 M, 100 µL) was quickly introduced. The solution was gently swirled to disperse the NaOH, resulting in a series of colour changes from cloudy white to yellow and several intermediate colours until the final colour was achieved. The ultimate colour of the solution depended on the seed concentration. The solution was centrifuged twice at 6000 RPM for 15 minutes to remove excess reagents and purify the nanostructures. After centrifugation, the platelet was re-dispersed in either 10 mL of Type I water or 10 mL of CTAB (10 mM).

### 2.2.3 Silver Gold-Core Nanorod Synthesis

The gold-core silver nanorods were synthesised using a multi-step seed-mediated growth method. This synthesis combines two previously reported methods by Zhuo et al.[59] and Sánchez-Iglesias et al.[11]

Gold seeds were prepared following the reported synthesis by Zhuo et al.[59] Ice-cold, freshly prepared $NaBH_4$ (10 mM, 150 µL) was quickly injected into an aqueous solution of $HAuCl_4$ (10 mM, 125 µL) and TSC (10 mM, 250 µL) in 9.5 mL of Type I water, under vigorous stirring. Upon addition, the solution changed from pale yellow to brown, and after several minutes, the solution turned red.

The gold bi-pyramids were prepared using the gold seeds described above following a previously reported synthesis by Sánchez-Iglesias et al.[11] $HAuCl_4$ (10 mM, 1 mL), $AgNO_3$ (10 mM, 200 µL), HCl (1 M, 400 µL) and AA (100 mM, 160 µL) was added to an aqueous solution of CTAB (100 mM, 20 mL) under vigorous stirring. The required volume of gold nanoseeds was added to this growth solution. Once added, stirring was stopped, and the mixture was kept at 30 °C for two hours. 10 mL of the solution was centrifuged twice at 8000 RPM for 30 minutes and re-dispersed in CTAC (10 mM, 79 mL).

To synthesise the silver nanorod coating, a 10 mL dispersion of purified gold bi-pyramid solution was heated to 60 °C. Various volumes of aqueous $AgNO_3$ (10 mM) and AA (100 mM) were added to this dispersion under vigorous stirring. The exact volumes were dependent on the required rod size. All experiments kept a constant molar ratio of $[AA] : [Ag^+] = 4$. The mixture was stirred at 60 °C for one hour. The obtained solution was centrifuged at 6000 RPM for 15 minutes, and the platelet was re-dispersed in Type I water.

### 2.2.4 Silver Triangular Nanoplate Synthesis

Silver triangular nanoplates were synthesised following a previously reported chemical reduction method by Zhang et al.[12]

Aqueous solutions of $AgNO_3$ (50 mM, 50 µL), TSC (75 mM, 500 µL), PVP (20 mg/mL, 29K or 44K, 100 µL) and $H_2O_2$ (30%, 60 µL) were added to 24 mL of Type I water under vigorous stirring. $NaBH_4$ (100 mM) was rapidly injected into the solution; upon the addition, the solution turned a pale yellow. After approximately 30 minutes, the solution turned bright yellow, followed by a series of interim colours until the final colour was reached. The obtained solution was centrifuged at 6000 RPM for 15 minutes, and the platelet was re-dispersed in Type I water.

## 2.3 Substrate Hydroxylation Methods

CITOGLAS coverslips (22x22 mm) were used as the glass substrate for surface modification. A range of hydroxylation methods, described below, were tested to evaluate functionalisation efficiency. All treated substrates were prepared fresh and used immediately.

### 2.3.1 Piranha Cleaning

Eight coverslips were placed onto a Teflon coverslip holder and submerged in a 3:1 mixture of sulfuric acid (98%, 45 mL) and hydrogen peroxide (30%, 15 mL). The substrates were left in the solution overnight. The following day, the coverslips and holder were removed from the solution and placed in a beaker of Type I water. The substrates were individually removed and rinsed thoroughly with Type I water to remove residual acid.

### 2.3.2 Concentrated Hydrochloric Acid and Methanol

Eight coverslips were placed into a Teflon coverslip holder and submerged in a solution of concentrated hydrochloric acid (36%, 30 mL) and methanol (99.85%, 30 mL). The substrates were sonicated in this solution for one hour. The coverslips and holder were then placed in methanol before being individually removed and rinsed thoroughly with methanol.

## 2.4 Substrate Functionalization Methods

The hydroxylated glass substrates described above were introduced to various silane functionalisation protocols. The most commonly employed hydroxylation method was the piranha cleaning method. The general functionalisation protocols are described below, and they remain unchanged regardless of the hydroxylation method used.

### 2.4.1 (3-aminopropyl) trimethoxysilane in Methanol

(3-aminopropyl) trimethoxysilane (APTES) was used to functionalise a glass substrate to provide a positively charged layer. The chemical structure of APTES is presented in Figure 18 below.

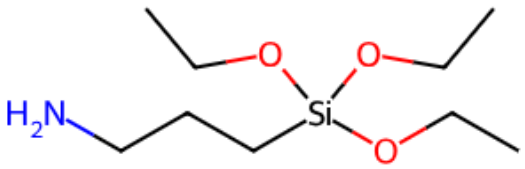


*Figure 18: Chemical structure of (3-aminopropyl) trimethoxysilane (APTES)*[93]

Eight hydroxylated substrates were placed into a Teflon coverslip holder and submerged in 60 mL of a 1% v/v solution of APTES (97%, 600 µL) and methanol (99.8%, 60 mL). The substrates were kept in this solution for five hours; a watch glass was placed on top of the container to mitigate evaporation. The substrates and holder were removed from the solution, placed in a beaker of methanol and sonicated for 15 minutes to remove unbound silane. This sonication step was repeated with methanol and Type I water.

### 2.4.2 (3-Mercaptopropyl) trimethoxysilane in Methanol

(3-Mercaptopropyl) trimethoxysilane (MPTMS) was used to functionalise a glass substrate to provide a negatively charged layer. The chemical structure of MPTMS is presented in Figure 19 below.

The hydroxylated substrates were placed into a Teflon coverslip holder and submerged in 60 mL of a 1% v/v solution of MPTMS (97%, 600 µL) and methanol (99.8%, 60 mL). The substrates were kept in this solution for five hours; a watch glass was placed on top of the container to mitigate evaporation. The substrates and holder were removed

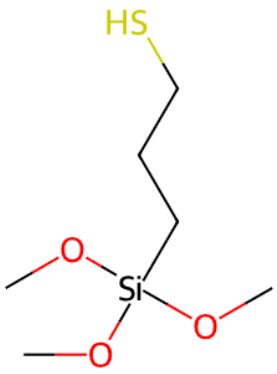


*Figure 19: Chemical structure of (3-Mercaptopropyl) trimethoxysilane (MPTMS)*[94]

from the solution and placed in methanol under sonication for 15 minutes. This sonication step was repeated with methanol and Type I water.

### 2.4.3 (3-Mercaptopropyl) trimethoxysilane in Toluene

A second protocol using (3-mercaptopropyl)trimethoxysilane (MPTMS) was investigated to increase binding efficiency.

A 1% v/v solution of MPTMS (97%, 100 µL) and toluene (99.5%, 10 mL) was poured into a glass petri dish under Nitrogen. Six hydroxylated substrates were placed face down into the solution and submerged for 15 minutes. The substrates were individually removed and rinsed with toluene to remove unbound silane. The substrates were sonicated in Type I water. This step was repeated to remove excess toluene.

## 2.5 Nanoparticle Film Fabrication Methods

Two protocols were investigated to adhere the silver nanoparticles to the above glass substrates. The general adhesion protocols are described below, and they remain unchanged regardless of the previous substrate surface modifications.

### 2.5.1 Immersion

Hydroxylated or functionalised glass substrates were submerged in 10 mL of purified nanoparticle solution overnight. The following day, they were removed from the solution, rinsed with Type I water, and dried in a stream of compressed air.

### 2.5.2 Deposition

Modified glass substrates were placed into a glass petri dish layered with Parafilm. Purified nanoparticle solution was slowly deposited onto the free surface until the entire surface was covered. The substrates were allowed to dry under air overnight. The following day, samples were rinsed with Type I water and dried in a stream of compressed air.

## 2.6 Rubrene Film Fabrication Methods

### 2.6.1 Spin coating

A Laurell Technologies WS-650-23 B spin coater was used. This model was fitted with a low-profile 1.5 cm diameter O-ring-sealed vacuum chuck. The pneumatic vacuum generator was pressurised using a nitrogen gas flow at 60 psi. The spin coater programme was kept constant between experiments. The only variable was the final rotation rate. The programme consisted of two steps. The parameters for step 1 were a rotation rate of 1000 RPM (accelerated 500 RPM) for 10 seconds. Once the maximum rotation rate had been achieved, 50 µL of Rubrene (11 mM) was quickly injected onto the substrate. The parameters for step 2 used a maximum rotation rate, and the acceleration was kept at 500 RPM for 30 seconds. The maximum rotation rate varied between 2000 and 12000 RPM and was adjusted depending on the experiment's aim; all other variables remained constant. Once the rubrene overlay was added, a second cleaned glass substrate was secured with epoxy under a nitrogen flow.

## 2.7 Instrumentation

### 2.7.1 Centrifugation

A Gyrozen 1580R centrifuge was used with a centrifugation adaptor capable of holding six 15 mL centrifuge tubes. Each centrifuge tube contained 10 mL of nanoparticle solution. The maximum rotation and time parameters were set based on the nanoparticle synthesis requirements. The temperature was kept constant at 25 °C for all splitting procedures.

### 2.7.2 Spectrophotometry

An Agilent Technology Cary 100 UV-Vis Spectrophotometer (G9821 A) was used. This instrument has a tungsten halogen light source and an R928 PMT detector. Wavelength

scans were collected from 300 to 900 nm at a scan rate of 600 nm/min with a data interval of 1 nm. This spectrophotometer was equipped with an internal diffuse reflectance accessory, enabling the collection of scattering and absorbance data for both solution and film samples. An Agilent Technology Cary 60 UV-Vis spectrophotometer was used for longer wavelength scans. Wavelength scans were collected from 300 to 1100 nm at a scan rate of 600 nm/min with a data interval of 1 nm.

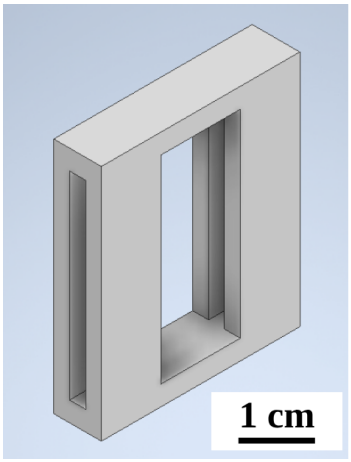


*Figure 20: Rendered design of UV-Vis spectrophotometer sample holder*

A Shimadzu UV-2600 UV-Vis spectrophotometer was used for wavelength scans into the NIR. Wavelength scans were collected from 300 to 1500 nm at a scan rate of 600 nm/min with a data interval of 1 nm. All spectrophotometry measurements were collected using Purshee 10 mm quartz cuvettes. A 3D-printed sample holder was utilised for solid sample measurements. The CAD part design is shown in Figure 20 above.

### 2.7.3 Dynamic Light Scattering

A Malvern Panalytical Zetasiser Nano ZS was used to obtain dynamic light scattering (DLS) measurements. 1.5 mL of purified nanoparticle solution was measured in a plastic cuvette. This instrument has a 632.8 nm laser operating a 4 mW. The analysis material was set to silver, with a refractive index of 0.135 and an adsorption coefficient of 3.99. Each measurement contained 50 runs, with three measurements collected per sample. These values were averaged to give the reported measurement.

### 2.7.4 Zeta Potential

A Malvern Panalytical Zetasiser Nano ZS was used to obtain zeta potential measurements. 2 mL of purified nanoparticle solution was injected into a zeta potential cell. This instrument has a 632.8 nm laser operating a 4 mW. The analysis material was set to silver,

with a refractive index of 0.135 and an adsorption coefficient of 3.99. Each measurement contained 50 runs, with three measurements collected per sample. These values were averaged to give the reported measurement.

### 2.7.5 Scanning Electron Microscopy

Images were captured using a Hitachi SU-70 Schottky field-emission SEM with a 10 kV setting at a working distance of 6 mm. Before imaging, samples were sputter-coated with a platinum target using a Hitachi E-1045. An energy-dispersive spectrometer (EDS) was also connected to the SEM for elemental analysis of the sample. The EDS operating system was Noran System 7 (NSS) version 3.3.113. Image J software was used to calculate particle size and density.

### 2.7.6 Transmission Electron Microscopy

Dr. Adrian Turner at the University of Auckland collected TEM images using a Tecnai 12 TEM (FEI Company, now Thermo Fisher). The instrument is equipped with a TWIN objective lens and was operated at an accelerating voltage of 120 kV using a lanthanum hexaboride source. The camera used for image collection was an Ultrascan 1000 (Gatan, Pleasanton, CA, USA) 2Kx2K pixel. The grids were 400-mesh copper, formvar/carbon-coated, purchased from Electron Microscopy Sciences, Hatfield, PA, USA.

### 2.7.7 Atomic Force Microscopy

Eda Vella collected AFM measurements at the University of Auckland using an Asylum Research Ltd MFP-3D Origin Atomic Force Microscope. Scans were taken with 90x90 µm scan area with a 35 µm vertical range within each scan. Measurements were taken using a TAP150Al-G probe from Budget Sensors Ltd. The nominal frequency was 150 kHz, featuring silicon with an aluminium backing layer for enhanced reflectivity of the laser spot.

### 2.7.8 Surface Contact Angle

The surface contact angles of the functionalised glass substrates were collected using an Ossila contact angle goniometer. Type I water was used to determine the average contact angle of the substrates.

### 2.7.9 Steady-State Fluorescence

An Agilent Cary Eclipse fluorescence spectrometer was used to obtain steady-state fluorescence measurements. The instrument features a Xenon flash lamp (80 Hz) light source. A 530 nm bandpass filter was used to block the excitation light in the fluorescence emission band.

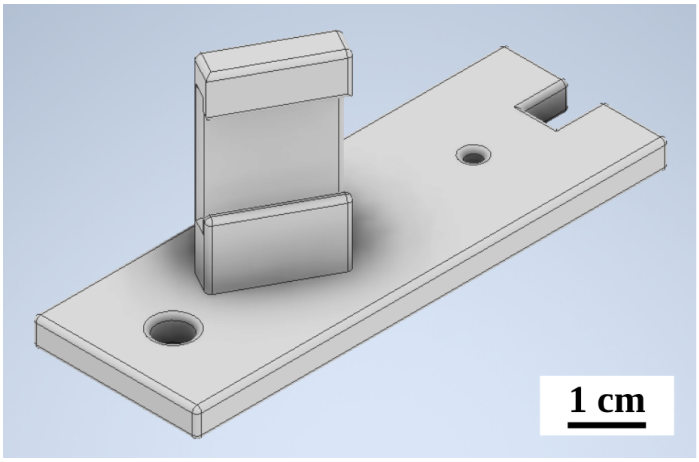


*Figure 21: Rendered design of 3D printed fluorescence spectrometer sample holder*

A 3D-printed sample holder was utilised for solid sample measurements. The CAD design is shown in Figure 21 above.

### 2.7.10 Time-Resolved Photoluminescence

Time-resolved photoluminescence (TRPL) data were recorded by time-correlated single photon counting using a home-built spectrometer. A SuperK Extreme supercontinuum laser (NKT) provided pulsed excitation, and wavelengths were selected using a SuperK Select acousto-optic tunable filter (NKT). Single photons were detected with an ID100 SPAD detector (ID Quantique), and photons were timed and counted in an ID900 Time Controller (ID Quantique). TRPL data were analysed by iterative re-convolution of the instrument response with a multi-exponential decay function followed by a comparison with the recorded decay.

## 2.8 Data Processing

### 2.8.1 Jacobian Transformation and Line Shape Conversion

Most of the spectral data recorded for this work has been corrected according to the Jacobian transformation and further reduced into a spectral line shape. This correction has been applied following the information published by Mooney et al.[95]

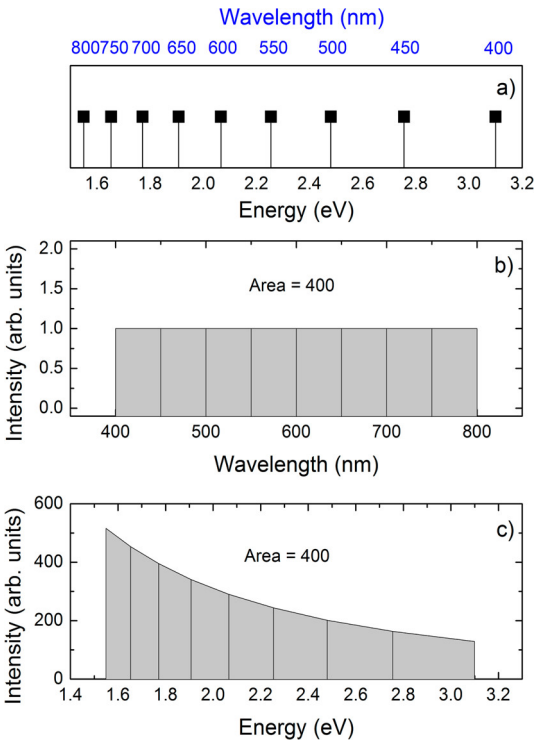


*Figure 22: Illustration comparing a constant signal of unity per nm between 400 and 800 nm to converted energy units through the Jacobian transformation. Reproduced from Mooney et al.*[95]

The article detailed that data points in wavelength units are not evenly spaced in energy units. This is due to the inverse relationship between wavelength and energy. Therefore, a direct conversion of photoluminescence intensities between these units is insufficient and further correction is necessary. Figure 22 above presents a visual representation of this. To correctly convert spectral data, recorded as signal intensity per unit wavelength, the wavelength scale must first be converted using:

$$E = \frac{hc}{\lambda}$$

However, as the data points in the energy scale are no longer uniformly spaced, the Jacobian transformation factor must also be applied to scale the signal intensity. Further correction is required to convert the spectra into a line shape spectrum, which allows us to gain insight into the population information of emitting states.

# 3 Chapter 3 - Nanoparticle Synthesis and Characterisation

| Abbreviations | |
|---|---|
| SPR | Surface Plasmon Resonance |
| TSPR | Transverse Surface Plasmon Resonance |
| LSPR | Longitudinal Surface Plasmon Resonance |
| FWHM | Full Width Half Maximum |
| NIR | Near-Infrared |
| FDTD | Finite Difference Time Domain |
| DDA | Discrete Dipole Approximation |
| SEM | Scanning Electron Microscopy |
| TEM | Transmission Electron Microscopy |
| DLS | Dynamic Light Scattering |
| nm | Nanometre |
| µL | Microlitre |
| mL | Millilitre |
| mV | Millivolt |
| eV | Electronvolt |
| mM | Millimole |

## 3.1 Introduction

This chapter focuses on the synthesis and post-synthetic treatment experiments for creating silver and silver gold-core nanoparticles. These experiments aim to refine the protocols for synthesising and purifying silver nanorods and nanoplates, ensuring consistent size and shape distributions. To achieve efficient spectral overlap with rubrene and correlate the positioning of the plasmon resonance peak, it is crucial that the particles' absorbance and scattering resonances can be effectively tuned across the visible and near-infrared (NIR) spectral windows.

### 3.1.1 Silver Nanorod Synthesis

The initial experiments aimed to replicate a previously reported silver nanorod synthesis by Rekha et al..[51] This article stated that the synthesis produced a high yield of nanorods with a tunable aspect ratio. It also detailed the characteristics of nanorods produced by adding 250, 125, or 100 µL of CTAB-capped seed solution following the synthetic method detailed in section 2.2.2. The attributed transverse surface plasmon resonance (TSPR) wavelength, longitudinal surface plasmon resonance (LSPR) wavelength, and aspect ratio produced from this range of seed solutions are detailed in Table 1.

*Table 1: Transverse and longitudinal SPR peaks and aspect ratios for nanoparticle solutions with 100, 125 or 250 µL of CTAB-capped seed solution, reported by Rekha et al. Values not directly stated in the text were approximated from the figures in the article.*[51]

| Seed Vol. (µL) | TSPR (nm) | LSPR (nm) | Aspect Ratio |
|---|---|---|---|
| 250 | 416 | 527 | 6.3 |
| 125 | 428 | 575 | 11 ± 0.43 |
| 100 | 447 | 633 | 15 ± 2.87 |

The surface plasmon resonance (SPR) wavelengths cited by Rekha et al. are supported by the spectrum reproduced in Figure 23 below. An observed red-shift of the LSPR peak, from 527 to 633 nm, corresponded to the elongation of nanorods. It was demonstrated that as the volume of the seed solution decreased, the elongation of the nanorods increased.

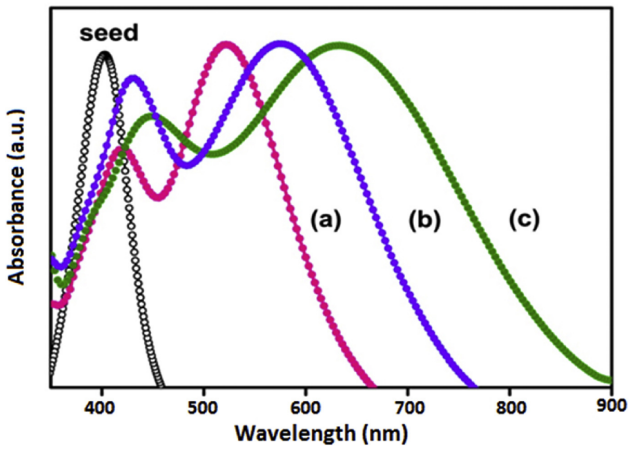


*Figure 23: Reproduced extinction spectrum of synthesised nanoparticle solutions with (a) 100, (b) 125 or (c) 250 µL of CTAB-capped seed solution, reported by Rekha et al.*[51]

A significant increase in the aspect ratio of these nanorods, from 6.3 to 15, was also noted as the seed volume decreased. SEM images of the nanorods can be found in Figure 24. These images display a substantial number of nanorods with an increasing aspect ratio. The average edge length of the nanorods was not specified in the article.

The article describes how the synthetic method resulted in a combination of nanorods, nanoplates, and nanospheres. The numerous nanoparticle morphologies were confirmed by the scanning electron microscopy (SEM) images below.

To separate the nanorods from any excess nanostructures, the mixture was allowed to sit undisturbed for 3 hours, allowing the rods to settle to the bottom of the reaction vessel. The reproduced spectrum in Figure 25 illustrates the difference in the optical properties of the mixture (a) and the isolated nanorods (b). In the isolated nanorod spectrum, the

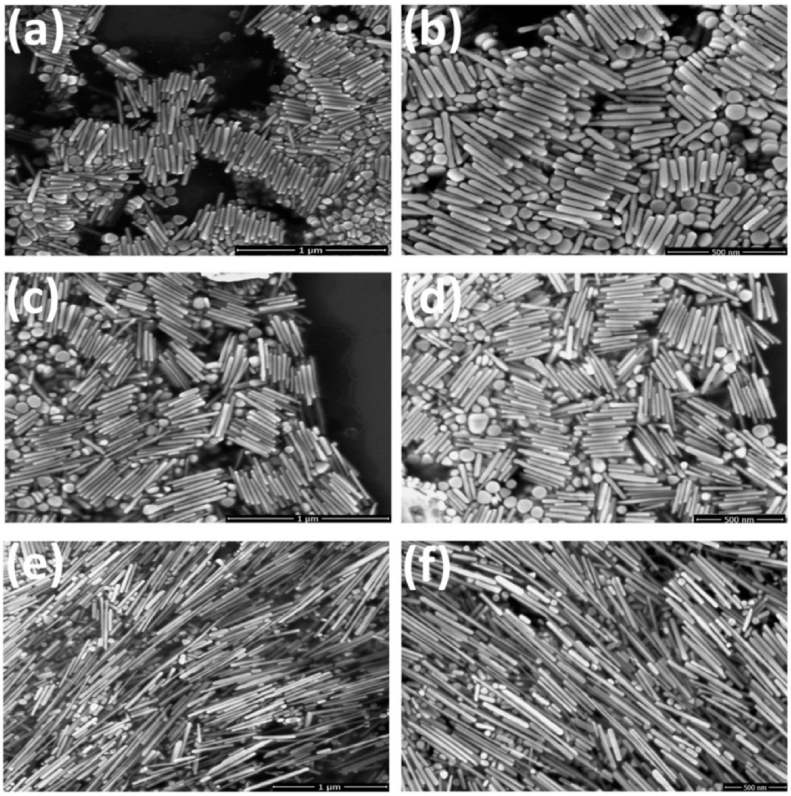


*Figure 24: Reproduced SEM images of synthesised nanoparticle solutions with 100 (e,f), 125 (c,d) or 250 µL (a,b) of CTAB-capped seed solution, reported by Rekha et al.*[51]

authors attribute the SPR maximum peak to the LSPR peak of the nanorods and the secondary peak to the TSPR peak, with centres at 575 and 428 nm, respectively.

The reproduced spectrum in Figure 25 illustrates the difference in the optical properties of the mixture (a) and the isolated nanorods (b). In the isolated nanorod spectrum, the authors attribute the SPR maximum peak to the LSPR peak of the nanorods and the secondary peak to the TSPR peak, with centres at 575 and 428 nm, respectively.

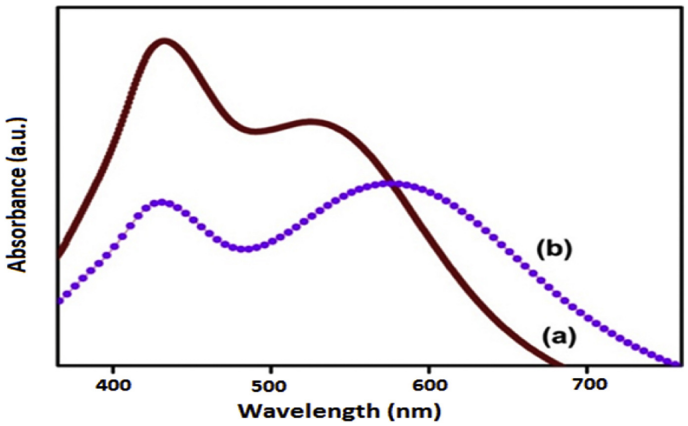


*Figure 25: Reproduced extinction spectrum of a synthesised nanoparticle solution containing 250 µL of CTAB-capped seed solution segregated into excess nanomaterials (a) and nanorods (b), as reported by Rekha et al.*[51]

An SEM image confirming the successful separation is shown in Figure 26. The image suggests that the separation method effectively isolated the nanorods. Although some larger excess nanostructures remain in the nanorod sample, most have been eliminated. Notably, the removed excess material yielded a high proportion of circular nanoplates and nanospheres.

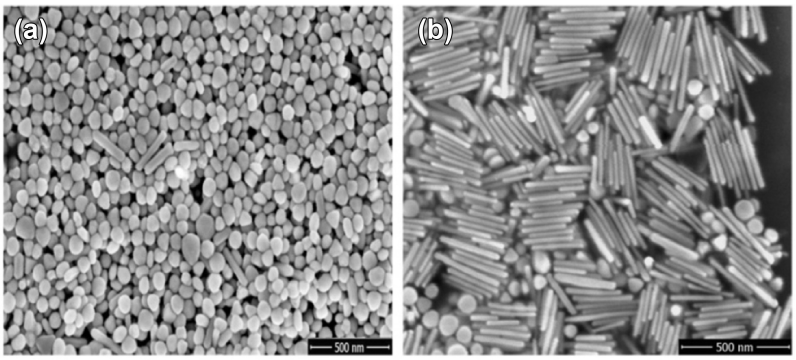


*Figure 26: Reproduced SEM images of a synthesised nanoparticle solution containing 250 µL of CTAB-capped seed solution segregated into excess nanomaterials (a) and nanorods (b), as reported by Rekha et al.*[51]

The article also claimed that these nanorods remain stable for 12 weeks. A reproduced spectrum demonstrating the particles' stability is presented in Figure 27 below. This spectrum shows no shift in the SPR wavelengths, confirming that these nanoparticles will not degrade or change morphology over 12 weeks. However, it is important to note that the exact conditions for their storage were not described. Previous studies have found that the stability of silver nanoparticles relies heavily on the choice of solvent, storage temperature and exposure to light.[96]

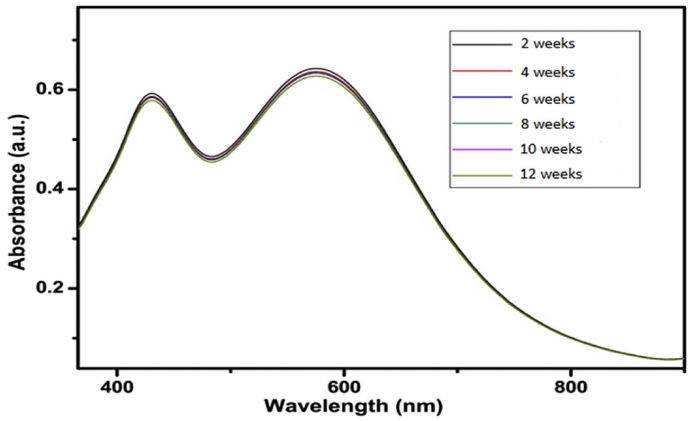


*Figure 27: Reproduced extinction spectrum demonstrating the stability of a synthesised nanoparticle solution containing 250 µL of CTAB-capped seeds, reported by Rekha et al.*[51]

The initial phase of our research involved replicating the results outlined in the article by Rekha et al. and exploring the effects of modifying the seed stabilising reagent on the

resulting nanostructures. Numerous seed solutions were prepared, each containing a different stabilising ligand. The reagent variations are detailed in Table 2 below. Besides adjusting the stabilising reagent and slightly reducing the Type I water volume from 19.92 mL to 19.50 mL, all other reagents and volumes remained unchanged.

*Table 2: Reagent volumes, concentrations and final solution colour for the alternative silver nanoseed syntheses*

| Reagent | Conc. | Vol. (µL) | MQ Vol. (mL) | Seed Colour |
|---|---|---|---|---|
| TSC | 10 (mM) | 500 | 19.5 | Dark Yellow |
| 10K PVP | 1% (v/v) | 500 | 19.5 | Bright Yellow |
| 29K PVP | 1% (v/v) | 500 | 19.5 | Bright Yellow |
| 44K PVP | 1% (v/v) | 500 | 19.5 | Bright Yellow |

The results section below presents experimental data illustrating the substantial impact on final nanostructures when the supporting ligand is changed from cetyltrimethylammonium bromide (CTAB) to polyvinylpyrrolidone (PVP) or trisodium citrate (TSC) in this synthetic method. Additionally, it outlines the influence of modifying the PVP chain length or introducing this polymer into the growth solution on the characteristics of the resulting nanoparticles.

### 3.1.2 Silver Gold Core Nanorod Synthesis

The second series of experiments aimed to reproduce a previously reported silver nanorod synthesis conducted by Sánchez-Iglesias et al..[11] This work demonstrated the production of silver nanorods with adjustable edge lengths in high quantities by integrating a gold bi-pyramidal core. Transmission electron microscopy (TEM) images of the synthesised nanorods are displayed in Figure 28 below.

The gold bi-pyramidal cores in this synthesis serve as a growth template. The silver (Ag) and ascorbic acid (AA) introduced in the growth phase are assisted by the CTAC in solution to produce silver nanorods. The dimensions of the nanorods were increased by increasing the Ag and AA concentrations while keeping the molar ratio of $[Ag^+]$:[AA] constant at 4:1. This occurred due to the increased availability of the silver ions. However, altering the $[Ag^+]$:[AA] ratios negatively impacts the kinetic control of the synthesis by reducing the silver reduction rate. In these images, a noticeable increase in the length of the nanorods is observed from a to i as the Ag and AA concentrations are increased. Upon closer examination, it is possible to discern the presence of a gold bi-pyramidal core within each rod. The increase in edge length of the nanorods results in a consistent

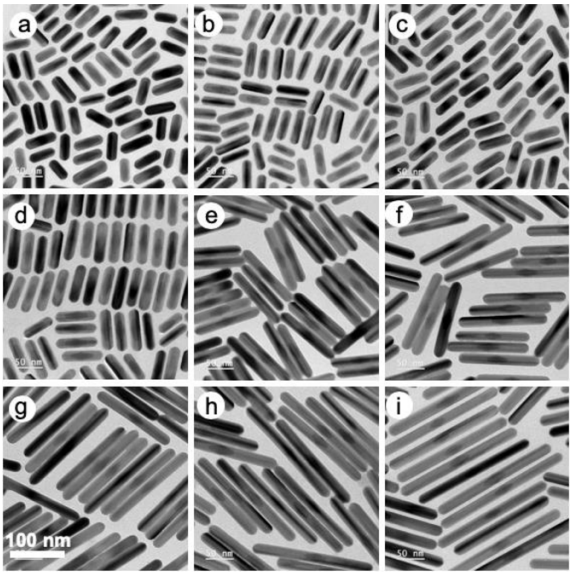


*Figure 28: TEM images of gold-core nanorods with increasing aspect ratios (a-i). As reported by Sánchez-Iglesias et al.*[11]

red-shift in the LSPR peak in the extinction spectra. The extinction spectra referenced in the article are reproduced in Figure 29.

These extinction spectra complement the computational extinction data for silver nanorods within this size range. As anticipated, the nanorods with an aspect ratio of 2.7 and an edge length of 54 nm exhibited an LSPR peak in the red region of the spectrum. As the aspect ratio and edge length were increased to 10.9 and 218 nm, respectively, the SPR peak notably shifted into the infrared region of the spectrum.

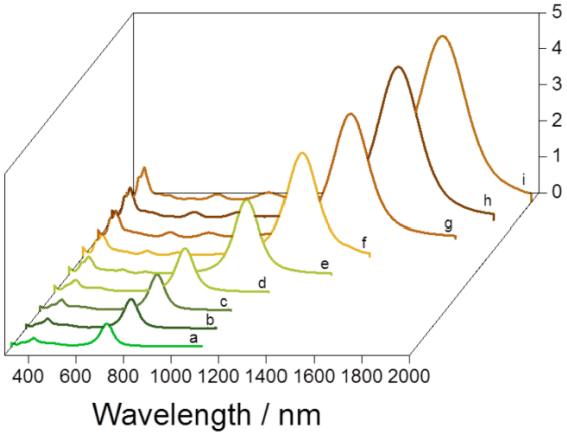


*Figure 29: Extinction spectra of gold-core nanorods with increasing aspect ratios (a-i). As reported by Sánchez-Iglesias et al.*[11]

The nanoparticle synthetic method reported by Sánchez-Iglesias et al. will be used to produce gold-core silver nanorods. These nanorod suspensions are designed for the fabrication of nanorod sublayers, which will enable the effective extension of the extinction

resonance range into the infrared region of the electromagnetic spectrum.

### 3.1.3 Silver Triangular Nanoplate Synthesis

The final series of experiments in this chapter aimed to replicate a previously reported method by Zhang et al.[12] for the synthesis of silver triangular nanoplates. This study investigated the impact of adding 29K PVP to a standard synthetic method that utilised TSC as the primary stabilising agent. This work extensively discussed the crucial role of $H_2O_2$ in facilitating the formation of anisotropic nanostructures. Figure 30 below illustrates the TEM images (b-d) and corresponding extinction spectra (a) of the nanostructures generated with different compositions of TSC, PVP, and $H_2O_2$, as provided in the referenced article.

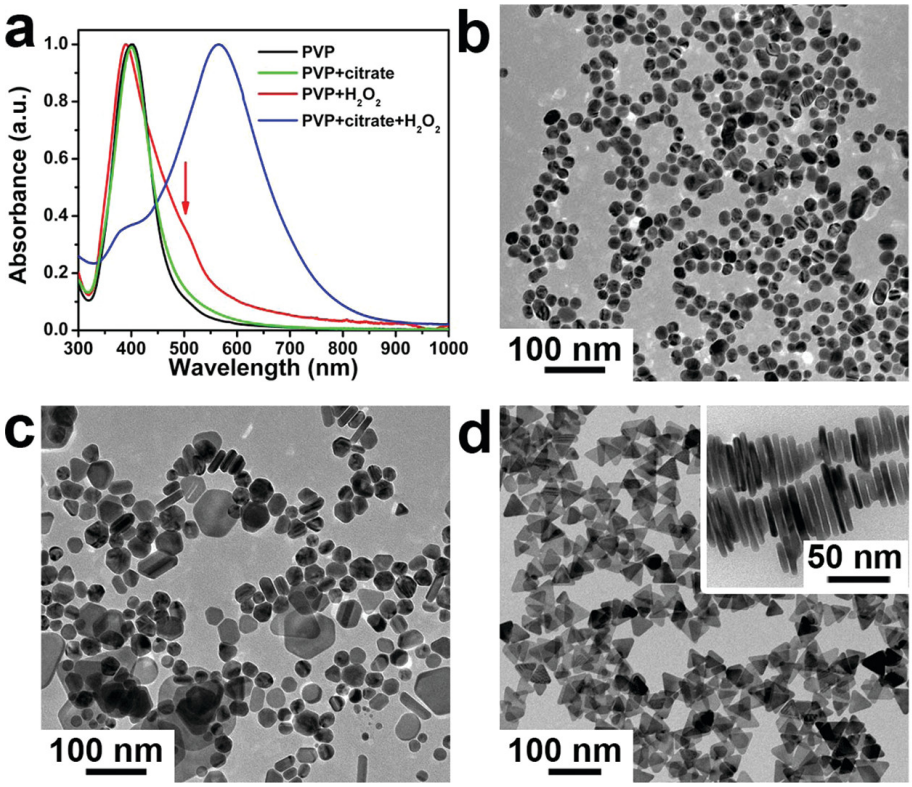


*Figure 30: Extinction spectra (a) and TEM images (b-d) of triangular nanoplates produced with different compositions of TSC, PVP and $H_2O_2$. As reported by Zhang et al.*[12]

The study revealed that introducing PVP into the synthesis led to a high yield of uniform triangular nanoplates; however, in the absence of $H_2O_2$, only quasi-spherical particles were produced. Furthermore, it was demonstrated that PVP is not indispensable for producing anisotropic structures and can be substituted with various hydroxyl-group-containing compounds. Nonetheless, the researchers noted that incorporating PVP led to triangular nanoplates with a more uniform size distribution.

Zhang and co-workers also explored the impact of substituting TSC with other carboxyl compounds on the yield and morphology of the resulting nanostructures. They determined that various di-carboxylate and tri-carboxylate compounds selectively adhere to the {111} crystal facet of Ag, producing triangular nanoplates with high yield. This was dependent on the carboxylate groups being separated by two or three carbon atoms. Ultimately, Zhang and co-workers offered comprehensive insights into the specific roles of each reagent in the synthesis of triangular nanoplates.

The nanoparticle synthetic method reported by Zhang et al. will be used to produce silver triangular nanoplates. The nanoplate suspensions will be immobilised onto a glass substrate to create films. This will enable a comparison between films composed solely of triangular nanoplates and those that contain a mixture of nanoplates and nanorods.

### 3.1.4 Theoretical Surface Plasmon Resonance Calculations

The theoretical surface plasmon resonance (SPR) data for nanoparticles can be calculated using various methods. Figure 31 presents the calculated SPR spectra for a range of silver nanospheres with diameters from 20 to 200 nm. These theoretical spectra were generated using the Nanocomposix Mie Theory calculator, which is a commonly used method for determining the optical cross-sections of nanoparticles.

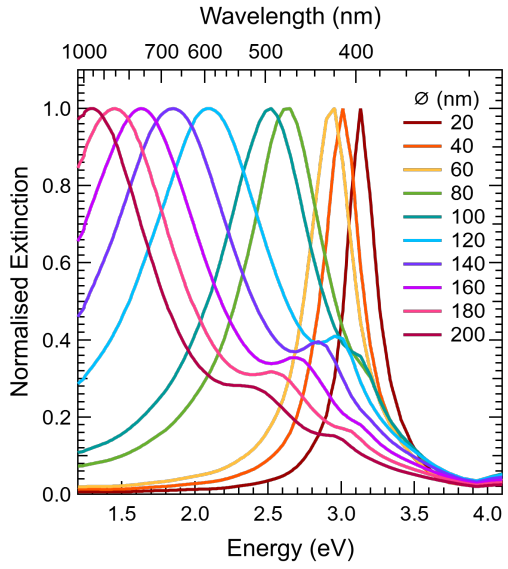


*Figure 31: Normalised theoretical extinction spectra of silver nanospheres with increasing diameter, from 20-200 nm. The theoretical data was produced using the Nanocomposix Mie theory calculator*[16]

As the diameter of the nanosphere increases, a noticeable red-shift in the SPR peak is observed. The spectrum profile also changes as the number of plasmonic modes increases

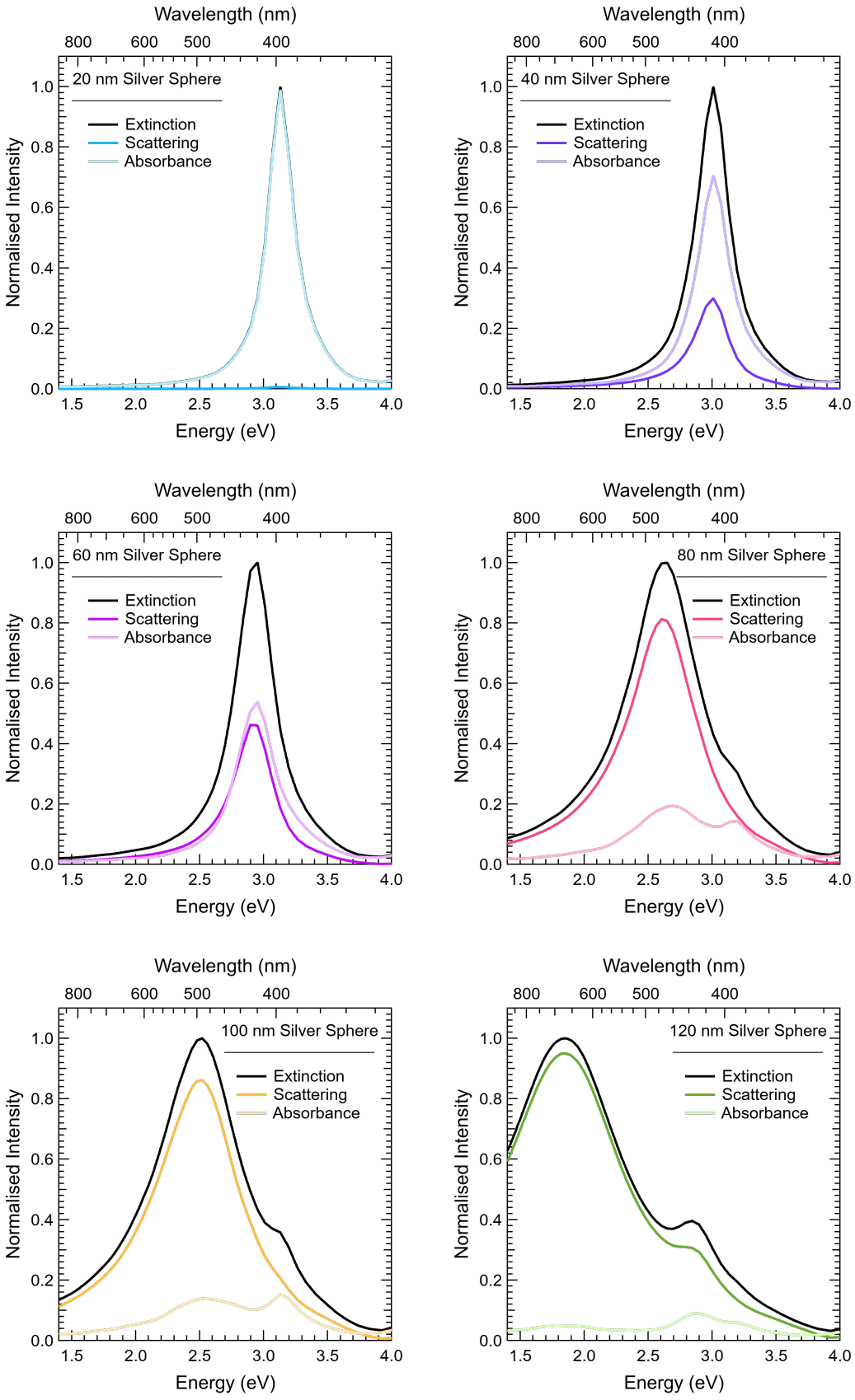


*Figure 32: Normalised theoretical extinction spectra of silver nanospheres with increasing diameter, from 20-120 nm. The extinction has been separated into scattering and absorption proportions. The theoretical data was produced using the Nanocomposix Mie theory calculator*[16]

with the growing diameter. While this theoretical data relates to a relatively straightforward geometry, the higher-order modes introduce multiple shoulders in the resonance spectrum. As the shape and size complexity of a particle increase, giving rise to higher-order resonance modes, the theoretical plasmon resonance data become more difficult to compute accurately.

The total extinction cross-section of a particle comprises scattering and absorption components, with the proportions varying based on the size, shape, and composition of the nanoparticle. Figure 32 above depicts the normalised extinction cross-section and the proportions of scattering and absorbance for spherical nanoparticles with diameters ranging from 20 to 120 nm in 20 nm increments. These results were generated using the Nanocomposix Mie Theory calculator. It is evident from the spectra that as the diameter of the nanospheres increases, the scattering proportion becomes more prominent while, in contrast, the absorbance proportion decreases. This trend persists across the size range, with the scattering proportion contributing over 95% of the extinction cross-section when the particles are 120 nm in diameter.

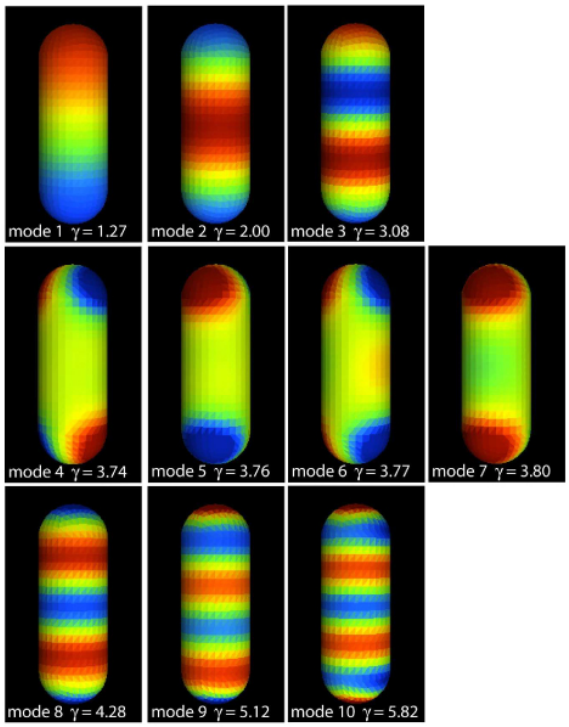


*Figure 33: Reproduced visual representation of the first ten localised surface plasmon modes of a nanorod. As reported by Davis et al.*[97]

Numerous studies have investigated different methods for modelling the localised SPR of more complex geometries.[97–100] A study by Davis et al. instigated the accuracy of the electrostatic approximation in modelling the resonant modes of a silver nanorod and

compared their calculations to a second series of calculations obtained using the finite-difference time-domain (FDTD) numerical model.[97]

The model parameters were chosen to simulate permittivity values similar to a silver nanorod in a water dielectric. The resonance mode for several nanorod lengths, including 90, 230, 460 and 690 nm rods, was calculated. The electrostatic approximation results indicated that nanorods of these sizes would exhibit higher-order modes. The first ten modes calculated are represented in a reproduced image in Figure 33. The colour represents the relative strength of the surface-dipole distribution, with blue indicating positive and red indicating negative. The authors confirmed that modes 1-3 and 8-10 are longitudinal, while modes 4-7 are transverse. The transverse modes come in symmetric and anti-symmetric pairs, and because their eigenvalues are close to one another, their resonances are clustered together, forming a resonant band.

The plasmonic resonances of the first ten modes are displayed in a reproduced excitation spectrum computed for a 90 nm nanorod in Figure 34. This excitation spectrum reveals that modes 3-10 display resonance peaks in the green-yellow region of the spectrum. The primary longitudinal mode, mode 1, resonates at 1.04 eV or 1190 nm. Davis and co-workers were interested in analysing how the resonance wavelengths would change when the length of the rod was increased. Therefore, Figure 34 also illustrates the excitation spectrum for a 230 nm nanorod. Interestingly, modes 3-10 exhibit only minor shifts and increased intensity, while mode 1 experiences a significant red-shift to approximately 0.88 eV or 1400 nm.

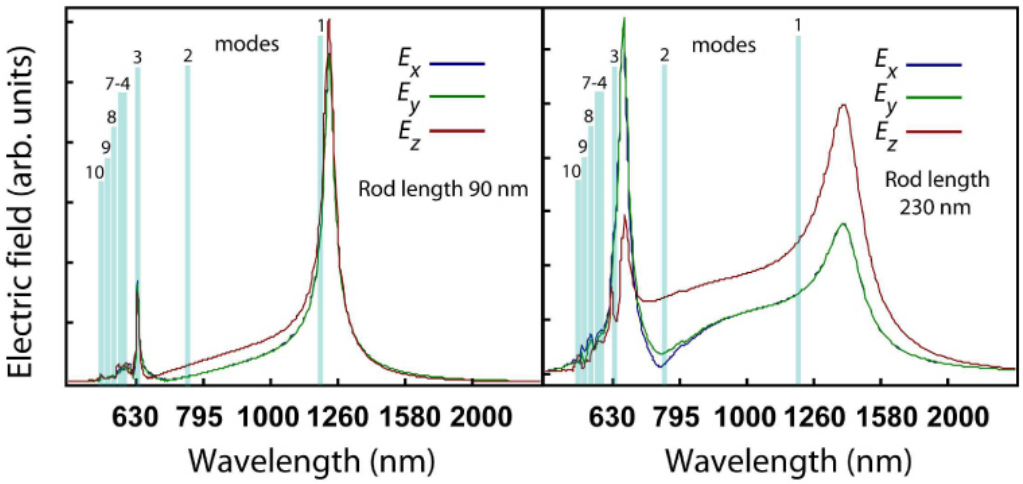


*Figure 34: Reproduced extinction spectrum comparing the theoretical electrostatic resonances of a 90 nm (left) and 230 nm (right) nanorod. As reported by Davis et al.*[97]

Some resonance peaks in the spectrum in Figure 34 are not readily visible. These particular peaks correspond to dark modes in the model, specifically modes 2, 4, 5, 8,

and 10. Dark modes have a zero dipole moment and cannot be excited by a plane wave of incident light. However, they can be excited by near-field coupling from neighbouring nanoparticles. This phenomenon can account for the increased complexity observed in the excitation spectrum of nanoparticle arrays. Another relevant study by He et al. involved calculating the SPR of silver triangular nanoplates using the discrete dipole approximation (DDA) method.[98] The model calculated the resonances of five equilateral triangular plates with a fixed thickness of 10 nm and increasing edge lengths of 50, 100, 150, 200, and 250 nm.

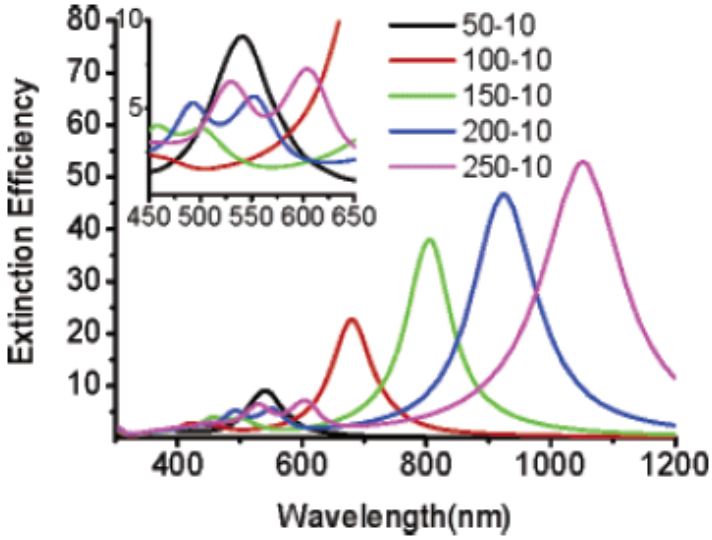


*Figure 35: Reproduced extinction spectra of the calculated resonances of five equilateral triangular plates with a fixed thickness of 10 nm and increasing edge lengths of 50, 100, 150, 200, and 250 nm. As reported by He et al.*[98]

The reproduced image in Figure 35 above displays the calculated extinction spectra for the five triangular plates. The SPR wavelengths of the three computed modes are displayed in the accompanying table in Table 3. The model revealed that as the edge length of the triangular plates increased, the dominant SPR peak (mode 1) underwent a noticeable red-shift by several hundred nanometres. This was accompanied by a minor

*Table 3: Reproduced table of the calculated SPR peak positions of Modes 1-3 of five equilateral triangular plates with increasing edge lengths of 50, 100, 150, 200, and 250 nm. As reported by He et al.*[98]

| Edge Length (nm) | 50 | 100 | 150 | 200 | 250 |
|---|---|---|---|---|---|
| Mode-I | 541 | 680 | 805 | 924 | 1052 |
| Mode-II | 413 | 458 | 503 | 552 | 604 |
| Mode-III | 385 | 420 | 456 | 493 | 529 |

red-shift in the peaks relative to modes 2 and 3.

The theoretical extinction spectrum for triangular nanoplates with edge lengths of 50, 100, and 150 nm, and thicknesses of 10, 20, and 30 nm, respectively, is reproduced in Figure 36. As the thickness of the nanoplates increases, a blue-shift in the mode 1 SPR peak was observed. Specifically, for the 100 nm plate, the peak shifted from 680 to 580 nm when the thickness of the nanoplate increased from 10 to 20 nm. Similarly, the shift for the 150 nm plate was from 805 to 640 nm as the thickness of the nanoplate increased from 10 to 30 nm. These findings demonstrated the change in spectral peaks associated with increasing the thickness of the nanoplates relative to their edge length.

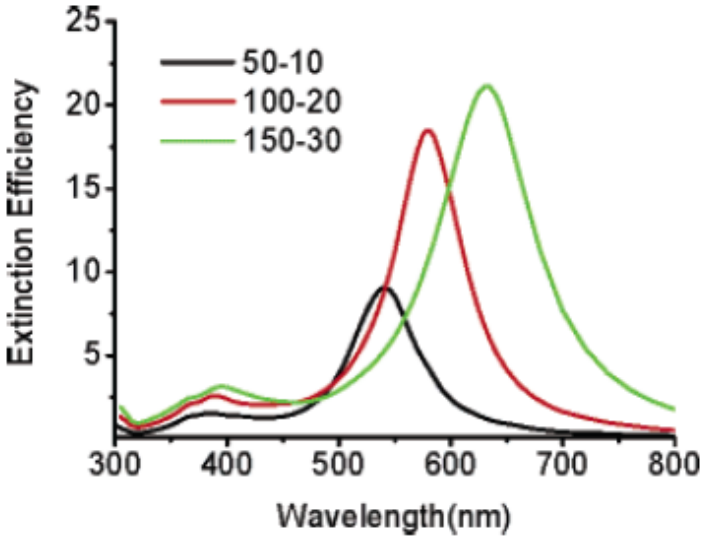


*Figure 36: Reproduced extinction spectra of the calculated resonances of three equilateral triangular plates, with increasing edge lengths of 50, 100 and 150 nm and increasing thicknesses of 10, 20 and 30 nm, respectively. As reported by He et al.*[98]

The extinction spectra obtained for the nanoparticle suspensions synthesised in this study will be compared to the theoretical extinction spectra reported in the literature. This comparative analysis, in addition to the collection of SEM and TEM imagery, will facilitate a comprehensive assessment of the size and morphology of the synthesised nanostructures.

## 3.2 Alteration of the Seed Capping Reagent

Silver nanorods were synthesised using the method described by Rekha et al.[51] The specific synthetic conditions are detailed in section 2.2.2. The results presented in this chapter include all reproduction, optimisation, purification and stability experiments. It is essential to note that the results are not presented in chronological order, but rather grouped

by seed variation and aim.

### 3.2.1 Results

#### 3.2.1.1 Seed Synthesis

Silver nanoseeds were synthesised following the synthetic method described in section 2.2.2. of which the variations to the methodology are described in the introduction of this chapter. To compare the effect of the stabilising reagent on the resulting nanoseeds characteristics, the extinction spectra, zeta potential, and average particle size were collected for each seed variation. The normalised extinction spectra for the five seed variations are presented in Figure 37 below.

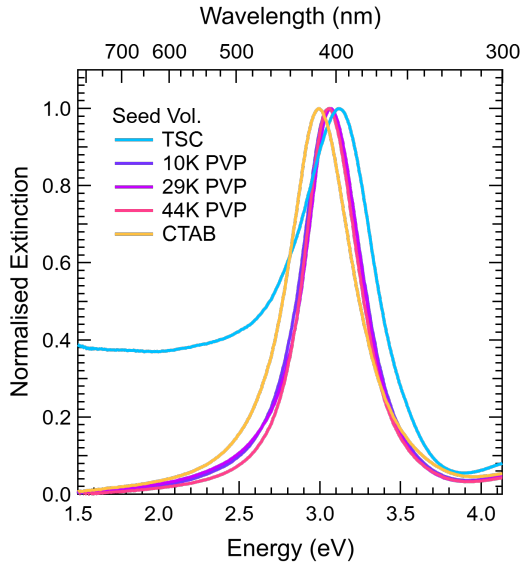


*Figure 37: Normalised extinction spectra of silver nanoseed solutions with CTAB, TSC or 10K, 29K and 44K PVP as stabilising reagents.*

A sharp peak in the violet range is observed in all the spectra for all five seed solutions, indicating the successful synthesis of silver nanoseeds. There are minor shifts of the SPR peak between each seed variation that result from the incorporation of the described stabilising reagents. The SPR maximum peak values are presented, in wavelength and energy units, alongside their relevant zeta potential values in Table 4 below.

The SPR peak for the CTAB-capped seeds occurs at 432 nm (2.87 eV), the longest wavelength among the five variations. On the other hand, all 3 PVP-capped seed solutions exhibit an SPR peak at 406 nm (3.05 eV). Conversely, the TSC-capped seed solution exhibits a blue-shifted SPR peak at 398 nm (3.12 eV), with a tail extending across the visible region into the NIR. The zeta potential values significantly differ among the three PVP seed solutions. Specifically, the zeta potential values for the 10K, 29K and 44K seed solu-

*Table 4: LSPR and zeta potential values of silver nanoseed solutions with varying stabilising reagents*

| Reagent | LSPR (nm) | LSPR (eV) | Zeta (mV) |
|---|---|---|---|
| CTAB | 432 | 2.87 | 29.3 |
| 10K PVP | 406 | 3.05 | -19.9 |
| 29K PVP | 406 | 3.05 | -10.3 |
| 44K PVP | 406 | 3.05 | -7.5 |
| TSC | 398 | 3.12 | -31.4 |

tions are -19.9, -10.3, and -7.5 mV, respectively. A direct correlation is observed between the zeta potential values and the tendency towards zero as the polymer chain length increases. Additionally, the CTAB and TSC-capped seeds had zeta potential values on opposite sides of the range at 29.3 and -31.4, respectively.

*Table 5: Average particle size of silver nanoseed solutions with varying stabilising reagents. Size-P is the average particle size, while Size-A is the average agglomerate size*

| Reagent | Size-P (nm) | Size-P (%) | Size-A (nm) | Size-A (%) |
|---|---|---|---|---|
| CTAB | $18.7 \pm 0.2$ | 67.6 | $172.4 \pm 4.9$ | 28.5 |
| 10K PVP | $92.1 \pm 1.0$ | 95.8 | $4111.2 \pm 29.2$ | 4.2 |
| 29K PVP | $84.3 \pm 0.5$ | 99.3 | $4210.3 \pm 18.2$ | 0.7 |
| 44K PVP | $38.9 \pm 3.1$ | 98.2 | $4674.0 \pm 42.9$ | 1.8 |
| TSC | $52.1 \pm 2.6$ | 63.0 | $2349.5 \pm 12.3$ | 37.0 |

Dynamic light scattering (DLS) was used to correlate the extinction data to the particle size. This data is presented in Table 5 above. The results show that CTAB-capped seeds were significantly smaller than those produced with PVP. Specifically, 67.6% of CTAB seeds had an average diameter of 18.7 nm, while the 10K, 29K, and 44K PVP-capped seeds had average diameters of 92.1 nm, 84.3 nm, and 38.9 nm, respectively. Additionally, the percentage of particles at these sizes averaged 95-99%, significantly higher than the percentage for the CTAB-capped seeds.

In the CTAB seed solution, the remaining 28.5% of the particles had a diameter of 172.4 nm, indicating significant agglomeration. Minor aggregation was observed in the PVP seed solutions, accounting for less than 5% in all three samples. Conversely, the TSC seeds displayed the highest percentage of aggregation, with 37% of the population consisting of large agglomerated particles at 2349 nm. The average particle size of the remaining 63% was 52.1 nm.

The existence of agglomerated particles in a seed solution leads to a greater degree of polydispersity in the seed sample. This, in turn, affects the resulting nanostructures when

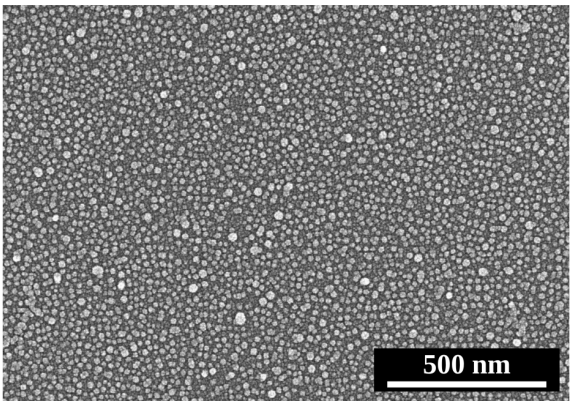


*Figure 38: SEM image of a 44K PVP-capped seed solution on a glass substrate*

introduced to the growth solutions, as the increased polydispersity at the starting point leads to more polydispersity in the final nanostructure suspension. Therefore, it was hypothesised that seed solutions with a high degree of monodispersity and a low degree of aggregation would produce the highest yield of nanorods. A visual representation of the monodispersity achieved by the 44K PVP seed variation is shown in the SEM image in Figure 38.

These five seed solution variations were introduced to the reported growth solution to investigate their impact on the characteristics of the resulting nanostructures. It was hypothesised that introducing the 44K PVP-capped seeds would significantly improve monodispersity in the final nanoparticle solution, as this stabilising reagent produced the most monodispersed seed solution.

#### 3.2.1.2 Initial Experiments

An initial experiment was attempted following the method described in the paper by Rekha et al.[51] The synthetic method is described in section 2.2.2. A similar seed volume range was used to directly compare the reported particle characteristics. This range was 100, 150 and 250 µL of CTAB-capped seed solution introduced into the growth solution.

The normalised extinction spectra for the resulting nanoparticle solutions are presented in Figure 39 below. In contrast to all other extinction data in this chapter, this data was not converted to line shape spectra to allow a direct comparison to the literature figures. The TSPR and LSPR peaks from the experimental solutions are presented in Table 6 below, along with the corresponding values from the literature.

The experimental LSPR peak values were significantly shifted and did not match the literature values. For both the 150 µL and the 100 µL samples, the LSPR value is significantly red-shifted from 575 nm to 678 nm and 633 nm to 738 nm, respectively. For the

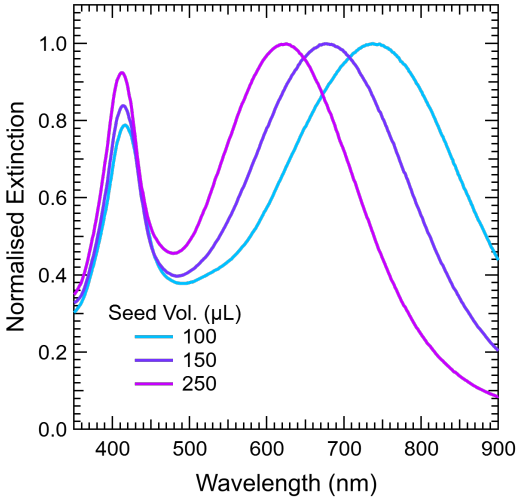


*Figure 39: Experimental extinction spectra of colloidal silver nanorod solutions with 100, 125 or 250 µL of CTAB-capped seed solution. Following the reported synthetic method by Rekha et al. with no deviations*[51]

250 µL sample, the LSPR value is blue-shifted compared to the literature value, from 527 nm to 475 nm. This suggests that the particles produced from the 150 µL and 100 µL seed volumes were larger than those reported in the literature, while the particles produced from the 250 µL seed volume were smaller.

*Table 6: Experimental and reported TSPR and LSPR values for nanoparticle solutions from 100, 150 and 250 µL of CTAB-capped seed solution introduced into a fixed growth solution. Following the previously reported method by Rekha et al. with no variations*[51]

| Seed Vol. (µL) | TSPR (nm) | Reported TSPR (nm) | LSPR (nm) | Reported LSPR (nm) |
|---|---|---|---|---|
| 250 | 412 | 416 | 475 | 527 |
| 150 | 414 | 428 | 678 | 575 |
| 100 | 416 | 447 | 738 | 633 |

The TSPR peaks are relatively constant, with the peak red-shifting 2 nm with each decrease in seed volume. In the literature, the TSPR peak shifts by as much as 31 nm, from 416 to 447 nm, with decreasing seed volumes. This suggests a significant change in the wavelengths of the transverse modes, implying a substantial variation in the thickness of the nanoparticles produced.[51]

From here, a secondary experiment was conducted to determine the limitations of tuning using seed volume. Only CTAB-capped seeds were used in these experiments. In the first series, the added seed solution volume changed in decrements of 10 µL, trending towards zero. In the second series, the volume of seed solution added was increased

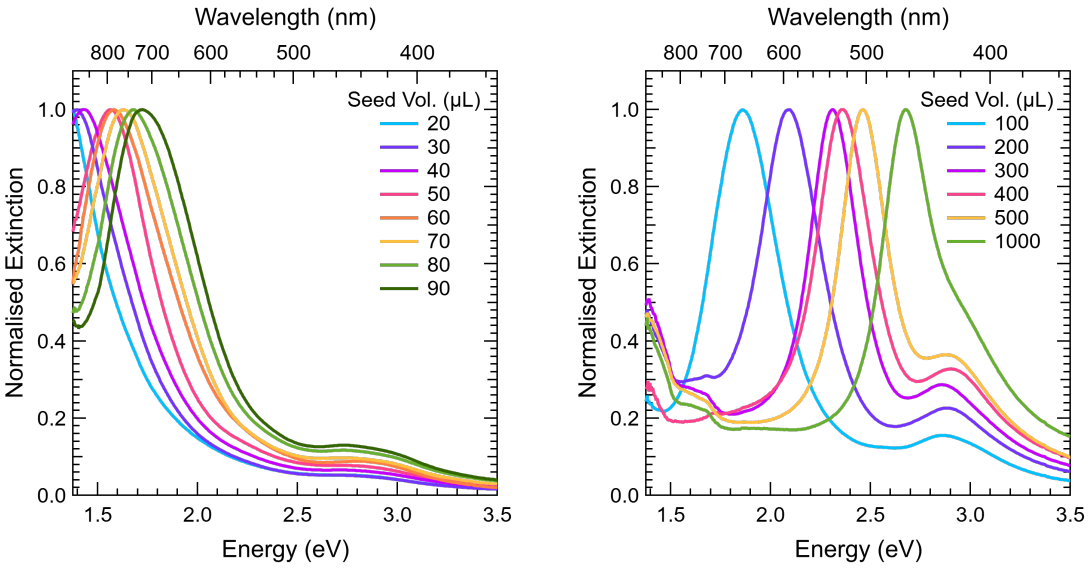


*(a) 20-90 µL Seed Volume*

*(b) 100-1000 µL Seed Volume*

*Figure 40: Normalised extinction spectrum of colloidal silver nanoparticle solutions with increasing CTAB-capped seed volumes, from 20-1000 µL, added to a fixed growth solution. This data was collected with particles in reaction conditions*

in 100 µL increments, from 100 to 1000 µL. The normalised extinction spectra for the resulting nanoparticle solutions are presented in Figure 40.

*Table 7: Localised surface plasmon resonance values, in energy and wavelength units, for nanoparticle solutions with increasing CTAB-capped seed volumes, from 20-1000 µL, added to a fixed growth solution. This data was collected with particles in reaction conditions*

| Seed Vol. (µL) | LSPR (eV) | LSPR (nm) |
|---|---|---|
| 20 | 1.377 | 900 |
| 30 | 1.382 | 897 |
| 40 | 1.428 | 868 |
| 50 | 1.566 | 791 |
| 60 | 1.580 | 784 |
| 70 | 1.626 | 763 |
| 80 | 1.681 | 738 |
| 90 | 1.727 | 718 |

*(a) Lower range - 20-90 µL*

| Seed Vol. (µL) | LSPR (eV) | LSPR (nm) |
|---|---|---|
| 100 | 1.860 | 666 |
| 200 | 2.094 | 606 |
| 300 | 2.310 | 539 |
| 400 | 2.365 | 524 |
| 500 | 2.462 | 503 |
| 1000 | 2.677 | 463 |

*(b) Upper range - 10-1000 µL*

Two clear trends were observed in this data. The first trend was a systematic red-shift of the maximum SPR peak as the volume of seed solution added decreased. For clarity, the LSPR values for both limitation experiments are presented in Table 7. A tunable red-shift in the first series, from 1.86 eV (666 nm) for the 100 µL seed solution to 1.37 eV (900 nm) for the 20 µL seed solution was observed. This shift occurs across the range of decreasing seed volumes, with each peak red-shifting an average of 25 nm per 10 µL of seed solution. The same trend was observed in the higher seed volume experiment, as a significant blue-shift was evident as the added seed solution volume increased. A blue-shift was observed from 1.86 eV (666 nm) for the 100 µL seed solution to 2.67 eV (463 nm) for the 1000 µL seed solution. The peaks in this experiment blue-shift an average of 40 nm per 100 µL of seed solution.

The second trend was an increase in the relative intensity of the secondary SPR peak as the seed volume increased, coupled with a minor blue-shift in the peak wavelength. Both of these trends were observed in all samples across both series. This data supports the theory by Rehka and coworkers that altering the seed volume is a critical tuning parameter for this synthesis, suggesting that the particle size in these solutions changes significantly.[51]

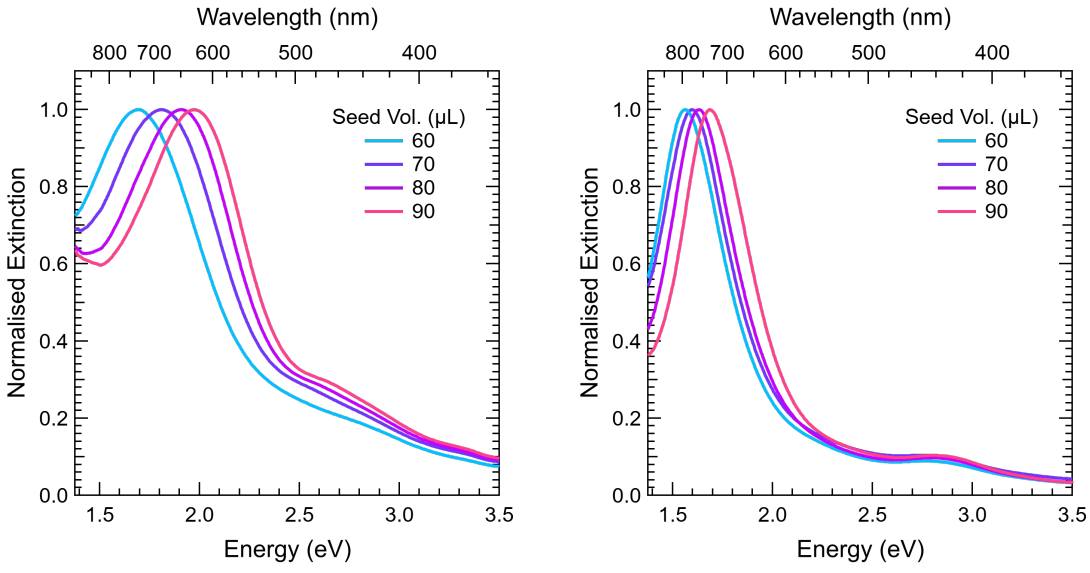


*(a) 44K PVP* *(b) 29K PVP*

*Figure 41: Normalised extinction spectrum of colloidal silver nanoparticle solutions with increasing (a) 44K PVP or (b) 29K PVP-capped seed volumes, from 60-90 µL, added to a fixed growth solution. This data was collected with particles in reaction conditions*

The next step was to use the information from the seed experiments to determine how changing the seed stabilising agent would impact the resulting nanostructures. For

these experiments, the 29 and 44K PVP-capped seeds were used. A small range of seed volumes, 60-90 µL in 10 µL increments, was selected, keeping all other reaction conditions the same. The extinction spectra from the resulting nanoparticle solutions in reaction conditions are presented in Figure 41.

The spectra produced from the PVP seed solutions had a similar shape to those from the CTAB seeds. All spectra had an SPR max peak in the orange/red region and a second less intense peak in the blue region. These samples also followed the same trend of a systematic red-shift of the maximum SPR peak as the volume of seed solution added decreased. However, for the 44K PVP sample spectra, the secondary peak appears as a shoulder rather than a defined peak as in the 29K and CTAB samples. There was also a second rise in the SPR peak after 800 nm. More in-depth experiments for each seed variation were conducted to gather characterisation data and confirm the size and shape of the produced particles.

#### 3.2.1.3 Comparing CTAB and 44K PVP-Capped Seeds

It has been demonstrated that nanoparticle solutions synthesised using the method described in section 2.2.2 and 44K PVP-capped seeds will produce spectral data comparable with solutions synthesised using CTAB-capped seeds. Further experiments were performed to compare the characteristics of the nanoparticles produced and their morphological distribution.

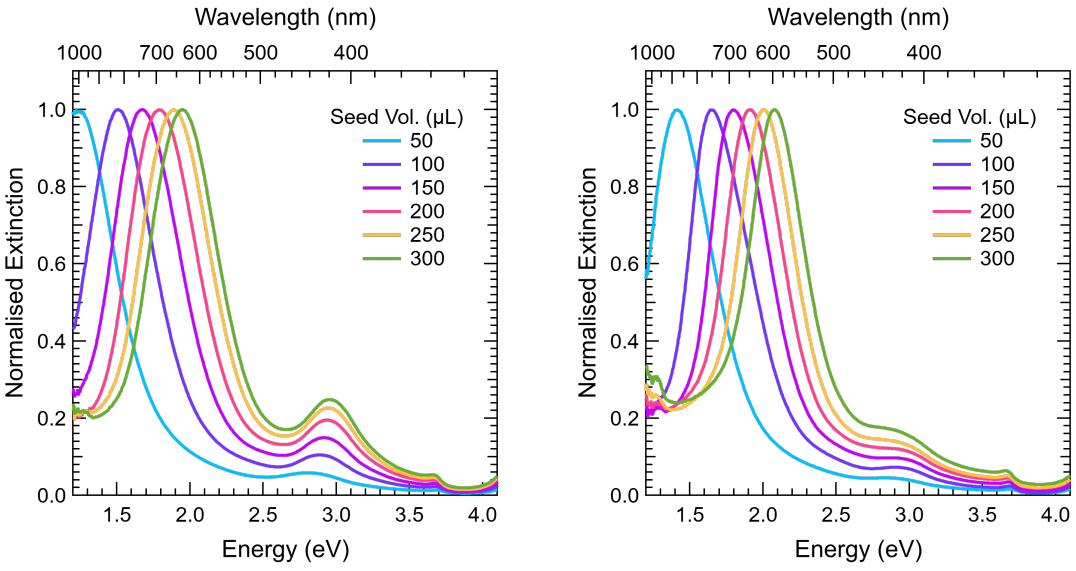


*(a) 44K PVP-capped Seed*

*(b) CTAB-capped Seed*

*Figure 42: Normalised extinction spectrum of colloidal silver nanoparticle solutions with increasing (a) 44K PVP or (b) CTAB-capped seed volumes. Seed volumes ranged from 50-300 µL in 50 µL increments. This data was collected with particles in reaction conditions*

For these experiments, the only independent variable was the volume of seed solution added to the fixed growth solution. To keep the experiments comparable, a range of 50-300 µL in 50 µL increments was used. The normalised extinction spectra for the nanoparticle solutions produced across this range from 44K PVP and CTAB-capped seeds are presented in Figure 42.

All samples in both series follow the trend of a systematic red-shift of the maximum SPR peak as the volume of the seed solution decreases. The maximum SPR peak wavelengths for each sample, in nanometers (8a) and energy units (8b), are presented in Table 8 below. This table also includes the SPR peak full-width half maximum (FWHM) (8c) and zeta potential value (8d) for each suspension.

*Table 8: Maximum SPR peak values of colloidal silver nanoparticle solutions with increasing 44K PVP or CTAB-capped seed volumes, from 50-300 µL, in reaction conditions*

| Seed Volume (µL) | 50 | 100 | 150 | 200 | 250 | 300 |
|---|---|---|---|---|---|---|
| 44K PVP | 1.23 | 1.51 | 1.67 | 1.79 | 1.88 | 1.95 |
| CTAB | 1.40 | 1.64 | 1.80 | 1.91 | 2.01 | 2.08 |

*(a) LSPR (eV)*

| Seed Volume (µL) | 50 | 100 | 150 | 200 | 250 | 300 |
|---|---|---|---|---|---|---|
| 44K PVP | 1008 | 821 | 742 | 692 | 659 | 626 |
| CTAB | 885 | 742 | 688 | 649 | 616 | 596 |

*(b) LSPR (nm)*

| Seed Volume (µL) | 50 | 100 | 150 | 200 | 250 | 300 |
|---|---|---|---|---|---|---|
| 44K PVP | 0.57 | 0.56 | 0.55 | 0.54 | 0.55 | 0.53 |
| CTAB | 0.55 | 0.50 | 0.49 | 0.50 | 0.48 | 0.49 |

*(c) SPR Peak Full Width Half Max*

| Seed Volume (µL) | 50 | 100 | 150 | 200 | 250 | 300 |
|---|---|---|---|---|---|---|
| 44K PVP | 34.8 | 33.5 | 31.2 | 30.0 | 27.2 | 29.3 |
| CTAB | 36.7 | 35.2 | 34.8 | 35.3 | 35.9 | 36.6 |

*(d) Zeta Potential (mV)*

This data suggests that the samples produced using the 44K PVP-capped seeds synthesised larger nanostructures for every seed volume when compared to those made using the CTAB-capped seeds. This was inferred from the red-shift of the SPR peak wavelength across the series. For example, for the 50 µL samples, the SPR wavelength for the 44K PVP sample was 1.23 eV (1008 nm), whereas the wavelength was 1.40 eV (885 nm) for the CTAB sample. This trend was consistent across the entire series and was reflected

in the final colour of the solutions. Photos of the solution vials from both series are shown in Figure 43.

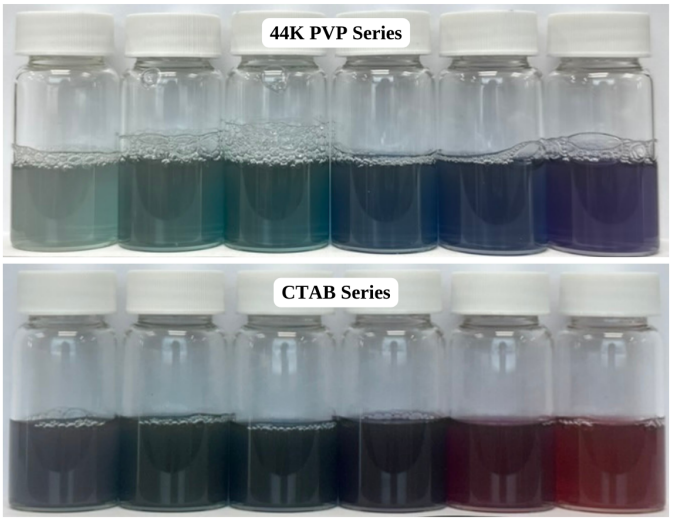


*Figure 43: Photos of colloidal silver nanoparticle solutions with increasing 44K PVP (top) or CTAB-capped (bottom) seed volumes in reaction conditions. Seed volumes ranged from 50-300 µL in 50 µL increments, from left to right*

This shift in SPR wavelengths was accompanied by a minor increase in the FWHM values for the 44K PVP samples. The FWHM values remained relatively consistent across

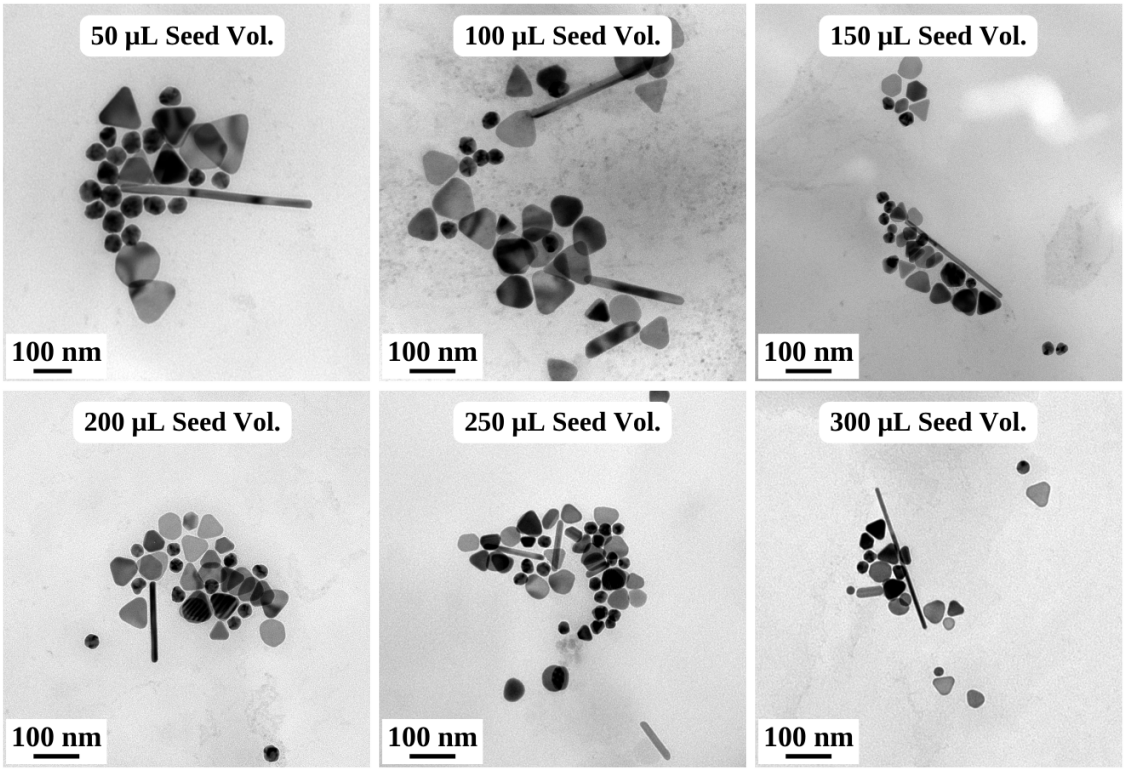


*Figure 44: TEM images of silver nanoparticle solutions with increasing 44K PVP-capped seed volumes in reaction conditions. Seed volumes ranged from 50-300 µL in 50 µL increments*

the series. However, there was a minor decrease in the value as the seed volume increased. It is also worth noting that the secondary resonance peak in the blue region was more pronounced in the 44K PVP samples compared to the CTAB samples. An increase in the relative intensity of this peak was also observed as seed volume increased.

The zeta potential values for the CTAB series remain relatively constant, ranging from 34.8 to 36.7 eV. These values are higher than those for the 44K PVP series, which range from 27.2 to 34.8 eV. A more significant shift exists between the highest and lowest values obtained across the 44K PVP series at 7.6 eV. This suggests that the excess PVP binds to the resulting nanostructures, decreasing the positive charge produced by the CTAB ions. TEM images of the 44K PVP nanostructures were collected and are presented in Figure 44. These images show that the synthetic conditions using the 44K PVP-capped seeds produce a mixture of nanostructures, including triangular nanoplates, circular nanoplates, nanorods and excess nanoseeds. This matches the shape distribution described in the article by Rekha et al. for the CTAB-capped seeds.[51]

The Rekha article also describes a purification protocol for effectively collecting the nanorods from each solution.[51] This protocol involves keeping the solution undisturbed for three hours. During this time, the nanorods precipitate naturally to the bottom of the reaction vessel. This method was never successfully replicated in our experiments. Instead, purification methods by centrifugation were investigated. More details on the optimisation and results of these experiments are described in section 3.2.1.9.

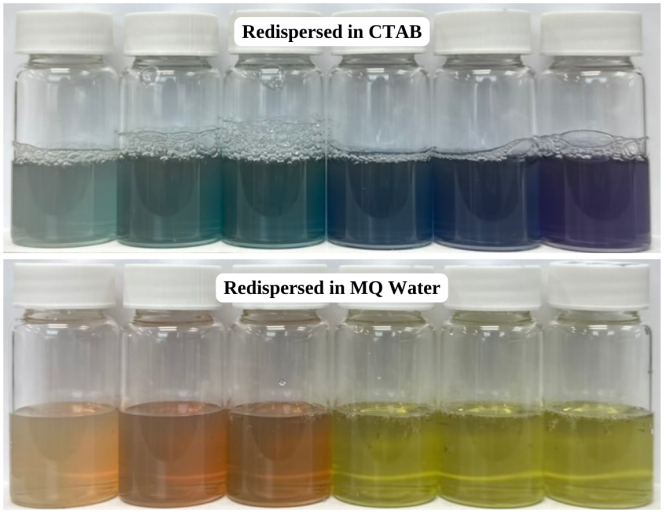


*Figure 45: Photos of colloidal silver nanoparticle solutions with increasing 44K PVP-capped seed volumes redispersed in CTAB (top) or Type I water (bottom). Seed volumes ranged from 50-300 µL in 50 µL increments, from left to right*

Ultimately, the particles were separated from their reaction conditions and redis-

persed in Type I water. This caused an immediate change to the colour of the solution, suggesting changes to the size and shape of the particles. A viable solution to avoid this colour change was a reintroduction of CTAB. The details of the optimisation and results of the experiments that determined the appropriate concentration of CTAB are described in section 3.2.1.10 below. The colour change for the 44K PVP series is shown in Figure 45.

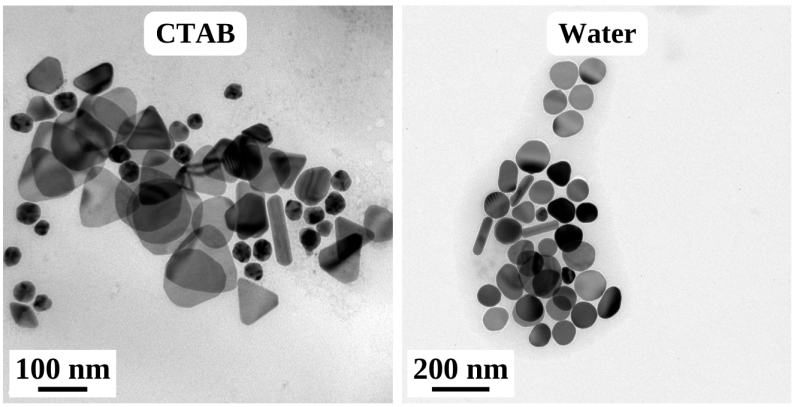


*Figure 46: TEM images of a silver nanoparticle solution with 50 µL of 44K PVP-capped seeds redispersed in CTAB (left) or Type I water (right)*

This dramatic colour change corresponds to a shift in the optical properties on the nanoparticle suspension and, therefore, a change in their size and shape. TEM images of particles from the same synthetic conditions, redispersed in either water or CTAB, were collected to confirm this. An example of the images collected for a sample made using 50 µL of 44K PVP-capped seeds is presented in Figure 46. This image shows that the nanoplates will decrease in size and angularity when redispersed in Type I water but will maintain their physical features when redispersed in a sufficient concentration of CTAB.

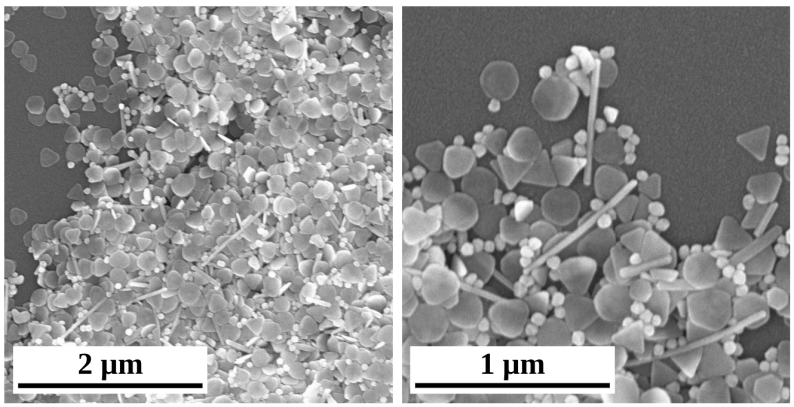


*Figure 47: SEM images of a silver nanoparticle solution with 50 µL of 44K PVP-capped seeds redispersed in CTAB*

SEM images of the nanoparticles produced from 50 µL of 44K PVP-capped seeds re-

dispersed in CTAB are presented in Figure 47. These images show a larger representation of the nanoparticle population. The resulting nanostructures from this synthesis are a mixture of triangular nanoplates, circular nanoplates, nanorods and excess nanoseeds.

When comparing the SEM images of the particles redispersed in Type I water, as shown in Figure 48, a noticeable decrease in the angularity and size of the excess nanostructures was observed. This particular change in particle shape was consistent across the series. Interestingly, these samples exhibit areas with high nanorod yields, surrounded by regions dominated by circular nanoplates and seeds. It was also evident from these SEM images that the length of the nanorods increases as the seed volume decreases. However, the width of the rods changes only minimally between samples.

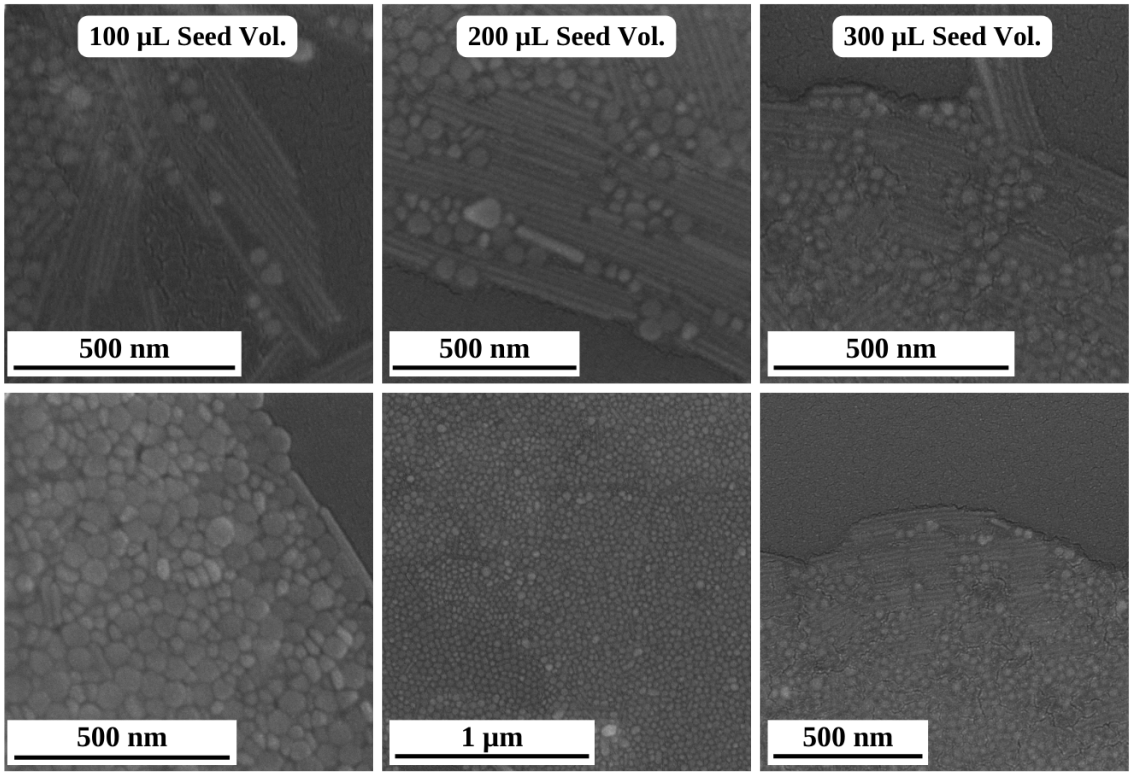


*Figure 48: SEM images of silver nanoparticle solutions with increasing 44K PVP-capped seed volumes redispersed in Type I water. Seed volumes ranged from 100-300 µL in 100 µL increments, from left to right*

The normalised extinction spectra for the 44K PVP series are presented in Figure 49. These spectra compare the optical properties of the particle in reaction conditions (59a), when redispersed in CTAB (59b), and when redispersed in Type I water (59c).

For clarity, the maximum SPR peak wavelengths for each sample, in nanometers (9a) and energy units (9b), are presented in Table 9 below. This table also includes the SPR peak (9a), FWHM (9c), and zeta potential value (9d) of each nanoparticle suspension, as

well as a comparison of these values for particles redispersed in CTAB and Type I water.

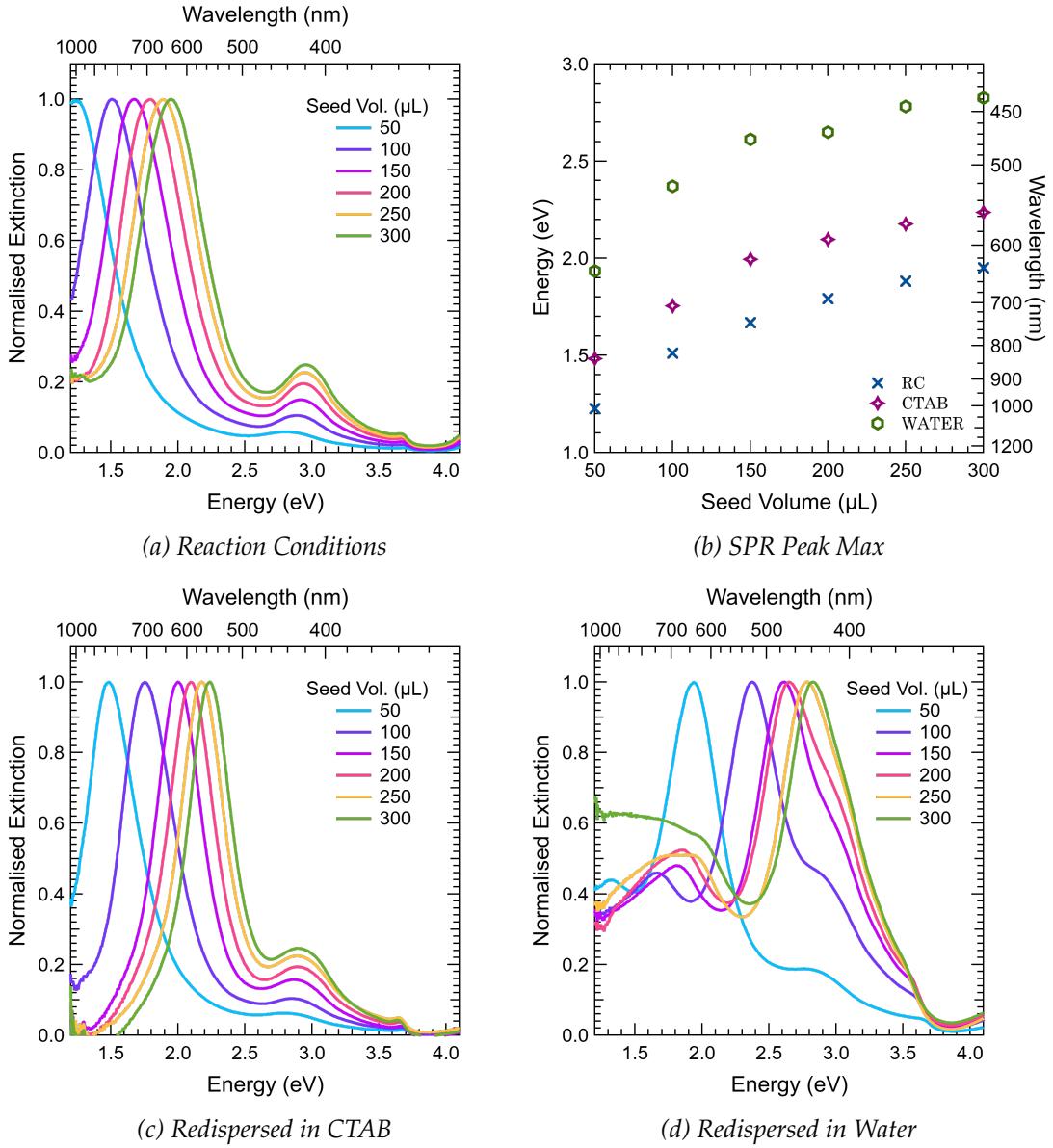


*(a) Reaction Conditions*

*(b) SPR Peak Max*

*(c) Redispersed in CTAB*

*(d) Redispersed in Water*

*Figure 49: Normalised extinction spectrum of colloidal silver nanoparticle solutions with increasing 44K PVP-capped seed volumes, from 50-300 µL, added to a fixed growth solution. The extinction data was collected with particles in (a) reaction conditions, (c) redispersed in 10 mL of 10 mM CTAB or (d) 10 mL of Type I water. The SPR peak minimum for each seed volume (b) is presented for comparison across the three conditions*

This dataset reveals several clear trends. The first trend was a minor blue-shift, approximately 112 nm, in the maximum SPR peak wavelength when the particles are redispersed in CTAB compared to the SPR wavelengths of the nanoparticle solutions before purification. This trend was consistent across the series and was coupled with decreased FWHM values. This suggests that the particles shrink during the purification process and that the final mixture was more monodisperse than the reaction condition solutions. The second trend was a significant blue-shift, approximately 260 nm, in the maximum SPR

peak wavelength when the particles are redispersed in Type I water compared to their reaction conditions.

*Table 9: Characteristics of colloidal silver nanoparticle solutions with increasing 44K PVP-capped seed volumes, from 50-300 µL, added to a fixed growth solution. Comparing the particles redispersed in 10 mL of 10 mM CTAB or 10 mL of Type I water*

| Seed Volume (µL) | 50 | 100 | 150 | 200 | 250 | 300 |
|---|---|---|---|---|---|---|
| CTAB | 1.48 | 1.76 | 1.99 | 2.10 | 2.18 | 2.24 |
| Water | 1.94 | 2.37 | 2.61 | 2.65 | 2.78 | 2.83 |

*(a) LSPR (eV)*

| Seed Volume (µL) | 50 | 100 | 150 | 200 | 250 | 300 |
|---|---|---|---|---|---|---|
| CTAB | 838 | 704 | 623 | 590 | 569 | 553 |
| Water | 639 | 523 | 475 | 467 | 445 | 438 |

*(b) LSPR (nm)*

| Seed Volume (µL) | 50 | 100 | 150 | 200 | 250 | 300 |
|---|---|---|---|---|---|---|
| CTAB | 0.48 | 0.44 | 0.39 | 0.39 | 0.38 | 0.38 |
| Water | 0.66 | 0.64 | 0.62 | 0.65 | 0.49 | 0.33 |

*(c) SPR Peak Full Width Half Max*

| Seed Volume (µL) | 50 | 100 | 150 | 200 | 250 | 300 |
|---|---|---|---|---|---|---|
| CTAB | 55.9 | 60.8 | 50.0 | 48.5 | 55.8 | 52.9 |
| Water | 30.8 | 35.4 | 34.3 | 31.8 | 32.7 | 29.9 |

*(d) Zeta Potential (mV)*

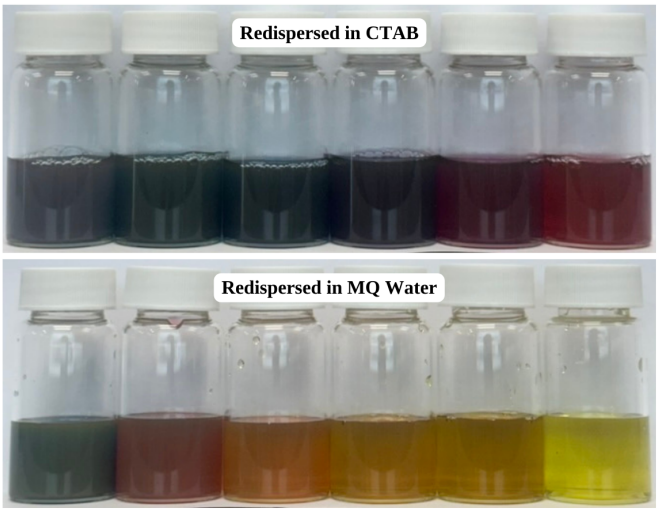


*Figure 50: Photos of colloidal silver nanoparticle solutions with increasing CTAB-capped seed volumes redispersed in CTAB (top) or Type I water (bottom). Seed volumes ranged from 50-300 µL in 50 µL increments, from left to right*

This was coupled with increased FWHM values and a change in spectrum shape. A single intense peak was still observed; however, the secondary peak was significantly less defined and appeared as a shoulder at an increased relative intensity in most samples. This new spectrum shape reflects the spectrum of circular nanoplates and supports the decrease in angularity observed in the TEM images. Optical activity was also observed in the green to NIR region of the spectrum. The lower intensity and multiple mode peaks suggest this is the optical signature for the nanorods in solution. The final trend was a

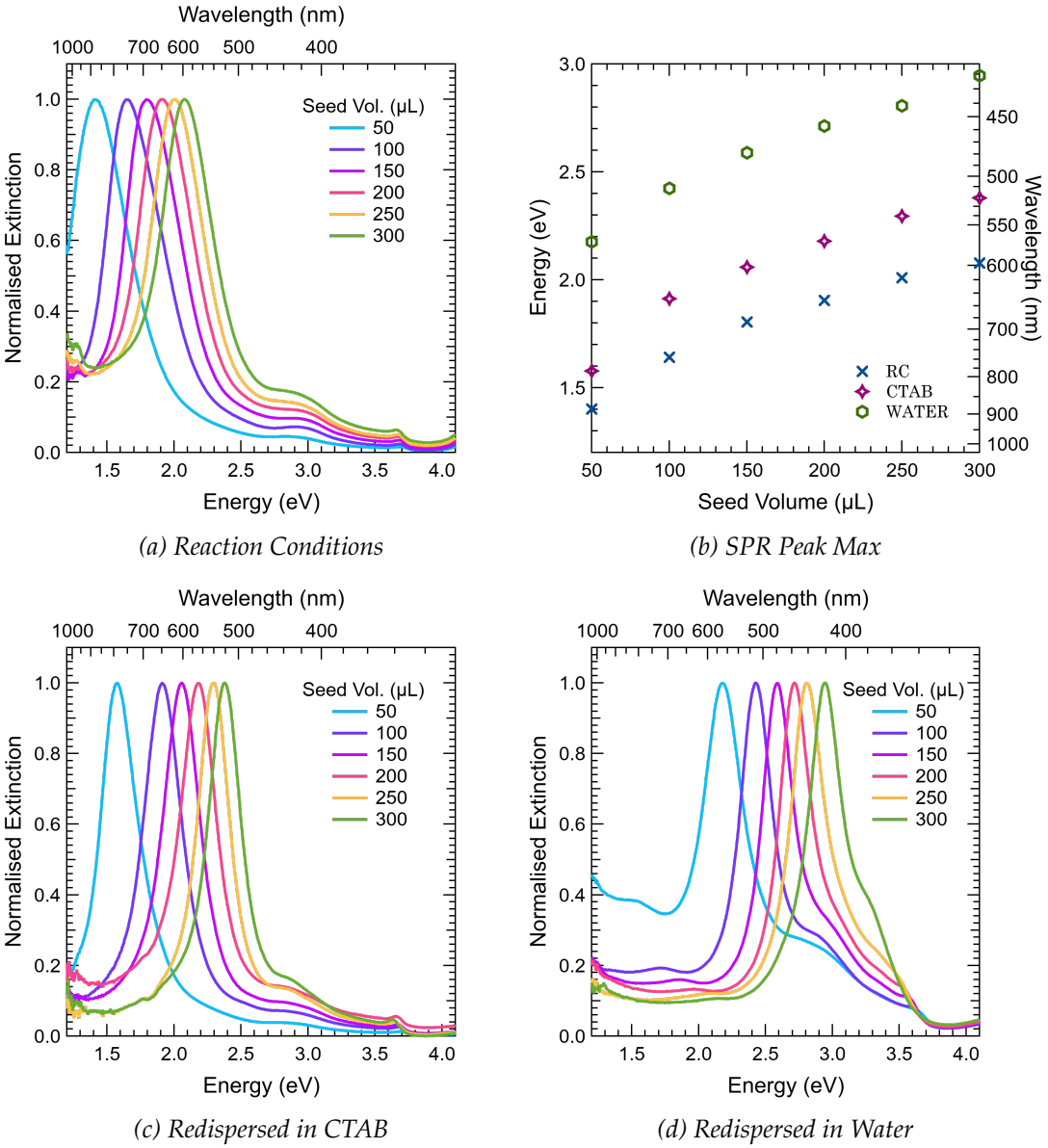


*(a) Reaction Conditions*

*(b) SPR Peak Max*

*(c) Redispersed in CTAB*

*(d) Redispersed in Water*

*Figure 51: Normalised extinction spectrum of colloidal silver nanoparticle solutions with increasing CTAB-capped seed volumes, from 50-300 µL, added to a fixed growth solution. The extinction data was collected with particles in (a) reaction conditions, (c) redispersed in 10 mL of 10 mM CTAB or (d) 10 mL of Type I water. The SPR peak minimum for each seed volume (b) is presented for comparison across the three conditions*

significant decrease in the zeta potential values when comparing the particles redispersed in CTAB to those in Type I water. The CTAB solutions range from 48.5 to 60.8 eV, which decreases an average of 21.3 eV compared to the Milli-Q solutions, which range from 29.9 to 35.4 eV.

To observe if these changes were exclusive to the 44K PVP series, the CTAB-capped seed solutions were exposed to the same conditions. The particles were separated from their reaction conditions and redispersed in Type I water, which caused an immediate and drastic alteration to the colour of the suspension. The colour change for the CTAB series is shown in Figure 50. The viable solution to avoid this colour change was a reintroduction of CTAB.

*Table 10: Characteristics of colloidal silver nanoparticle solutions with increasing CTAB-capped seed volumes, from 50-300 µL, added to a fixed growth solution. Comparing the particles redispersed in 10 mL of 10 mM CTAB or 10 mL of Type I water*

| Seed Volume (µL) | 50 | 100 | 150 | 200 | 250 | 300 |
|---|---|---|---|---|---|---|
| CTAB | 1.58 | 1.92 | 2.06 | 2.18 | 2.30 | 2.38 |
| Water | 2.18 | 2.42 | 2.59 | 2.71 | 2.81 | 2.95 |

*(a) LSPR (eV)*

| Seed Volume (µL) | 50 | 100 | 150 | 200 | 250 | 300 |
|---|---|---|---|---|---|---|
| CTAB | 784 | 645 | 601 | 568 | 539 | 520 |
| Water | 568 | 512 | 478 | 457 | 441 | 420 |

*(b) LSPR (nm)*

| Seed Volume (µL) | 50 | 100 | 150 | 200 | 250 | 300 |
|---|---|---|---|---|---|---|
| CTAB | 0.35 | 0.34 | 0.34 | 0.33 | 0.29 | 0.30 |
| Water | 0.46 | 0.31 | 0.31 | 0.31 | 0.34 | 0.36 |

*(c) SPR Peak Full Width Half Max*

| Seed Volume (µL) | 50 | 100 | 150 | 200 | 250 | 300 |
|---|---|---|---|---|---|---|
| CTAB | 57.0 | 51.5 | 54.5 | 54.1 | 58.5 | 61.6 |
| Water | 45.4 | 44.3 | 35.9 | 32.2 | 31.4 | 33.7 |

*(d) Zeta Potential (mV)*

The normalised extinction spectra for the CTAB series are presented in Figure 51. These spectra compare the optical properties of the particle in reaction conditions (51a), when redispersed in CTAB (51b), and when redispersed in Type I water (51c). The maximum SPR peak wavelengths for each sample, in nanometers (10a) and energy units (10b), are presented in Table 10. This table also includes the FWHM (10c) and zeta potential value (10d) and compares these values for particles redispersed in CTAB and Type I wa-

ter.

This data set shows the same three trends observed in the 44K PVP series. The first trend was a minor blue-shift, approximately 86.5 nm, in the maximum SPR peak wavelength between the CTAB and reaction conditions solutions. This was coupled with decreased FWHM values. The second trend was a significant blue-shift, approximately 226.7 nm, in the maximum SPR peak wavelength when the particles are redispersed in Type I water. However, this trend was coupled with a decrease in the FWHM values for this series. This suggests a higher degree of monodispersity in the particle morphologies in this series when the particles were redispersed in Type I water.

Compared to the samples redispersed in CTAB, the presence of a single intense peak remained; however, a secondary shoulder appeared at an increased relative intensity. The final trend was a significant decrease in the zeta potential values when comparing the particles redispersed in CTAB to those in Type I water. The CTAB solutions range from 51.5 to 61.6 eV, which decreases an average of 19.1 eV compared to the Milli-Q solutions, which range from 31.4 to 45.4 eV.

The significant difference in the excitation data for each series was the optical activity seen in the green to NIR region of the spectrum in the Type I water samples. In the 44K PVP series, these peaks are ill-defined and show no clear wavelength shift trends.In contrast, the CTAB series has more defined peaks in this region that show a minor red-shift and an increase in relative intensity when the seed solution volume is decreased.

#### 3.2.1.4 Comparing 10K and 29K PVP-Capped Seeds

The following experiment investigated the impact of changing the polymer chain length of PVP on the characteristics of the nanostructures produced. The nanoparticle solutions were synthesised for direct comparison using the method described in section 2.2.2. However, the seeds were substituted for the 10K and 29K PVP-capped seeds. The independent variable was the volume of seed solution added to the fixed growth solution. For these experiments the range was altered to 50-250 µL in 100 µL increments. The normalised extinction spectra for the nanoparticle solutions produced across this range for the 10K (52a) and 29K (52b) PVP series are presented in Figure 52 below.

All samples in both series follow the trend of a systematic red-shift of the maximum SPR peak as the volume of the seed solution decreases. However, compared to the 44K PVP and CTAB series, the maximum SPR peak wavelengths are red-shifted further. Presented in Table 11 below are the maximum SPR peak wavelengths for each sample, in nanometers (11a) and energy units (11b). This table also includes the FWHM (11c) and

zeta potential value (11d).

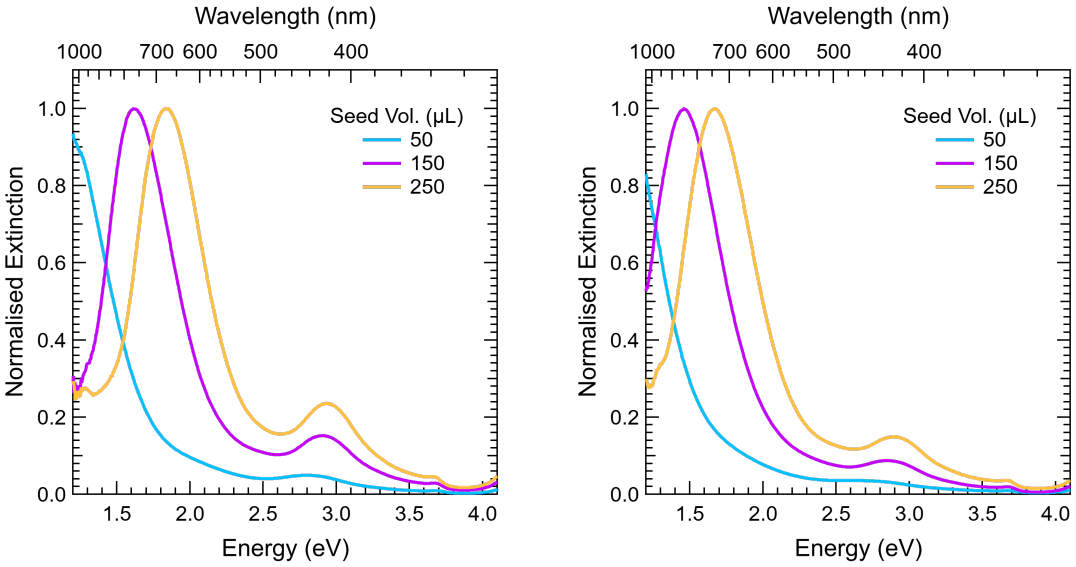


*(a) 10K PVP-capped Seed*

*(b) 29K PVP-capped Seed*

*Figure 52: Normalised extinction spectrum of colloidal silver nanoparticle solutions with increasing (a) 10K or (b) 29K PVP-capped seed volumes. Seed volumes ranged from 50-250 µL in 100 µL increments. This data was collected with particles in reaction conditions*

*Table 11: Maximum SPR peak values of colloidal silver nanoparticle solutions with increasing 10K PVP or 29K PVP-capped seed volumes, from 50-250 µL, in reaction conditions*

| Seed Volume (µL) | 50 | 150 | 250 |
|---|---|---|---|
| 10K PVP | 1.17 | 1.61 | 1.83 |
| 29K PVP | 1.13 | 1.46 | 1.67 |

*(a) LSPR (eV)*

| Seed Volume (µL) | 50 | 150 | 250 |
|---|---|---|---|
| 10K PVP | 1059 | 770 | 667 |
| 29K PVP | 1097 | 849 | 742 |

*(b) LSPR (nm)*

| Seed Volume (µL) | 50 | 150 | 250 |
|---|---|---|---|
| 10K PVP | 0.57 | 0.53 | 0.53 |
| 29K PVP | N/A | 0.58 | 0.57 |

*(c) SPR Peak Full Width Half Max*

| Seed Volume (µL) | 50 | 150 | 250 |
|---|---|---|---|
| 10K PVP | 34.9 | 35.1 | 37.7 |
| 29K PVP | 35.8 | 37.2 | 37.2 |

*(d) Zeta Potential (mV)*

For the sample with 50 µL of seed solution introduced, the maximum SPR peak wavelengths for the CTAB, 44K, 29K and 10K series are 1.40 (885 nm), 1.23 (1008 nm), 1.13 (1097 nm) and 1.17 eV (1059 nm), respectively. A significant red-shift of 0.1 eV or 89 nm was observed between the 44K and 29K PVP series. This suggests that the shorter polymer chain lengths produce larger nanostructures. The SPR peak wavelength blue-shifts slightly, 0.04 eV or 38 nm, from the 29K to the 10K PVP sample. The extended red-shift of the SPR peak wavelength was consistent across the 10K and 29K PVP series.

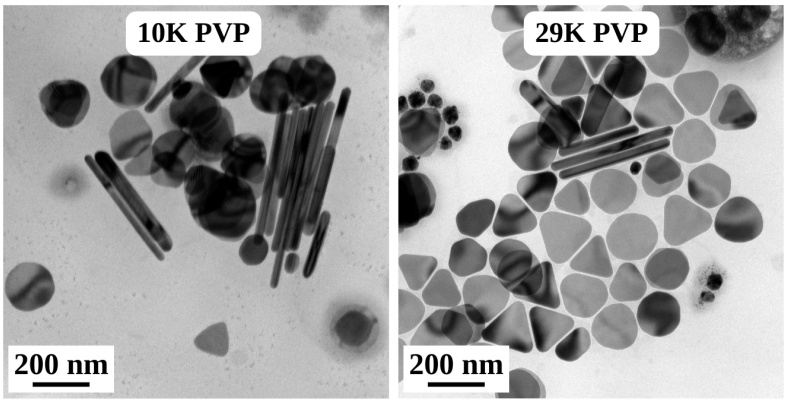


*Figure 53: TEM images of 10K and 29K PVP-capped seed solutions redispersed in water*

The 29K PVP series had the longest wavelength peaks and produced the largest particles. TEM images comparing the 10K and 29K particles from 50 µL of seed solution are presented in Figure 53. These images show that the synthetic conditions using both the 10K and 29K PVP-capped seeds also produce a mixture of nanostructures, including

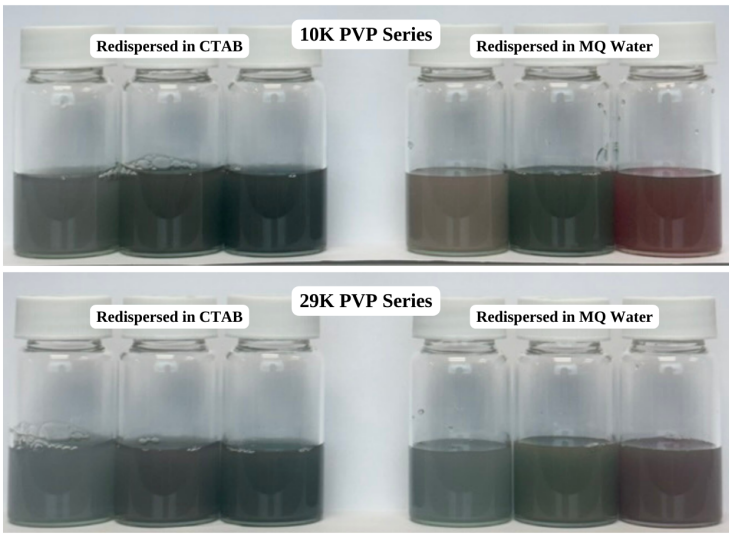


*Figure 54: Photos of colloidal silver nanoparticle solutions with increasing 10K (top) or 29K (bottom) PVP-capped seed volumes redispersed in CTAB (left) or Type I water (right). Seed volumes ranged from 50-250 µL in 100 µL increments*

triangular nanoplates, circular nanoplates, nanorods and excess nanoseeds. Notably, the 10K PVP-capped seeds produced longer nanorods, whereas the 29K PVP-capped seeds produced shorter nanorods but a higher yield of triangular nanoplates with an increased edge length.

The particles were separated from their reaction conditions and redispersed in Type I water. A colour change was observed; however, the change was less drastic than the 44k PVP and CTAB series. This was supported by the higher degree of angularity maintained in the TEM image of these particles redispersed in water. The solution colours for the 10k and 29K PVP series are shown in Figures 54. This image also includes the solution colours when a reintroduction of CTAB stabilises the particles.

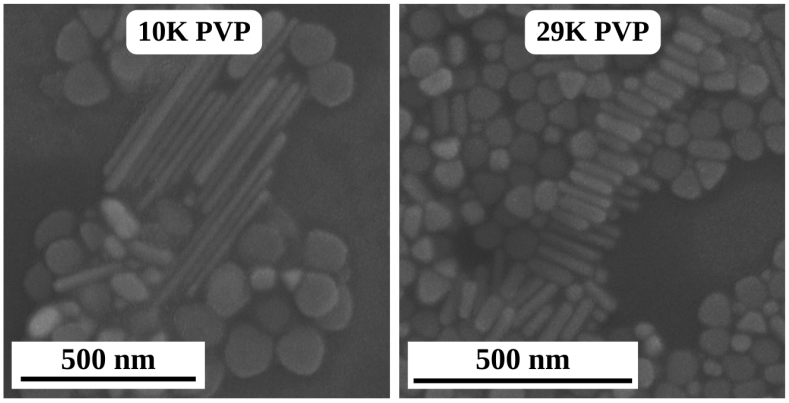


*Figure 55: SEM images of 10K and 29K PVP-capped seed solutions redispersed in Type I water*

The SEM images of the 10K and 29K samples in Figure 55 demonstrate that the particles exhibit reduced angularity when redispersed in water. Interestingly, the 29K PVP samples maintain their angularity better than the 10K particles. Additionally, it is worth noting that the rods in the 29K PVP sample are notably shorter than those produced with the 10K PVP.

For comparison, the normalised extinction spectra for the 10K and 29K PVP series are presented in Figure 56. These spectra compare the optical properties of the nanoparticles redispersed in CTAB (56a,c) or Type I water (56b,d). For clarity, the maximum SPR peak wavelengths for each sample, in nanometers (12a,b) and energy units (12c,d), are presented in Table 12. This table also includes the FWHM (12e,f) and zeta potential value (12g,h) and compares these values for particles redispersed in CTAB and Type I water.

This data set shows the same three trends observed in the 44K PVP and CTAB series. The first trend was a minor blue-shift in the maximum SPR peak wavelength between the CTAB and reaction conditions solutions, coupled with decreased FWHM values. This blue-shift averages 60.3 and 20.3 nm for the 10K and 29K PVP series, respectively. The

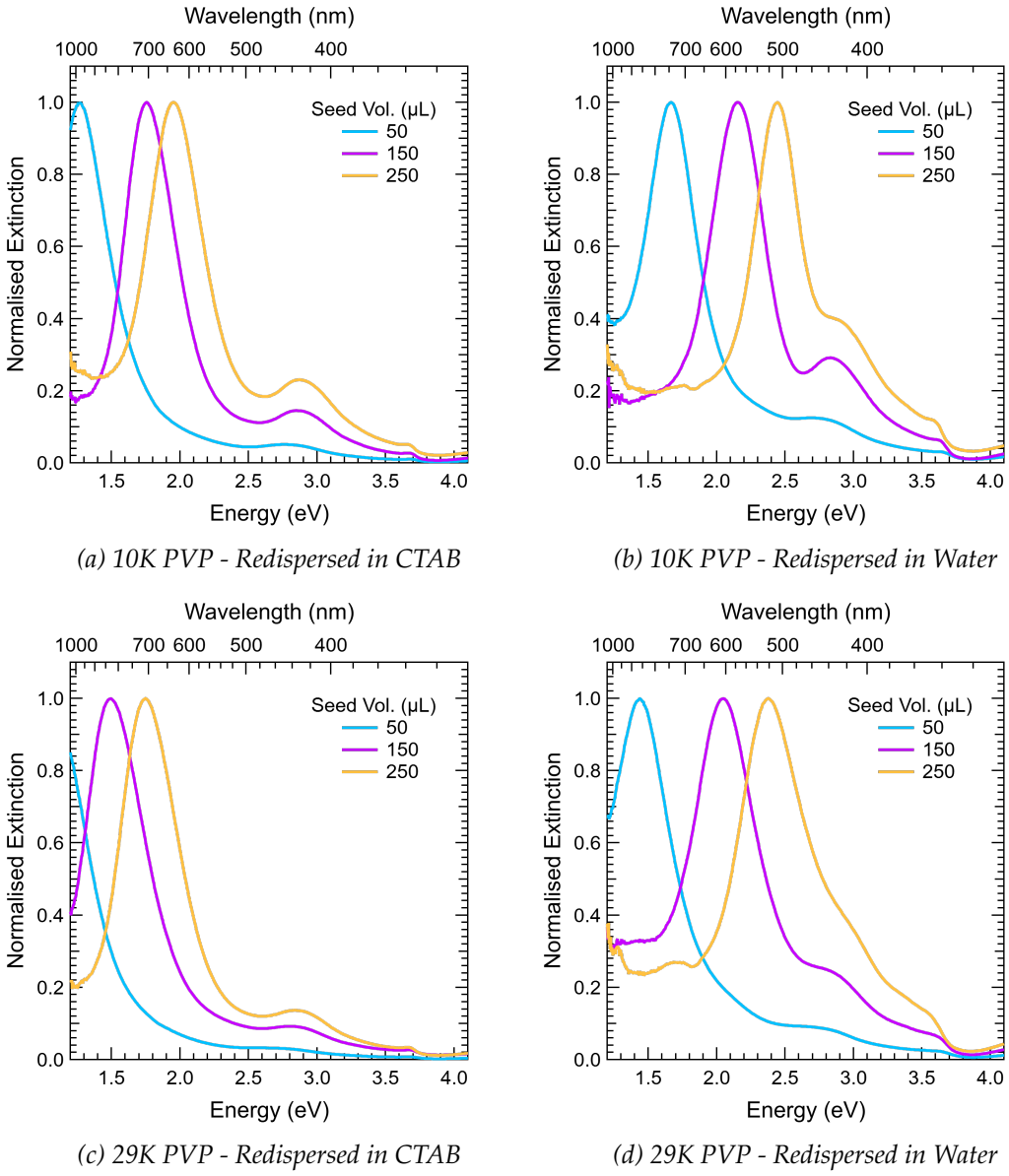


*(a) 10K PVP - Redispersed in CTAB*

*(b) 10K PVP - Redispersed in Water*

*(c) 29K PVP - Redispersed in CTAB*

*(d) 29K PVP - Redispersed in Water*

*Figure 56: Normalised extinction spectrum of colloidal silver nanoparticle solutions with increasing 10K (a,b) or 29K (c,d) PVP-capped seed volumes. Seed volumes ranged from 50-250 µL in 100 µL increments. This data was collected with particles redispersed in 10 mL of 10 mM CTAB or 10 mL of Type I water for comparison*

second trend was a significant blue-shift in the maximum SPR peak wavelength when the particles were redispersed in Type I water. This blue-shift averages 224.1 and 233.3 nm for the 10K and 29K PVP series.

Contrary to the 44K PVP and CTAB series, the FWHM values between the reaction condition and CTAB spectra change minimally. The FWHM values for the 10K PVP series decreased slightly when the particles were dispersed in water. For the 29K PVP series, a single intense peak was still observed, and a secondary shoulder appeared at an increased relative intensity compared to the samples redispersed in CTAB. For the 10K

PVP series, this shoulder peak was more defined.

The final trend was a decrease in the zeta potential values when comparing the particles redispersed in CTAB to those in Type I water. For the 10K PVP series, the CTAB redispersed solutions range from 48.5 to 57.0 eV. This was an average decrease of 17.0 eV

*Table 12: Characteristics of colloidal silver nanoparticle solutions with increasing 10K or 29K PVP-capped seed volumes, from 50-250 µL, in 100 µL increments. This data was collected with particles redispersed in 10 mL of 10 mM CTAB or 10 mL of Type I water for comparison*

| Seed Volume (µL) | 50 | 150 | 250 |
|---|---|---|---|
| CTAB | 1.27 | 1.76 | 1.95 |
| Water | 1.67 | 2.15 | 2.45 |

*(a) 10K PVP - LSPR (eV)*

| Seed Volume (µL) | 50 | 150 | 250 |
|---|---|---|---|
| CTAB | 1.14 | 1.49 | 1.75 |
| Water | 1.44 | 2.04 | 2.38 |

*(b) 29K PVP - LSPR (eV)*

| Seed Volume (µL) | 50 | 150 | 250 |
|---|---|---|---|
| CTAB | 976 | 704 | 635 |
| Water | 742 | 576 | 506 |

*(c) 10K PVP - LSPR (nm)*

| Seed Volume (µL) | 50 | 150 | 250 |
|---|---|---|---|
| CTAB | 1087 | 832 | 708 |
| Water | 861 | 607 | 520 |

*(d) 29K PVP - LSPR (nm)*

| Seed Volume (µL) | 50 | 150 | 250 |
|---|---|---|---|
| CTAB | 0.49 | 0.43 | 0.48 |
| Water | 0.53 | 0.48 | 0.45 |

*(e) 10K PVP - SPR Peak Full Width Half Max*

| Seed Volume (µL) | 50 | 150 | 250 |
|---|---|---|---|
| CTAB | 0.51 | 0.54 | 0.49 |
| Water | 0.62 | 0.67 | 0.65 |

*(f) 29K PVP - SPR Peak Full Width Half Max*

| Seed Volume (µL) | 50 | 150 | 250 |
|---|---|---|---|
| CTAB | 55.1 | 57.0 | 48.5 |
| Water | 38.4 | 35.3 | 35.9 |

*(g) 10K PVP - Zeta Potential (mV)*

| Seed Volume (µL) | 50 | 150 | 250 |
|---|---|---|---|
| CTAB | 51.0 | 58.4 | 52.5 |
| Water | 37.8 | 38.2 | 36.8 |

*(h) 29K PVP - Zeta Potential (mV)*

compared to the Type I water solutions, ranging from 35.3 to 38.4 eV. For the 29K PVP series, the CTAB redispersed solutions range from 51.0 to 58.4 eV. This was an average decrease of 16.4 eV when compared to the Type I water solutions, which range from 36.8 to 38.2 eV. Similarly to the 44K PVP series, the optical activity seen in the green to NIR of the spectrum in the Type I water samples consists of ill-defined peaks with no clear trend in wavelength shifting.

#### 3.2.1.5 TSC Seed Experiments

A single experiment investigated the impact of incorporating the TSC-capped seeds. For this experiment, the independent variable was the volume of seed solution added to the fixed growth solution. To keep the experiments comparable, a range of 100-300 µL in 50 µL increments was used. The normalised extinction spectra for the TSC series are

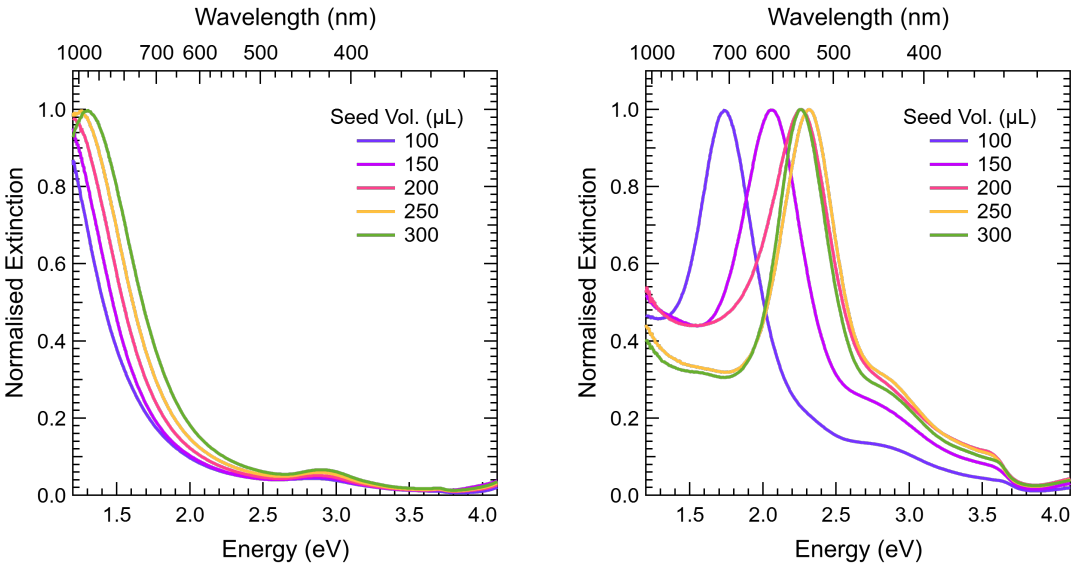


*(a) Redispersed in CTAB*

*(b) Redispersed in Type I water*

*Figure 57: Normalised extinction spectrum of colloidal silver nanoparticle solutions with increasing TSC-capped seed volumes. Seed volumes ranged from 100-300 µL in 50 µL increments. This data was collected with particles in reaction conditions (a) or redispersed in Type I water (b)*

presented in Figure 57. The figure compares the normalised extinction spectra of the solutions in reaction conditions (58a) and redispersed in water (58b).

Similarly to the other seed series, the SPR peak maximum consistently red-shifts as the seed volume decreases. The relative intensity of the secondary peak was noticeably reduced compared to the CTAB and PVP series. The maximum peak values are also considerably red-shifted by comparison. The 100 µL sample in the TSC series has a peak position of 1.12 eV (1107 nm) compared to 1.51 eV (821 nm) and 1.64 eV (742 nm) for the 44K PVP and CTAB-capped seed samples of the same volume. This indicated that the TSC-capped seeds were producing significantly larger nanostructures. This was con-

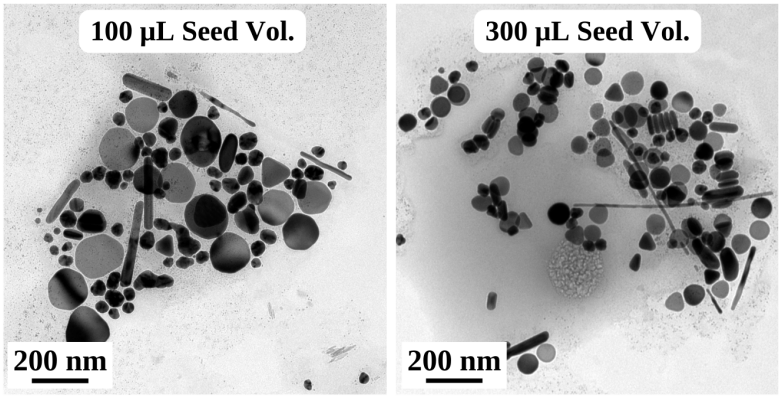


*Figure 58: TEM images of a silver nanoparticle solution with 100 µL (left) or 300 µL (right) of TSC-capped seeds redispersed in Type I water*

firmed by the TEM images presented in Figure 58.

When the seed volume was increased, a decrease in particle size was observed, supporting the blue-shift in the spectrum. The TEM images show particles redispersed in Type I water. This has led to a decrease in the angularity of the nanoplates, coupled with a blue-shift in the extinction spectrum. Additionally, the spectrum of the water condition samples displays numerous extra peaks across the visible and infrared regions. This indicates a high degree of polydispersity in these samples, which aligns with the TEM images that show a range of shapes of varying sizes.

### 3.2.2 Discussion

#### 3.2.2.1 Initial experiments

The preceding results revealed disparities between the experimental data and the data documented by Rekha et al.[51] The significant red-shift in the SPR peak for the lower seed volume in the initial comparison samples indicated notable differences in the size of the experimentally produced particles compared to those reported. Importantly, the observed shift in the reported TSPR peaks was not replicated experimentally, suggesting that the reported particles did not exhibit the level of uniformity claimed by the authors. The impact of the excess nanostructures on the optical properties of nanoparticle solutions was not effectively considered.

The identification of the SPR resonance peaks by the author does not align with our findings. The reproduced extinction spectrum in Figure 25 depicts two spectra with differing SPR peak positions and widths. The authors associated these two spectra with the excess nanostructures and segregated nanorods obtained after their purification method. They attributed the longer wavelength peak, around 580 nm, to the LSPR of the nanorods and the shorter wavelength peak, at approximately 435 nm, to the TSPR. However, the nanorods in the SEM images are about 250 nm long.[51]

Comparing this length with the theoretical extinction spectra of a 230 nm long nanorod in Figure 34, the LSPR peak for mode 1 should occur at a significantly longer wavelength of 1400 nm. The theoretical spectrum suggests these peaks could correspond to the transverse and less prominent longitudinal modes of the nanorod.[97] However, the SEM image of the sample shows an excess of nanoplates, suggesting that the prominent nanoplate modes could overshadow the nanorod resonances.

The excess nanoplates appear to be approximately 80 nm in diameter, but their size varies significantly across the image. The theoretical extinction spectrum of silver nano-

spheres in Figure 31 suggests that 80 nm spheres will produce a spectrum with a maximum SPR peak at 470 nm with a blue-shifted shoulder. Comparing theoretical data with experimental data presents challenges due to the precision of shape and size. The theoretical data is calculated for a specific shape and size, while experimentally achieving this level of uniformity is challenging. Consequently, these shifts in peak positions are to be expected.

Analysis of the experimental SEM and TEM images of the nanoparticle solutions resulting from this method indicates a combination of triangular and circular nanoplates, nanorods, and excess nanoseeds. This concurs with the findings stated in the Rekha article. The conditions of the purification protocol were not detailed in the article.[51] However, the minimal angularity observed in the reported nanoplate images implies that these particles were subjected to low CTAB concentration conditions before segregation.

The SEM images presented in Figure 48 show the mixture of circular nanoplates and nanorods that result from re-dispersing these nanoparticle solutions in Type I water after centrifugation. It should be noted that two images were captured in different areas of the same sample to display the overall particle distribution in these samples. Although areas with a high yield of nanorods can be deliberately selected to create the impression of satisfactory segregation, a substantial number of excess nanoplates still remain in the surrounding areas.

Our initial findings highlighted the challenges associated with achieving a highly reproducible synthesis of silver nanoparticles. The subsequent experiments in this chapter aimed to deepen our understanding of the critical parameters involved in this synthesis. We adjusted the synthetic conditions and reagents to optimise the production of triangular nanoplates or nanorods with higher yields. Additionally, these experiments aimed to further explore the optical properties of the nanoparticle suspensions and examine how the various nanoparticle morphologies influence the overall extinction spectral profile.

#### 3.2.2.2 Seed Variations

In each series of experiments, regardless of the seed capping reagent used, a consistent red-shift in the SPR peak wavelength was observed as the seed volume decreased. One notable difference when the seed capping reagent was changed was the varying degree of this shift and the relative intensity of the secondary resonance peak. The size of the seed particles changed significantly depending on the capping reagent used. The CTAB-capped seeds had the smallest diameter but exhibited high levels of aggregation.

Upon introduction into the growth solution, the CTAB-capped seed series displayed

a less defined secondary peak than the three PVP series. The CTAB-capped seeds, being single crystalline in nature, produced nanorods and nanoplates with lower angularity than the PVP series. On the other hand, the TSC seeds yielded a high percentage of large multiply twinned and planar-twinned seeds with low monodispersity, resulting in a high degree of polydispersity in the produced nanoparticles.

The noticeable secondary resonance peak in the three PVP series suggests that PVP-capped seeds produced thicker triangular nanoplates. Our findings align with a study by Xia et al., which showed that adjusting the PVP chain length directly impacted the size and shape of the resulting nanoparticles.[64] We observed a significant red-shift in the SPR peak as we reduced the PVP chain length from 44K to 10K PVP. TEM images confirmed that nanoplates produced with 10K PVP were considerably larger. Furthermore, a further red-shift occurred when the PVP chain length was changed to 29K, resulting in nanoplates with the largest edge lengths.

The TEM images revealed significant differences between the 10K and 29K PVP particles. The 10K PVP-capped seeds produced predominantly large circular nanoplates, whereas the 29K PVP-capped seeds yielded a higher proportion of triangular nanoplates. Notably, the nanorods produced with the 10K seed showed similarities to those generated with the 44K seed. In both cases, the rod length increased while the thickness remained constant. These findings contrasted with the 29K PVP seeds, where the nanorod length decreased and the thickness increased as the seed volume increased.

These variations are attributed to the differing preferential binding facets of PVP chain lengths. Similar to the observations made by Tsuji et al., altering the PVP chain length influenced particle size and the yield of each particle shape.[63] Tsuji and co-workers reported an increased nanorod yield with increasing chain length, noting a significant shift in preferential facet binding between 10K and 55K. Our results support this, suggesting that this shift in preferential binding may have contributed to the differences observed between the particles produced with 29K PVP-capped seeds and those produced with 10K or 44K. The dominant absorption of the 10K PVP onto the {111} facets influenced the high yield of large, circular nanoplates. In contrast, the shift in binding to the {100} facet with increasing chain length led to a higher proportion of triangular nanoplates in the 29K and 44K PVP-capped seed samples.

The primary distinction between this work and prior studies lies in the incorporation of a secondary capping agent. The presence of CTAB in the growth solution significantly influenced the size and shape of the resulting particles. The soft template provided by

CTAB is crucial for producing nanorods and has been extensively studied in the production of gold nanorods. However, based on the extinction data and images, it appears that nanoplates are generated at higher yields than nanorods in this synthesis. In a previous article, Chen and Carroll described a method for producing truncated triangular silver nanoplates using the same reagents and ratios as those utilised for the nanorods synthesised by Rekha et al.[9651]

The critical difference between the two papers is that the synthesis by Chen et al. was conducted at a scale 10-fold higher and used TSC-capped seeds. However, Rekha and co-workers claimed that their synthesis was an optimisation of a previously reported synthesis by Murphy and co-workers, which employed TSC-capped seeds.[34] Chen and Carroll acknowledged the production of nanorods in their synthesis, along with other excess nanostructures that made up over 20% of the yield. Still, the authors demonstrated that the majority of the nanostructures formed were triangular nanoplates.[96]

They also highlighted the changes observed when these nanoplates are removed from their reaction conditions and redispersed in water. They noted the observed blue-shift in the maximum SPR peak as the triangular nanoplates become more disk-like. Similar blue-shifts of the resonance peak and decreased angularity of the particles are observed in our experiments when the particles are dispersed in water. However, the severity of the truncation is hindered in the 29K PVP-capped seed samples. This supports the theory that the 29K PVP preferentially binds and stabilises multiple crystal facets.

These experiments have demonstrated that altering the capping reagent on the seed particle used in this seed-mediated growth synthesis plays a pivotal role in determining the resultant nanostructures. The findings indicate that, regardless of the capping reagent used, the synthesis yields a variety of nanoparticles, including triangular nanoplates, nanorods, and nanospheres. Additionally, the collected imagery and extinction spectra of the nanoparticle suspensions highlight the instability and significant morphological transformations that occur when the triangular nanoplates are redispersed in low concentrations of CTAB. The subsequent experiments focus on enhancing the stability of these nanoplates to preserve the broad spectral range observed across these suspensions.

## 3.3 Introduction of PVP into the Growth Solution

### 3.3.1 Results

In these experiments, PVP was introduced into the growth solution to investigate the impact of adding a secondary stabilising ligand. The first independent variable was

the volume of 44K PVP-capped seed solution added to the fixed growth solution. For these experiments the range was 100-300 µL in 100 µL increments. To the growth solution 500 µL or 1000 µL of 10, 29 or 44K PVP was introduced. The normalised extinction spectra for the nanoparticle solutions produced across this range for the 10K, 29K and 44K PVP series are presented in Figures 59, 60, 61, respectively.

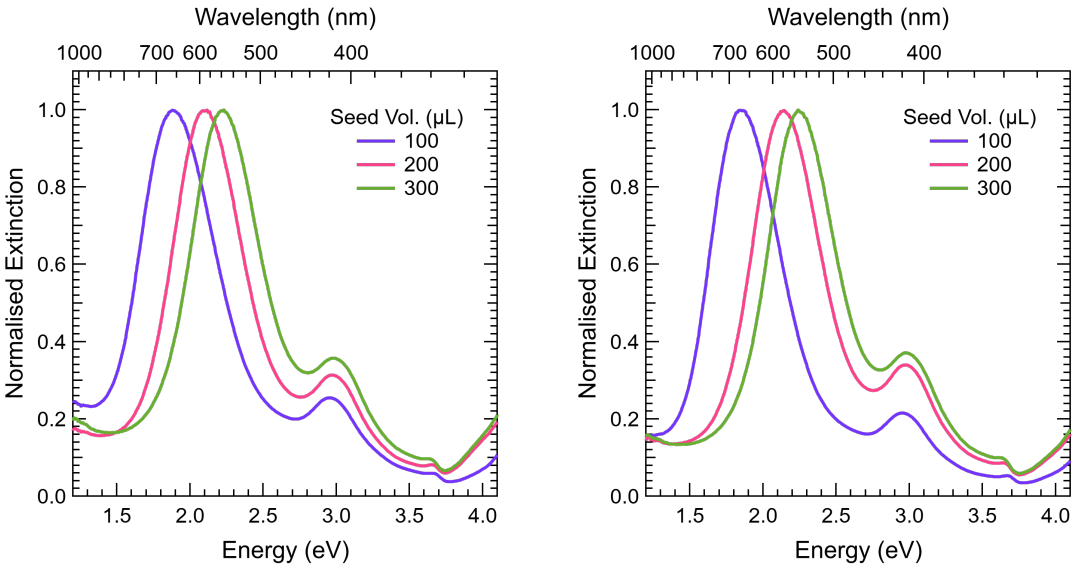


*(a) 500 µL of 1% 10K PVP*

*(b) 1000 µL of 1% 10K PVP*

*Figure 59: Normalised extinction spectrum of colloidal silver nanoparticle solutions with increasing 44K PVP-capped seed volumes, from 100-300 µL, in 100 µL increments. 500 (a) or 1000 µL (b) of 1% 10K PVP was added to the growth solutions before the seed introduction*

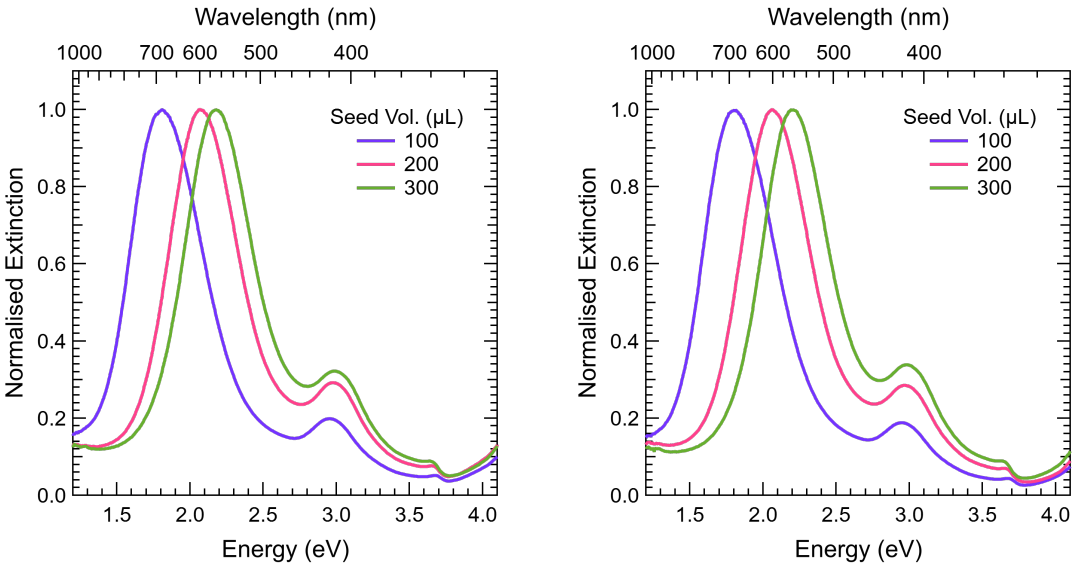


*(a) 500 µL of 1% 29K PVP*

*(b) 1000 µL of 1% 29K PVP*

*Figure 60: Normalised extinction spectrum of colloidal silver nanoparticle solutions with increasing 44K PVP-capped seed volumes, from 100-300 µL, in 100 µL increments. 500 (a) or 1000 µL (b) of 1% 29K PVP was added to the growth solutions before the seed introduction*

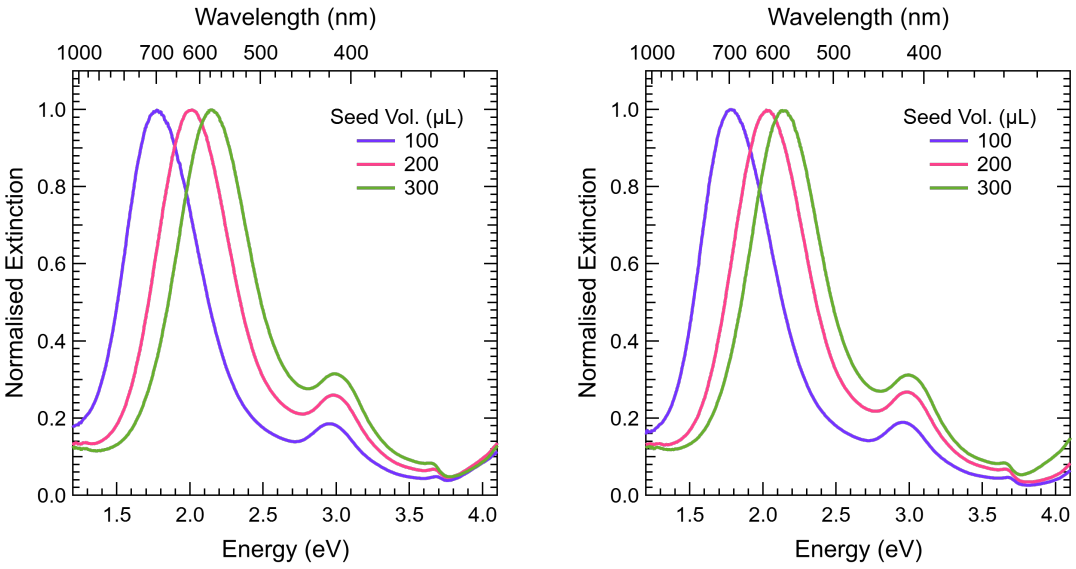


*(a) 500 µL of 1% 44K PVP*

*(b) 1000 µL of 1% 44K PVP*

*Figure 61: Normalised extinction spectrum of colloidal silver nanoparticle solutions with increasing 44K PVP-capped seed volumes, from 100-300 µL, in 100 µL increments. 500 (a) or 1000 µL (b) of 1% 44K PVP was added to the growth solutions before the seed introduction*

All samples show the trend of a systematic red-shift of the maximum SPR peak as the volume of the seed solution decreases. The peak positions shift minimally when the PVP chain length decreases. The samples with 100 µL of 44K PVP-capped seed solution and 44K, 29K, or 10K PVP in the growth solution exhibit SPR peaks at 1.78 eV (697 nm), 1.81 eV (685 nm), and 1.88 eV (659 nm), respectively. This was a shift of 0.1 eV across the series. This minimal shift was observed at all seed volumes, and the volume of PVP introduced has no notable impact on these values.

For clarity, the maximum SPR peak wavelengths for each sample, in nanometers (13a) and energy units (13b), are presented in Table 13. This table also includes the FWHM (13c) and zeta potential value (13d). The SPR peak position for the 100 µL of 44K PVP-capped seed solution without PVP in the growth solution was 1.76 eV (704 nm). This suggests that the introduction of PVP into the growth solution has a minimal impact on the size of the nanostructures produced. However, the PVP was affecting the zeta potential value of these particles.

The zeta potential for the 100 µL seed sample without PVP in the growth solution was 33.5 mV. This value was decreased to 8.7, 17.7 and 14.3 mV for the samples with 10K, 29K or 44K PVP, respectively. The zeta potentials compared here were collected with the nanoparticles in reaction conditions. This significant decrease in potential was observed in all samples across the range. The only exception to this observation was a more minor decrease in the values for the series with 1000 µL of 10K PVP introduced. The reduction

*Table 13: Maximum SPR peak values of colloidal silver nanoparticle solutions with increasing 44K PVP-capped seed volumes, from 100-300 µL, in 100 µL increments. 500 or 1000 µL of 1% 10K, 29K or 44K PVP was added to the growth solutions before the seed introduction*

| Seed Volume (µL) | 100 | 200 | 300 |
|---|---|---|---|
| 10K | 1.88 | 2.11 | 2.23 |
| 29K | 1.81 | 2.06 | 2.18 |
| 44K | 1.78 | 2.01 | 2.13 |

*(a) 500 µL of 44K PVP - LSPR (eV)*

| Seed Volume (µL) | 100 | 200 | 300 |
|---|---|---|---|
| 10K | 1.85 | 2.14 | 2.24 |
| 29K | 1.80 | 2.06 | 2.19 |
| 44K | 1.78 | 2.03 | 2.13 |

*(b) 1000 µL of 44K PVP - LSPR (eV)*

| Seed Volume (µL) | 100 | 200 | 300 |
|---|---|---|---|
| 10K | 659 | 587 | 556 |
| 29K | 685 | 602 | 569 |
| 44K | 697 | 617 | 582 |

*(c) 500 µL of 44K PVP - LSPR (nm)*

| Seed Volume (µL) | 100 | 200 | 300 |
|---|---|---|---|
| 10K | 670 | 579 | 554 |
| 29K | 688 | 602 | 566 |
| 44K | 697 | 611 | 582 |

*(d) 1000 µL of 44K PVP - LSPR (nm)*

| Seed Volume (µL) | 100 | 200 | 300 |
|---|---|---|---|
| 10K | 0.59 | 0.52 | 0.54 |
| 29K | 0.55 | 0.52 | 0.54 |
| 44K | 0.56 | 0.55 | 0.58 |

*(e) 500 µL of 44K PVP - SPR Peak FWHM*

| Seed Volume (µL) | 100 | 200 | 300 |
|---|---|---|---|
| 10K | 0.53 | 0.52 | 0.54 |
| 29K | 0.55 | 0.54 | 0.54 |
| 44K | 0.55 | 0.56 | 0.55 |

*(f) 1000 µL of 44K PVP - SPR Peak FWHM*

| Seed Volume (µL) | 100 | 200 | 300 |
|---|---|---|---|
| 10K | 8.7 | 12.5 | 12.6 |
| 29K | 17.7 | 13.8 | 20.1 |
| 44K | 14.3 | 12.8 | 13.7 |

*(g) 500 µL of 44K PVP - Zeta Potential (eV)*

| Seed Volume (µL) | 100 | 200 | 300 |
|---|---|---|---|
| 10K | 28.1 | 27.1 | 24.9 |
| 29K | 18.8 | 17.7 | 19.9 |
| 44K | 11.3 | 12.5 | 10.4 |

*(h) 1000 µL of 44K PVP - Zeta Potential (eV)*

in zeta potential went from 33.5 mV without PVP to 28.1 mV with PVP.

The shift in zeta potential values suggested that the PVP was binding to the surface of the nanoparticles. A second experiment was run to observe if the PVP would stabilise the particles' angularity when redispersed in water. For this experiment, only the samples with 1000 µL of PVP in each series were investigated. The particles were separated from their reaction conditions to observe these changes and redispersed in Type I water or CTAB (10 mM) solution. As the previous experiments showed, the SPR peaks shifted minimally when the particles were dispersed in CTAB. Still, a significant alteration to the spectra was observed when the particles were redispersed in Type I water. For comparison, the normalised extinction spectra for the 10, 29, and 44K PVP introduction series are presented in Figures 62, 63, and 64, respectively. These spectra compare the optical properties of the particle redispersed in CTAB (a) or Type I water (b).

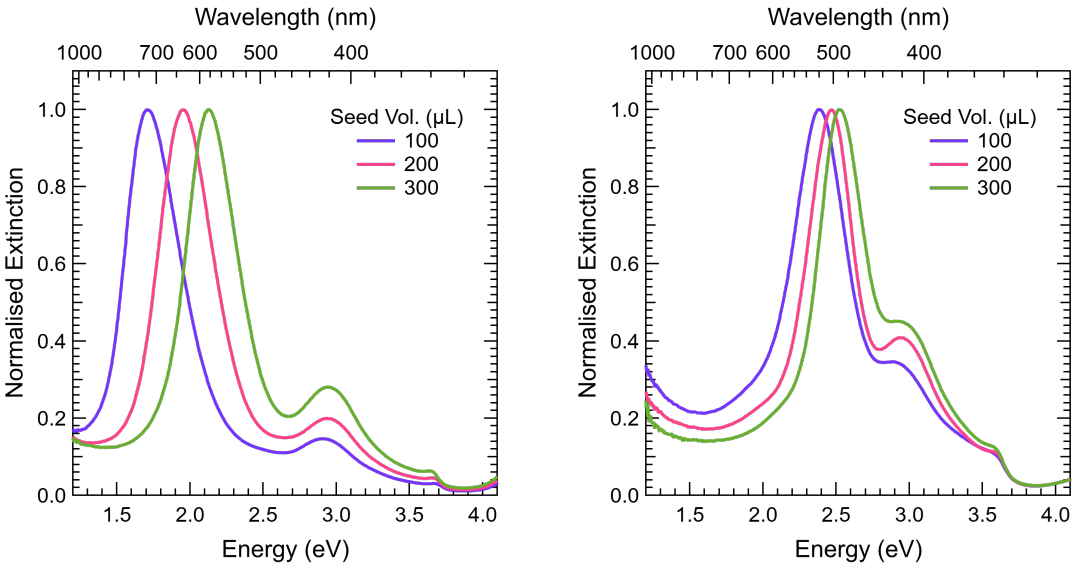


*(a) Redispersed in CTAB* *(b) Redispersed in Type I water*

*Figure 62: Normalised extinction spectrum of colloidal silver nanoparticle solutions with increasing 44K PVP-capped seed volumes, from 100-300 µL, in 100 µL increments. 1000 µL of 1% 10K PVP was also added to the growth solutions before the seed introduction. These particles were redispersed in (a) 10 mL of 10 mM CTAB solution or (b) 10 mL of Type I water*

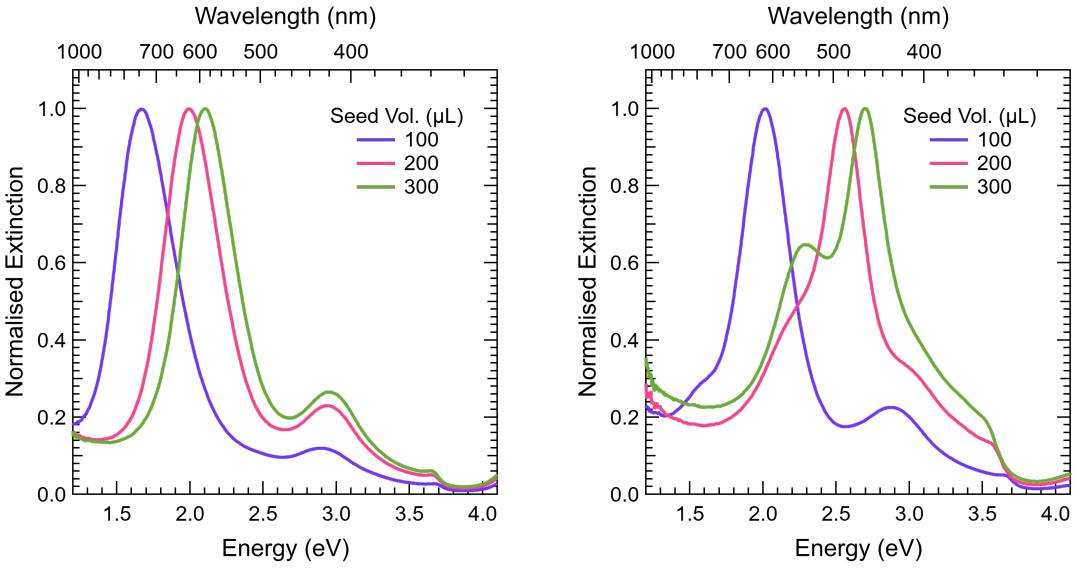


*(a) Redispersed in CTAB* *(b) Redispersed in Type I water*

*Figure 63: Normalised extinction spectrum of colloidal silver nanoparticle solutions with increasing 44K PVP-capped seed volumes, from 100-300 µL, in 100 µL increments. 1000 µL of 1% 29K PVP was also added to the growth solutions before the seed introduction. These particles were redispersed in 10 mL of 10 mM CTAB solution (a) or 10 mL of Type I water (b)*

For clarity, the maximum SPR peak wavelengths for each sample, redispersed in CTAB (14a,c) or Type I water (14b,d), are presented in Table 14 below. This table also includes the FWHM (14e,f). For the 10K PVP series, a significant shift in the SPR peak

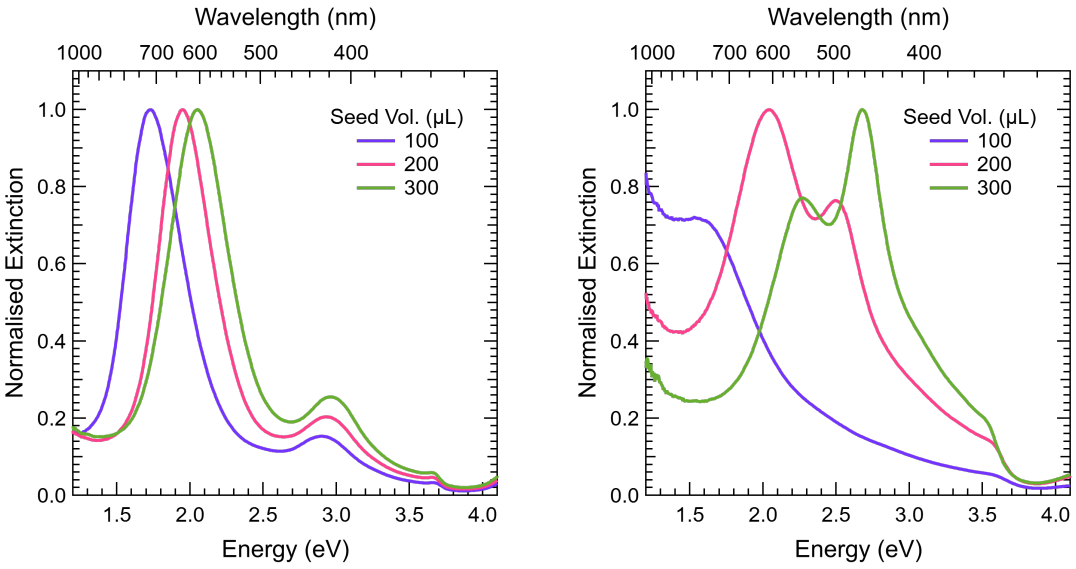


*(a) Redispersed in CTAB*

*(b) Redispersed in Type I water*

*Figure 64: Normalised extinction spectrum of colloidal silver nanoparticle solutions with increasing 44K PVP-capped seed volumes, from 100-300 µL, in 100 µL increments. 1000 µL of 1% 44K PVP was also added to the growth solutions before the seed introduction. These particles were redispersed in 10 mL of 10 mM CTAB solution (a) or 10 mL of Type I water (b)*

was observed when the particles were redispersed in Type I water. The SPR max shifts from 1.70 (729 nm), 1.95 (635 nm) and 2.13 eV (582 nm) to 2.38 (521 nm), 2.46 (504 nm) and 2.52 (492 nm) for the 100, 200 and 300 µL samples, respectively. This shift was comparable to that observed in the 44K PVP-capped seed series without PVP in the growth solution. This suggests that the 10K PVP addition has little effect on stabilising the particles' angularity without a sufficient CTAB concentration.

A blue-shift was also observed in the 29K PVP series. However, unlike in the 10K PVP series, the severity of the peak shift and the overall spectral fingerprint changes significantly as the seed volume increases. The SPR max shifts from 1.66 (747 nm), 1.99 (623 nm) and 2.10 eV (590 nm) to 2.01 (617 nm), 2.56 (484 nm) and 2.69 (461 nm) for the 100, 200 and 300 µL samples, respectively. For the 100 µL sample, the peak shift and spectral shape were comparable to the 29K PVP-capped seed samples redispersed in Type I water in section 3.2.1.4 above. The TEM imaging of those samples, shown in Figure 55, revealed that samples with this spectral shape contain particles that have maintained a higher degree of angularity. Alternatively, the 200 and 300 µL samples show a significant blue shit in the peak max and overall spectrum shape.

In the 44K PVP series, we observed a noticeable change in the maximum SPR peak and the overall shape of the spectrum. The SPR peak maximum shifted from 1.73 eV (717 nm), 1.95 eV (636 nm), and 2.05 eV (605 nm) to 1.15 eV (1078 nm), 2.04 eV (608 nm), and

*Table 14: Maximum SPR peak and FWHM values of colloidal silver nanoparticle solutions with increasing 44K PVP-capped seed volumes, from 100-300 µL, in 100 µL increments. 1000 µL of 1% 44K PVP was also added to the growth solutions before the seed introduction. These particles were redispersed in 10 mL of 10 mM CTAB solution or 10 mL of Type I water*

| Seed Volume (µL) | 100 | 200 | 300 |
|---|---|---|---|
| 10K | 1.70 | 1.95 | 2.13 |
| 29K | 1.66 | 1.99 | 2.10 |
| 44K | 1.73 | 1.95 | 2.05 |

*(a) Redispersed in CTAB - LSPR (eV)*

| Seed Volume (µL) | 100 | 200 | 300 |
|---|---|---|---|
| 10K | 2.38 | 2.46 | 2.52 |
| 29K | 2.01 | 2.56 | 2.69 |
| 44K | 1.15 | 2.04 | 2.68 |

*(b) Redispersed in Water - LSPR (eV)*

| Seed Volume (µL) | 100 | 200 | 300 |
|---|---|---|---|
| 10K | 729 | 635 | 582 |
| 29K | 747 | 623 | 590 |
| 44K | 717 | 636 | 605 |

*(c) Redispersed in CTAB - LSPR (nm)*

| Seed Volume (µL) | 100 | 200 | 300 |
|---|---|---|---|
| 10K | 521 | 504 | 492 |
| 29K | 617 | 484 | 461 |
| 44K | 1078 | 608 | 463 |

*(d) Redispersed in Water - LSPR (nm)*

| Seed Volume (µL) | 100 | 200 | 300 |
|---|---|---|---|
| 10K | 0.43 | 0.42 | 0.40 |
| 29K | 0.46 | 0.43 | 0.42 |
| 44K | 0.43 | 0.41 | 0.47 |

*(e) Redispersed in CTAB - SPR Peak FWHM*

| Seed Volume (µL) | 100 | 200 | 300 |
|---|---|---|---|
| 10K | 0.48 | 0.43 | 0.48 |
| 29K | 0.42 | 0.52 | 0.53 |
| 44K | N/A | N/A | N/A |

*(f) Redispersed in Water - SPR Peak FWHM*

2.68 eV (463 nm) for the 100, 200, and 300 µL samples, respectively. In the 100 µL sample, we observed a red-shift and a complete change in the spectrum shape. The sharp peak signal transformed into a peak with a significant shoulder of intensity that spans the visible region and extends into the infrared spectral window.

Conversely, the 200 and 300 µL samples showed a significant blue-shift in the peak maximum. An alteration in the spectrum shape was only observed in the 300 µL sample, and it appears to mirror the spectrum of the 200 µL sample. The maximum SPR peak for this sample was more blue than the secondary peak.

A final experiment was run to observe if the angularity of the nanoparticles would be stabilised when different capped seeds were introduced. For this experiment, 150 µL of CTAB-capped and 10K, 29K or 44K PVP-capped seeds were added to growth solutions that included 1000 µL of 10K, 29K or 44K PVP. The normalised extinction spectra comparing the optical properties of the nanoparticles in reaction conditions (a) or redispersed in Type I water (b) are presented in Figures 65, 66, 67, 68 below. For clarity, the maximum SPR peak energy and wavelengths for each series, in reaction conditions (15a,c) or redispersed in Type I water (15b,d), are presented in Table 15 below. This table also includes the FWHM (15e,f) and zeta potential values (15g,h).

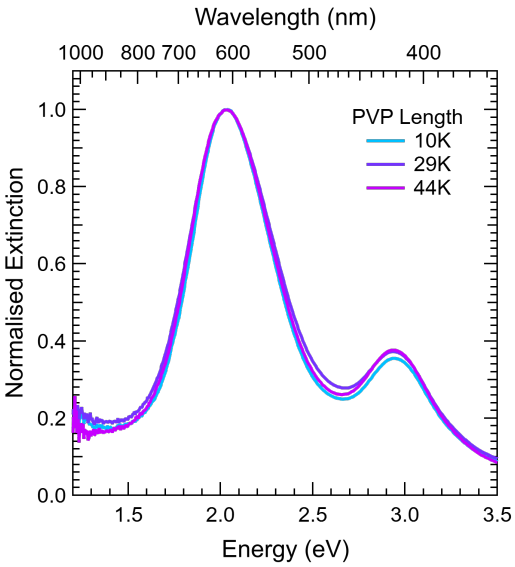


*(a) Reaction Conditions*

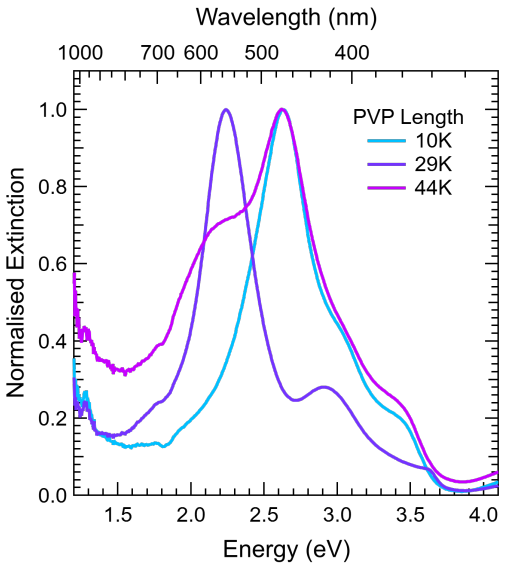


*(b) Redispersed in Type I water*

*Figure 65: Normalised extinction spectrum of colloidal silver nanoparticle solutions with 100 µL of 44K PVP-capped seed solution. 1000 µL of 1% 10, 29 or 44K PVP was also added to the growth solutions before the seed introduction. These particles were analysed in reaction conditions (a) or redispersed in 10 mL of Type I water (b)*

The normalised extinction spectra for the 44K PVP-capped seed series can be seen in Figure 65 above. The addition of PVP to the growth solution did not significantly change the size of the particles produced. The SPR peak maximum for the 10K, 29K, and 44K

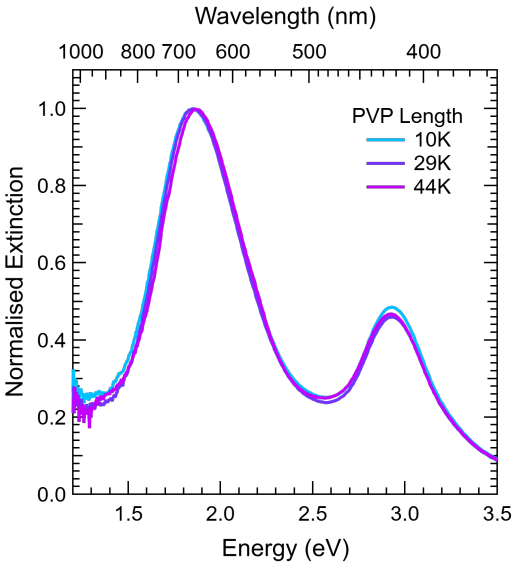


*(a) Reaction Conditions*

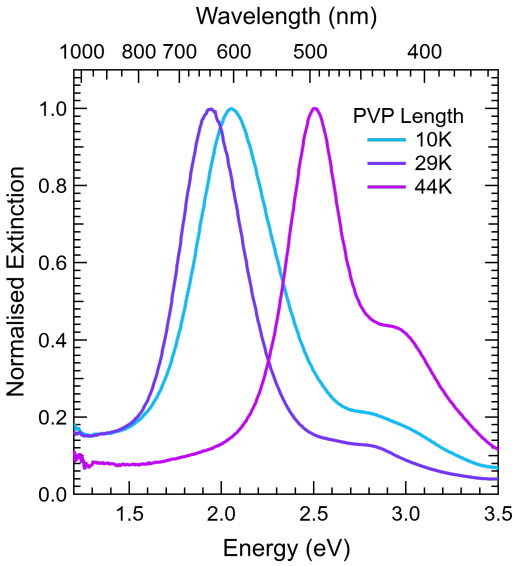


*(b) Re-dispersed in Type I water*

*Figure 66: Normalised extinction spectrum of colloidal silver nanoparticle solutions with 100 µL of 10K PVP-capped seed solution. 1000 µL of 1% 10, 29 or 44K PVP was also added to the growth solutions before the seed introduction. These particles were analysed in reaction conditions (a) or redispersed in 10 mL of Type I water (b)*

PVP samples remained relatively constant at 2.04 eV (607 nm), 2.04 eV (607 nm), and 2.03 eV (610 nm), respectively.

When the particles were redispersed in Type I water, a significant shift in the SPR peak values occurred. The 10K PVP sample exhibited a considerable blue-shift in the peak to 2.63 eV (525 nm), similar to the observed shift in the 44K PVP-capped seed series when PVP was absent in the growth solution. The 29K PVP sample showed a minor blue-shift to 2.24 eV (553 nm). The 44K PVP sample also exhibited a significant shift in the peak to 2.63 eV (472 nm), accompanied by a substantial change in the spectral shape. In this case, the peak maximum was more blue than the secondary peak, indicating a significant change in the shape and size of the particles.

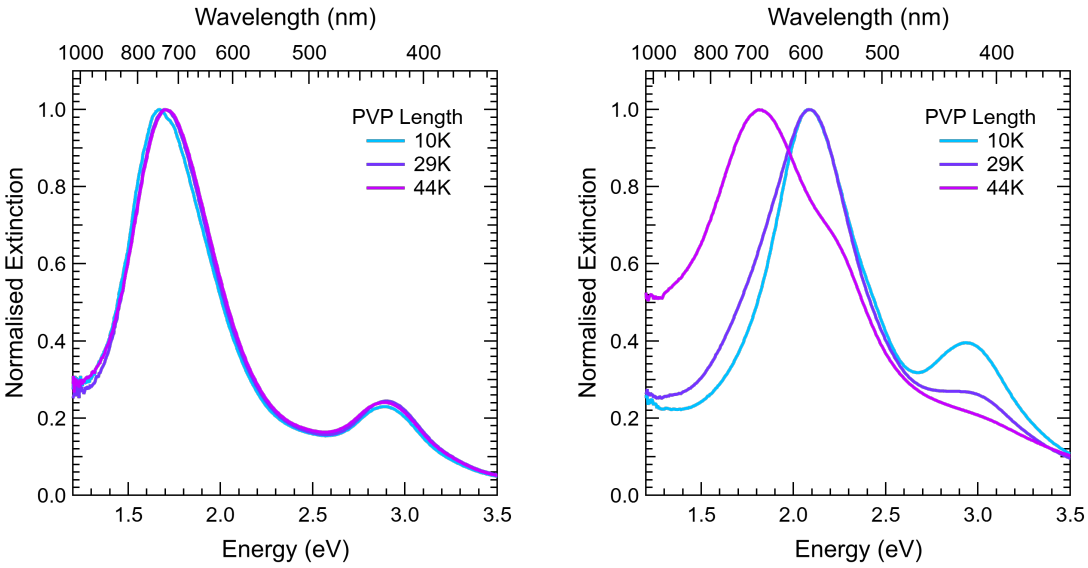


*(a) Reaction Conditions*

*(b) Redispersed in Type I water*

*Figure 67: Normalised extinction spectrum of colloidal silver nanoparticle solutions with 100 µL of 29K PVP-capped seed solution. 1000 µL of 1% 10, 29 or 44K PVP was also added to the growth solutions before the seed introduction. These particles were analysed in reaction conditions (a) or redispersed in 10 mL of Type I water (b)*

The normalised extinction spectra for the 10K PVP-capped seed series are shown in Figure 66. Again, the addition of PVP to the growth solution did not significantly change the size of the particles produced. The SPR peak maximum for the 10K, 29K, and 44K PVP samples remained consistent at 1.85 eV (670 nm), 1.85 eV (670 nm), and 1.87 eV (663 nm), respectively.

After the particles were dispersed again in Type I water, there was a significant shift in the SPR peak value in the 44K PVP sample to 2.50 eV (495 nm). The 10K and 29K PVP samples showed a minor shift in the peak towards the blue to 2.05 eV (604 nm) and 1.93 eV (642 nm), respectively. A single sharp peak was observed in all three samples, with a

less intense secondary peak in the blue-green region. This secondary peak decreases in intensity and definition when compared to the spectra of the particle in reaction conditions.

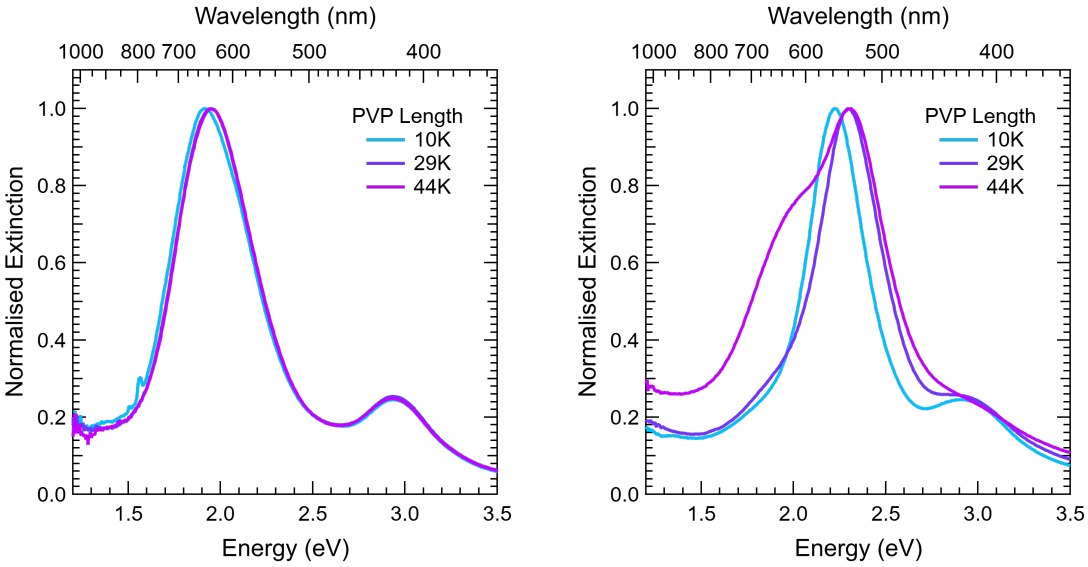


*(a) Reaction Conditions*

*(b) Redispersed in Type I water*

*Figure 68: Normalised extinction spectrum of colloidal silver nanoparticle solutions with 100 µL of CTAB-capped seed solution. 1000 µL of 1% 10, 29 or 44K PVP was also added to the growth solutions before the seed introduction. These particles were analysed in reaction conditions (a) or redispersed in 10 mL of Type I water (b)*

The normalised extinction for the 29K PVP-capped seed series is shown in Figure 67. The SPR peak maximum for the 10K, 29K, and 44K PVP samples was less consistent than that of the other series at 1.67 eV (742 nm), 1.69 eV (733 nm), and 1.70 eV (729 nm), respectively. After the particles were dispersed in Type I water, the SPR peak value in the 10K and 29K PVP samples shifted to 2.07 eV (598 nm) and 2.08 eV (596 nm), respectively, representing a shift of approximately 0.4 eV, which was significantly smaller than the shift observed in other samples. The 44K PVP sample showed a minor blue-shift to 1.81 eV (684 nm). The shape of the 10K and 29K PVP samples was consistent with a decrease in particle size and angularity. However, the spectrum shape of the 44K PVP sample has changed, with a third shoulder appearing between the two feature peaks. This spectral profile and increased FWHM value suggest a highly polydisperse solution.

Figure 68 shows the normalised extinction for the CTAB-capped seed series. The SPR peak maximum for the 10K PVP sample was 1.91 eV (649 nm), while the 29K and 44K PVP samples had a peak of 1.95 eV (635 nm). After the particles were redispersed in Type I water, the SPR peak values shifted noticeably. The 10K and 29K PVP peaks shifted to 2.22 eV (558 nm) and 2.29 eV (541 nm).

*Table 15: Maximum SPR peak, FWHM and zeta potential values of colloidal silver nanoparticle solutions 100 µL of 10K, 29K or 44K PVP or CTAB-capped seed solution. 1000 µL of 1% 10, 29 or 44K PVP was also added to the growth solutions before the seed introduction. These particles were redispersed in 10 mL of 10 mM CTAB solution or 10 mL of Type I water*

| PVP Chain | 10K | 29K | 44K |
|---|---|---|---|
| CTAB | 1.91 | 1.95 | 1.95 |
| 10K | 1.85 | 1.85 | 1.87 |
| 29K | 1.67 | 1.69 | 1.70 |
| 44K | 2.04 | 2.04 | 2.03 |

*(a) Reaction Conditions - LSPR (eV)*

| PVP Chain | 10K | 29K | 44K |
|---|---|---|---|
| CTAB | 2.22 | 2.29 | 2.31 |
| 10K | 2.05 | 1.93 | 2.50 |
| 29K | 2.07 | 2.08 | 1.81 |
| 44K | 2.63 | 2.24 | 2.63 |

*(b) Redispersed in Water - LSPR (eV)*

| PVP Chain | 10K | 29K | 44K |
|---|---|---|---|
| CTAB | 649 | 635 | 635 |
| 10K | 670 | 670 | 663 |
| 29K | 742 | 733 | 729 |
| 44K | 607 | 607 | 610 |

*(c) Reaction Conditions - LSPR (nm)*

| PVP Chain | 10K | 29K | 44K |
|---|---|---|---|
| CTAB | 558 | 541 | 536 |
| 10K | 604 | 642 | 495 |
| 29K | 598 | 596 | 684 |
| 44K | 525 | 553 | 471 |

*(d) Redispersed in Water - LSPR (nm)*

| PVP Chain | 10K | 29K | 44K |
|---|---|---|---|
| CTAB | 0.50 | 0.48 | 0.48 |
| 10K | 0.55 | 0.52 | 0.53 |
| 29K | 0.54 | 0.53 | 0.55 |
| 44K | 0.50 | 0.50 | 0.53 |

*(e) Reaction Conditions - SPR Peak FWHM*

| PVP Chain | 10K | 29K | 44K |
|---|---|---|---|
| CTAB | 0.39 | 0.47 | 0.88 |
| 10K | 0.53 | 0.42 | 0.49 |
| 29K | 0.65 | 0.73 | 1.16 |
| 44K | 0.53 | 0.42 | 1.29 |

*(f) Redispersed in Water - SPR Peak FWHM*

| PVP Chain | 10K | 29K | 44K |
|---|---|---|---|
| CTAB | 33.2 | 26.9 | 19.4 |
| 10K | 29.5 | 30.1 | 23.3 |
| 29K | 31.0 | 27.8 | 21.5 |
| 44K | 25.9 | 18.1 | 14.0 |

*(g) Reaction Conditions - Zeta Potential (eV)*

| PVP Chain | 10K | 29K | 44K |
|---|---|---|---|
| CTAB | 22.4 | 23.0 | 19.9 |
| 10K | 22.6 | 21.1 | 21.4 |
| 29K | 29.2 | 26.6 | 19.1 |
| 44K | 22.7 | 21.2 | 14.0 |

*(h) Redispersed in Water - Zeta Potential (eV)*

The shapes of these spectra were similar to the CTAB-capped seed samples with no PVP addition. The 44K PVP peak also blue-shifted to 2.31 eV (471 nm). Similarly, the spectrum shape of the 44K PVP sample in the 44K PVP-capped series changed significantly, with the peak maximum being blue-shifted in relation to the secondary peak.

The zeta potential data from this experiment display several trends. Firstly, there was a consistent decrease in the zeta potential value as the length of the PVP chain increased, regardless of the seed used. For the 44K PVP-capped seed series, a decline in zeta potential from 25.9 mV to 18.1 mV, then to 14.0 mV for the 10K, 29K, and 44K PVP additions, respectively. The same trend was seen when the CTAB-capped seeds were used, with the zeta potential value decreasing from 33.2 mV to 26.9 mV and 19.4 mV as the PVP chain

length increased.

A less dramatic decrease in zeta potential values was observed for the 10K and 29K PVP-capped seed series. Zeta potential values decreased as the PVP chain length capping the seed increased, with the 44K PVP-capped seed series having the lowest overall values. This trend is also observed when the particles are redispersed in water. The zeta potential values for the redispersed particles remain relatively consistent, with only minor increases and decreases observed across all four series.

### 3.3.2 Discussion

The experiments involving the introduction of PVP as a secondary stabilising reagent in the growth solution revealed a significant decrease in the zeta potential when the particles are in reaction conditions. The particles produced using 44K PVP-capped seeds grown in unmodified growth solutions exhibited an average zeta potential of 31 mV. The introduction of negatively charged PVP resulted in almost a halving of these values.

This decrease in potential was most pronounced for the 10K PVP, but significant decreases were also observed for the 29K and 44K PVP. These findings suggest that PVP binds synergistically with CTAB to the silver as the particles grow, ultimately influencing the zeta potential values. The confirmation of this is supported by the heightened positive zeta potential values, which are typically observed for particles synthesised without the inclusion of PVP. The cooperative interaction of the negatively charged PVP serves to reduce the positive zeta potential values.

It is worth noting that minimal blue shifting in the SPR peaks was observed when PVP was introduced compared to the samples with no PVP when the 44K PVP-capped seed was used. However, this shift was consistent regardless of the chain length of the introduced PVP. The consistencies observed in the spectral data, including peak shape and position, suggest that the particle size and shape remained unchanged when the chain length was altered. Nevertheless, the significant decrease in zeta potential values for the introduction of 10K PVP suggests that the shorter chain length led to increased PVP surface coverage.

When the seed variation is altered, some peak shifting is detected, which was expected based on previous results. There was no shifting in the peak positions when the chain length of the PVP was changed. However, significant peak changes were observed when the particles were redispersed in Type I water.

In all experiments, regardless of the seed particle variation used, the samples with

29K PVP in the growth solution demonstrated increased stability. Only a minor blue-shift was observed, indicating that the particles did truncate but maintained a higher degree of angularity compared to the samples with 10K or 44K PVP. This suggests that the 29K PVP binds and stabilises multiple crystal facets, increasing the stability of the triangular nanoplates when the CTAB concentration is reduced.

The optical activity observed in the NIR region of the extinction spectra for the particles redispersed in Type I water indicates the presence of larger secondary particles formed under these synthetic conditions. Previous experiments suggested that this synthesis would yield a combination of nanoplates, nanorods, and excess seeds. The distinct shape of the extinction spectrum in all these samples suggests that the primary product of this synthesis is triangular nanoplates with adjustable edge lengths.

The optical properties of the nanoparticle suspensions analysed in these experiments indicate that the inclusion of PVP within the growth solution significantly enhanced the stabilisation of the angularity of the triangular nanoplates. This effect was particularly evident with the incorporation of shorter PVP polymer chains, specifically the 10K and 29K chain lengths. The observed enhancement in stability can be attributed to the synergistic binding of PVP and CTAB at the edges of the nanoparticles, which further stabilises the thermodynamically unstable features of the nanoplates.

## 3.4 Synthesis Optimisation

### 3.4.1 Results

Optimisation experiments were conducted to see if changing the growth solution could increase the yield of nanorods. The initial experiment focused on the concentration of NaOH. The normalised extinction spectrum for this experiment is shown in Figure 69 below. To provide a baseline for comparison, each growth solution included 100 µL of 44K PVP-capped seed solution.

The sample with no NaOH did not progress or form any secondary nanostructures. This was confirmed by the lack of colour change in the solution and is reflected in the excitation spectrum for this solution. The sample with 50 µL of NaOH did react as anticipated, but only larger spherical particles were formed, as indicated by the single peak observed in the spectrum. However, when the NaOH volume was increased to 200 µL, the shape and peak position of the extinction spectrum were similar to those of the 100 µL samples. For this sample, the minor red-shift suggested a slightly larger particle was produced.

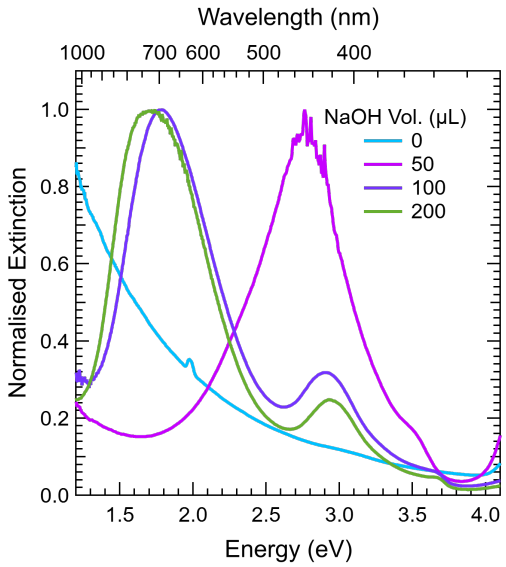


*Figure 69: Normalised extinction spectrum of colloidal silver nanoparticle solutions with 100 µL of 44K PVP-capped seed added to the growth solution. The NaOH volume was increased from 0 to 50, 100 and 200 µL for comparison*

The second experiment aimed to investigate the effect of doubling the concentration of CTAB in the growth solution from 0.075 mM to 0.15 mM. The second independent variable was the volume of the seed solution. To keep the experiments comparable, a range of 50-300 µL in 50 µL increments was used, and both CTAB and 44K PVP-capped seeds were investigated. Figure 70 below shows the normalised extinction spectra for

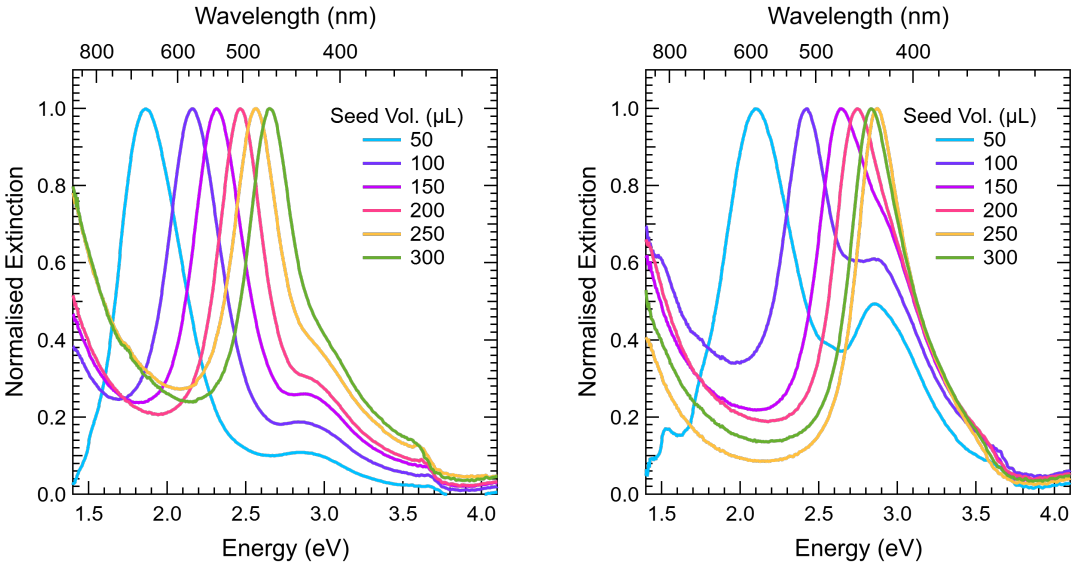


*(a) 44K PVP-capped seed*

*(b) CTAB-capped seed*

*Figure 70: Normalised extinction spectrum of colloidal silver nanoparticle solutions with increasing 44K PVP (a) or CTAB-capped (b) seed volumes, from 50-300 µL, in 50 µL increments. The CTAB concentration in the growth solution was increased from 100 mM to 200 mM. This data was collected with particles in reaction conditions*

both series.

As observed in all other experiments, there was a consistent red-shift of the SPR peak maximum energy as the volume of the seed solution decreased. However, the SPR peak energies are significantly blue-shifted compared to the original concentration samples. For example, the 100 µL 44K PVP-capped seed sample with double the CTAB concentration had a maximum peak at 1.86 eV (666 nm). In contrast, the original solution had a significantly red-shifted peak at 1.23 eV (1008 nm).

This trend was consistent across all CTAB and 44K PVP-capped seed series samples. A significant difference in the spectrum shape was also observed. The secondary peak in all samples was relatively more intense and less defined in these spectra. In the CTAB series, the secondary peak forms when the seed volume is below 150 µL. The spectrum appeared as a single sharp peak at seed volumes higher than this. This suggested that the formation of nanoplates was not favoured when the CTAB concentration was increased.

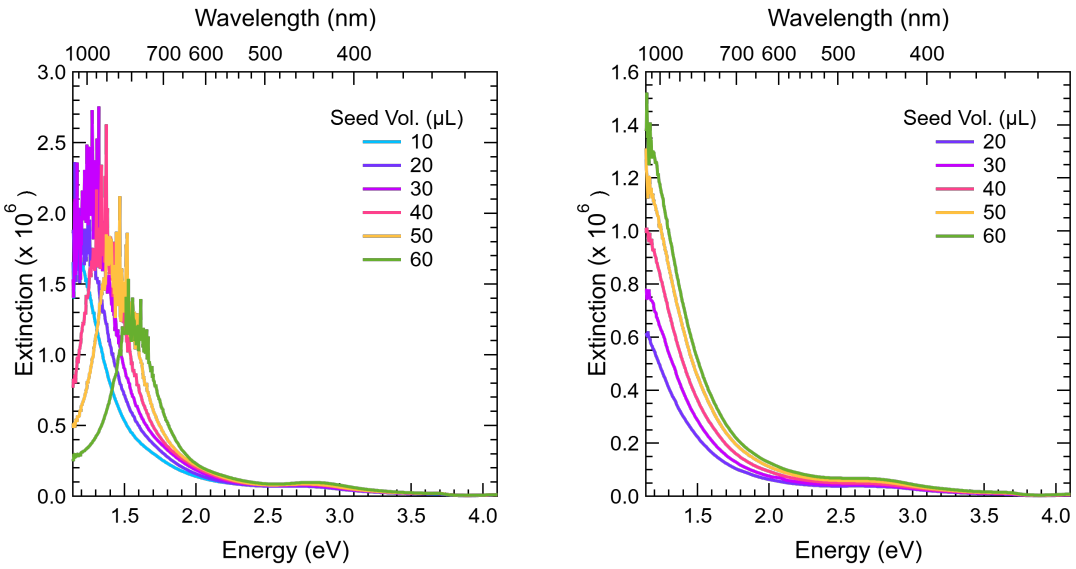


*(a) No change* *(b) Increased Ag: AA Conc.*

*Figure 71: Extinction spectrum of colloidal silver nanoparticle solutions with increasing 44K PVP-capped seed volumes, from 20-60 µL, added to the growth solution. The second spectrum has the same seed volume range as the silver nitrate and ascorbic acid concentrations increased from 0.5 mM to 0.75 mM and 5 mM to 7.5 mM, respectively*

In previous experiments, it was found that the size of the nanoparticles produced by this synthesis can be adjusted by changing the volume of the seed solution. However, there are limits to this adjustment. The size of the nanoparticles can be further increased by reducing the seed solution volume below 50 µL; once the volume goes below 30 µL, the efficacy of this tuning parameter decreases. The extinction spectra shown in Figure 71 display a range of solutions with 44K PVP-capped seeds ranging from 60 to 10 µL in

10 µL increments.

As expected, a red-shift trend was observed, but the noise in the spectrum makes it difficult to determine the maximum wavelengths. The second spectrum in this figure shows a series of solutions containing 44K PVP-capped seeds ranging from 60 to 20 µL in 10 µL increments. In the second series, the concentrations of $AgNO_3$ and AA have increased from 0.5 mM to 0.75 mM and 5 mM to 7.5 mM, respectively. Again, a red-shift trend was observed, but the maximum wavelengths of the SPR peaks across the series have been red-shifted. This experiment confirmed that simultaneously increasing the concentrations of $AgNO_3$ and AA would result in larger particles.

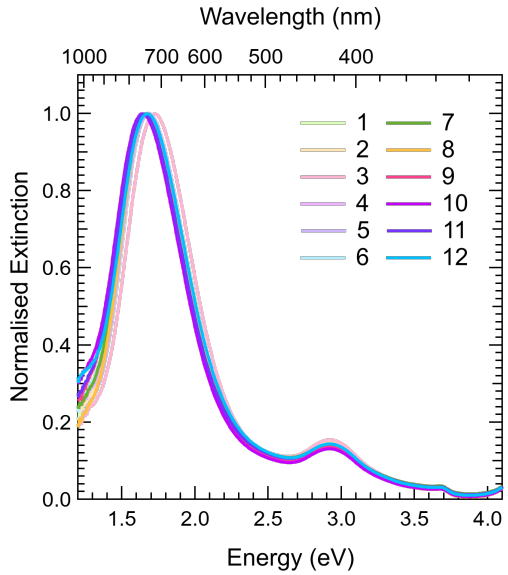


*Figure 72: Normalised extinction spectrum of colloidal silver nanoparticle solutions with 100 µL of 44K PVP-capped seed added to the growth solution. This same synthesis was repeated 12 times, and the spectra overlapped to demonstrate the reproducibility of the synthesis*

The normalised extinction spectrum presented in Figure 72 demonstrates the reproducibility of this optimised synthesis. All 12 solutions were synthesised using 100 µL of 44K PVP-capped seeds. The average SPR peak maximum energy was 1.66 eV (775 nm) across this series. The peak energies range from 1.64 eV (756 nm) to 1.68 eV (738 nm), with one outlier at 1.72 eV (720 nm). The reproducibility confirms that this synthesis was reliable for producing nanostructures with a specified size and shape.

### 3.4.2 Discussion

This synthesis of Ag nanoparticles included numerous reagents to influence the kinetic control of the nanoparticle growth. Previous studies have shown that the growth of metal nanoparticles can be dictated by kinetic control or selective surface passivation.[37] The

kinetic control of nanoparticle synthesis is ultimately dictated by the reduction potential of the metal complexes, the metal ion availability, and the relative binding strength of metal adsorbates. The additional reagents added to a nanoparticle synthesis can regulate these three chemical principles.

The shift in kinetic control is evident in the optimisation experiments. NaOH is used as a selected reagent to regulate the reduction rate in the synthesis. In the synthesis, ascorbic acid (AA) serves as a mild reducing agent, and the reduction rate is manipulated by introducing NaOH. The pH of the solution is shifted towards the pKa of the ascorbate dianion by NaOH, which acts as a stronger reducing agent, thereby increasing the reduction rate. However, there is a limit to this increase in the reduction rate, as doubling the concentration of NaOH resulted in only a minimal change to the extinction spectra.

In contrast, when the NaOH concentration was halved, a significant change in the extinction spectra was observed, including a notable blue-shift in the SPR maximum peak and a continued rise of the spectrum into the NIR region. According to Murphy and coworkers, a decrease in pH would favour the formation of the ascorbate monoanion, leading to a decrease in the reduction rate and, consequently, the production of nanowires.[34]

Our experiments also revealed a noteworthy difference in the shape of the nanoparticles produced when the volume of NaOH and pH of the solution were decreased. A single blue-shifted peak is observed in the extinction spectrum when 50 µL of NaOH is introduced. This suggests that reducing the reduction rate could eliminate the formation of triangular nanoplates in this synthesis. These experiments confirm that the concentration of NaOH was critical in controlling the reduction rate and kinetic control in this synthesis.

The role of CTAB in synthesising gold nanorods has been extensively researched.[17,44] It has been found to form a cationic bi-layer and assist in the growth of nanorods by facet-sensitive surface adsorption. When no CTAB is present in the growth solution, the synthesis does not result in the synthesis of nanorods, and any secondary nanoparticles formed quickly aggregate due to a lack of stability. However, increased CTAB concentration leads to a significant change in the nanostructures.

The blue-shift of the SPR peak maximum and an increase in the relative intensity of the secondary resonance peak for the 44K PVP series indicate that increasing the CTAB concentration produces thicker triangular nanoplates. In the CTAB series, a notable blue-shift of the maximum SPR peak is observed, and the secondary peak diminishes as the volume of seed particles introduced increases. This suggests that the nanoplates and

excess material produced at higher CTAB concentrations have a significantly lower angularity. The rise in the spectra also indicates a significantly intense resonance peak in the NIR region, potentially pointing to the formation of short nanorods.

It has been demonstrated that the CTAB and NaOH concentrations are crucial for controlling the kinetics of this synthesis. In contrast, the seed concentration and relative silver ion ratio have a significant impact on the particle aspect ratios. Previous experiments have demonstrated that increasing the seed volume in a fixed growth solution with a constant silver concentration leads to the formation of smaller nanoparticles, as there is a limit to the ion availability in a fixed concentration of silver precursor.

Samples with lower seed volumes produced notably larger particles. However, our experiments revealed that simultaneous increases in the silver and AA concentrations further shift the maximum SPR to longer wavelengths, indicating the growth of even larger nanostructures. This highlights the critical role of silver ion availability in this synthesis. However, achieving this increase in particle size requires a subsequent increase in the AA concentration to ensure that the reduction rate remains unchanged.

These experiments demonstrated that this nanoparticle synthesis can be effectively controlled by selectively adjusting the concentrations of key reagents. The concentration of NaOH plays a crucial role in regulating the kinetics of the reaction. If the NaOH concentration is insufficient, the reaction fails to proceed to form anisotropic secondary nanostructures. Additionally, the concentration of CTAB has been identified as a significant factor in determining the resulting morphology of the synthesised nanoparticles. While both CTAB and NaOH concentrations are essential in managing the reaction kinetics, the volume of seed solution has proven to be the most influential factor in controlling the size of the produced nanoparticles.

## 3.5 Post-Synthetic Treatments and Nanoparticle Stability

### 3.5.1 Results

#### 3.5.1.1 Post Synthesis Additives

In the initial experiments, it was observed that altering the reaction conditions by removing particles and dispersing them in water resulted in significant changes to the nanoparticle shape and the optical properties of the solution. To mitigate this issue, a stabilising reagent was reintroduced after the purification of the nanoparticles.

A post-synthetic experiment was carried out to determine the most suitable stabilising reagent. In this experiment, six nanoparticle solutions were synthesised, each con-

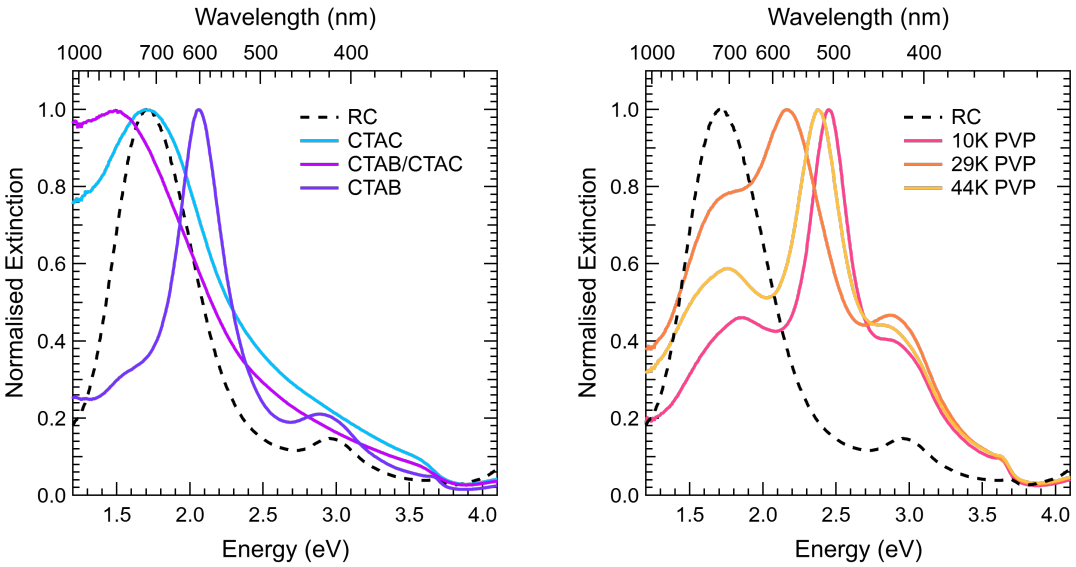


*(a) Redispersed in CTAB or CTAC*

*(b) Redispersed in 10, 29 or 44K PVP*

*Figure 73: Normalised extinction spectrum of colloidal silver nanoparticle solutions with 100 µL of 44K PVP-capped seed added to the growth solution. Particle solutions were centrifuged for 15 minutes at 6000 RPM. The supernatant was removed, and the pellet was redispersed in either 10 mL CTAB, CTAC, CTAB/CTAC solution or 10 mL of 0.1% 10, 29 or 44K PVP solution*

taining 100 µL of 44K PVP-capped seeds. Subsequently, the nanoparticles in these solutions were removed from the reaction conditions and redispersed in 10 mL of either CTAB (10mM), CTAC, CTAB/CTAC, or 1% v/v 10K, 29K, or 44K PVP. The normalised extinction spectra obtained from this experiment are depicted in Figure 73.

The extinction spectrum of the solutions under reaction conditions is depicted with a dotted line for comparison. Upon re-dispersion of the sample in CTAB, the spectrum displayed the expected blue-shift and peak narrowing, which was consistent with previous experiments. Subsequently, it was established that CTAB was the most suitable stabilising reagent. A follow-up experiment was conducted to determine the optimal concentration. The spectra of the samples redispersed in CTAC and the CTAB/CTAC mixture exhibited a red-shift of the SPR peak, along with broadening of the peak and the noticeable absence of secondary features. These changes suggest substantial alterations in the particles' shape and increased polydispersity. These observations held true for both the 100 µL series and the 200 µL series. The normalised extinction spectra for the 200 µL series can be found in Figure 74.

The two series were run to investigate how the stabilising capabilities would change with varying particle sizes. The impact of PVP addition was particularly noticeable in the experiments. Similarly to the experiments where PVP was added to the growth solution, 29K PVP appeared to be the most effective polymer chain length. In the 200 µL

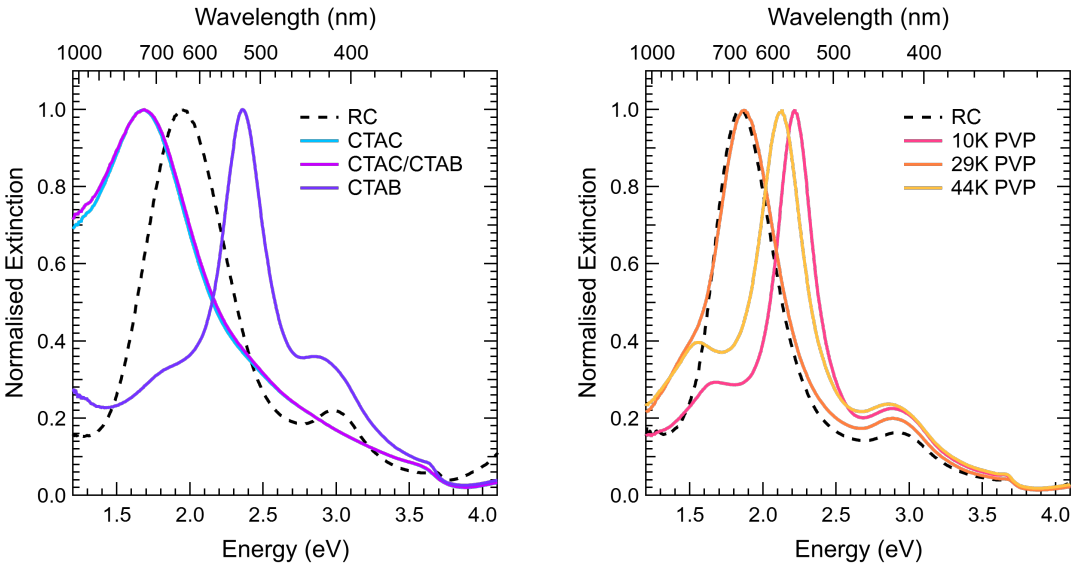


*(a) Redispersed in CTAB or CTAC*

*(b) Redispersed in 10, 29 or 44K PVP*

*Figure 74: Normalised extinction spectrum of colloidal silver nanoparticle solutions with 200 µL of 44K PVP-capped seed added to the growth solution. Particle solutions were centrifuged for 15 minutes at 6000 RPM. The supernatant was removed, and the pellet was redispersed in either 10 mL CTAB, CTAC, CTAB/CTAC solution or 10 mL of 0.1% 10, 29 or 44K PVP solution*

series, where smaller particles were tested, the extinction spectrum appeared essentially unchanged compared to the reaction condition spectrum. However, in the 100 µL series, where larger particles were tested, the spectrum showed a blue-shift and significant change in shape. This indicates that the 29K PVP might not effectively stabilise the particles at the larger size, suggesting that a 1% solution might not have been sufficient. Further investigation is necessary to determine if a higher concentration would be more effective in stabilising across the size range.

The previous experiment showed that CTAB was the most effective stabilising reagent. This led to a second experiment to determine the necessary CTAB concentration to maintain the particles' angularity. Five nanoparticle solutions were synthesised for this experiment, each containing 150 µL of 44K PVP-capped seeds. The nanoparticles in these solutions were removed from the reaction conditions and redispersed in 10 mL of aqueous solution containing 0, 0.5, 2.5, 5, or 10 mM of CTAB.

The normalised extinction spectra for these redispersed solutions, alongside their reaction condition spectrum, are presented in Figure 75 below. The solution with no CTAB showed a significant blue-shift and change in spectral shape, as described previously. The 0.5-5 mM solutions exhibited a significantly smaller blue-shift but increased peak width. This suggests that there was insufficient CTAB available at these concentrations to stabilise the particles effectively.

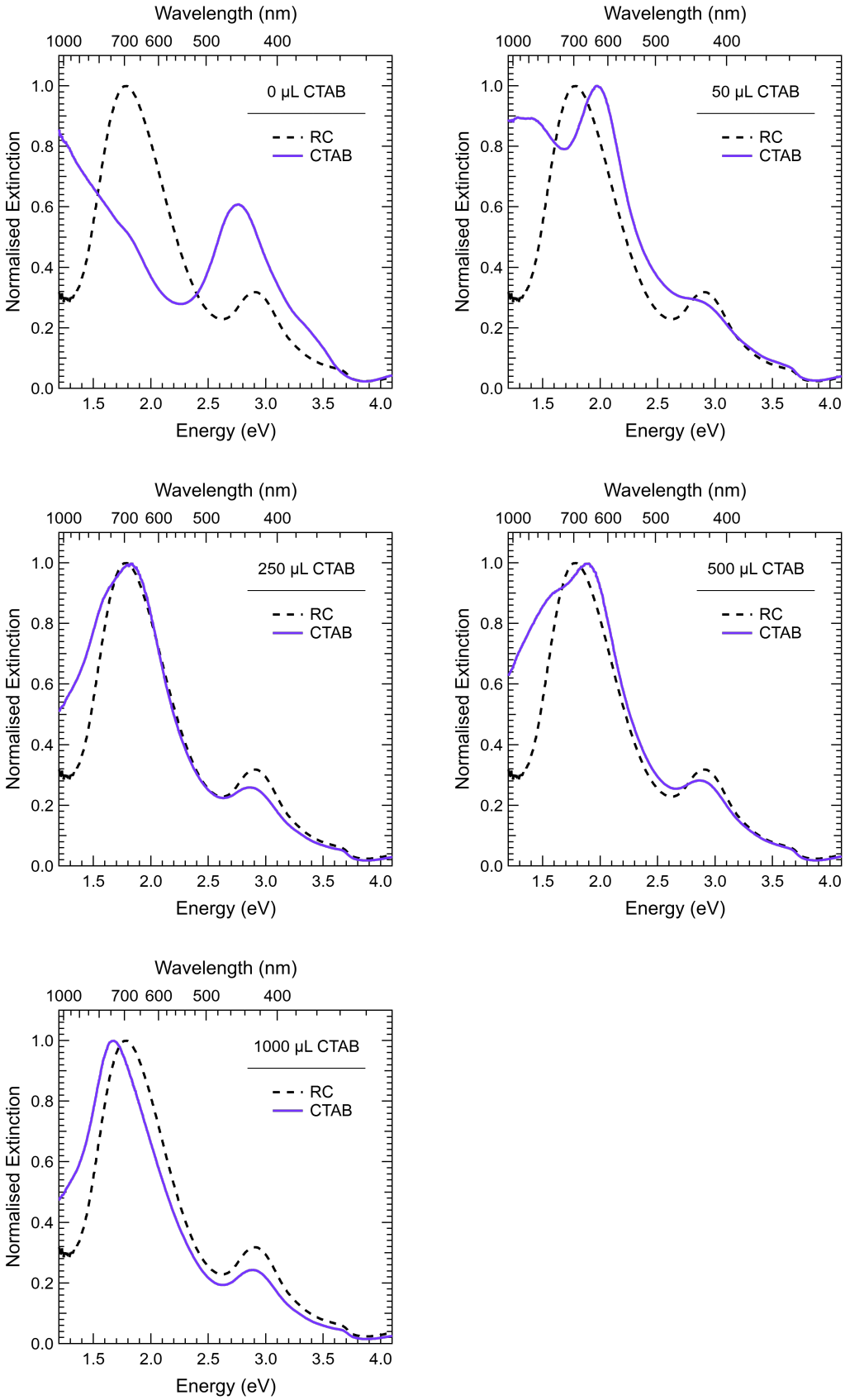


*Figure 75: Normalised extinction spectrum of colloidal silver nanoparticle solutions with 100 µL of 44K PVP-capped seed added to the growth solution. Particle solutions were centrifuged for 15 minutes at 6000 RPM. The supernatant was removed, and the pellet was redispersed in either 10 mL of Type I water with 0, 50, 250, 500 or 1000 µL of CTAB added*

Consequently, there was an increase in the shape and size diversity of the nanoparticles, demonstrated by the broader SPR peak. The solution containing 10 mM of CTAB maintained the peak width and shape; however, in this instance, the energy of the SPR peak had red-shifted from 1.78 eV (696 nm) to 1.67 eV (742 nm). While not commonly observed, this could be explained by stabilising the largest particles removed from the reaction conditions solution during the purification steps.

#### 3.5.1.2 Stability Tests

Several experiments were conducted to assess the stability of nanoparticles under various conditions. The initial experiment focused on 44K PVP-capped seed particle solutions. These solutions had a range of seed volumes from 50-300 µL in 50 µL increments.

*Table 16: Maximum SPR peak values of colloidal silver nanoparticle solutions with increasing 44K PVP-capped seed volumes, from 50-300 µL, in 50 µL increments. Comparing the stability of particles in reaction conditions or redispersed in CTAB*

| Seed Volume (µL) | 50 | 100 | 150 | 200 | 250 | 300 |
|---|---|---|---|---|---|---|
| Day 0 | 1.24 | 1.52 | 1.68 | 1.75 | 1.86 | 1.89 |
| Day 1 | 1.38 | 1.67 | 1.85 | 1.95 | 2.05 | 2.09 |
| Day 7 | 1.47 | 1.77 | 1.99 | 2.15 | 2.30 | 2.37 |

*(a) Reaction Conditions - LSPR (eV)*

| Seed Volume (µL) | 50 | 100 | 150 | 200 | 250 | 300 |
|---|---|---|---|---|---|---|
| Day 0 | 999 | 815 | 738 | 708 | 666 | 656 |
| Day 1 | 898 | 742 | 670 | 635 | 604 | 593 |
| Day 7 | 843 | 700 | 623 | 576 | 539 | 523 |

*(b) Reaction Conditions - LSPR (nm)*

| Seed Volume (µL) | 50 | 100 | 150 | 200 | 250 | 300 |
|---|---|---|---|---|---|---|
| Day 0 | 1.36 | 1.64 | 1.81 | 1.93 | 2.00 | 2.07 |
| Day 1 | 1.45 | 1.68 | 1.82 | 1.97 | 2.04 | 2.11 |
| Day 7 | 1.47 | 1.71 | 1.89 | 2.03 | 2.12 | 2.18 |

*(c) Redispersed in CTAB - LSPR (eV)*

| Seed Volume (µL) | 50 | 100 | 150 | 200 | 250 | 300 |
|---|---|---|---|---|---|---|
| Day 0 | 911 | 756 | 684 | 642 | 619 | 598 |
| Day 1 | 855 | 738 | 681 | 629 | 607 | 587 |
| Day 7 | 843 | 725 | 656 | 610 | 584 | 568 |

*(d) Redispersed in CTAB - LSPR (nm)*

The normalised extinction spectra for the nanoparticle solutions in reaction conditions, redispersed in 5 mM CTAB, are shown in Figures 76 and 77 below. For each sam-

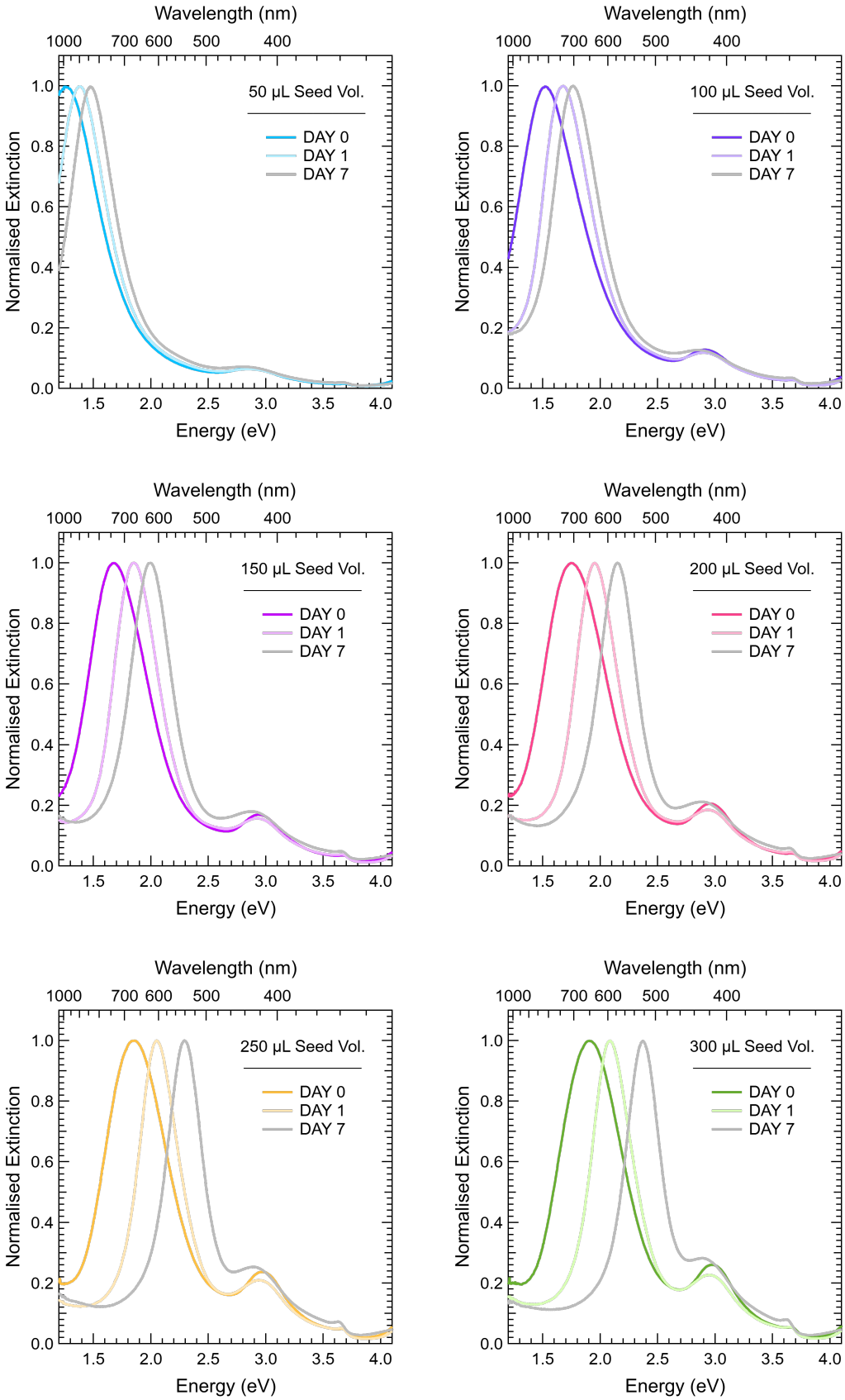


*Figure 76: Normalised extinction spectrum of colloidal silver nanoparticle solutions with increasing 44K PVP-capped seed volumes, from 50-300 µL, in 50 µL increments. The extinction spectrum for each sample was collected 1 hour after the synthesis (Day 0), 24 hours later (Day 1) and again six days later (Day 7). This data was collected with particles in reaction conditions*

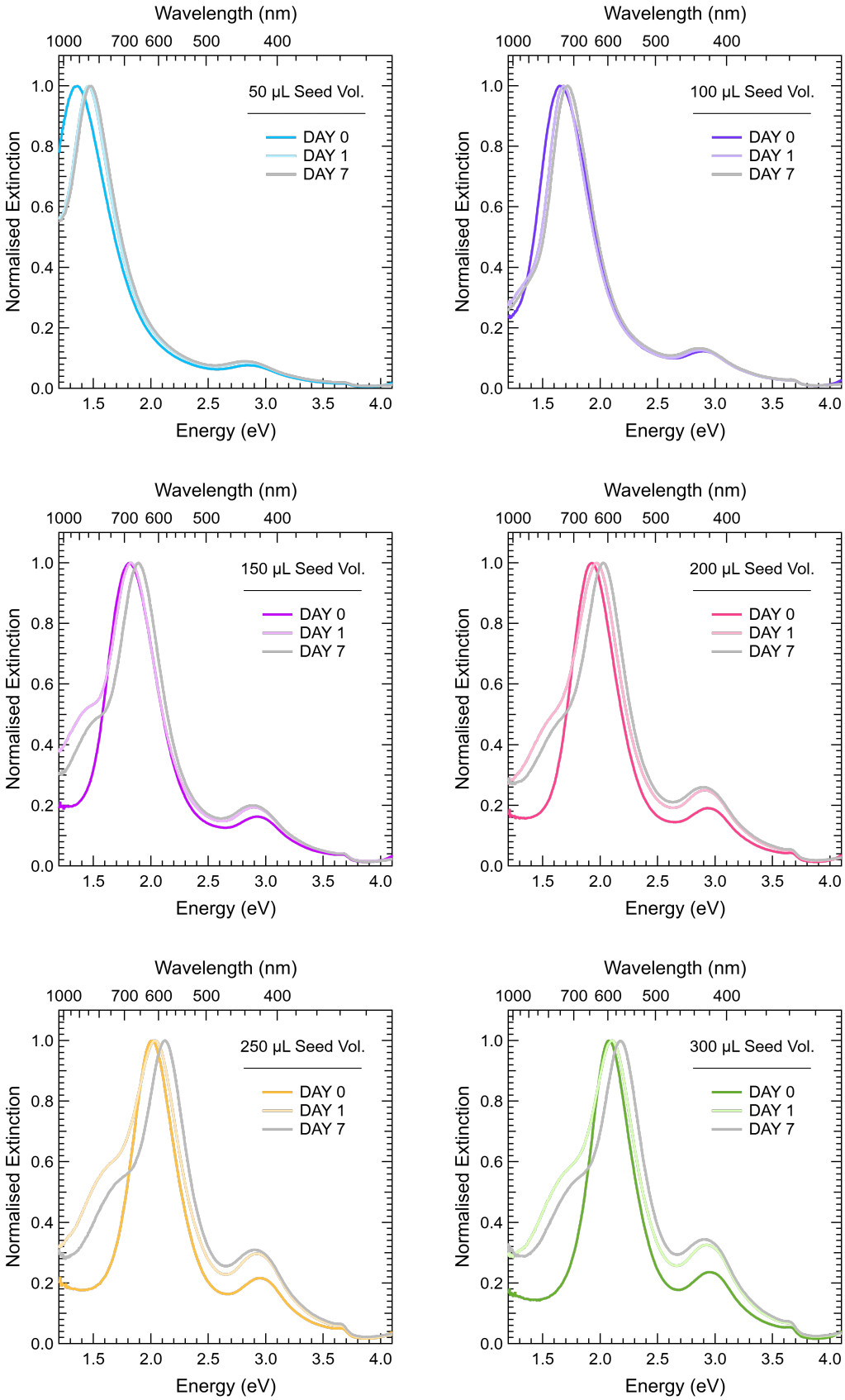


*Figure 77: Normalised extinction spectrum of colloidal silver nanoparticle solutions with increasing 44K PVP-capped seed volumes, from 50-300 µL, in 50 µL increments. The extinction spectrum for each sample was collected 24 hours after synthesis when the particles were redispersed in CTAB (Day 0), 24 hours later (Day 1) and again six days later (Day 7). These particles were redispersed in 10 mL of 5 mM CTAB solution*

ple, the extinction spectrum was measured on Days 0, 1, and 7. In the reaction condition spectra, Day 0 represents the day of synthesis, whereas in the CTAB spectra, Day 0 is the day after synthesis when the particles have been centrifuged and redispersed.

A steady blue-shift of the SPR peak was observed when the particles were kept in reaction conditions. The SPR peaks shift on average 0.17 eV or 73 nm from Day 0 to Day 1. The breadth of the peak also decreases significantly from Day 0 to Day 1. This suggests that the reaction proceeds quickly until the most thermodynamically stable particles have been formed. The particles, particularly the nanoplates, decrease edge length and angularity when kept in reaction conditions. However, this process occurs significantly slower, with the SPR peak blue shifting an average of 0.17 eV, or 73 nm, from Day 1 to Day 7. The SPR peak values for the reaction conditions and CTAB samples in the 44K PVP series, in energy (16a,b) and wavelength (16c,d), are presented in Table 16.

A slight blue-shift occurs when the particles are purified and redispersed in CTAB. The particles are purified on the day following the synthesis to achieve the most thermodynamically stable and evenly dispersed nanoparticles. Therefore, Day 0 in this experiment was when the particles were purified and redispersed in CTAB.

Under these conditions, the SPR peaks shift an average of 0.04 eV or 19 nm from Day 0 to Day 1. Furthermore, the rate of shape change decreases with time, as the SPR peak blue shifts an average of 0.05 eV or 23 nm from Day 1 to Day 7. This indicates that the particles are highly stable when redispersed in CTAB. Still, some minor particle shape and angularity changes will occur over an extended period. It is important to note that this stability experiment was conducted before the CTAB concentration experiment. The

*Table 17: Maximum SPR peak values of colloidal silver nanoparticle solutions with increasing 10K or 29K PVP-capped seed volumes, from 100-300 µL, in 100 µL increments. Comparing the stability of particles in reaction conditions or redispersed in CTAB*

| Seed Volume (µL) | 100 | 200 | 300 |
|---|---|---|---|
| Day 0 | 1.58 | 1.85 | 1.95 |
| Day 1 | 1.86 | 2.19 | 2.36 |
| Day 7 | 1.92 | 2.27 | 2.47 |

*(a) 10K PVP Series - LSPR (eV)*

| Seed Volume (µL) | 100 | 200 | 300 |
|---|---|---|---|
| Day 0 | 1.36 | 1.63 | 1.77 |
| Day 1 | 1.74 | 2.07 | 2.26 |
| Day 7 | 1.80 | 2.15 | 2.35 |

*(b) 29K PVP Series - LSPR (eV)*

| Seed Volume (µL) | 100 | 200 | 300 |
|---|---|---|---|
| Day 0 | 784 | 670 | 635 |
| Day 1 | 666 | 566 | 525 |
| Day 7 | 645 | 546 | 501 |

*(c) 10K PVP Series - LSPR (nm)*

| Seed Volume (µL) | 100 | 200 | 300 |
|---|---|---|---|
| Day 0 | 911 | 760 | 700 |
| Day 1 | 712 | 598 | 548 |
| Day 7 | 688 | 576 | 527 |

*(d) 29K PVP Series - LSPR (nm)*

concentration of CTAB used here was 5 mM, which explains the unexpected shoulder observed in the red-infrared region of the spectrum.

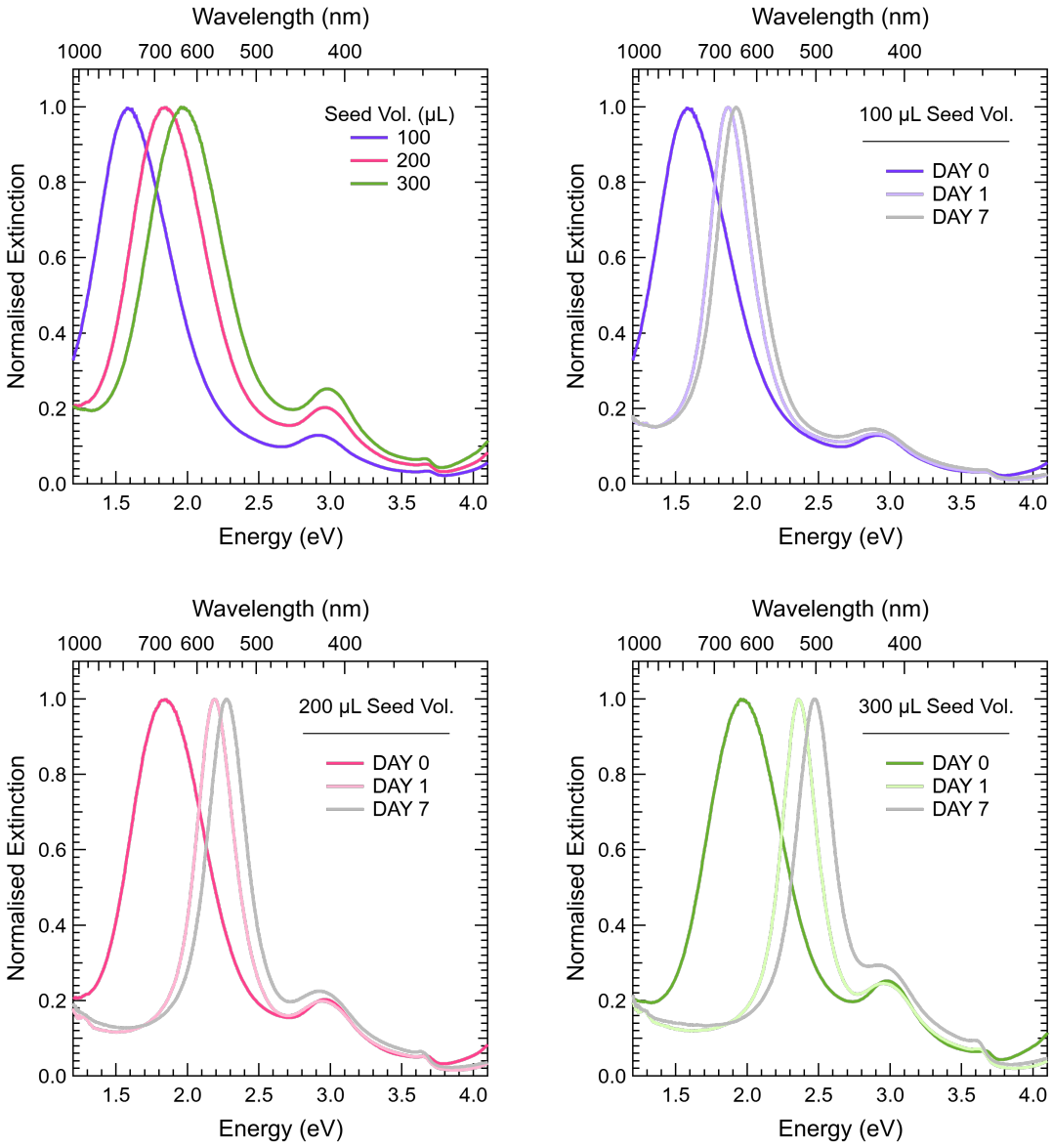


*Figure 78: Normalised extinction spectrum of colloidal silver nanoparticle solutions with increasing 10K PVP-capped seed volumes, from 100-300 µL, in 100 µL increments. The extinction for each sample was collected 1 hour after the synthesis (Day 0), 24 hours later when the particles were redispersed in CTAB (Day 1) and again six days later (Day 7). These particles were redispersed in 10 mL of 10 mM CTAB solution*

The following experiments investigated the stability of nanoparticle solutions produced using 10K and 29K PVP-capped seeds. Each series included a range of seed volumes from 100-300 µL in 100 µL increments. Figures 78 and 79 show the normalised extinction spectra for the 10K and 29K PVP series. For each sample, the extinction spectrum was measured on Days 0, 1, and 7. Day 0 represents the day of synthesis, and on

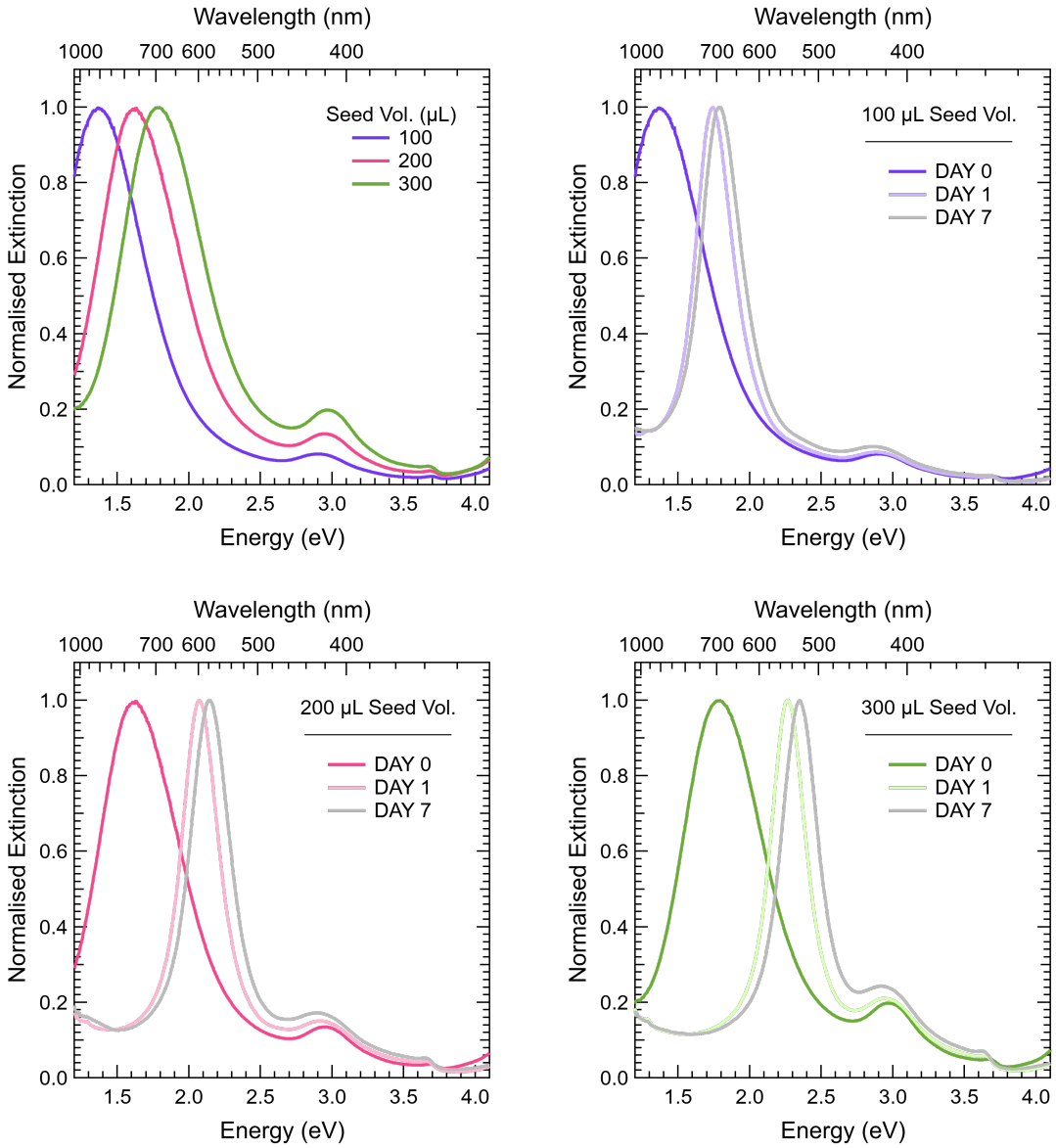


*Figure 79: Normalised extinction spectrum of colloidal silver nanoparticle solutions with increasing 29K PVP-capped seed volumes, from 100-300 µL, in 100 µL increments. The extinction for each sample was collected 1 hour after the synthesis (Day 0), 24 hours later when the particles were redispersed in CTAB (Day 1) and again six days later (Day 7). These particles were redispersed in 10 mL of 10 mM CTAB solution*

Day 1, the particles were centrifuged and then redispersed in a 10 mM CTAB solution.

The SPR peak values for the 10K and 29K series, in energy (17a,b) and wavelength (17c,d), are presented in Table 17. In the 10K and 29K series, the SPR peak blue shifts significantly between Day 0 and 1; a significant decrease in the breadth of the peak accompanies this. Again, this suggests that the reaction proceeds quickly until the most thermodynamically stable particles have been formed in reaction conditions. However, over 24 hrs, a significant decrease in the size of the nanoparticles occurs.

In the 10K PVP series, the SPR peak blue-shifts an average of 0.34 eV, or 110 nm, from Day 0 to Day 1. In the 29K series, this increases slightly to an average of 0.44 eV or 171 nm. We see a significantly slower rate of change from Day 1 to Day 7 when the particles are redispersed in CTAB. For the 10K and 29K PVP series, the SPR peaks blue-shift an average of 0.08 eV or 21 nm from Day 1 to 7. This indicates that the particles are highly stable when redispersed in CTAB. However, as a blue-shift is still observed, it confirms that minor particle shape and angularity changes will occur over an extended period.

### 3.5.2 Discussion

As discussed by Rekha et al., CTAB plays a crucial role in the synthesis as a template for nanorod production. However, our experiments indicate that the primary nanostructure yielded by this synthetic method is triangular nanoplates. This is consistent with the earlier work of Chen and Carroll, which noted the production of truncated triangular silver nanoplates when TSC-capped seeds were used, in contrast to the nanorods described in the original Murphy paper on which the Rekha synthesis is based.[34,51,96]

Chen and Carroll explained that the nanoplates stack along their basal plane and exhibit a rod-like appearance in SEM images when viewed from only above the sample.[96] They further observed robust interactions between these nanostructures, attributing this to a monolayer of CTAB molecules covering the basal planes, forming strong van der Waals interactions with the alkyl chains of neighbouring particles. This stacking phenomenon has been observed in our samples of nanoplates and nanorods. The substantial difference in edge length between the rods and plates has enabled us to distinguish between the two. The observation of similar stacking in the rod particles supports that CTAB binds along the directional edge of the nanorods and serves as a growth template. However, it is noticeable that this stacking does not occur at the ends of the rods or the tips of the nanoplates, implying a lower coverage of CTAB along the tips and free edges of these particles.

The stability of nanoparticles is crucially defined by their ability to maintain size and shape and prevent aggregation.[101] Typically, stabilising reagents are incorporated during synthesis to support nanoparticle stability, with CTAB playing a significant role in this process. In our experiments, we have also utilised PVP with varying chain lengths. Although the inclusion of stabilising reagents initially proves adequate, prolonged exposure to reaction conditions leads to a systematic blue-shift in the maximum SPR peak, accompanied by a narrowing of the peak width.

Previously reported DDA calculations have indicated that the in-plane dipole resonance peak experiences a blue-shift and sharpening due to truncation, particularly under aggressive conditions with excess reagents leading to oxidative etching.[102] However, when the nanoparticles are removed from the reaction conditions and redispersed in a sufficient concentration of CTAB, their stability is notably improved. Alternatively, redispersion in Type I water or at lower CTAB concentrations results in significant changes to the resonance spectrum. When excess CTAB is unavailable in the solution, the molecules stabilising the nanostructures dissociate to achieve equilibrium for micelle production. This leaves high-energy facets vulnerable to morphology transformation.

Understandably, this will significantly impact the thermodynamically unstable structural features of the nanoparticles, particularly the tips of the triangular nanoplates. This is evidenced by the pronounced morphological transformation that occurs when the particles are redispersed in Type I water. This phenomenon has been consistently observed across all our experimental series, as evidenced by notable changes in the solution spectra and a substantial decrease in the zeta potential of the nanoparticle solutions.

These experiments have shown that the stability of the particles when redispersed in Type I water increases only when the secondary stabilising reagent, PVP, is introduced into the growth solution or when particles are synthesised using seeds capped with shorter-chain PVP molecules. Otherwise, incorporating CTAB at concentrations higher than 10 mM is required post-purification to maintain nanoparticle stability.

## 3.6 Gold-Core Nanorod Synthesis

Silver nanorods with a gold bipyramidal core were synthesised using a modified method that combines the methods described by Zhuo et al.[59] and Sánchez-Iglesias et al..[11] The specific synthetic reaction conditions are detailed in section 2.2.3.

### 3.6.1 Results

#### 3.6.1.1 Gold Seed Synthesis

The gold nanoseeds were synthesised using the method outlined in section 2.2.3. The normalised extinction spectra of four synthesised seed samples are displayed in Figure 80 below. Additionally, the figure includes the calculated theoretical SPR spectra for 30 nm gold nanospheres, which were generated using the Nanocomposix Mie Theory calculator.

The seed synthesis demonstrated high reproducibility, as evidenced by the significant

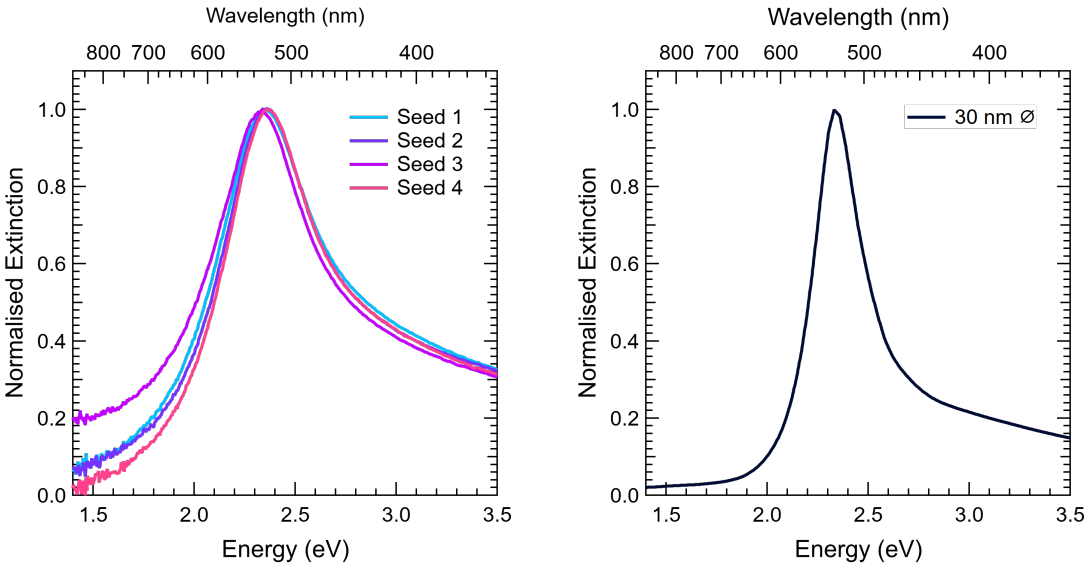


*(a) Experimental* *(b) Theoretical*

*Figure 80: Experimental (a) and theoretical (b) normalised extinction spectra of gold nanoseeds.The theoretical extinction data for 30 nm gold nanoseeds was produced using the Nanocomposix Mie theory calculator*[16]

overlap in the extinction spectra of each seed sample. The average maximum SPR peak value for the experimental seed samples was determined to be 2.34 eV (528 nm). Similarly, theoretical calculations for a 30 nm gold nanoseed also yielded a maximum SPR peak at 2.34 eV (528 nm). Analysis of the extinction spectrum obtained from the synthesised seed samples indicated an average gold seed size of 30 nm. However, it is important to note that the experimental peaks exhibited broader profiles, suggesting potential polydispersity and aggregation within the seed samples. The average zeta potential value for the gold nanoseed samples is -6.52 mV. The incorporation of negatively charged TSC in the seed synthesis directly influenced this.

#### 3.6.1.2 Bi-pyramid Synthesis

Gold bi-pyramids were synthesised using the seed-mediated growth method described in section 2.2.3. For this experiment, the only independent variable was the volume of seed solution added to the fixed growth solution. A range of 500-3000 µL in 500 µL increments was used. The bi-pyramidal cores will be labelled BP1-BP6 for the corresponding 500-3000 µL range. The normalised extinction spectra for the gold bi-pyramid solutions produced across this range are presented in Figure 81.

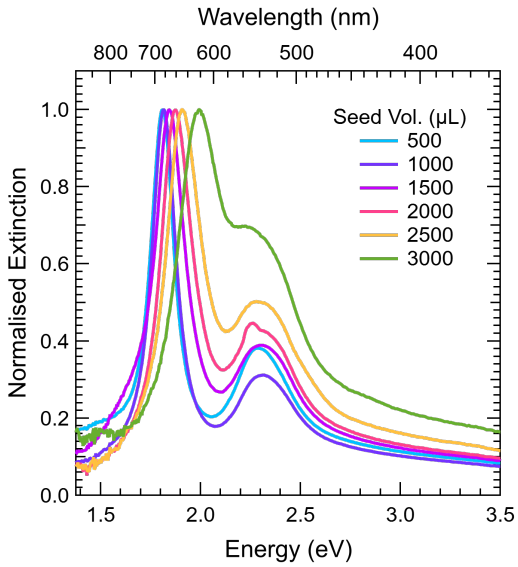


*Figure 81: Normalised extinction spectra of gold bipyramids with increasing gold seed volumes, from 500-3000 µL, added to the growth solution*

*Table 18: Maximum SPR peak values of colloidal silver nanoparticle solutions with increasing gold volumes from 500-3000 µL*

| Seed Volume (µL) | 500 | 1000 | 1500 | 2000 | 2500 | 3000 |
|---|---|---|---|---|---|---|
| LSPR (eV) | 1.80 | 1.81 | 1.84 | 1.87 | 1.91 | 1.99 |
| LSPR (nm) | 688 | 684 | 673 | 663 | 649 | 623 |
| Zeta (mV) | 72.6 | 72.4 | 76.0 | 74.0 | 75.4 | 70.6 |

The gold bi-pyramid samples exhibit the same trend of a red-shift of the maximum SPR peak as the volume of the seed solution decreased. For clarity, the maximum SPR peak wavelengths for each sample, in nanometers and energy units, as well as the zeta potential values, are presented in Table 18. A red shit of the maximum SPR peak from 1.99 (623 nm) to 1.80 eV (688 nm) as the seed volume is decreased from 3000 to 500 µL is observed.

The red-shift observed is accompanied by an increase in the relative intensity of the secondary resonance peak. The TEM images of the bi-pyramids in Figure 82 below validate that the length of the bi-pyramids from tip to tip increases as the seed volume decreases. It is also evident that the bi-pyramids' width and angularity change in response to changes in the seed volume. When higher seed volumes are introduced, the bi-pyramids appear less structured and more ellipsoidal in shape.

The bi-pyramid samples exhibit a consistent zeta potential across the series, with values ranging from 70.6 to 76.0 mV and an average of 73.5 mV. These samples were redispersed in CTAC and demonstrated higher zeta potential values than particles redispersed

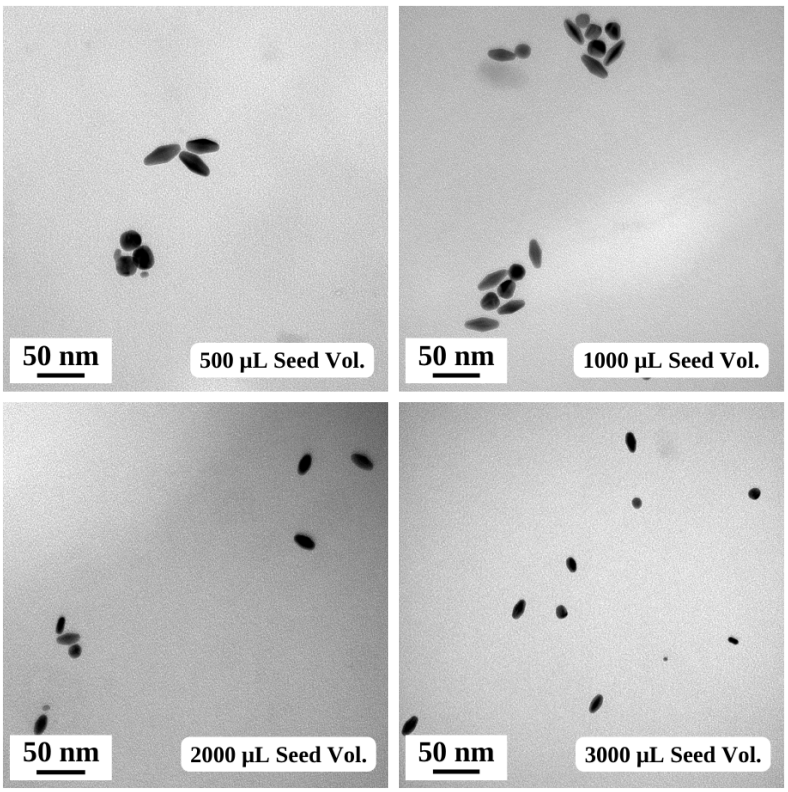


*Figure 82: TEM images of gold bipyramids with increasing gold seed volumes from 500-3000 µL*

in CTAB.

#### 3.6.1.3 Silver Overcoat

The above gold bi-pyramids were employed as the seeds for a seed-mediated growth synthesis to fabricate gold-core silver nanorods. The detailed synthetic method is described in section 2.2.3. The independent variable was the volume of $AgNO_3$ and AA in the growth solution. The concentration of silver in each series varied from 0.125 to 0.75 mM in 0.125 mM increments while maintaining a constant $[Ag^+]$:[AA] ratio of 4 for each sample. For each series, the bi-pyramidal core solution was altered from BP1-BP6 to investigate the influence of changing the size and shape of the gold core on the resulting nanorods. The normalised extinction spectra of the resulting nanorod solutions are presented in Figure 83. The corresponding TEM images of the 0.5 mM Ag samples for each BP variation are presented in Figure 84. We assume that the lighter spots on these TEM images are CTAB micelles. However, we are unable to confirm their composition as the EDS component for this TEM was not available when these images were taken.

The BP1 series exhibits a noticeable blue and red-shift in the LSPR peak compared to the extinction spectrum of the corresponding gold bi-pyramid solution. TEM imaging and extinction spectrum analysis confirm that larger bi-pyramidal cores lead to the pro-

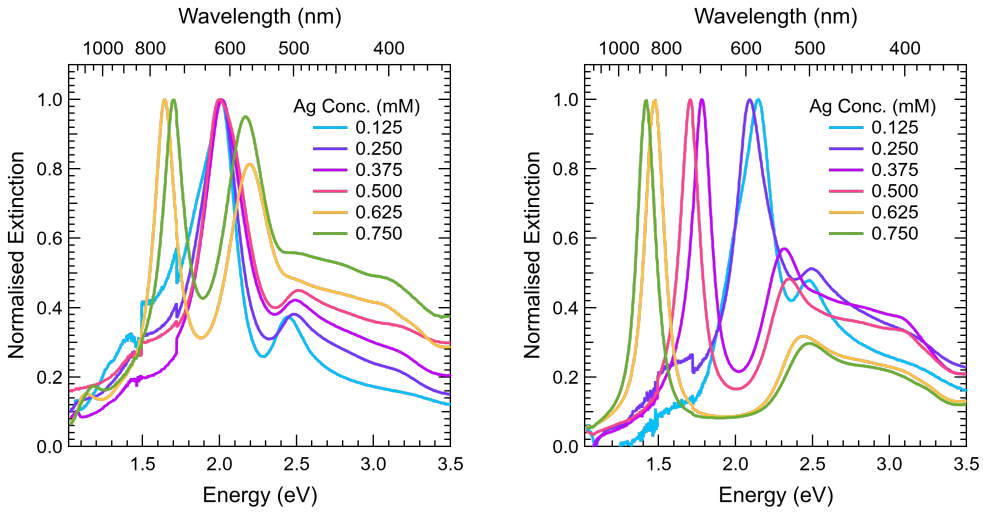


*(a) BP1 Series*




*(b) BP2 Series*

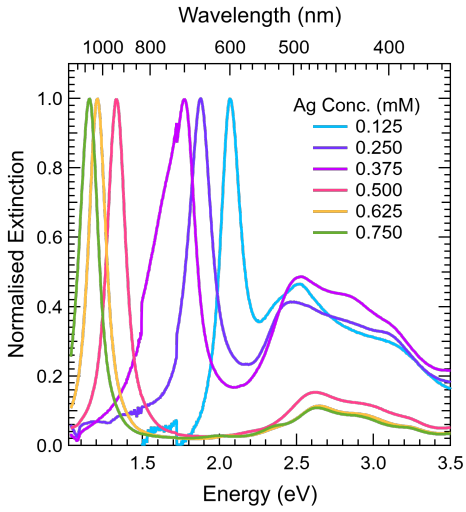


*(c) BP3 Series*

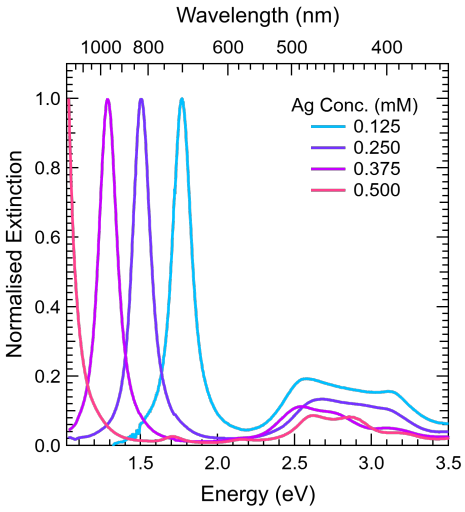


*(d) BP4 Series*

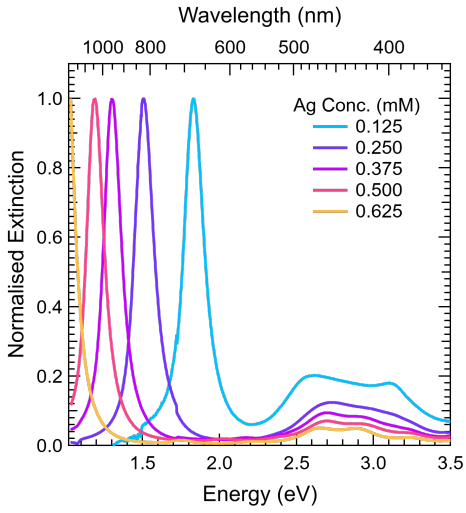


*(e) BP5 Series*

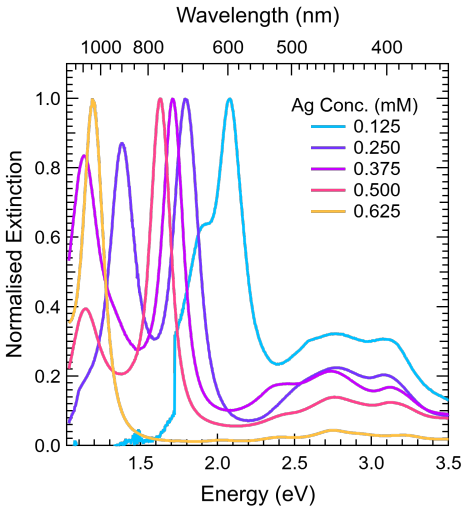


*(f) BP6 Series*

*Figure 83: The normalised extinction spectrum of a nanorod solution series with increasing Ag concentrations. Each series was synthesised using a distinct gold bi-pyramidal core fabricated with incrementally increasing seed volumes*

duction of shorter nanorods, while smaller cores with lower angularity result in longer nanorods. This is evidenced by the red-shift of the maximum SPR peak as the core size decreases.

This trend remains consistent across each series with increasing silver concentration. The rod length exhibits a dynamic increase as the core size decreases, with a significant initial shift observed between the BP1, BP2, and BP3 series. In the BP1 series, it is apparent that larger cores are only partially covered by the silver overcoat, whereas decreasing the core size leads to a substantial increase in rod length, almost doubling with each reduction in core size.

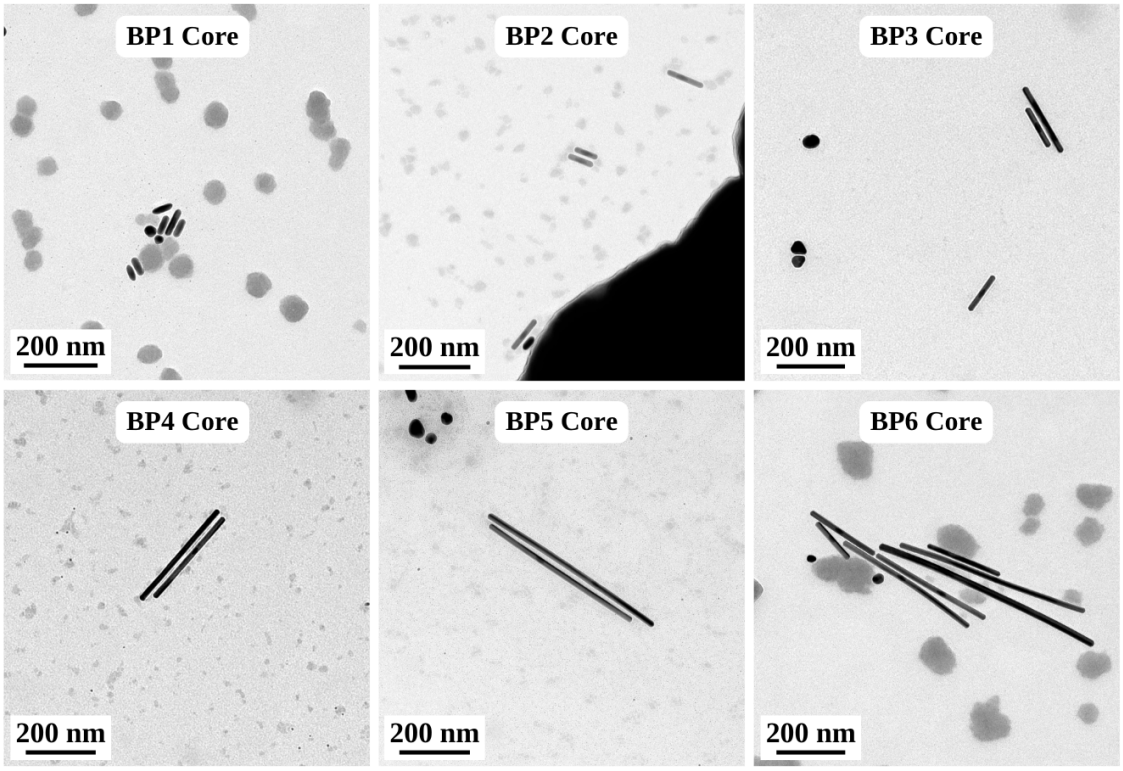


*Figure 84: TEM images of gold-core silver nanorods produced with a 0.5 mM Ag concentration with varying bi-pyramidal cores from BP1-BP6*

The BP4, 5, and 6 cores yield wire-like rods, with the BP6 bi-pyramids producing rods averaging 600 nm in length. The intense SPR peak in the red region for the BP4, 5, and 6 series is attributed to the less prominent longitudinal modes of the nanorods of these wire-like nanorods. On the other hand, the intense SPR peak in the BP1, 2, and 3 series is attributed to the main longitudinal mode of the significantly shorter nanorods.

In the observed SEM images for the 0.5 mM Ag concentration samples of BP1 and BP3, as illustrated in Figure 85, it is evident that the larger core solutions yield an abundance of large silver nanosphere particles in addition to the presence of nanorods and cubes. In

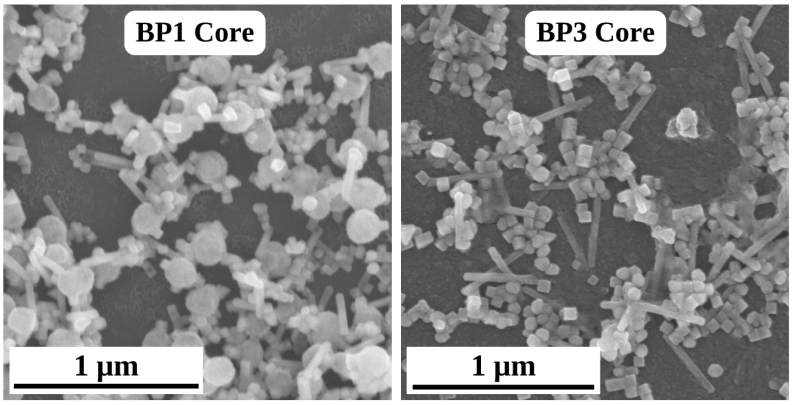


*Figure 85: SEM images of gold-core silver nanorods made from BP1 (left) and BP3 (right) seeds with a 0.5 mM Ag concentration*

contrast, the smaller gold cores produce a mixture primarily comprising nanorods and nanocubes.

### 3.6.2 Discussion

The results of this experiment indicate that increasing the seed volume during the synthesis of gold bi-pyramids leads to a decrease in the length and angularity of the nanostructures produced. This change is accompanied by an expected blue-shift in the SPR peak. The observed blue-shift and the increased intensity of the secondary resonance peak align with the extinction spectrum described in the Sánchez-Iglesias et al. article.[11] However, the silver overgrowth exhibited a contrasting trend compared to the findings in the article.

In our experiment, we observed a significant increase in the length of the nanorods when the smaller and less structured bi-pyramidal cores were overcoated with the same concentration of $AgNO_3$. Although Sánchez-Iglesias and colleagues mention that overcoating smaller cores results in significantly shorter nanorods, it is important to note that the small decahedral cores were synthesised using a different method that involved an alternative shape-directing reagent, BDAC.

The augmented surface area of the larger bi-pyramidal cores requires a higher concentration of silver to achieve coverage before any increase in rod length occurs. This phenomenon could account for the generation of shorter nanorods. It is crucial to emphasise the surplus of spherical nanoparticles observed in the BP1 and BP2 rod samples. These redundant structures will account for a substantial portion of the attainable silver. Notably, the excess nanospheres are absent in the BP3-6 rod samples, resulting in a greater amount of available silver. This, coupled with the smaller surface area of the core,

resulted in the production of longer nanorods.

The observed red-shift in the longitudinal SPR resonance peak was consistent across each series of nanorods as the silver concentration increased and the nanorods elongated. However, the TEM images indicate a lower level of uniformity in these samples compared to those provided in the article. This discrepancy may be due to the significantly higher variability in the solutions containing bi-pyramidal cores. In all seed-mediated growth nanoparticle syntheses, the uniformity of the final nanostructure solution is influenced by the uniformity of the seed solutions. This three-step synthesis process carries a higher risk of errors and will increase polydispersity without effective purification at each step.

When the extinction spectra of these nanorod solutions are compared with the particle solutions obtained in the previous nanorod synthesis, it is evident that a secondary nanostructure greatly influences the resonance peaks of the other solutions. In contrast, the resonance peaks in these nanorod solutions are notably sharper. The TEM imagery and comparison to the computational extinction spectrum for nanorods of the observed length confirm that the intense SPR peak, particularly in the BP1, 2 and 3 series, can be assigned to the primary longitudinal resonance mode.

## 3.7 Silver Triangular Nanoplate Synthesis

Silver triangular nanoplates were synthesised using a chemical reduction method previously reported by Zhang et al.[12] The synthetic method is described in section 2.2.4.

### 3.7.1 Results

Zhang and colleagues noted that the final concentration of $NaBH_4$ is the crucial variable that can be adjusted in this synthesis. The original synthesis employed 29K PVP. A series of experiments investigated the effect of increasing the chain length to 44K PVP on the resulting nanostructures. Two separate series were carried out: one using 29K PVP and the other using 44K PVP. In both series, the $NaBH_4$ concentration was raised from 1.2 to 2.2 mM in 0.2 mM increments. A preliminary trial revealed that final $NaBH_4$ concentrations below 1 mM did not yield a uniform solution of triangular nanoplates. This conclusion was drawn from the normalised extinction spectra in Figure 86, which compares samples with final $NaBH_4$ concentrations of 0.6, 0.8, and 1 mM. Notably, the spectrum profile shifts from a single sharp peak for the 0.6 mM sample to the anticipated spectrum for triangular nanoplates as the concentration increases.

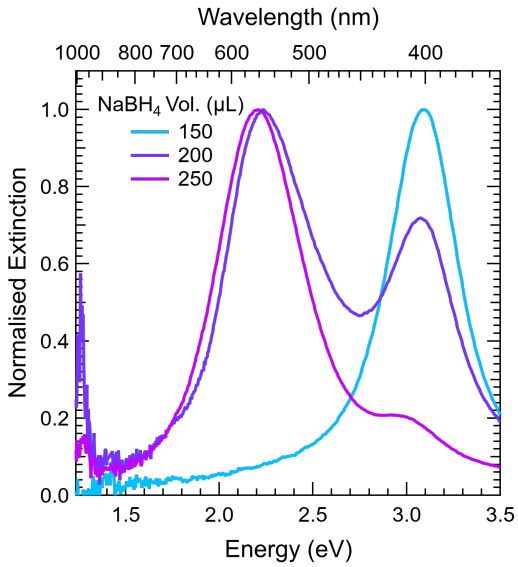


*Figure 86: Normalised extinction spectra of colloidal silver nanoplate solutions with $NaBH_4$ volumes increasing from 150 to 250 µL in 50 µL increments*

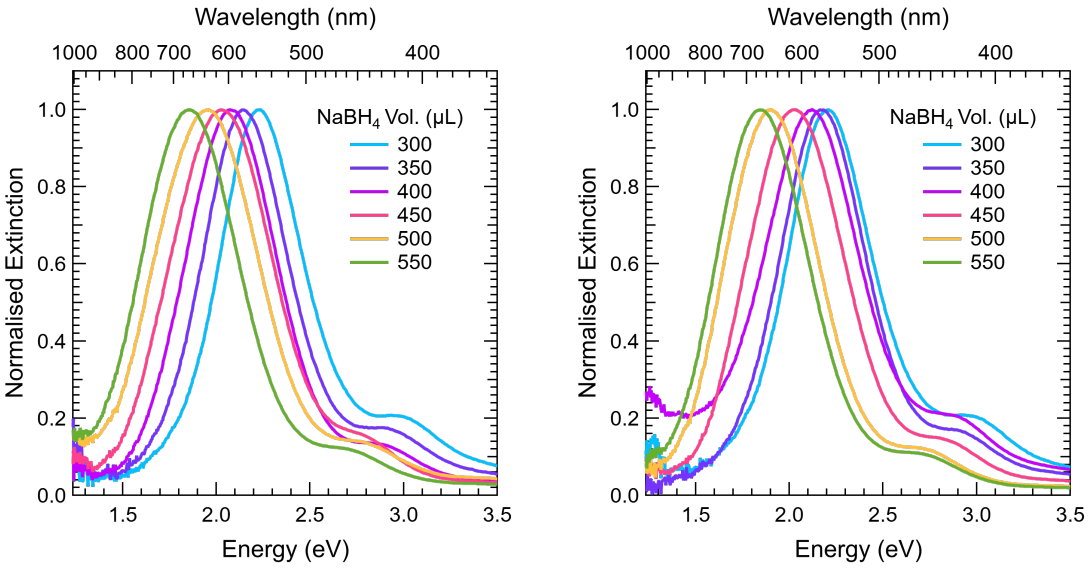


*(a) 29K PVP Series*

*(b) 44K PVP Series*

*Figure 87: Normalised extinction spectra of colloidal silver nanoplate solutions with $NaBH_4$ volumes increasing from 300 to 550 µL in 50 µL increments with 29K (a) or 44K (b) PVP*

The normalised extinction spectra for the 29 and 44K PVP series with increasing sodium borohydride ($NaBh_4$) concentrations are depicted in Figure 87. The shape or SPR peak maximums across the two series do not show any significant changes. Table 19 presents each sample's maximum SPR peak wavelengths in nanometers and energy units for clarity.

Both series exhibit a consistent red-shift in maximum SPR peak as the concentration of $NaBH_4$ is increased. In the 29K PVP series, the shift occurs from 2.23 eV (555 nm)

*Table 19: Maximum SPR values of 29 and 44K PVP triangular nanoplate solutions with increasing $NaBH_4$ volumes from 300 to 550 µL in 50 µL increments*

| $NaBH_4$ Conc. (mM) | 1.2 | 1.4 | 1.6 | 1.8 | 2.0 | 2.2 |
|---|---|---|---|---|---|---|
| 29K (eV) | 2.23 | 2.15 | 2.07 | 2.03 | 1.95 | 1.86 |
| 29K (nm) | 555 | 576 | 598 | 610 | 635 | 666 |
| 44K (eV) | 2.21 | 2.17 | 2.12 | 2.02 | 1.89 | 1.84 |
| 44K (nm) | 561 | 571 | 584 | 616 | 656 | 673 |

to 1.86 eV (666 nm), and in the 44K PVP series, the shift occurs from 2.21 eV (561 nm) to 1.84 eV (673 nm) as the $NaBH_4$ concentration increases from 1.2 to 2.2 mM. This red-shift is uniform across both series, indicating that the 29 and 44K PVP samples produce triangular nanoparticles of similar edge lengths.

### 3.7.2 Discussion

According to the extinction data gathered from this experiment, it was determined that the chain length of PVP had minimal impact on the size and shape of the resulting nanostructures. The consistent red-shift in the SPR peaks indicates that the edge length of the particles increased as the concentration of $NaBH_4$ increased, aligning with previous findings by Zhang et al.[12]

Similar red-shifts in the SPR peaks were observed for both the 29K and 44K PVP series, suggesting the production of triangular nanoparticles with comparable edge lengths under both synthetic conditions. Adding PVP into the synthesis also decelerated the initiation rate, consistent with Zhang's and co-workers' findings. The authors noted that an increase in $NaBH_4$ concentration further decelerates the initiation rate, which was also evident in this experiment for both series. Additionally, the increase in $NaBH_4$ concentration affected the particles' edge length and thickness, resulting in thinner nanoplates. Previous studies have indicated that the change in preferred binding facets of PVP with varying edge lengths can affect the thickness of nanoplates.

Our findings corroborated the observations made by Zhang and colleagues, indicating that the concentration of $NaBH_4$ is a crucial parameter for controlling the size of the triangular nanoplates. A comparison of the extinction spectra from these nanoparticle suspensions with those obtained from the optimised synthesis discussed in Section 3.2 highlighted the predominance of the triangular nanoplates in the extinction spectra.

## 3.8 Conclusion

This chapter explores the synthesis and characterisation of various silver and silver-gold core nanoparticles. Most significantly, this chapter details a variation of the reported silver nanoparticle synthesis by Rekha et al.[51] Our findings confirmed that this synthesis produces a mixture of nanoparticles in suspension, including triangular nanoplates, nanorods and nanospheres. Unlike the reported synthesis, we attribute the observed extinction response in the visible to NIR region to the high yield of triangular nanoplates in the suspension.

This chapter highlighted that the seed capping reagent significantly influences the size, shape and stability of the resulting nanoparticles. Our findings confirmed that the monodispersity of the seed solution significantly influences the uniformity of the secondary nanostructures. It was concluded that the 44K PVP-capped seeds were the most monodisperse and produced a highly reproducible suspension of secondary nanostructures. Our work also demonstrated that the SPR frequencies of these nanoparticle suspensions could be effectively tuned across the electromagnetic spectrum by altering the seed volume introduced into the growth solution. The SPR peaks were also influenced by the seed capping reagent, with the seeds capped by shorter chain PVP polymers, resulting in the synthesis of significantly larger nanoplates.

This work concluded that the concentration of CTAB in the nanoparticle suspension is critical for stabilising the nanoparticle morphology. When the CTAB concentration is decreased, the triangular nanoplates undergo rapid truncation, which is most notably observed when the particles are re-dispersed in Type I water. As a result, the triangular nanoplates undergo a morphology transformation to circular nanoplates. This change in morphology is reflected in the significant blue-shift of the SPR peak. This morphology change can be prevented by reintroducing CTAB into the nanoparticle suspension after purification. The CTAB concentration of the redispersion solutions directly influences the zeta potential of the nanoparticles. A high CTAB concentration produces highly positive zeta potential values, increasing the stability of the nanoparticle suspension. In contrast, the zeta potential values significantly decrease when the nanoparticles are dispersed in Type I water.

This work has also demonstrated that the introduction of PVP into the growth solution significantly influences the zeta potential values and stability of the nanoparticles. Specifically, the presence of PVP, a negatively charged polymer, dramatically reduced the zeta potential of the nanoparticles in their reaction conditions. Additionally, when these

nanoparticles were redispersed in Type I water, they maintained a higher degree of angularity. This observation is attributed to the synergistic binding of PVP and CTAB to the edges of the nanoparticles, which ultimately influences their surface charge and increases their stability. This enhanced stability is attributed to the ability of PVP to bind and stabilise multiple crystal facets, mitigating truncation when the CTAB concentration is reduced.

This chapter has described the experimental variations investigated to develop a robust nanoparticle seed-mediated growth synthesis. The characteristics and optical properties of these nanoparticles produced through this synthetic method can be effectively tuned by varying the seed volume and the seed capping reagent. The synthetic methods optimised in this chapter will be used to develop a nanoparticle immobilisation protocol to produce a series of monolayer nanoparticle films with tunable optical properties.

# 4 Chapter 4 - Film Fabrication and Characterisation

| Abbreviations | |
|---|---|
| XPS | X-ray Photoelectron Spectroscopy |
| QAuNP | Quasi-Spherical Gold Nanoparticles |
| AuNRs | Gold Nanorod |
| SEM | Scanning Electron Microscopy |
| nm | Nanometre |
| µL | Microlitre |
| mL | Millilitre |
| eV | Electronvolt |
| mM | Millimole |

## 4.1 Introduction

This chapter focuses on the optimisation experiments for the immobilisation of the nanoparticles discussed in section 3.2 onto modified glass substrates. A series of cleaning protocols and functionalisation methods were investigated to determine the most suitable protocol for fabricating these films when the particles were redispersed in either cetyltrimethylammonium bromide (CTAB) (10 mM) or Type I water. Protocols were also investigated for the fabrication of nanoparticle films using the gold-core nanorods and silver triangular nanoplates discussed in sections 3.6 and 3.7, respectively.

### 4.1.1 Substrate Functionalisation

The functionalisation of silica and glass substrates with functional organosilanes has been extensively investigated for numerous nanofabrication and biosensing systems.[103–105] Figure 88 below presents a schematic of a typical silanisation process.

The main steps in a silanisation protocol include cleaning, surface activation and reaction with the silane molecule. The cleaning step ensures that any contaminants have been removed from the substrate surface. The surface activation step involves the generation of hydroxyl (-OH) groups on the surface. These hydroxyl groups play a crucial role in providing binding sites for silane molecules to adhere to the surface. Previous studies have confirmed that the effective functionalisation of substrates is heavily influenced by the efficacy of the cleaning and surface activation steps.[106]

A recent study by Cras et al. determined the efficacy of numerous chemical cleaning and surface activation protocols on the hydroxylation of glass substrates.[106] Cras and coworkers used contact angle measurements to determine the effectiveness of activating hydroxyls on the substrate surface for each protocol. They also used surface contact

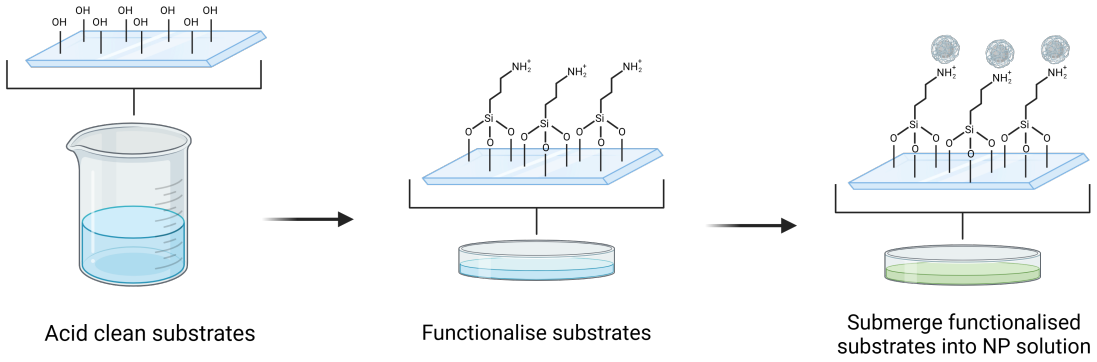


*Figure 88: A schematic showing the typical steps involved in a nanoparticle immobilisation protocol. First, a cleaning step is performed to remove any contaminants and activate the surface. Next, a functionalisation step is carried out to facilitate the adhesion of silane. Finally, the substrate is immersed in a solution containing nanoparticles to ensure their attachment.*[14]

angle measurements to confirm the deposition of a (3-Mercaptopropyl)trimethoxysilane (MPTMS) monolayer. The surface contact angles collected from this study comparing the various cleaning methods before and after functionalisation are reproduced in Figure 89 below.

Crass et al. aimed to determine the most effective cleaning method.[106] Although no universally accepted cleaning protocol exists, piranha solution is extensively used in the nanofabrication industry as an effective cleaning and hydroxylation protocol. However,

| Method | Steps |
|---|---|
| 1 | 30 min in 1:1 MeOH:HCl<br>Rinse in $H_2O$, dry under $N_2$ |
| 2 | Method 1+additional incubation (30 min) in conc. $H_2SO_4$<br>Rinse in $H_2O$, dry under $N_2$ |
| 3 | Method 2+additional incubation (30 min) in 100°C $H_2O$<br>Dry under $N_2$ |
| 4 | 5 min in 1:1:5 $NH_4OH$:$H_2O_2$ (30%):$H_2O$ at 80°C<br>Rinse in $H_2O$, dry under $N_2$ |
| 5 | Method 4+additional incubation (5 min) in 1:1:5 HCl:$H_2O_2$ (30%):$H_2O$ at 80°C<br>Rinse in $H_2O$, dry under $N_2$ |
| 6 | 30 min in 10% KOH in isopropanol<br>Rinse in $H_2O$, dry under $N_2$ |
| 7 | 20 min in 1 M NaOH<br>Rinse in $H_2O$, dry under $N_2$ |
| 8 | Method 7+additional incubation (30 min) in piranha (1:2 $H_2O_2$:$H_2SO_4$)<br>Rinse in $H_2O$, dry under $N_2$ |

*(a) Cleaning Method Description*

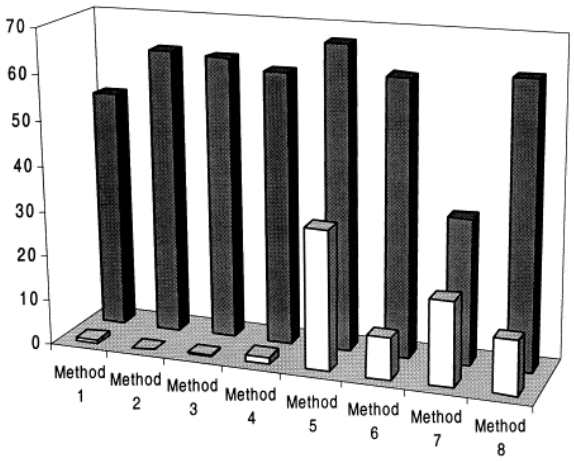


*(b) Surface Contact Angles*

*Figure 89: Surface contact angle measurements of glass substrates cleaned using various methods (1-8) compared with and without MPTMS functionalisation, as reported by Cras et al..*[106] *The white bars in Figure (b) represent the surface contact angles after the cleaning protocol, and the black bars represent those after silanisation with MPTMS.*

using this solution requires careful handling and comes with a significant safety concern due to its highly corrosive and oxidative nature.[107]

This study determined that method 2, a 1:1 methanol/hydrochloric acid (HCl) wash, followed by a concentrated sulphuric acid ($H_2SO_4$) bath, removed contaminants and hydroxylated the surface most effectively. The surface contact angle measurements in Figure 89 confirmed that this method, along with methods 1, 3 and 4, resulted in an angle measurement below 8° confirming the increased hydrophilicity of the substrate. Other methods, such as methods 5, 6, and 8, which incorporate piranha solution or potassium hydroxide (KOH), decreased the contact angle, but did so to a lesser extent than the previously mentioned methods. Upon silane treatment, a significant increase in contact angle was observed. This confirmed an increase in hydrophobicity, suggesting the effective deposition of an MPTMS monolayer.[106]

Cras et al. noted that only the 1:1 methanol/HCl wash followed by a concentrated $H_2SO_4$ bath method resulted in a contact angle of 53° after the MPTMS deposition, consistent with previously reported values for a monolayer of MPTMS on silica. The contact angles for the other cleaning methods, including the one that incorporated piranha solution, were higher than previously reported and ranged from 60-70° . The authors hypothesised that this was due to the increased heterogeneity between soda lime glass and silica substrates.[106]

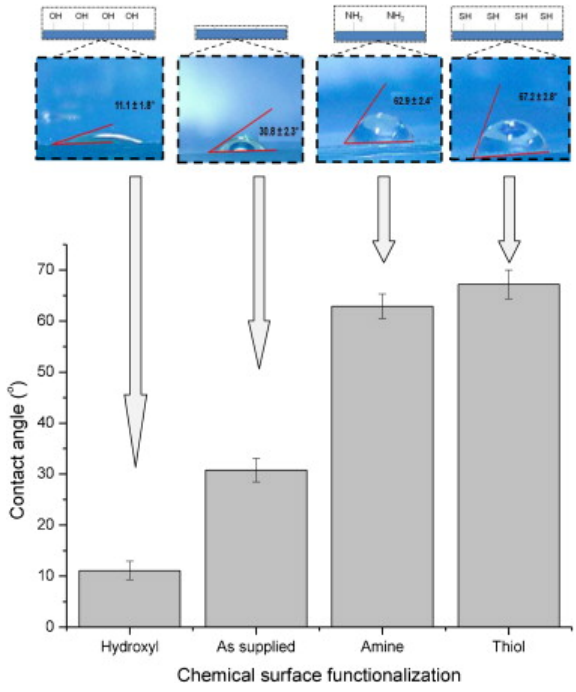


*Figure 90: Comparison of the surface contact angle measurements for as supplied, hydroxylated and MPTMS or APTES functionalised glass substrates, as reported by Marques et al.*[108]

Another study by Marques and co-workers investigated the functionalisation of glass substrates with (3-aminopropyl)trimethoxysilane (APTES) and MPTMS to develop biosensors based on enzymatic systems.[108] The substrates underwent hydroxylation through treatment with piranha solution before sol-gel deposition of a 2% APTES or MPTMS process.

Marques confirmed the functionalisation of the glass substrates through surface contact angle and FTIR measurements. The average contact angles alongside the measured droplet images are reproduced in Figure 90. An apparent decrease in the contact angle is observed from the "as supplied" substrate, with an average angle of 30.8° to the hydroxylated substrate, with an average angle of 11.1°.[108]

This shift shows that the substrate has been successfully hydroxylated and cleaned of contaminants after treatment with piranha solution. Upon the deposition of APTES, this surface contact angle increased to 62.9° . Additionally, the surface contact angle increased to 67.3° after the deposition of MPTMS. The significant increase in angle measurement suggests an increase in hydrophobicity after the successful deposition of APTES or MPTMS.[108]

The development of effective protocols for the functionalisation of glass substrates is a pivotal element in the successful fabrication of a plasmonic sublayer for our proposed device. Critical components of the protocol, particularly the cleaning and surface activation procedures, will be carefully evaluated to establish an optimised methodology for the immobilisation of the synthesised nanoparticles. This systematic approach aims to enhance the efficacy and reproducibility of the resulting plasmonic sublayer.

### 4.1.2 Immobilisation of Nanoparticles

Functionalised silicon and glass substrates have been extensively studied as substrates for immobilising noble metal nanoparticles.[109,110] The development of reproducible fabrication methods is crucial for advancing several devices. The physical and chemical properties of such devices are dictated not only by the characteristics of the nanoparticles but also by the spatial arrangements and particle density achieved by the immobilisation process. Developing a reproducible fabrication method that produces densely packed and regularly arranged nanoparticle films is crucial in ensuring these devices have optimal signal transduction amplification while allowing quantitative optimisation analysis.[69]

A recent study by Haddada et al. investigated the immobilisation of spherical gold

nanoparticles onto silicon substrates functionalised with APTES, MPTMS or (3-aminopropyl)trimethoxysilane/mercaptoundecanoic acid (APTES/MUA). Surface contact angle measurements were used to confirm the effectiveness of the functionalisation methods.[110]

The contact angle measurements for APTES and MPTMS were in agreement with previously stated values. The substrate grafted with MUA on the APTES-modified layer produces a low surface contact angle measurement of 40° this suggests that the increase in chain length increased hydrophilic character. Their findings agreed with previous findings and can be explained by the increase in layer crystallinity and organisation produced by the increased interactions between the alkyl chains, ultimately reducing the folding of terminal groups and exposing the hydrophilic part of the grafted molecule.[110]

One of the significant findings of this article was the implication of sonicating the nanoparticle solution during the particle deposition step. The reproduced SEM images in Figure 91 compare the films produced with APTES, MPTMS or APTES-MUA functionalised substrates with (b-c) or without (a) sonication.[110]

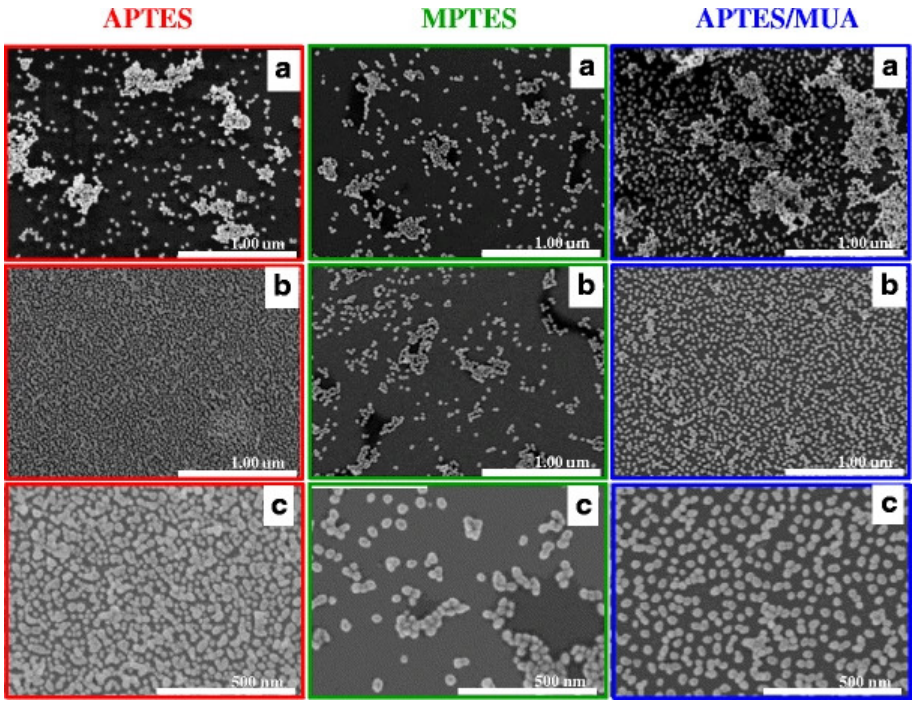


*Figure 91: SEM images comparing the particle density of gold nanoparticles immobilised on APTES, MPTMS, or APTES/MUA functionalised glass substrates, with (b,c) or without (a) sonication. As reported by Haddada et al.*[110]

Haddada and co-workers found that sonicating the nanoparticle solution during deposition significantly enhanced the particle density on APTES and APTES-MUA substrates. This process also minimised the occurrence of aggregation areas on the sub-

strates, which were noted in the absence of sonication. In contrast, a substantial reduction in particle coverage was observed on the MPTMS functionalised substrates. Unlike the APTES and APTES-MUA substrates, the introduction of sonication did not improve particle coverage on the MPTMS substrates. The authors attributed this decrease to the lower degree of surface coverage provided by MPTMS.[110]

X-ray photoelectron spectroscopy (XPS) measurements confirmed that the silane coverage with MPTMS was four times lower than that with APTES. The authors also noted that the greater flexibility of the propyl chain in MPTMS, compared to the ethyl chain in APTES, may adversely affect the interaction between the MPTMS layer and the nanoparticles. This could lead to less stable binding and explain the reduced particle density observed in nanoparticle films immobilised on MPTMS functionalised substrates.[110]

### 4.1.3 Immobilisation of CTAB-Capped Metal Nanoparticles

An alternative approach to nanoparticle immobilisation is the use of hydroxylated substrates without further modification with an organosilane. This approach yields a negatively charged substrate and has been demonstrated to be particularly effective with CTAB-capped nanostructures that exhibit an overall positive charge.

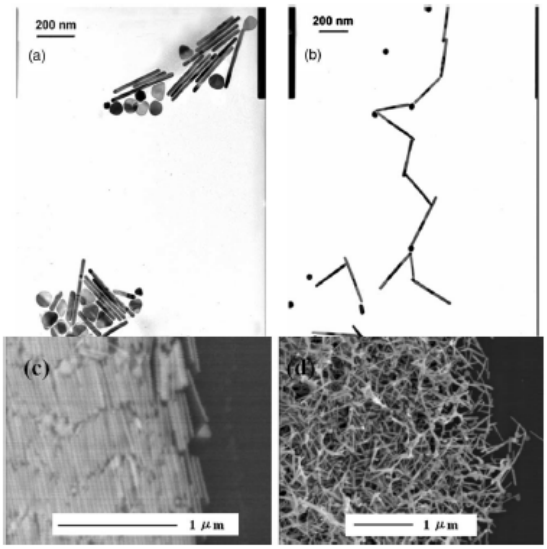


*Figure 92: TEM and SEM images showing the configuration of gold nanorods at high (left) and low (right) CTAB concentrations, as reported by Kawamura et al.*[111]

A study by Huang and Kim detailed a method for immobilising highly monodisperse quasi-spherical gold nanoparticles (QAuNP). In this study, glass substrates were hydroxylated through piranha cleaning before being immersed in diluted QAuNP suspensions

for varying incubation times. The article detailed the tendency of CTAB-capped particles to stack and assemble multi-layer superstructures on the substrate.

Huang and Kim hypothesised that, unlike gold nanoparticles capped with trisodium citrate (TSC), which have a high zeta potential to prevent aggregation, CTAB-capped nanoparticles offer interconnecting networks to neighbouring particles in multiple directions. When these particles dry down onto a substrate, the alkyl groups of the CTAB collapse and reduce the interparticle distance, favouring the aggregation of neighbouring particles.[112]

A similar phenomenon was observed in a study by Kawamura and co-workers; their study looked at the self-assembly of gold nanorods on a substrate to maintain the surface plasmon resonance (SPR) effect.[111] They found that the nanorods assembled in either parallel or linear-aligned structures; this depended on the final CTAB concentration of the particle solution. A reproduction of the SEM images of both configurations is presented in Figure 92.

The SEM images showed that at higher CTAB concentrations, the nanorods assemble in a parallel alignment. Meanwhile, at lower CTAB concentrations, they assemble in a linear alignment. Kawamura and co-workers suggested that the CTAB concentration dictated the favoured configuration of the nanorods.[111] Their simplified schematic of the CTAB coverage on the gold nanorods at high and low concentrations is reproduced in

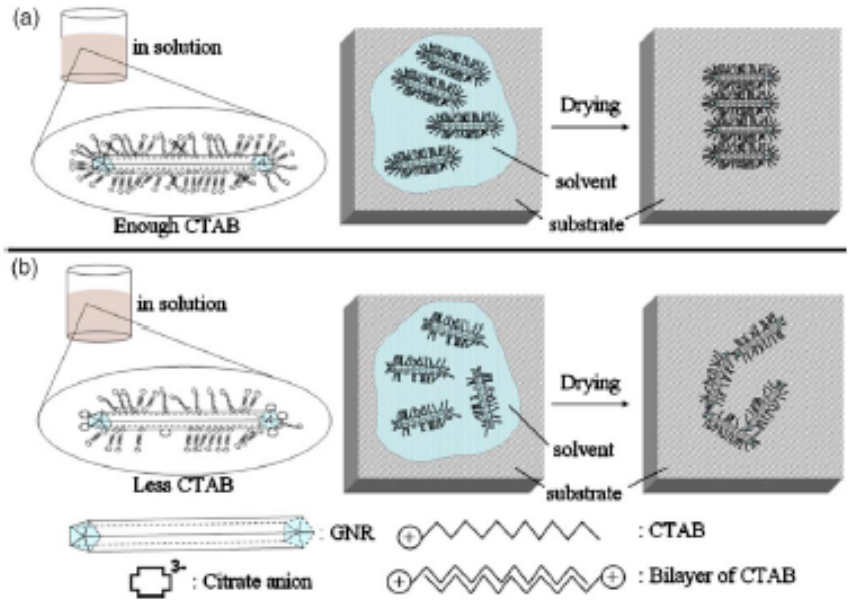


*Figure 93: Schematic showing the configuration and molecular coverage of gold nanorods at high (a) and low (b) CTAB concentrations, as reported by Kawamura et al.*[111]

Figure 93.

At high CTAB concentrations, the nanorods are entirely capped with a bilayer of the CTAB molecule. Whereas, at lower concentrations, the nanorods are not entirely capped, particularly across the {111} facets at each end of the rod. As a result, the entirely capped nanorods will prefer to assemble in parallel, with alkyl chain interactions occurring between the bilayers on neighbouring nanorods. In contrast, the partially capped rods will assemble in a linear alignment as the negatively charged tips attract the positively charged regions of neighbouring rods. The self-assembly configuration of the nanorods directly influences the optical properties of the nanoparticle film.[111] The extinction spectra of a parallel and linear alignment of gold nanorods on a substrate are reproduced in Figure 94.

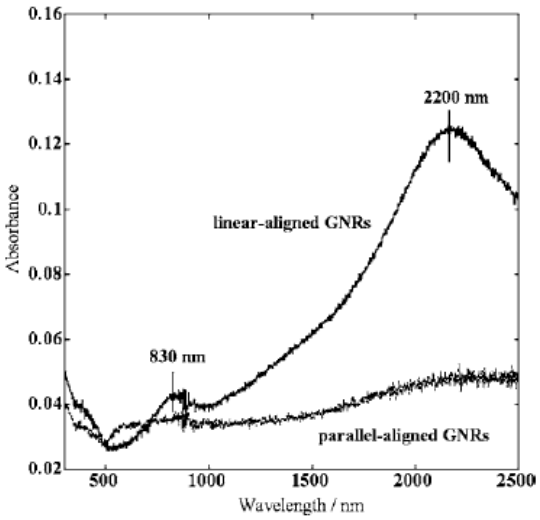


*Figure 94: Extinction spectra of gold nanorods immobilised on a hydroxylated glass substrate. The nanorods are assembled in a parallel or linear alignment, subject to the CTAB concentration. As reported by Kawamura et al.*[111]

When the particles self-assemble in a parallel alignment on the substrate, the spectrum exhibits a weak intensity across the 2500-500 nm wavelength range. This indicates the dense packing of the nanorods on the substrate, which causes the SPR bands to couple strongly and results in a decrease in the SPR signal. In contrast, two distinct peaks are observed at 830 and 2200 nm when the particles are arranged in a linear alignment. Kawamura and co-workers assigned the peak at 830 nm to the resonance of the excess nanoplates on the substrate and the peak at 2200 nm to the weakly coupled longitudinal mode.[111]

### 4.1.4 Condition Variations in Immobilisation Protocols

Numerous studies have been conducted to improve the understanding of the immobilisation process of noble metal nanoparticles onto silicon or glass substrates. A study by Guo and co-workers investigated the impact of nanoparticle concentration, CTAB concentration, and incubation time on the particle density and inter-particle distances of the resulting gold nanorod (AuNRs) chips.

In this study, CTAB-capped gold nanorods were immobilised onto glass substrates that were hydroxylated using a piranha cleaning protocol. The authors increased the nanoparticle concentration, CTAB concentration and incubation time to observe how these parameters impacted the final particle density on the substrates.[113] The reproduced image in Figure 95 below shows their observed trends in particle density.

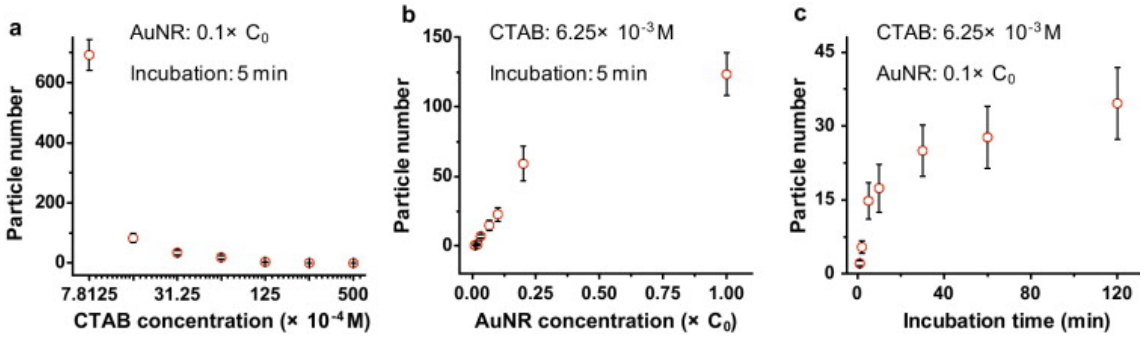


*Figure 95: Comparison of the particle density achieved for the immobilisation of gold nanorods on hydroxylated glass substrates when fabrication parameters such as CTAB concentration (a), AuNR concentration (b), and incubation time (c) are increased. As reported by Guo et al.*[113]

Their findings corroborate those from previous studies,[114] which indicated that increasing nanoparticle concentration and incubation time lead to a higher particle density on the substrate. Notably, they observed that increasing the CTAB concentration caused a significant reduction in particle density.

The authors attributed this observation to the competitive binding between the positively charged, CTAB-capped AuNR and the positively charged, free CTAB molecules in the suspension. Both species are attracted to the negatively charged glass substrate. Higher concentrations of CTAB significantly increase the availability of free CTAB molecules in the suspension, diminishing the binding efficiency of AuNRs by reducing the number of available sites for attachment. This competition for binding is substantially decreased at lower CTAB concentrations, allowing more AuNRs to adhere to the substrate and resulting in a higher particle density.[113]

A study by Ferhan et al. investigated the effect of altering the ionic strength on the

resulting particle density. They introduced increasing concentrations of sodium chloride (NaCl) to solutions of suspended CTAB-capped gold nanorods and immobilised them on glass substrates functionalised with polystyrene sulfonate (PSS) grafted onto an APTES-modified surface.[109]

To observe the correlation between the NaCl and CTAB concentrations, suspensions with the same concentration of gold nanorods were redispersed in either low, moderate or high CTAB concentration before the fabrication process. In most previously reported

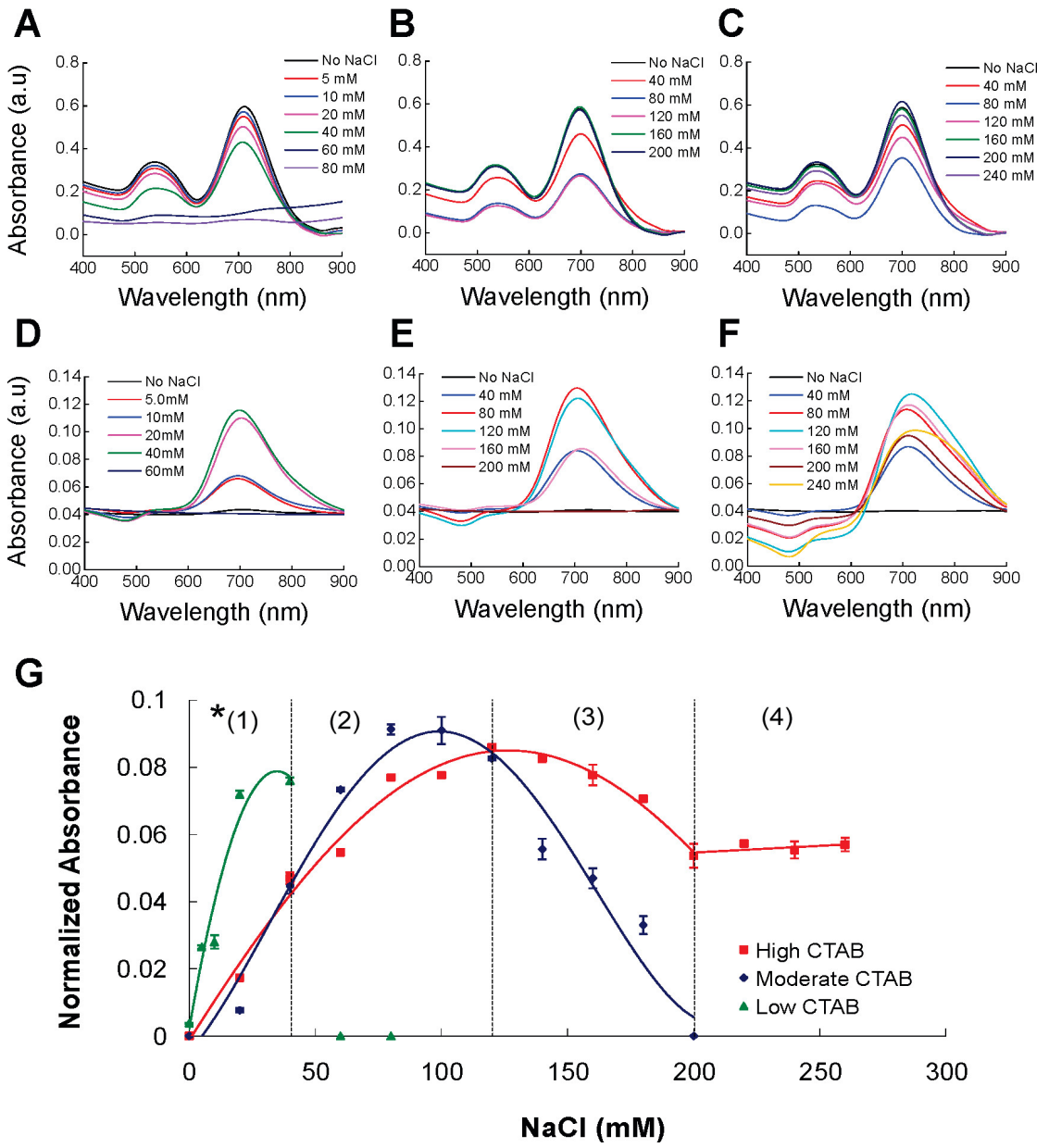


*Figure 96: Extinction spectra of nanoparticle solutions at low (a), moderate (b) and high (c) CTAB concentrations. Alongside the extinction spectra of immobilised gold nanorod films at low (d), moderate (e) and high (f) CTAB concentrations. The relative absorbance of the nanoparticle films compared to the CTAB and NaCl concentration (g) is also presented, as reported by Ferhan et al.*[109]

methods, the CTAB concentration is kept at a minimum before fabrication. Ferhan and co-workers determined that the surfactant concentration was a critical factor in the particle assembly and density. The reproduced image in Figure 96 shows the parabolic trend observed by Ferhan and co-workers as the NaCl concentration was increased.[109]

At low CTAB concentrations, only low NaCl concentrations were tolerable before severe aggregation between the nanoparticles occurred. As the NaCl concentration increased, the particle density also increased. However, any further increase past 60 mM caused aggregation to occur. For suspensions with moderate and high CTAB concentrations, the particle density increased with an increased NaCl concentration. In contrast to the low CTAB samples, the particle density decreased as the NaCl concentration was increased past a critical concentration. The concentrations were 100 and 120 mM for the moderate and high CTAB suspensions, respectively. The authors attributed this trend to a two-tiered shielding effect.[109] A reproduction of a schematic detailing this effect is presented in Figure 97 below.

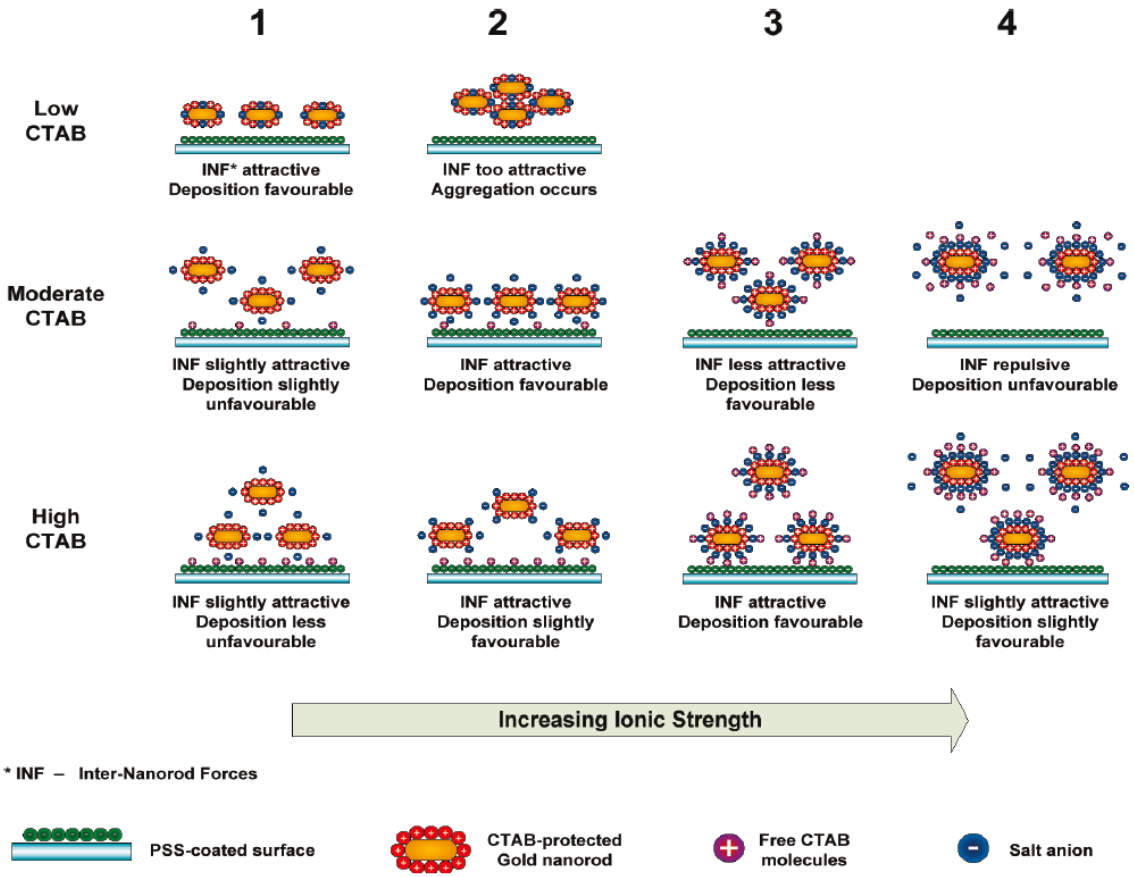


*Figure 97: Schematic of the shielding effect caused by the increase of ionic strength at low, moderate and high CTAB concentrations, as reported by Ferhan et al.*[109]

The schematic gives a detailed representation of the two-tiered shielding effect ob-

served at increasing NaCl and CTAB concentrations. At low CTAB concentrations, the surface coverage of CTAB was dictated by the on/off equilibrium. The low CTAB concentration in the solution led to the CTAB molecule desorbing from the nanorods. Therefore, when NaCl was introduced, the salt anions bound to the free surface area.[109]

At lower NaCl concentrations, the increasing ionic strength increased the inter-particle force, increasing the number of particles that adhered to the functionalised substrate. The nanoparticles began to aggregate when the attractive inter-particle force rose too high. This aggregation can be observed in the absorbance spectra. Notably, the intensity of the spectra decreases as the ionic strength increases; a sharp decline in intensity and a shift in the profile is observed at NaCl concentrations of 60 mM and higher.[109]

At moderate and high CTAB concentrations, the proposed two-tiered shielding effect was observed. Without the incorporation of NaCl, particles would not adhere to the functionalised substrate. As the NaCl concentration increased, the particle density also increased. At lower concentrations, the salt anions create a negative shield around the nanorods through attraction to the positive CTAB bilayer. This increases inter-particle attractive forces, which favours deposition onto the functionalised substrate.[109]

As the NaCl concentration was further increased, the surface potential around the nanorods became more negative, and the excess CTAB molecules in the solution formed a second shielding effect. This caused a reintroduction of the repulsive forces between the nanorods, which limited their deposition onto the substrate. This created the parabolic trend observed in the particle density and absorbance intensity observed in Figure 97.[109]

## 4.2 MPTMS Functionalisation Experiments

Subsequent experiments were conducted to identify the optimal protocol parameters for the fabrication of MPTMS-functionalised glass substrates. The solutions outlined in section 3 were employed to evaluate substrate performance and assess the efficacy of these substrates in facilitating the immobilisation of nanoparticles.

### 4.2.1 Results

#### 4.2.1.1 Submersion Time Trials

Initial experiments were conducted to determine the optimal time for submerging hydroxylated glass substrates in MPTMS solution. The concentration of MPTMS in toluene remained constant at 1% v/v, and the glass substrates were hydroxylated in piranha solution before functionalisation. The submersion time was increased from 5 to 15 and finally

to 30 minutes. The functionalised substrates were immersed in a nanoparticle solution overnight.

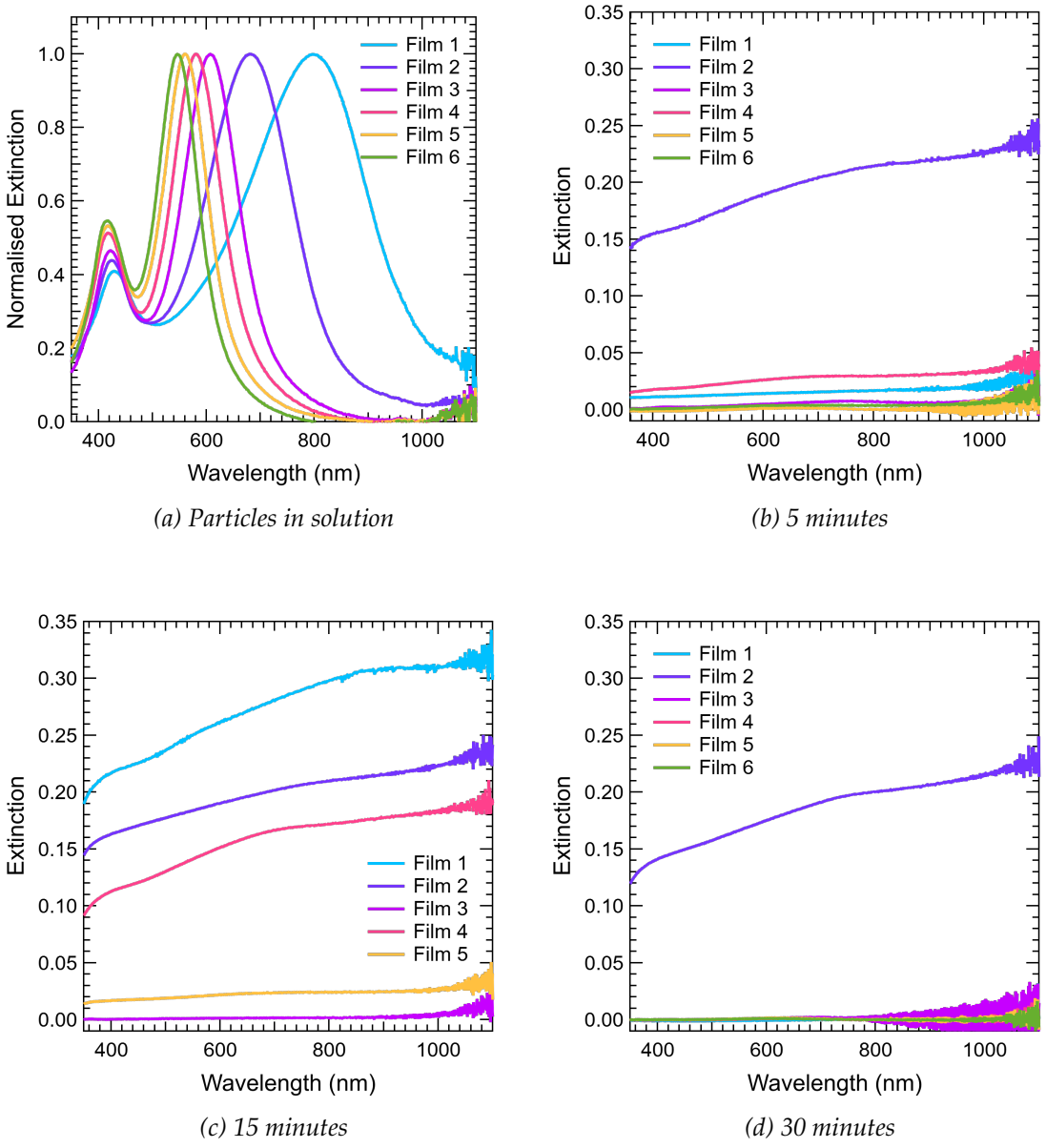


*(a) Particles in solution*

*(b) 5 minutes*

*(c) 15 minutes*

*(d) 30 minutes*

*Figure 98: Extinction spectrum of silver nanoparticle films fabricated using solutions with increasing 44K PVP-capped seeds from 50-300 µL in 50 µL increments (Film 1-6). Each film series shows an increased MPTMS submersion time, from 5 minutes (b) to 15 minutes (c) and 30 minutes (d). Alongside the extinction spectra of the nanoparticle suspensions (a) used to fabricate each film*

For each submersion time, six substrates were used, and they were immersed in nanoparticle solutions created with increasing volumes of 44K PVP-capped seed, ranging from 50 to 300 µL in 50 µL increments. The nanoparticles were redispersed in CTAB (10 mM) before nanoparticle film fabrication. The normalised extinction spectra for the

nanoparticle solutions are displayed in Figure 98, in conjunction with the extinction spectra of the resulting nanoparticle films as the MPTMS submersion times increase.

For many of the nanoparticle solutions, the nanoparticle films generated from a 5-minute submersion time exhibited minimal optical response. However, the optical response significantly increased in the films produced from a 15-minute submersion. Interestingly, this response declined rapidly when the submersion time was further increased to 30 minutes. These findings suggest that a 5-minute submersion was insufficient for forming an effective MPTMS film, and that increasing the submersion time to 15 minutes notably improved nanoparticle coverage. However, a further increase in submersion time proved to be less effective.

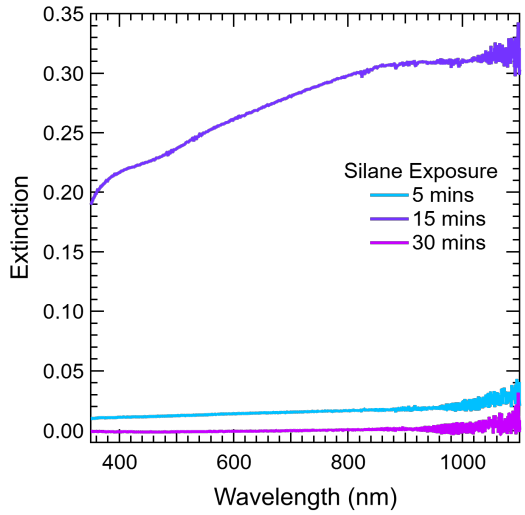


*Figure 99: Extinction spectrum of silver nanoparticle films fabricated using a 50 µL 44K PVP-capped seed solutions, comparing MPTMS submersion times of 5, 15 and 30 minutes. Particles were redispersed in CTAB (10 mM) before fabrication*

Figure 99 compares the extinction spectra of the nanoparticle films produced with the 50 µL 44K PVP capped-seed volume solution for the 5, 15, and 30-minute MPTMS submersion times. From the analysis of the scanning electron microscopy (SEM) images of the nanoparticle films depicted in Figure 100, it was evident that an increase in particle density occurred with an extension of the submersion time from 5 to 15 minutes, followed by a notable reduction as the submersion time was further extended to 30 minutes. This fluctuation in particle density accounted for the observed variation in the optical response intensity between the 5 and 15-minute submersion times, and the subsequent sharp decline for the 30-minute film. Notably, a monolayer of nanoparticles was not achieved in any of the films, as the particles retained their original shape and formed

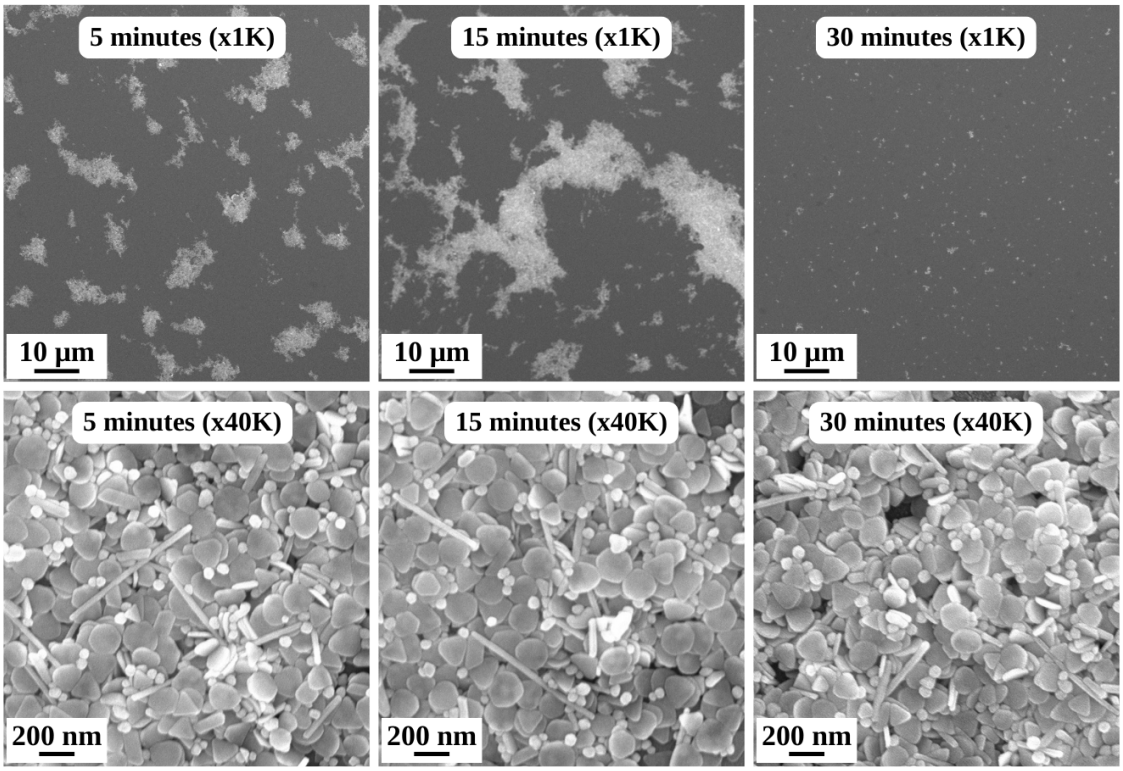


*Figure 100: SEM images of silver nanoparticle films fabricated using a 50 µL 44K PVP-capped seed solutions, comparing MPTMS submersion times of 5, 15 and 30 minutes. Particles were redispersed in CTAB (10 mM) before fabrication*

clusters in island-like structures across the substrate. This clustering phenomenon accounts for the featureless appearance of the extinction spectra across all films.

Further investigation was conducted into the fabrication protocol to achieve a monolayer film. In this experiment, the MPTMS submersion time remained constant at 15 minutes. Six substrates were immersed in nanoparticle solutions generated with progressively increasing volumes of 44K PVP-capped seed ranging from 50-300 µL in 50 µL increments. Before nanoparticle film fabrication, the particles were redispersed in Type I water.

Low and high-magnification images of the resulting films are displayed in Figure 101, respectively. These images reveal a notable reduction in particle density with increasing seed volume, accompanied by a decrease in particle size. The particles were arranged in island formations. In contrast to the previous series, these island formations appear smaller and more dispersed. A significant alteration in the angularity of the nanoplates was observed when the particles were redispersed in water. However, the nanorods in each sample have not changed shape or decreased in length, suggesting they have remained stable. In some instances, these nanorods appear to form a bridging link between

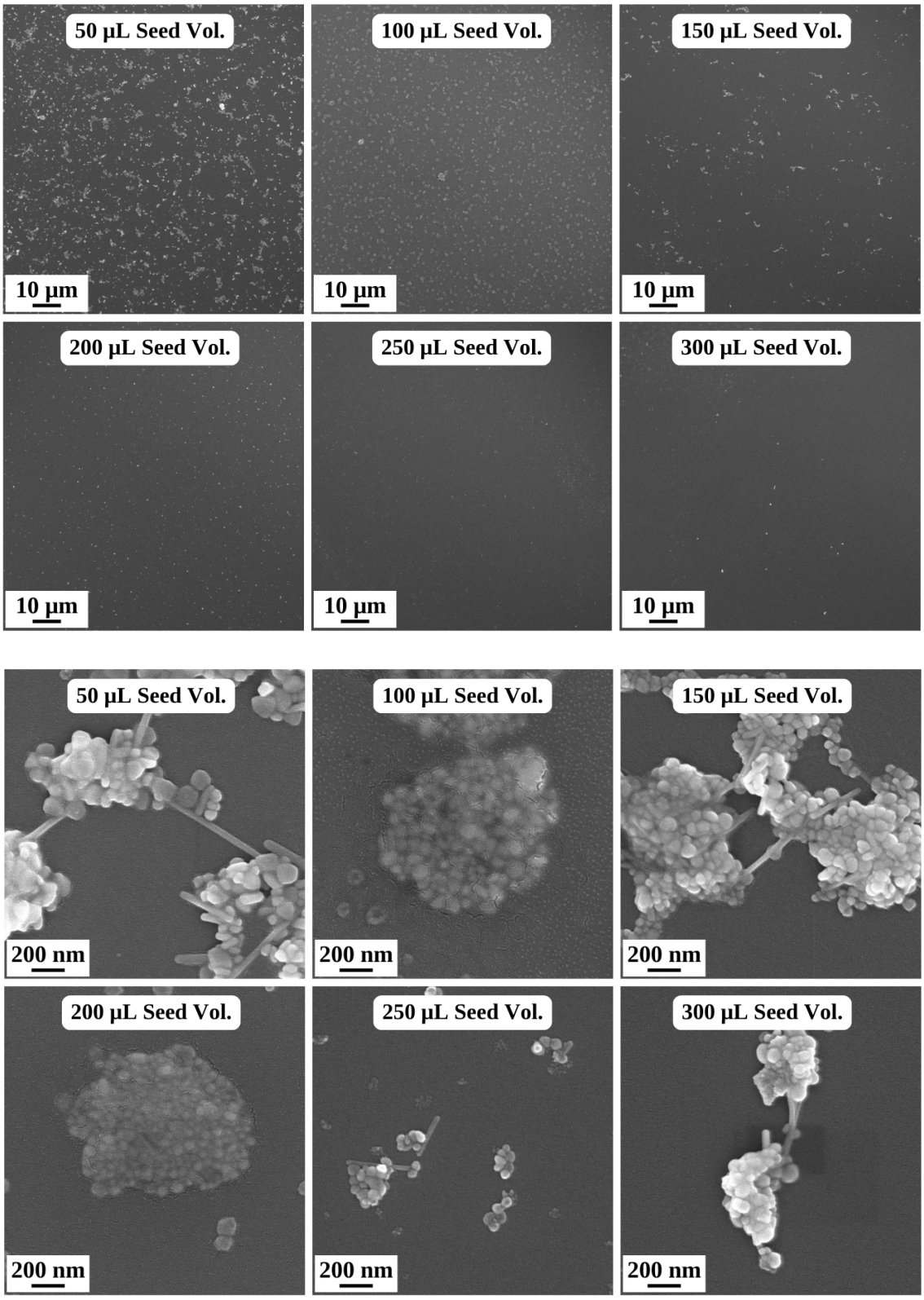


*Figure 101: SEM images of silver nanoparticle films fabricated using solutions with increasing 44K PVP-capped seeds from 50-300 µL in 50 µL increments. The MPTMS submersion time was kept constant at 15 minutes, and particles were redispersed in Type I water before fabrication*

the particle island formations.

#### 4.2.1.2 Comparing Piranha Cleaning to MeOH:HCl Cleaning

The first experiment compared the hydroxylation efficiency between the MeOH:HCl and piranha cleaning methods. Following hydroxylation by either method, the substrates underwent functionalisation for 15 minutes in a 1% v/v MPTMS/toluene submersion. These treated substrates were then immersed in nanoparticle solutions overnight. Each

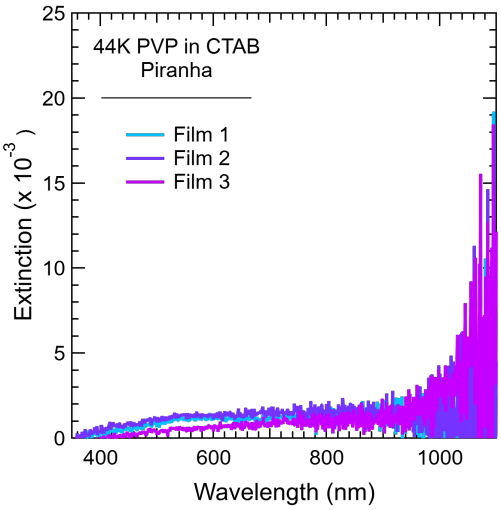


*(a) Piranha Cleaned - Particles in CTAB*

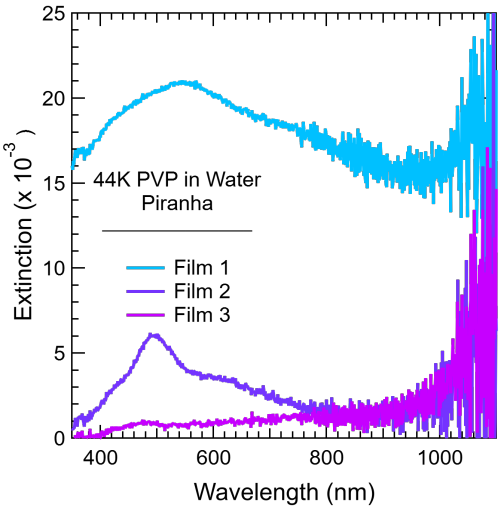


*(b) Piranha Cleaned - Particles in Water*

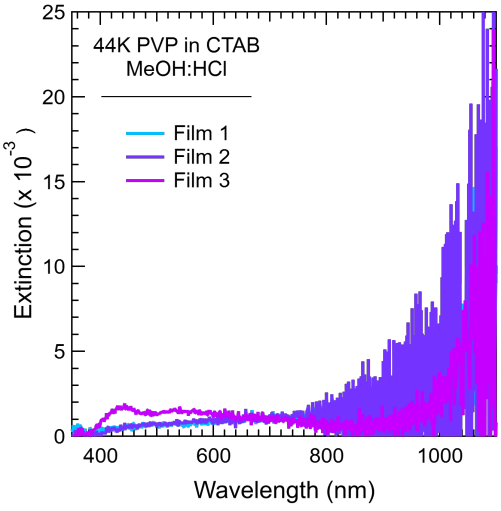


*(c) MeOH:HCl Cleaned - Particles in CTAB*

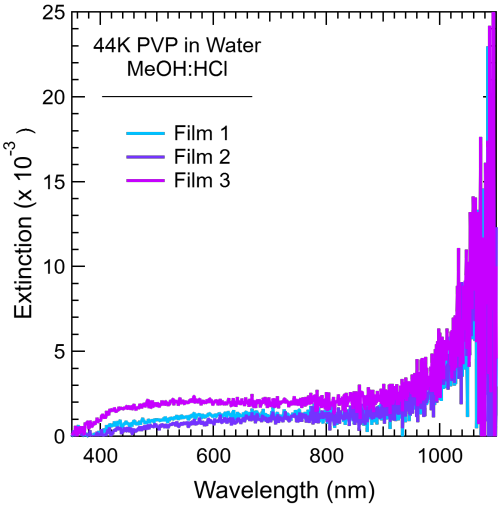


*(d) MeOH:HCl Cleaned - Particles in Water*

*Figure 102: Extinction spectrum of silver nanoparticle films fabricated using 50 (Film 1), 100 (Film 2) or 150 µL (Film 3) 44K PVP-capped seed solutions. Comparing the efficacy of piranha and MeOH:HCl cleaning before MPTMS submersion for 15 minutes. Particles were redispersed in CTAB (10 mM) or Type I water before fabrication*

series consisted of three substrates, which were immersed in nanoparticle solutions generated with increasing volumes of 44K PVP-capped or CTAB-capped seeds ranging from 50-150 µL in 50 µL increments (Film 1-3). Before film fabrication, the particles were redispersed in either CTAB (10 mM) or Type I water.

The extinction spectra derived from the films fabricated using the 44K PVP-capped seed nanoparticle solutions are presented in Figure 102. Films prepared with particles redispersed in CTAB exhibit minimal optical response, particularly when fabricated on

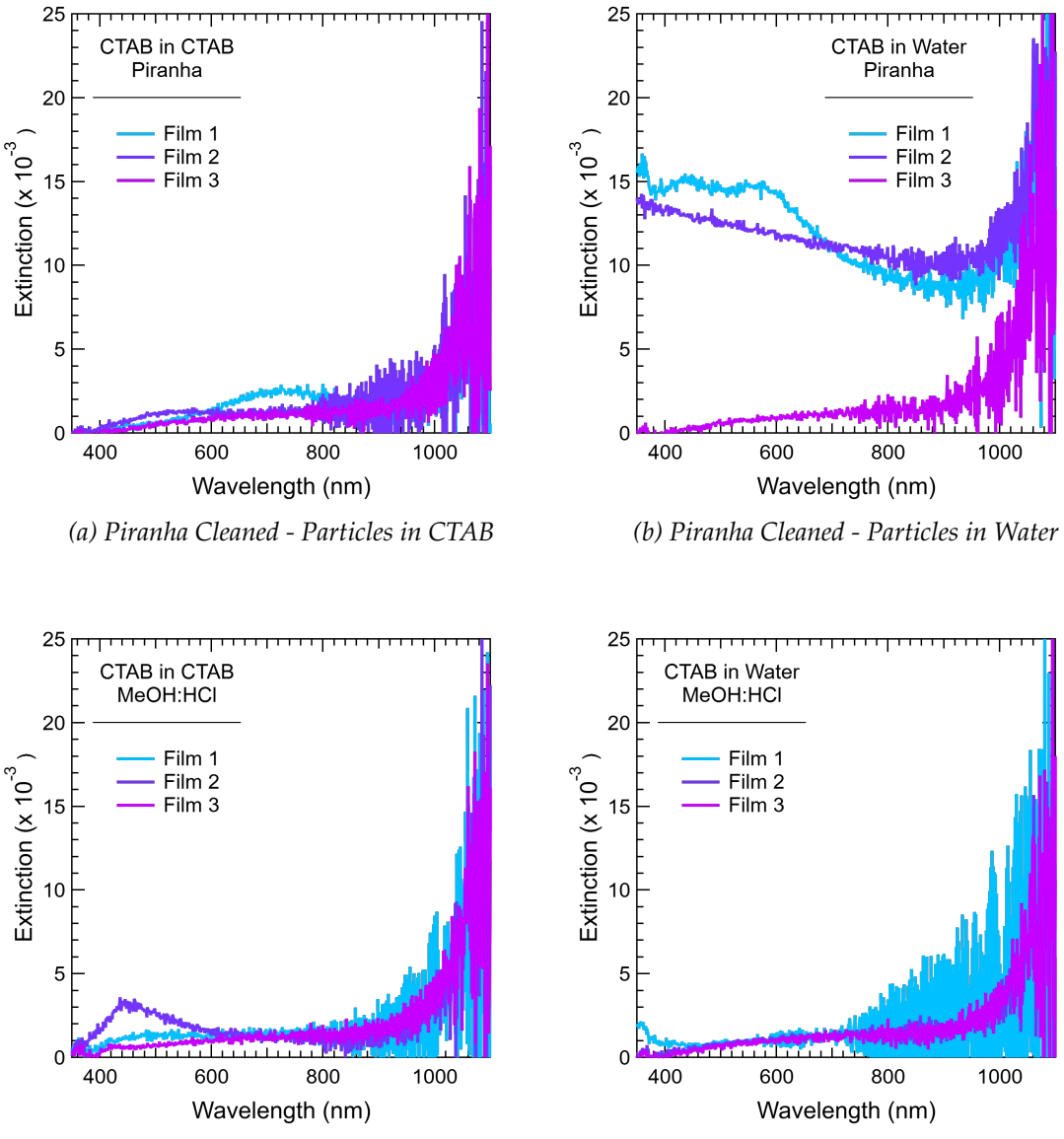


*(a) Piranha Cleaned - Particles in CTAB*

*(b) Piranha Cleaned - Particles in Water*

*(c) MeOH:HCl Cleaned - Particles in CTAB*

*(d) MeOH:HCl Cleaned - Particles in Water*

*Figure 103: Extinction spectrum of silver nanoparticle films fabricated using 50 (Film 1), 100 (Film 2) or 150 µL (Film 3) CTAB-capped seed solutions. Comparing the efficacy of piranha and MeOH:HCl cleaning before MPTMS submersion for 15 minutes. Particles were redispersed in CTAB (10 mM) or Type I water before fabrication*

piranha and MeOH:HCl cleaned substrates. A significant increase in optical response is observed for the film created from the particles redispersed in water. Consistent with the previous experiment, films fabricated using nanoparticle solutions made with lower seed volumes demonstrate higher spectrum intensity. Notably, this substantial increase is only evident in films produced on piranha-cleaned substrates, as the intensity of the spectra for the MeOH:HCl cleaned films is significantly lower. These results suggest that the MeOH:HCl cleaning method may not be an effective hydroxylation process, thereby resulting in a low-coverage MPTMS substrate and consequently limiting nanoparticle coverage.

The extinction spectra obtained from films created using CTAB-capped seed nanoparticle solutions are shown in Figure 103. Similar observations are noticeable in these films as in the previous 44K PVP-capped seed films. The most significant optical response is observed when the films are produced from piranha-cleaned substrates and when the particles are redispersed in Type I water.

To assess the efficacy of depositing the particle solution onto the substrate versus submerging the substrate in the solution, two additional films were fabricated. These films were created using piranha-cleaned MPTMS functionalised substrates with a 50 µL 44K PVP-capped seed volume solution. The particles were redispersed in either CTAB (10 mM) or Type I water, and an adequate volume of the particle solution was applied to

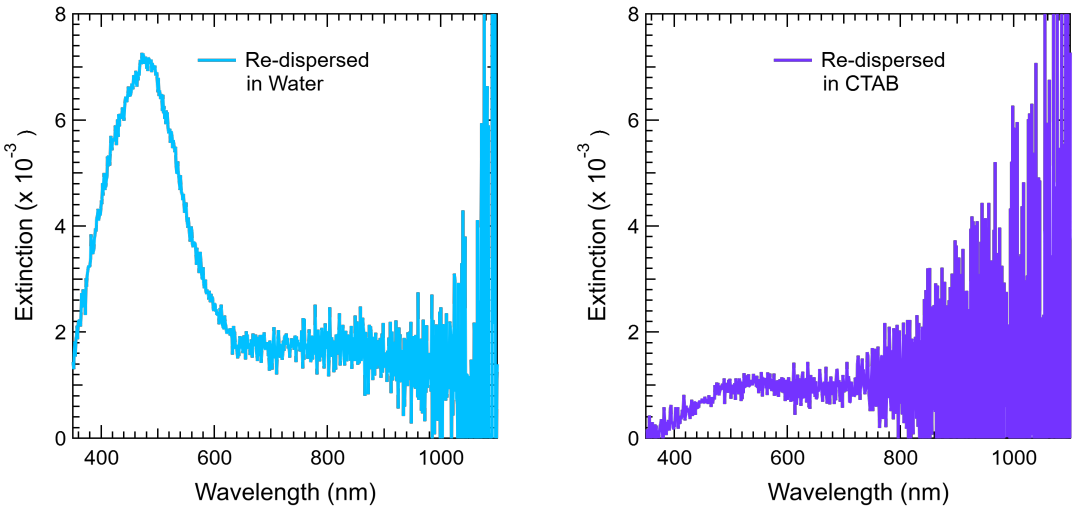


*(a) Redispersed in CTAB*

*(b) Redispersed in Type I Water*

*Figure 104: Extinction spectrum of silver nanoparticle films fabricated using the deposition method and 50 µL 44K PVP-capped seed solutions. The spectra compare films produced from particles redispersed in CTAB (10 mM) or Type I water. Films were functionalised in MPTMS for 15 minutes*

cover the substrate completely.

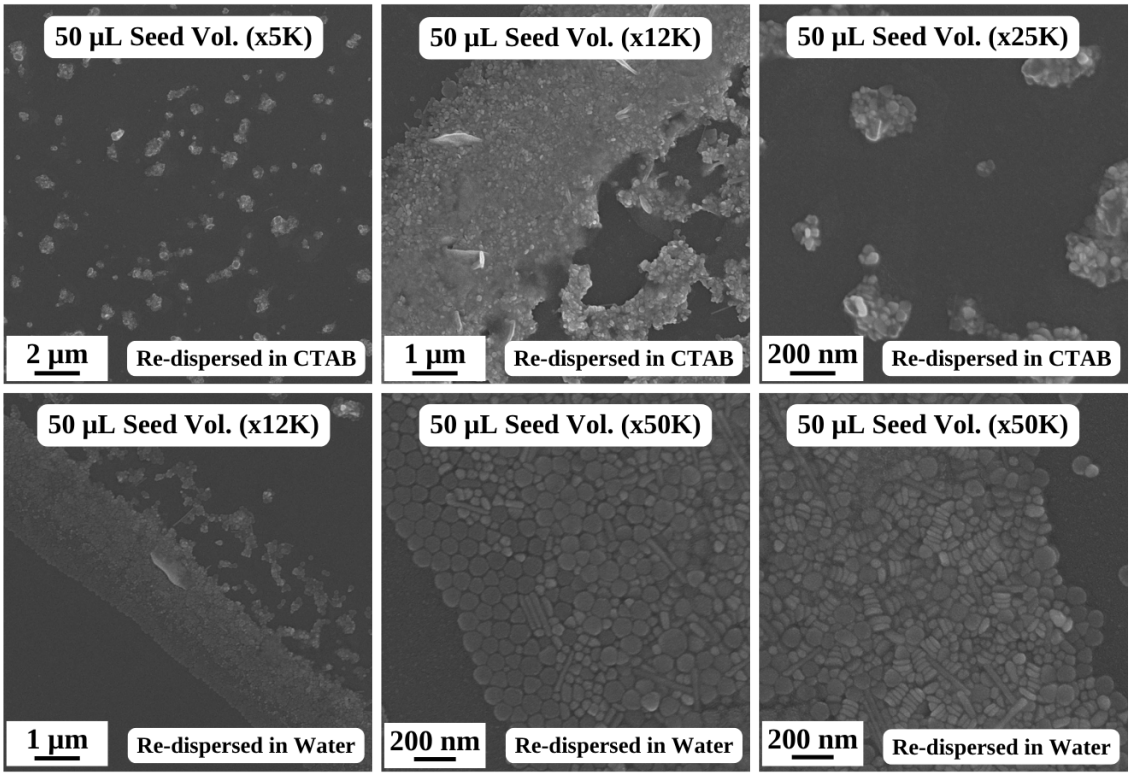


*Figure 105: SEM images of silver nanoparticle films fabricated using the deposition method using 50 µL 44K PVP-capped seed solutions. Comparing films produced from particles redispersed in CTAB (10 mM) or Type I water*

The extinction spectra of the two films are illustrated in Figure 104, while a comparison of the SEM images of the films is presented in Figure 105. The SEM images of the film created from particles redispersed in CTAB reveal the formation of island-like structures across the substrate. Immobilising the nanoparticles through a deposition method and the high concentration of CTAB caused a high degree of clumping. This clumping accounts for the minimal spectral features observed in the extinction spectrum. In contrast, the spectrum for the water particle film exhibits an intense peak in the blue-green region. This can be attributed to the high population of circular nanoplates observed in the film images. The broad nature of the peak can be attributed to plasmon coupling occurring between particles in close proximity.

The SEM images of the film produced from particles redispersed in water demonstrate the tendency for the nanoparticles to arrange side by side or in basal plate formations. The structure of the particles is viable without the excess CTAB coating. However, it is worth noting that these particles demonstrated a ring formation upon drying, unlike the island formations observed in the CTAB film, primarily due to the slow evaporation.

### 4.2.2 Discussion

The optimisation of the APTES fictionalisation process for silicon and glass substrates has been extensively researched. In contrast, the research surrounding the use of substrates functionalised with MPTMS is less extensive. Previous studies have demonstrated that MPTMS functionalisation is feasible but leads to less uniform coverage on glass substrates than APTES. Unfortunately, the positive charge on the nanoparticles synthesised for this work required a silane with a negative terminal group. This decrease in surface coverage is evident by the high surface contact angle measurements and nonuniform clustering observed in the fabricated nanoparticle films.

Marques et al. demonstrated that APTES and APTES/MUA functionalised substrates produced uniform nanoparticle films.[108] In contrast, the MPTMS functionalised substrates exhibited a significant decline in particle density. The above results also show a decrease in nanoparticle coverage on MPTMS functionalised substrates. Limited coverage and clustering in the nanoparticle films are observed at all MPTMS submersion times, resulting in a featureless spectral profile for all nanoparticle films regardless of MPTMS submersion time or nanoparticle size. The marked decrease in coverage as the MPTMS submersion time increases from 15 to 30 minutes is attributed to the formation of disulfide bonds between the available terminating thiol groups. The occurrence of these bonds decreases the possible binding locations for the nanoparticles, ultimately reducing the particle density.

The nanoparticle films fabricated with the particles redispersed in Type I water showed a similar lack of coverage. These films were fabricated using a 15-minute MPTMS submersion, the most successful method in the initial experiment. A high degree of clustering was also noticed in these nanoparticle film samples. Notably, the nanorods in the film formed bridges between the clusters of circular nanoplates. This is consistent with the findings of Kawamaru et al., who studied the different assembly configurations of nanorods at high and low CTAB concentrations.[111]

Kawamaru and co-workers discovered that at higher CTAB concentrations, the entirely capped particles were drawn to each other upon solvent evaporation due to strong interactions between the CTAB bilayers, leading to the observed clustering of the nanorods. Their investigation focused on a single particle shape, so they referred to this phenomenon as parallel self-assembly. However, in our experiments, the nanoparticle solutions contained a mixture of morphologies, with all these morphologies visible in the clusters.[111]

At lower CTAB concentrations, they observed the nanorods assembling in a more lin-

ear configuration. The authors attribute this to the lower coverage of CTAB at the tips of the nanorods, causing the negatively charged tips to be attracted to the positive charge on neighbouring particles.[111] This phenomenon is also observed in our experiments. However, the range of morphologies in these samples results in numerous configurations, with the nanorods appearing as bridges between the clusters of circular nanoplates.

This second experiment in this section compared the particle density on MPTMS functionalised glass substrates cleaned using MeOH:HCl or piranha treatment. Notably, the nanoparticles used in this series were synthesised with either 44k PVP or CTAB-capped seeds and were redispersed in either CTAB (10 mM) or Type I water. In a previous study, Cras et al. discovered that alternative cleaning protocols, such as sonication in a MeOH:HCl mixture, eliminated contaminants and hydroxylated glass substrates as effectively as a piranha cleaning protocol.[106] They confirmed their findings by comparing the surface contact angles of the substrates after the cleaning protocol and again after the MPTMS functionalisation step. They emphasised the importance of the efficacy of the cleaning protocol on the success of any functionalisation protocol, as a dirty or less hydroxylated surface can adversely affect the silane coverage.

The films fabricated with the particles redispersed in CTAB showed low extinction intensities, indicating a low particle density and coverage. Previous research, such as the study by Guo and colleagues, has demonstrated that as the concentration of CTAB increased, the observed particle density on functionalised glass substrates decreased significantly.[113] This occurs as the excess CTAB in the solution binds preferentially to the negatively charged substrate, hindering the easy deposition of the nanoparticles. However, when these identical particles were redispersed in Type I water, the particle density and extinction intensity of the films increased significantly.

The most significant increase in intensity was noted when the substrates were cleaned using the piranha protocol. In contrast, only a minor increase was observed in the films made using substrates cleaned through the MeOH:HCl protocol.

In the second phase of the experiment, two films were created by depositing the particle solution onto a flat substrate. The film made with the solution containing excess CTAB exhibited high-particle-density regions due to the formation of a thick overcoat caused by the excess CTAB. This overcoat made it challenging to obtain clear SEM images.

In contrast, the film created with a low CTAB concentration solution resulted in the nanoparticles drying down in a ring on the substrate. The low CTAB concentration altered the morphology of the particles, causing them to pack together favourably. This

packing significantly influenced the optical response of the films, with the high CTAB concentration film showing a dampened extinction intensity. In contrast, the low CTAB film produced a high-intensity sharp peak in the blue-green region of the spectrum. This peak is representative of the in-plane excitation of the circular nanoplates, indicating a densely packed monolayer in many areas of the film.

The results of these experiments suggest that MPTMS functionalisation may not be the most effective method for producing uniform monolayer nanoparticle films, as the films generated exhibited low particle density and a notable degree of clustering. This issue was especially evident in films created using nanoparticles that were redispersed in CTAB. However, as previously discussed in Section 3.5.1.1, reintroducing CTAB after the nanoparticle purification step is essential for maintaining the angularity of the nanoparticles. Consequently, alternative fabrication methods were investigated to develop a negatively charged glass substrate that would facilitate the effective immobilisation of these nanoparticles.

## 4.3 Comparison of Functionalisation Methods

The following set of experiments examined the characteristics of nanoparticle films formed using various functionalised substrates. The nanoparticles in these experiments were redispersed in either Type I water or a CTAB (10 mM) solution before film fabrication.

Incorporating CTAB into the nanoparticle solutions after purification is essential for preserving the angularity of the nanoparticles. Redispersion in Type I water leads to truncation of particles; this observation is previously discussed in section 3.5.1.1. However, it has been previously shown that excess CTAB in the nanoparticle solution tends to bind preferentially to the functionalised substrates, thereby disrupting particle adhesion to the substrate.[111] Therefore, this set of experiments also aimed to evaluate whether the addition of NaCl and the resulting change in ionic strength could facilitate the adhesion of particles to the substrate. This approach has been previously reported to have successfully immobilised CTAB-capped gold nanorods on hydroxylated glass substrates.[109]

### 4.3.1 Results

#### 4.3.1.1 Comparison of Substrate Functionalisation Molecules

The study compared substrates hydroxylated by piranha solution cleaning with those functionalised using MPTMS or APTES/PSS. Two substrates were used for each series, and they were immersed in nanoparticle solutions created with either 50 µL (Film 1) or

300 µL (Film 2) of 44K PVP-capped seeds redispersed in Type I water.

| Functionalization | Contact (Â°) |
|---|---|
| Piranha | 19.29 |
| MPTES | 77.69 |
| APTES | 55.99 |
| APTES/PSS | 34.43 |

*Table 20: Average surface contact angle measurements for functionalised glass substrates*

The surface contact angle measurement for each substrate was used to confirm the successful modification of the substrate. The surface contact angle measurements for each substrate are presented in Table 20.

This experiment investigated four sets of nanoparticle films. Set 1 (a) served as a baseline for comparison and utilised a piranha-cleaned substrate without further modification or addition to the nanoparticle suspension. Sets 2 (b) and 3 (c) used an APTES/PSS or MPTMS functionalised substrate, respectively, with the addition of NaCl (20 mM). The NaCl was introduced to investigate the influence of changing the ionic strength of the nanoparticle suspension on the immobilisation efficiency. Set 4 (d) used an MPTMS

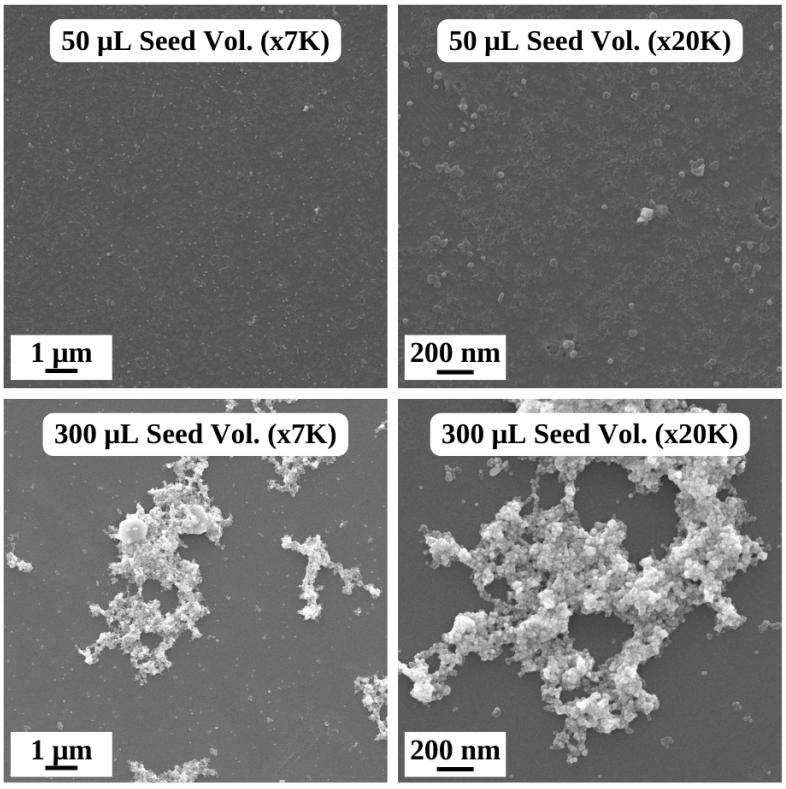


*Figure 106: SEM images of silver nanoparticle films fabricated using 50 or 300 µL 44K PVP-capped seed solutions and APTES/PSS functionalised glass substrates. Particles were redispersed in Type I water, and NaCl (20 mM) was introduced before fabrication*

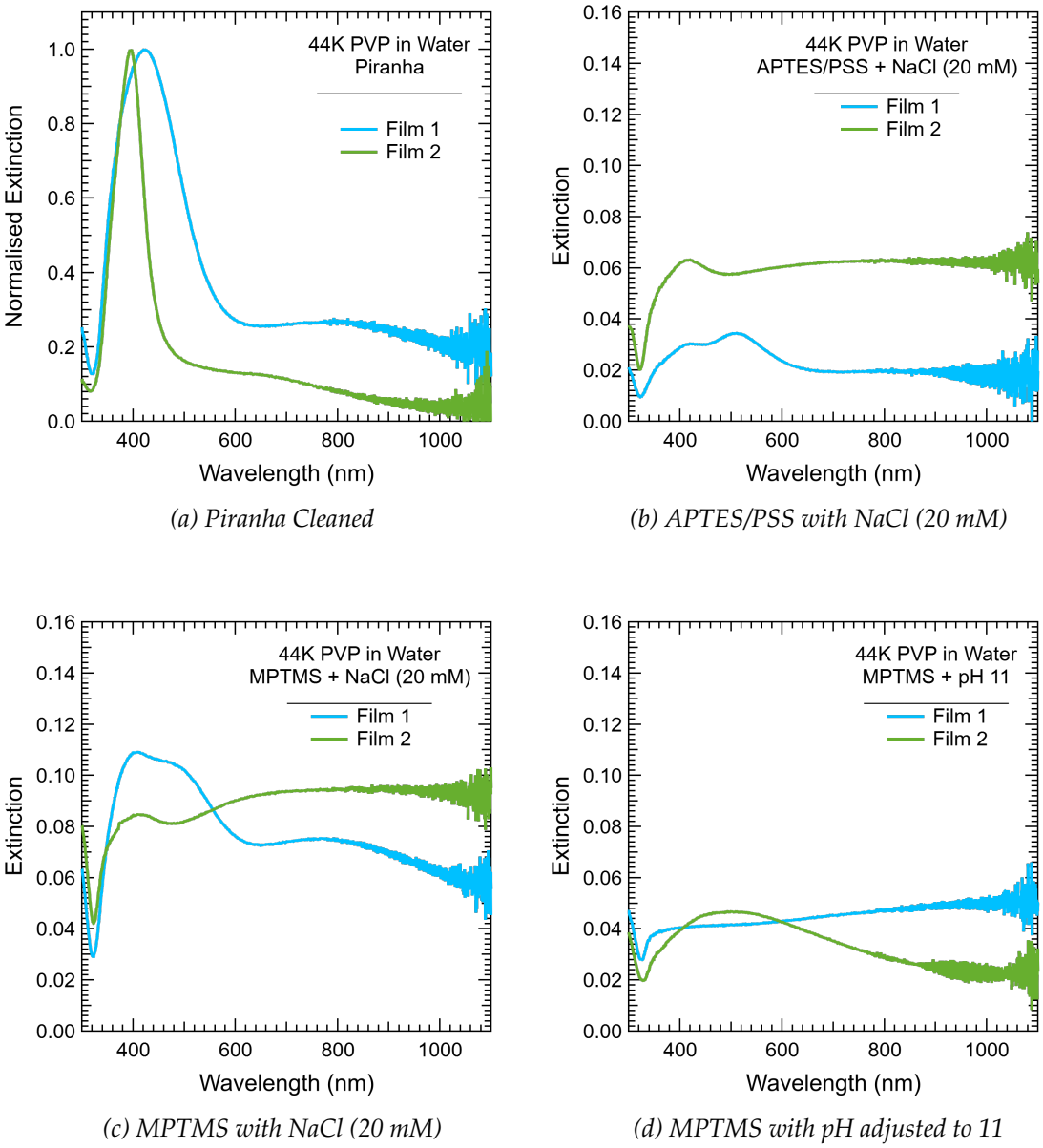


*(a) Piranha Cleaned*

*(b) APTES/PSS with NaCl (20 mM)*

*(c) MPTMS with NaCl (20 mM)*

*(d) MPTMS with pH adjusted to 11*

*Figure 107: Extinction spectra of silver nanoparticle films fabricated using 50 µL (Film 1) or 300 µL (Film 2) 44K PVP-capped seed solutions and various substrate functionalisation conditions. Particles were redispersed in Type I water before fabrication*

functionalised substrate with the addition of sodium hydroxide (NaOH). The NaOH was introduced to investigate the influence of increasing the pH of the nanoparticle suspension on the immobilisation efficiency. The extinction spectra for each set are shown in Figure 107.

The SEM images of the APTES/PSS functionalised films are presented in Figure 106. These images indicated that while the APTES/PSS functionalised substrate adhered to some particles, it did not yield the same monolayer on nanoparticles as achieved by a piranha cleaned substrate. Notably, the film produced using the particle solution with

300 µL of 44K PVP-capped seeds exhibited a significant amount of clustering. This clustering accounts for the observation of an ill-defined spectral profile.

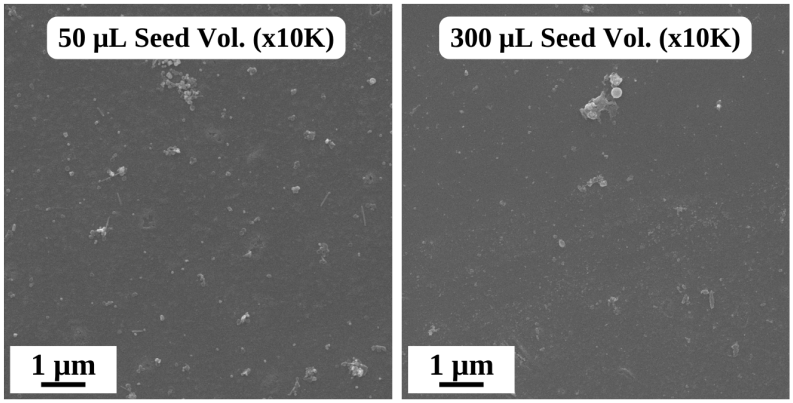


*Figure 108: SEM images of silver nanoparticle films fabricated using 50 or 300 µL 44K PVP-capped seed solutions and MPTMS functionalised glass substrates. Particles were redispersed in Type I water, and NaCl (20 mM) was introduced before fabrication*

The SEM images of the films produced using MPTMS functionalised substrates with a 20 mM NaCl introduction are displayed in Figure 108. These images reveal a mix of high and low particle density on the films. In the case of the film made with a 50 µL nanoparticle solution, numerous circular plates and rods are visible on the substrate, along with some evidence of clustering. These observations account for the spectral profile, which features a broad and shouldered peak in the blue-green region. The optical response diminishes across the visible and near-infrared regions, influenced by the clustering throughout the film. Overall, the particle density on these films is low compared to the density observed on other substrates in this experiment.

SEM images of the films produced using MPTMS functionalised substrates and nanopar-

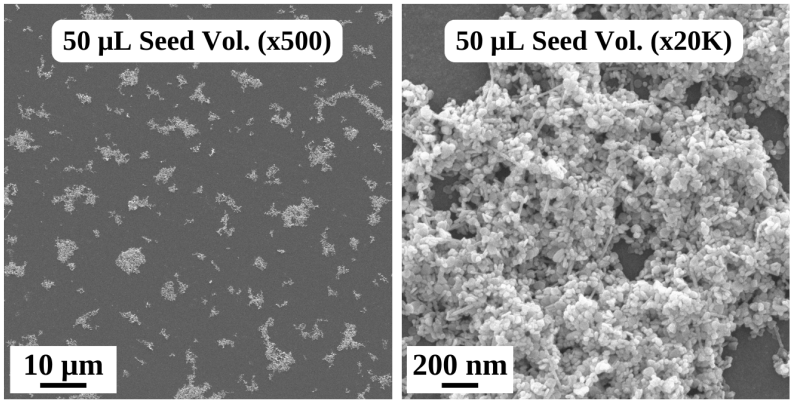


*Figure 109: SEM images of silver nanoparticle films fabricated using 50 or 300 µL 44K PVP-capped seed solutions and MPTMS functionalised glass substrates. Particles were redispersed in Type I water, and the solution pH was increased to 11 before fabrication*

ticle solutions subjected to a pH increase to pH 11 are shown in Figure 109. The pH increase led to more particles adhering to the film, but a monolayer was not achieved. Instead, numerous large clusters were evident across the substrate. These clusters comprised a mix of circular nanoplates, nanorods, and spherical particles. Similarly to the film sets that incorporated NaCl, the increase in pH has caused the nanoplates to truncate. A high degree of clustering is also observed, as reflected in the ill-defined spectral profile.

#### 4.3.1.2 Particles Redispersed in Type I Water with NaCl on Piranha-Cleaned Substrates

In the following four experiments, the efficacy of modifying the NaCl concentration in the fabrication process was examined. In the initial experiment, the nanoparticles were redispersed in Type I water and fabricated on piranha-cleaned substrates. Each nanoparticle solution was prepared using 50 µL of 44K PVP-capped seeds, with the final NaCl concentration being increased from 20-40 mM in 10 mM increments.

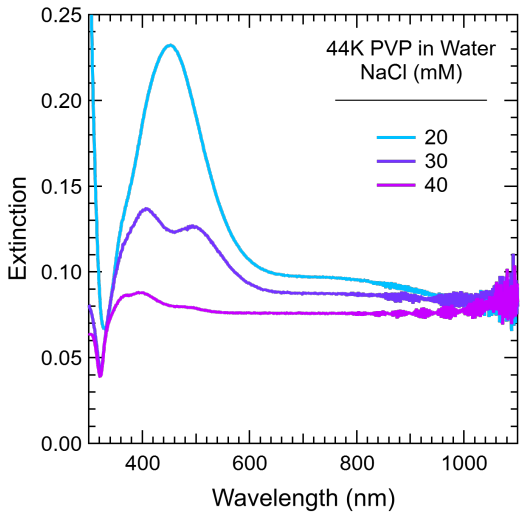


*Figure 110: Extinction spectrum of silver nanoparticle films fabricated using 50 µL 44K PVP-capped seed solutions and piranha cleaned glass substrates. Particles were redispersed in Type I water, and increasing concentrations of NaCl were introduced before fabrication*

The extinction spectra for the three fabricated films are displayed in Figure 110, while the corresponding SEM images are presented in Figure 111. The SEM images revealed that the film with the lowest NaCl concentration, 20 mM, formed a monolayer with a high particle density. As the NaCl concentration increased, this density notably decreased.

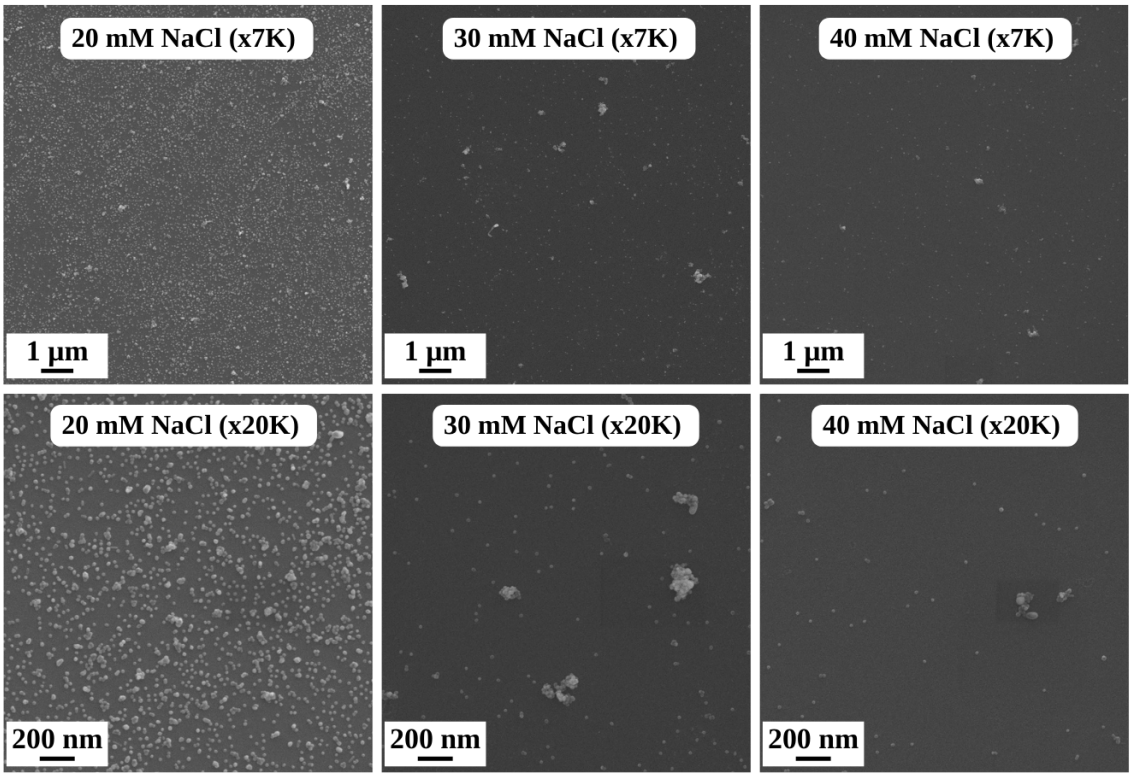


*Figure 111: SE images of silver nanoparticle films fabricated using 50 µL 44K PVP-capped seed solutions and piranha cleaned glass substrates. Particles were redispersed in Type I water, and increasing concentrations of NaCl were introduced before fabrication*

A decline in the intensity of the resonance peak in the blue-to-yellow spectral region accompanies this reduction in particle density. A prominent peak is evident for the film with a NaCl concentration of 20 mM, with a maximum extinction at 450 nm. This peak undergoes a blue-shift as the NaCl concentration rises, coinciding with a decrease in the size of the visible particles. Additionally, an increase in clustering is observed with an elevated NaCl concentration, contributing to the shoulder and extended tail into the NIR region, which is noticeable in the spectra of the higher NaCl concentration films.

#### 4.3.1.3 Particles Redispersed in CTAB (10 mM) with NaCl on Piranha-Cleaned Substrates

The nanoparticles were redispersed in a CTAB (10 mM) solution and fabricated on piranha-cleaned substrates in the second experiment. Each nanoparticle solution was prepared using 50 µL of 44K PVP-capped seeds, with the final NaCl concentration being increased from 60-120 mM in 20 mM increments.

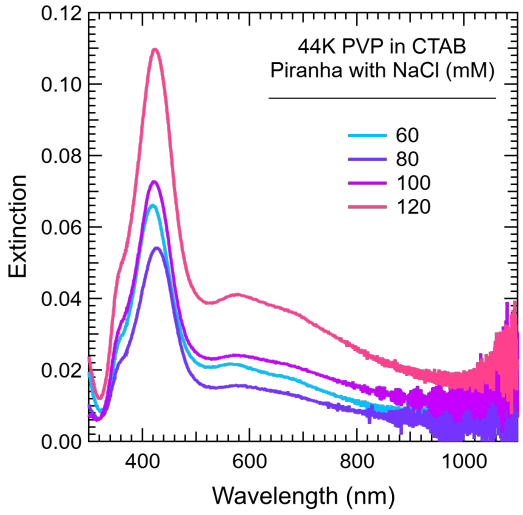


*Figure 112: Extinction spectrum of silver nanoparticle films fabricated using 300 µL 44K PVP-capped seed solutions and piranha cleaned glass substrates. Particles were redispersed in CTAB (10 mM), and increasing concentrations of NaCl were introduced before fabrication*

The extinction spectra for the four fabricated films are presented in Figure 112, while the corresponding SEM images are depicted in Figure 113. It is evident from the SEM images that the particle density on the substrates exhibits a significant increase as the NaCl concentration is increased. This observed increase in density accounts for the amplified intensity of the optical response, as portrayed in the extinction spectra, when the NaCl concentration is increased.

All four films display a combination of nanorods and circular nanoplates, but none show triangular nanoplates. The previous chapter highlighted the dominant production of triangular nanoplates under these synthetic conditions. However, introducing NaCl decreases the angularity of these particles, leaving only circular nanoplates. This explains the blue-shift of the primary resonance peak observed in the extinction spectra of the films in contrast to the particles in the suspension.

The tail that stretches across the visible and into the NIR corresponds to the plasmon coupling attainable with a monolayer film; its relative intensity escalates as the particle density increases and more particle-to-particle interactions become available.

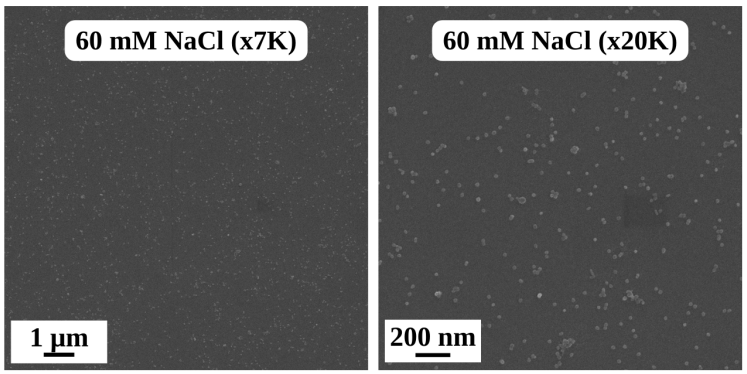


*(a) 60 mM NaCl*

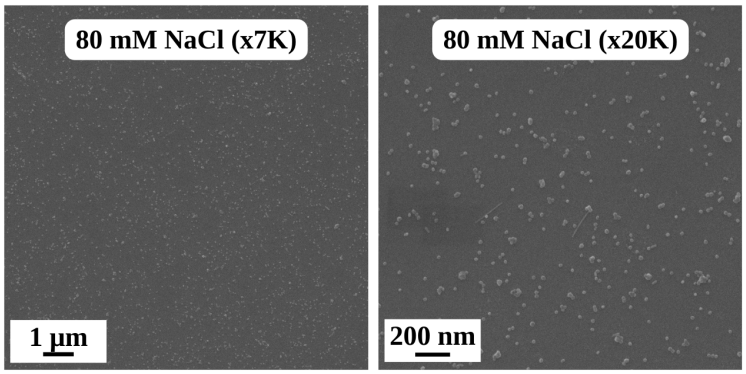


*(b) 80 mM NaCl*

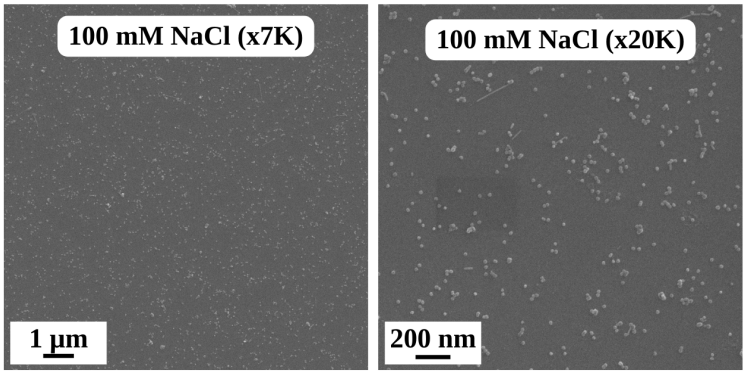


*(c) 100 mM NaCl*

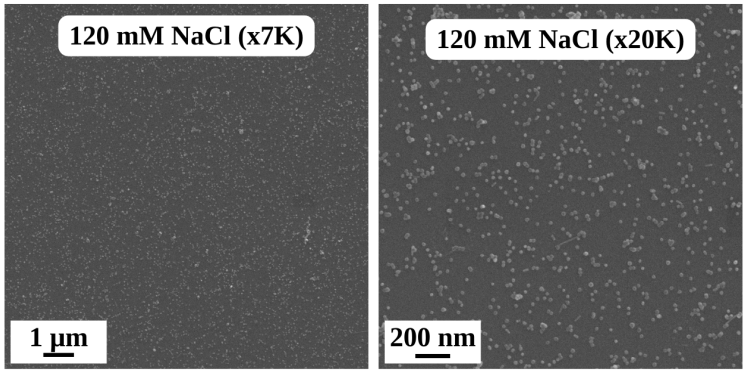


*(d) 120 mM NaCl*

*Figure 113: SEM images of silver nanoparticle films fabricated using 300 µL 44K PVP-capped seed solutions and piranha cleaned glass substrates. Particles were redispersed in CTAB (10 mM), and increasing concentrations of NaCl from 60-120 mM were introduced before fabrication*

#### 4.3.1.4 Particles Redispersed in CTAB (10 mM) with NaCl on APTES/PSS Substrates

In the third experiment, the particles were once again redispersed in CTAB (10 mM). Following this, the piranha-cleaned substrates underwent additional modification with APTES and PSS. Each nanoparticle solution was prepared using 50 µL of 44K PVP-capped seeds, with the final NaCl concentration being increased from 60-120 mM in 20 mM increments.

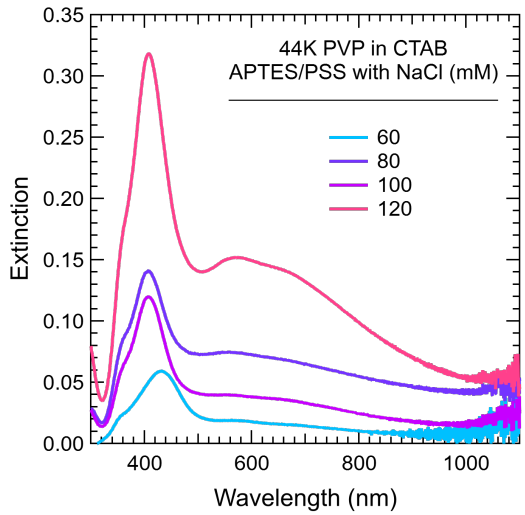


*Figure 114: Extinction spectrum of silver nanoparticle films fabricated using 300 µL 44K PVP-capped seed solutions and APTES/PSS functionalised glass substrates. Particles were redispersed in CTAB (10 mM), and increasing concentrations of NaCl were introduced before fabrication*

The extinction spectra for the four fabricated films are depicted in Figure 114, while the corresponding SEM images are displayed in Figure 115. The SEM images substantiate the findings from the preceding experiment, indicating a rise in particle density with an increase in NaCl concentration. When the piranha cleaned substrates are substituted for APTES/PSS functionalised substrates, the particle density across the series increases. A minor rise in clustering on the film is also observed.

Notably, the particles in the film exhibit a combination of nanorods and circular plates, which further supports the findings from the previous experiment, which is that the addition of NaCl reduces the angularity of the previously stable nanoparticles. A uniform blue-shift in the primary resonance peak is noticeable in the film extinction spectra compared to the particles in suspension. Additionally, a significant increase in intensity is observed compared to the films produced with piranha-cleaned substrates, validating the observed rise in particle density.

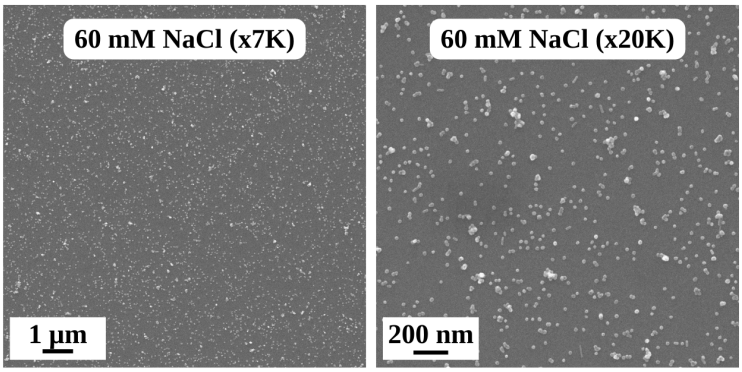


*(a) 60 mM NaCl*

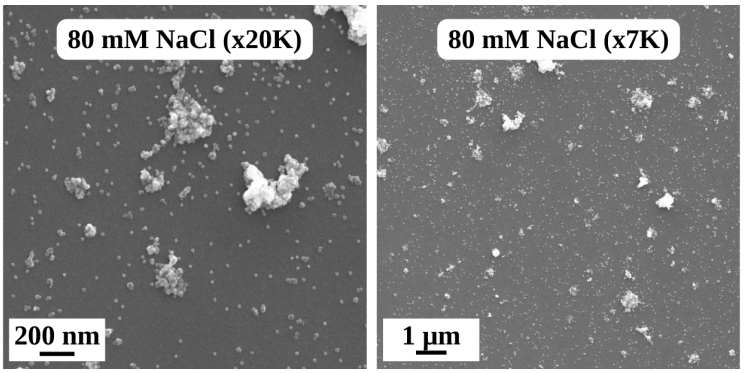


*(b) 80 mM NaCl*

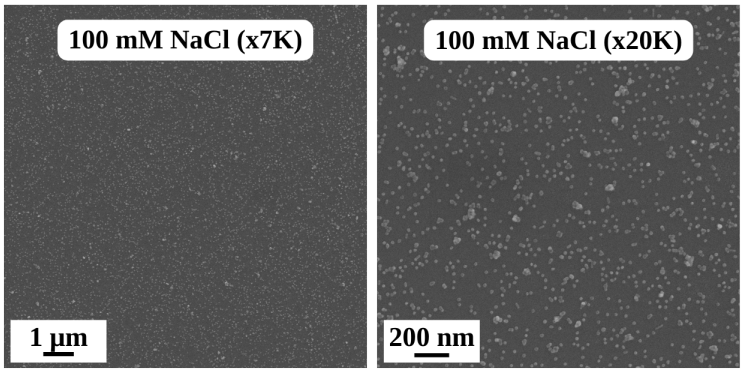


*(c) 100 mM NaCl*

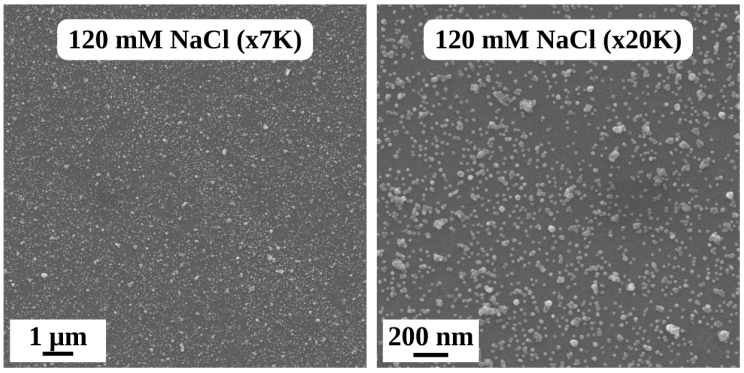


*(d) 120 mM NaCl*

*Figure 115: SEM images of silver nanoparticle films fabricated using 300 µL 44K PVP-capped seed solutions and APTES/PSS functionalised glass substrates. Particles were redispersed in CTAB (10 mM), and increasing concentrations of NaCl were introduced before fabrication*

#### 4.3.1.5 Particles Redispersed in CTAB (10 mM) with NaCl on MPTMS Substrates

The particles were again dispersed in CTAB (10 mM) for the final experiment. However, in this experiment, the substrates were functionalised with MPTMS. Each nanoparticle solution was prepared using 50 µL of 44K PVP-capped seeds, with the final NaCl concentration being increased from 60-120 mM in 20 mM increments.

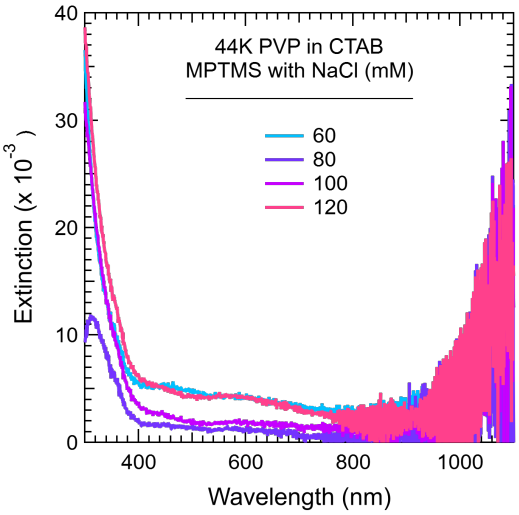


*Figure 116: Extinction spectrum of silver nanoparticle films fabricated using 300 µL 44K PVP-capped seed solutions and MPTMS functionalised glass substrates. Particles were redispersed in CTAB (10 mM), and increasing concentrations of NaCl were introduced before fabrication*

The extinction spectra for the four fabricated films are depicted in Figure 116, and the SEM images of two of the corresponding films are displayed in Figure 117. The SEM images validate that the particle density of these films is the lowest among the three investigated functionalised substrates. A final concentration of 60 mM NaCl resulted in a

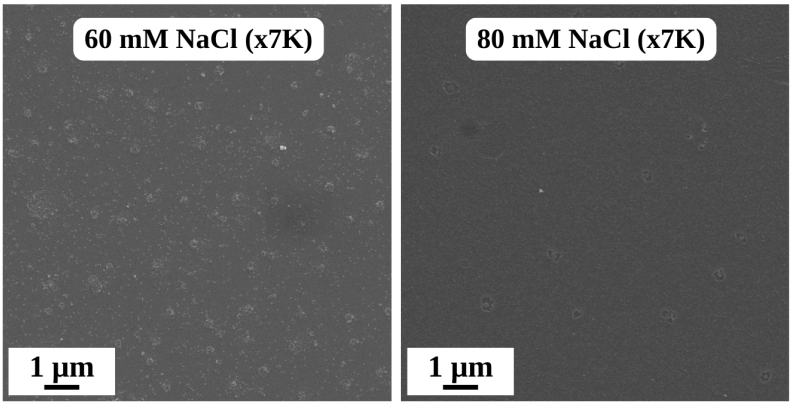


*Figure 117: SEM images of silver nanoparticle films fabricated using 300 µL 44K PVP-capped seed solutions and MPTMS functionalised glass substrates. Particles were redispersed in CTAB (10 mM), and increasing concentrations of NaCl were introduced before fabrication*

film with small clusters of nanoparticles with a high particle proximity. An increase in concentration to 80 mM resulted in a sharp decrease in particle density. This low particle density is apparent in the extinction spectra, as indicated by the low intensity and ill-defined spectral profile. This limited nanoparticle immobilisation on MPTMS functionalised substrates has been observed in previous experiments in this chapter.

### 4.3.2 Discussion

The successful modification of the glass substrates was confirmed using surface contact angle measurements. An average angle of 19.29 ° was observed for the piranha-cleaned substrates, which is higher than the reported average of 11.1 ° . This measurement suggests some substrate regions may not have been effectively hydroxylated. The functionalisation of the hydroxylated substrates with MPTMS, ATPES, or APTES/PSS resulted in a significant increase in contact angle. The average contact angle measurement of 55.99 ° for APTES is slightly lower than the reported average, while the recorded measurement of 77.69 ° for MPTMS is higher. A significant decrease to 34.43 ° was observed for the APTES-modified substrates grafted with PSS. This decline is consistent with the findings of Haddada and co-workers, who attributed the decrease in contact angle measurement to the increased hydrophilic nature resulting from the longer chain length.

In the initial series of experiments, we compared the particle density and optical response of large and small nanoparticles redispersed in Type I water and immobilised onto hydroxylated substrates or MPTMS or APTES/PSS functionalised substrates. Our findings confirmed that substrates hydroxylated using the piranha cleaning protocol produce the intended monolayer nanoparticle film. Additionally, we observed that with this fabrication protocol, the extinction resonance can be tuned across the spectrum by increasing the size of the nanoparticles. A minor red-shift in the extinction resonance peak was noted with an increase in particle size.

Similarly to the previous experiments in this chapter, the films fabricated with MPTMS functionalised substrates showed a significantly lower particle density than those with hydroxylated substrates. This is reflected in low particle numbers observed in the SEM images and low intensity observed in the extinction spectra for this series. Once again, we attribute this decrease in particle immobilisation to the formation of disulfide bonds between the termination thiol groups and a decreased binding strength induced by the increased flexibility of the MPTMS chain.

The introduction of NaCl into the fabrication protocol resulted in a change in the

ionic strength of the nanoparticle suspension. This caused the particles in suspension to aggregate, limiting the number of particles available for deposition. The NaCl caused the CTAB molecules, which were stabilising the nanoparticles, to desorb. This decrease in nanoparticle stability is evident by the significant morphology changes and aggregation observed in these films.

Incorporating NaOH into the fabrication protocol decreased the pH of the nanoparticle solution to 11. This decrease in pH resulted in an increase in particle density within the film. However, this pH shift also led to a high degree of particle clustering. Both of these series suggest that incorporating NaCl or NaOH is not a practical solution for optimising the fabrication of monolayer nanoparticle films on MPTMS functionalised substrates.

The second experiment focused on fabricating films using nanoparticles redispersed in Type I water deposited onto hydroxylated substrates. The NaCl concentration was increased for each film. The SEM images and extinction spectra confirmed that when NaCl concentrations exceeded 20 mM, the rapid desorption of CTAB from the nanoparticle surface and increased inter-particle attractive forces led to particle aggregation and limited deposition.

The opposite effect was observed when the nanoparticles were redispersed in CTAB. Our findings align with previous reports by Ferhan and co-workers.[109] At high CTAB concentrations, the addition of NaCl resulted in the formation of a negative shield around the particles by the salt anions, increasing inter-particle attractive forces and facilitating deposition. With further increases in NaCl concentration, the number of particles deposited on the functionalised surface also increased. This was confirmed by a notable increase in the number of particles observed in the SEM images and the rise in extinction intensity.

The SEM images confirmed that the CTAB-capped nanoparticle films fabricated on hydroxylated glass substrates resulted in a monolayer of nanoparticles with good particle density. The use of an APTES/PSS substrate in the fabrication protocol resulted in a significant increase in particle density. This was attributed to the more hydrophilic surface and high negative charge. The increase in particle density increased the intensity of the extinction spectra. Similarly to the previous series of experiments, where the nanoparticles were redispersed in Type I water, films fabricated on MPTMS functionalised substrates did not produce uniform monolayer particle films. The SEM images and extinction spectra confirmed that this fabrication method resulted in low particle

density with limited coverage.

These experiments demonstrated that the highest particle density was achieved using APTES/PSS functionalised substrates. However, the film fabricated on hydroxylated substrates also produced a monolayer nanoparticle film with high particle density. The increase in particle density was not significant enough to warrant the increased complexity required for the fabrication of APTES/PSS substrates. As a result, it was decided that all further experiments would be conducted on hydroxylated glass substrates without further modification.

## 4.4 Nanoparticle Immobilisation on Hydroxylated Substrates

This series of experiments compares the immobilisation of a range of nanoparticle solutions onto hydroxylated glass substrates prepared using a piranha cleaning protocol.

### 4.4.1 Results

#### 4.4.1.1 Particles Redispersed in CTAB

The first series of experiments was conducted to identify the most effective method for introducing NaCl into the fabrication process, aiming to achieve a monolayer nanoparticle film while maintaining the stability of the nanoparticles in suspension.

For each experiment, six nanoparticle films were produced on a hydroxylated glass

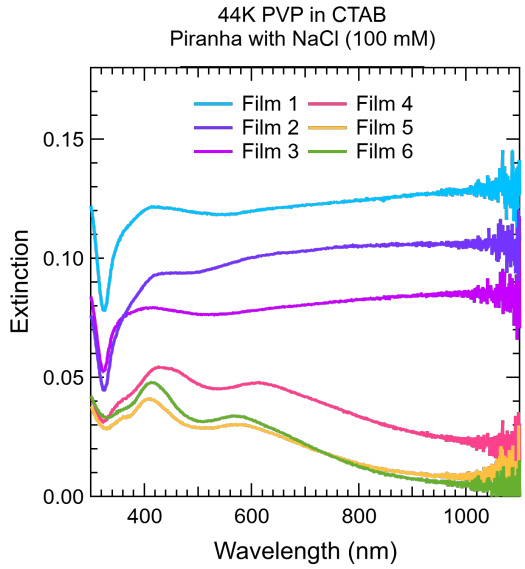


*Figure 118: Extinction spectrum of silver nanoparticle films fabricated using solutions with increasing 44K PVP-capped seeds from 50-300 µL in 50 µL increments (Film 1-6). The glass substrates were piranha cleaned. Particles were redispersed in CTAB (10 mM), and NaCl (100 mM) was introduced before fabrication*

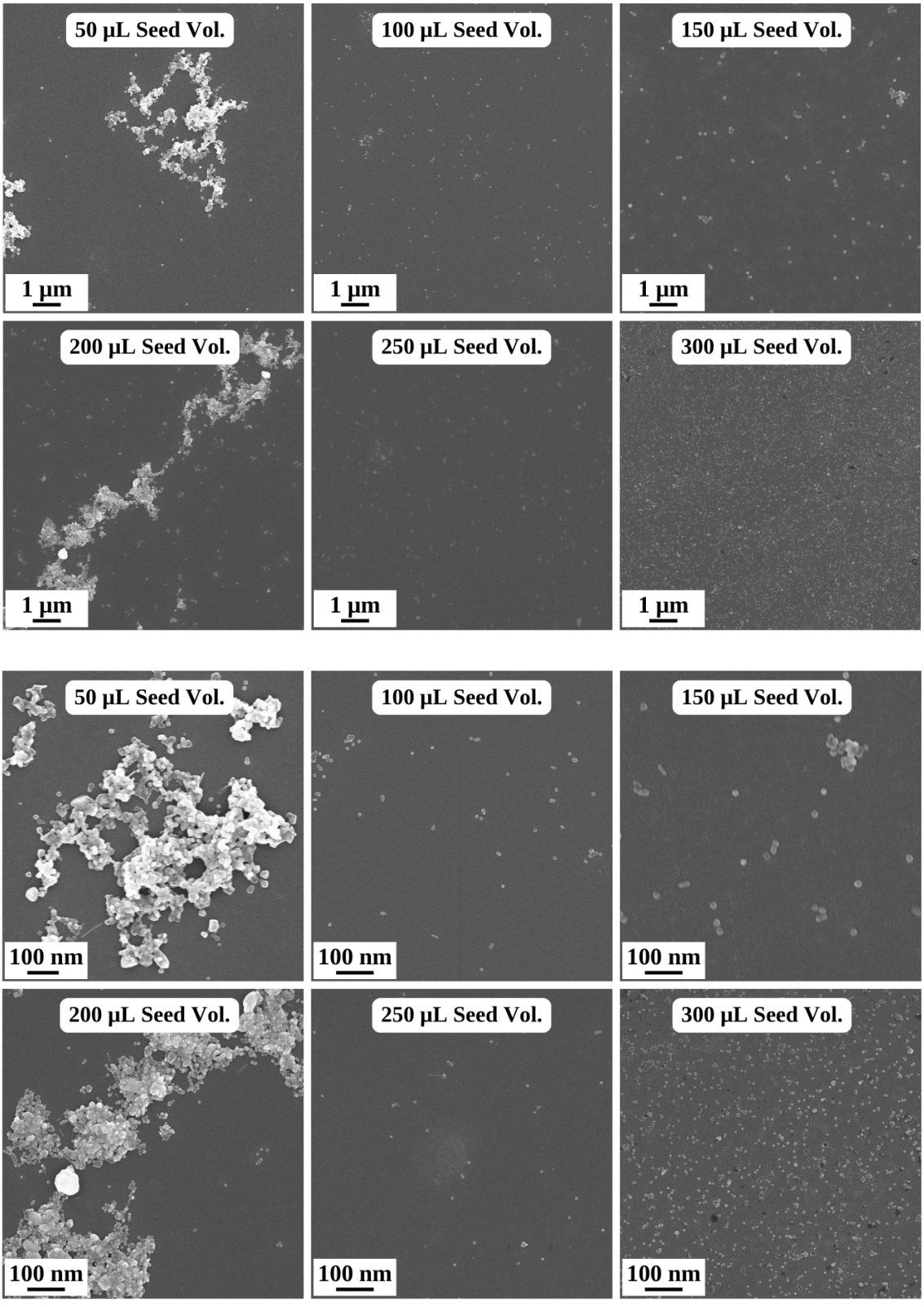


*Figure 119: SEM images of silver nanoparticle films fabricated using solutions with increasing 44K PVP-capped seeds from 50-300 µL in 50 µL increments. The glass substrates were piranha cleaned. Particles were redispersed in CTAB (10 mM), and NaCl (100 mM) was introduced before fabrication*

substrate. Each of the six substrates was immersed in nanoparticle solutions overnight, which were created with increasing volumes of 44K PVP-capped seeds, ranging from 50-300 µL in 50 µL increments. The particles were redispersed in CTAB (10 mM) before fabrication, and varying volumes and concentrations of NaCl were added to the nanoparticle solution before the substrate was introduced to alter the ionic strength of the solution.

For the first experiment, a final NaCl concentration of 100 mM was introduced to each nanoparticle solution in a 1:1 volume ratio of nanoparticle solution to NaCl solution. The extinction spectra for the six fabricated films are displayed in Figure 118, with the corresponding SEM images presented in Figure 119. The SEM images show a noticeable degree of clustering, particularly in films 1-4, which accounted for the absence of features in the spectral profile. This clustering decreased in the 250 and 300 µL seed volume films.

This change to a monolayer film was reflected in a significant difference in the spectral profile. Notably, two distinct peaks are present in the blue-to-yellow region of the spectra, with the peaks being prominently defined in the 300 µL seed volume film. The SEM images depict the high particle density of this film. Indicating potential plasmon coupling occurring from the significant number of particles in near-field proximity.

The previous experiment revealed significant clustering and degradation, indicating that the addition of NaCl in a 1:1 volume led to a substantial decrease in CTAB concentration, consequently affecting the stability of the particles. To address this issue, a

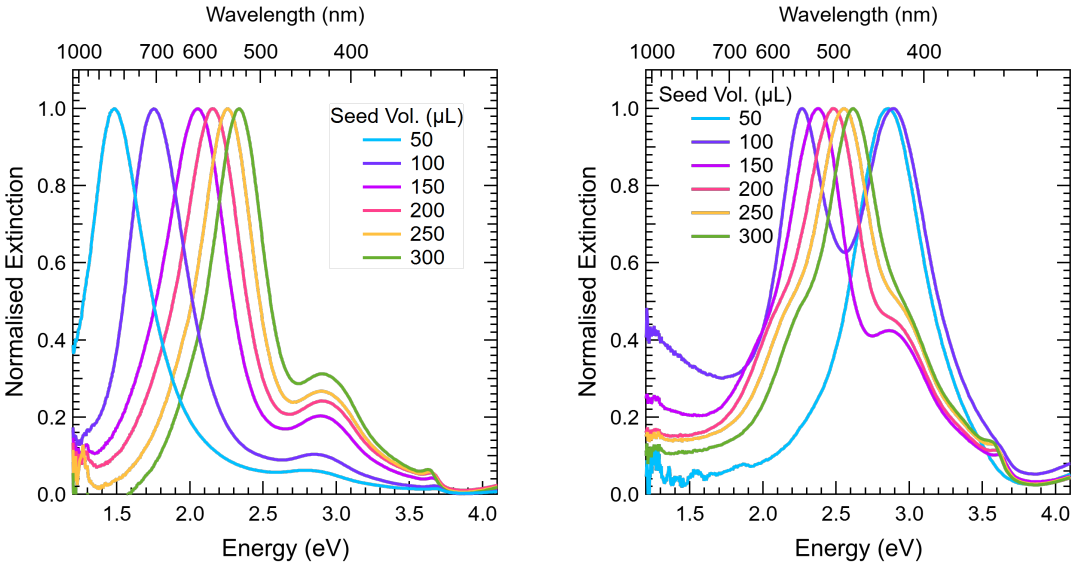


*(a) Without NaCl*

*(b) With NaCl (100 mM)*

*Figure 120: Normalised extinction spectra of silver nanoparticle solutions with increasing 44K PVP-capped seeds from 50-300 µL in 50 µL increments, with and without NaCl (100 mM) introduced*

follow-up experiment was conducted with all parameters held constant except for the volume of NaCl. In this subsequent experiment, the final NaCl concentration in each solution was adjusted to 100 mM by adding 500 µL of 2.1 M NaCl.

The normalised extinction spectra shown in Figure 120 compare the nanoparticle solutions with and without the addition of NaCl. There is a significant blue-shift in the SPR peak maximum in all samples after the addition. Furthermore, the spectral profile changes to resemble the extinction spectra when these particles are redispersed in Type I water. This suggests that the addition of NaCl adversely affects the stability achieved by the post-production CTAB addition. Figure 121 below presents the extinction spectra of the films produced using these solutions.

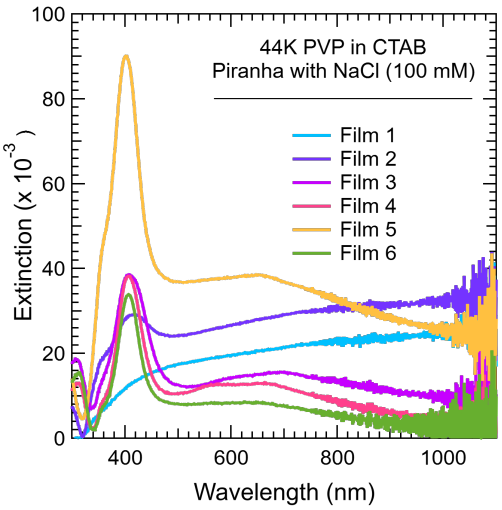


*Figure 121: Extinction spectrum of silver nanoparticle films fabricated using solutions with increasing 44K PVP-capped seeds from 50-300 µL in 50 µL increments (Film 1-6). The glass substrates were piranha cleaned. Particles were redispersed in CTAB (10 mM), and NaCl (100 mM) was introduced before fabrication*

These spectra exhibit a similar profile to films fabricated on piranha-cleaned slides using particle solutions redispersed in Type I water. A distinct sharp peak in the blue-green region of the spectrum is observed, with a tail extending across the remaining visible and NIR regions. The resemblance to the films produced with particles redispersed in Type I water suggests that small circular nanoplates significantly contribute to the extinction spectral profile.

In the previous experiment, it was observed that maintaining a consistent solution volume after adding NaCl had a less detrimental effect compared to adding NaCl in a 1:1 ratio. Nonetheless, the 100 mM concentration still resulted in a decrease in the stability of the CTAB-stabilised particles. A final experiment was conducted to determine the

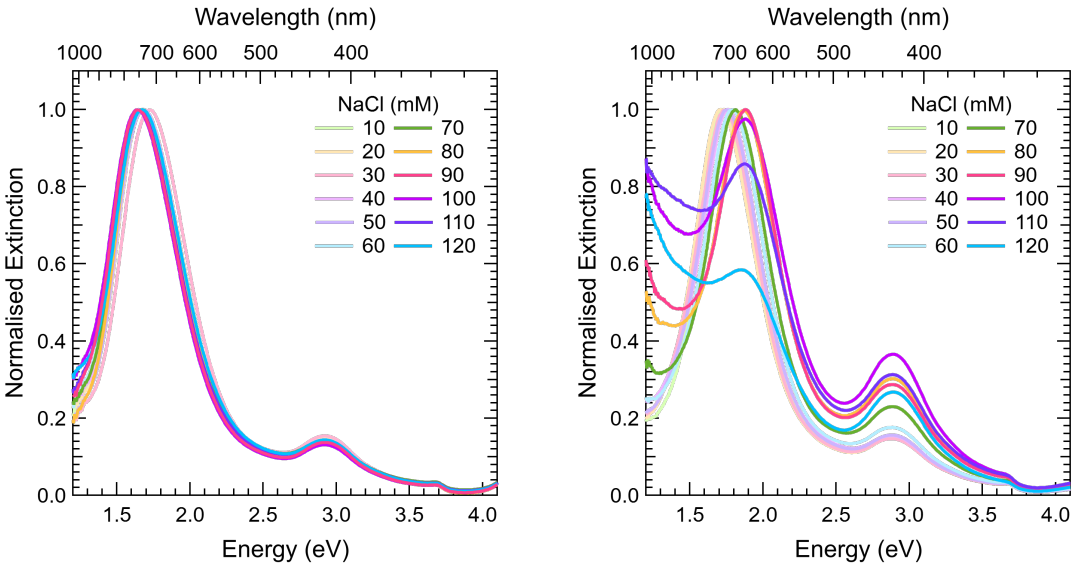


*(a) Without NaCl* *(b) With NaCl (10-120 mM)*

*Figure 122: Normalised extinction spectra of silver nanoparticle solutions produced from 150 µL of 44K PVP-capped seeds. With and without increasing NaCl concentrations introduced, from 10-120 mM*

NaCl concentration that would promote particle adhesion without adversely impacting the stability of the nanoparticles.

For this experiment, 12 nanoparticle solutions were synthesised and redispersed in CTAB (10 mM) using 150 µL of 44K PVP-capped seeds. The NaCl concentration was increased from 10 to 120 mM in 10 mM increments. The extinction spectra comparing the solutions with and without the NaCl addition are presented in Figure 122.

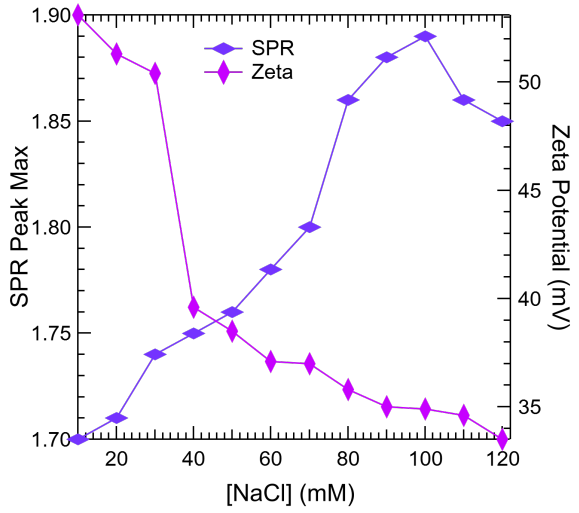


*Figure 123: Comparison of SPR peak shifts and zeta potential values of silver nanoparticle solutions produced from 150 µL of 44K PVP-capped seeds, with increasing NaCl concentrations from 10-120 mM*

The extinction spectra of the particle redispersed in CTAB exhibit excellent reproducibility, with the SPR peak averaging 1.66 $\pm$ 0.07 eV (775 nm). Upon the addition of NaCl, there is a noticeable blue-shift in the SPR peak. This blue-shift becomes more pronounced at higher NaCl concentrations. The resulting SPR peak energy and zeta potential value at each NaCl concentration are depicted in Figure 123.

The data reveals that the zeta potential values decrease rapidly as the NaCl concentration increases, accompanying the observed blue-shift in the SPR peaks. This indicates that higher NaCl concentrations lead to a greater reduction in nanoparticle stability and a more significant decrease in angularity. The most substantial shift in zeta potential value occurs with the introduction of 40 mM NaCl, where the zeta potential value decreases from 54 to 39 mV. This value continues to decline as the NaCl concentration increases, reaching 33.2 eV at a NaCl concentration of 120 mM.

The spectral profile also changes with higher NaCl concentrations. The spectra indicate a decrease in the relative intensity of the maximum SPR peak, accompanied by the formation of a secondary, more intense peak in the NIR region. This observation suggests substantial degradation of the triangular nanoplates at higher NaCl concentrations,

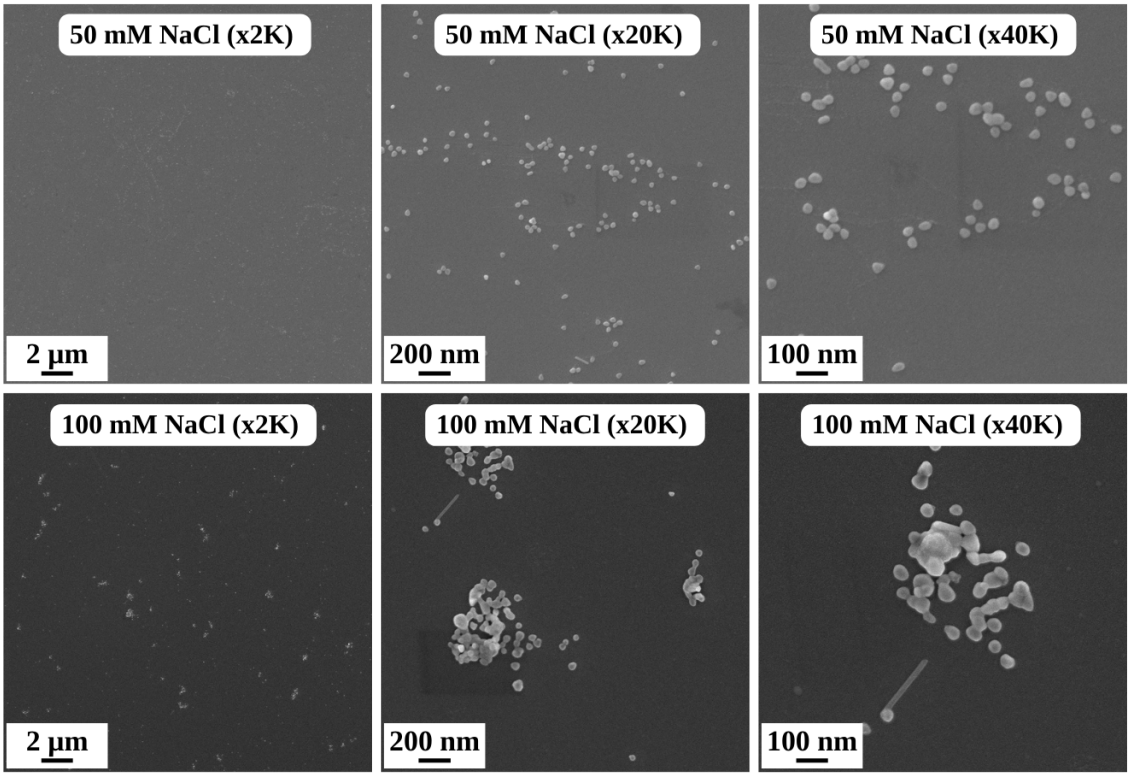


*Figure 124: SEM images of silver nanoparticle films fabricated using solutions made with 150 µL of 44K PVP-capped seeds. The glass substrates were piranha cleaned. Particles were redispersed in CTAB (10 mM) and incorporated at a final concentration of 50 mM (top row) or 100 mM (bottom row) NaCl introduced before fabrication*

leading to the formation of agglomerating clusters.

This is further supported by the SEM images provided in Figure 124. The images compare films created using particle solutions with final NaCl concentrations of 50 mM and 100 mM. The 50 mM concentration resulted in a monolayer film with particles exhibiting greater angularity compared to the film produced at the 100 mM concentration. At the higher concentration, the particles merge, giving rise to large clusters with limited shape and size distinction as observed in Figure 124

A final filming process was conducted to investigate further the impact of reducing the NaCl concentration on the fabrication outcome. In this experiment, six piranha-cleaned substrates were immersed in nanoparticle solutions created using increasing 44K PVP-capped seed volumes ranging from 50 to 300 µL in 50 µL increments. The particles were redispersed in CTAB (10 mM), and the NaCl concentration was adjusted to 50 mM by adding 250 µL of 2.1 M NaCl before fabrication.

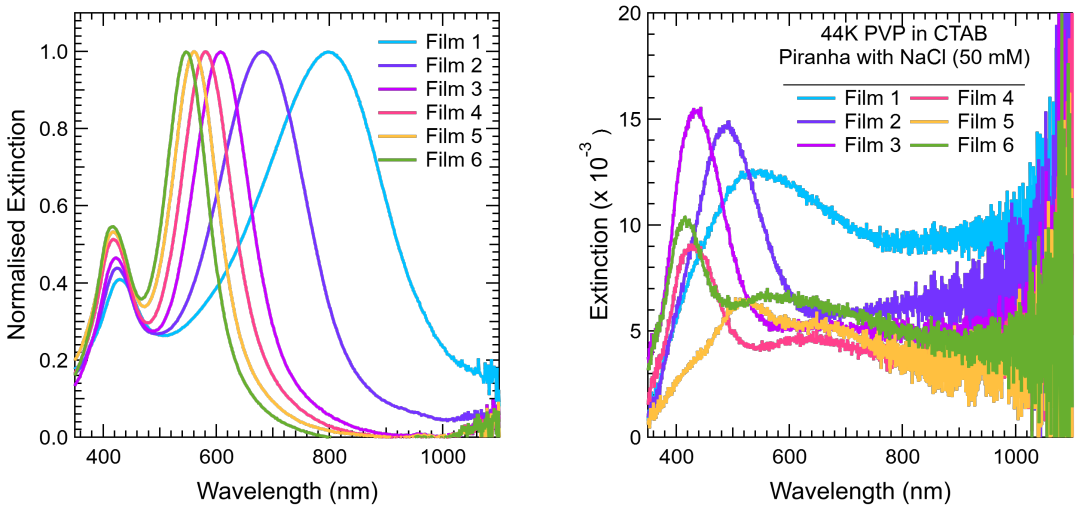


*(a) Solutions* *(b) Films*

*Figure 125: Normalised extinction spectra of silver nanoparticle solutions and resulting films with increasing 44K PVP-capped seeds from 50-300 µL in 50 µL increments (Film 1-6). The glass substrates were piranha cleaned. Particles were redispersed in CTAB (10 mM), and NaCl (50 mM) was introduced before fabrication*

Figure 125 shows the extinction spectra of the nanoparticle solution and the resulting films. The extinction spectra indicate that these fabrication parameters were the first to yield a monolayer of nanoparticles with a tunable SPR peak corresponding to a change in particle size. The primary resonance peak for the films is notably blue-shifted compared to the corresponding solution. However, except for the 250 µL seed volume film, the same trend in peak shift is observed as the seed volume increases. The spectral profile

suggests the formation of a monolayer of particles, with plasmon coupling occurring between particles in near-field proximity.

#### 4.4.1.2 Particles Redispersed in Type I Water

A final experiment was conducted to validate the effectiveness of the optimised fabrication method across a range of nanoparticle sizes. It was established from previous experiments that the most favourable outcomes were attained using a piranha-cleaned substrate without any additional modifications or additives. The piranha-cleaned substrates were immersed in the nanoparticle solutions overnight.

A total of six substrates were utilised, each submerged in nanoparticle solutions made with increasing 44K PVP-capped seed volumes ranging from 50 to 300 µL in 50 µL increments. The particles were redispersed in Type I water before film fabrication. The normalised extinction spectra for the nanoparticle solutions are presented in Figure 126, alongside the extinction spectra of the resulting nanoparticle films.

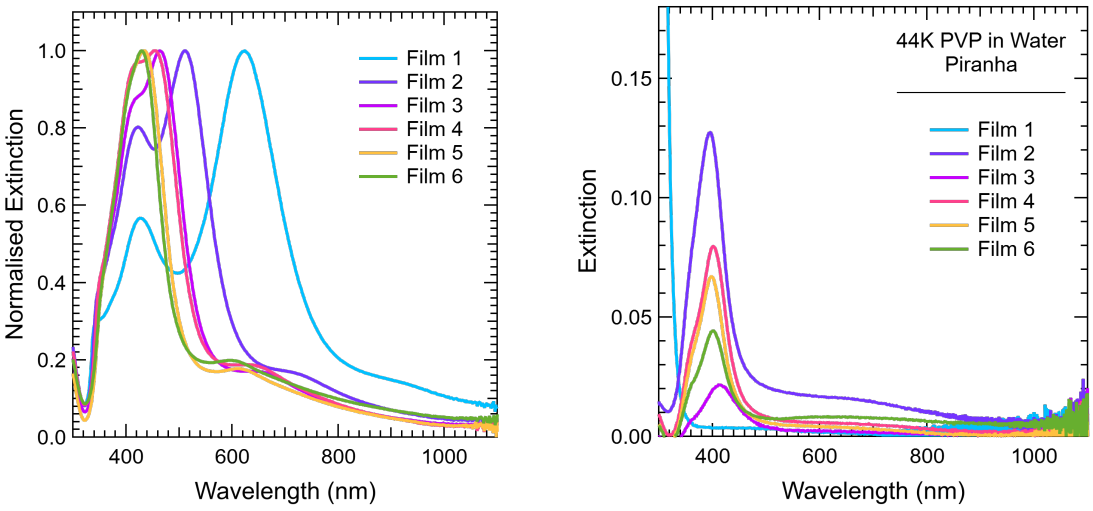


*Figure 126: Normalised extinction spectra of silver nanoparticle solutions with increasing 44K PVP-capped seeds from 50-300 µL in 50 µL increments (Film 1-6). Particles were redispersed in Type I water with and without NaCl (20 mM)*

The normalised extinction spectra of the nanoparticles in solution show a blue-shift in the maximum SPR peak as the seed volume is increased. As previously discussed in the synthesis chapter, this phenomenon is anticipated due to the reduction in the angularity and size of the nanoplates when the particles are redispersed in Type I water.

The SEM images of the corresponding films are presented in Figure 127. The im-

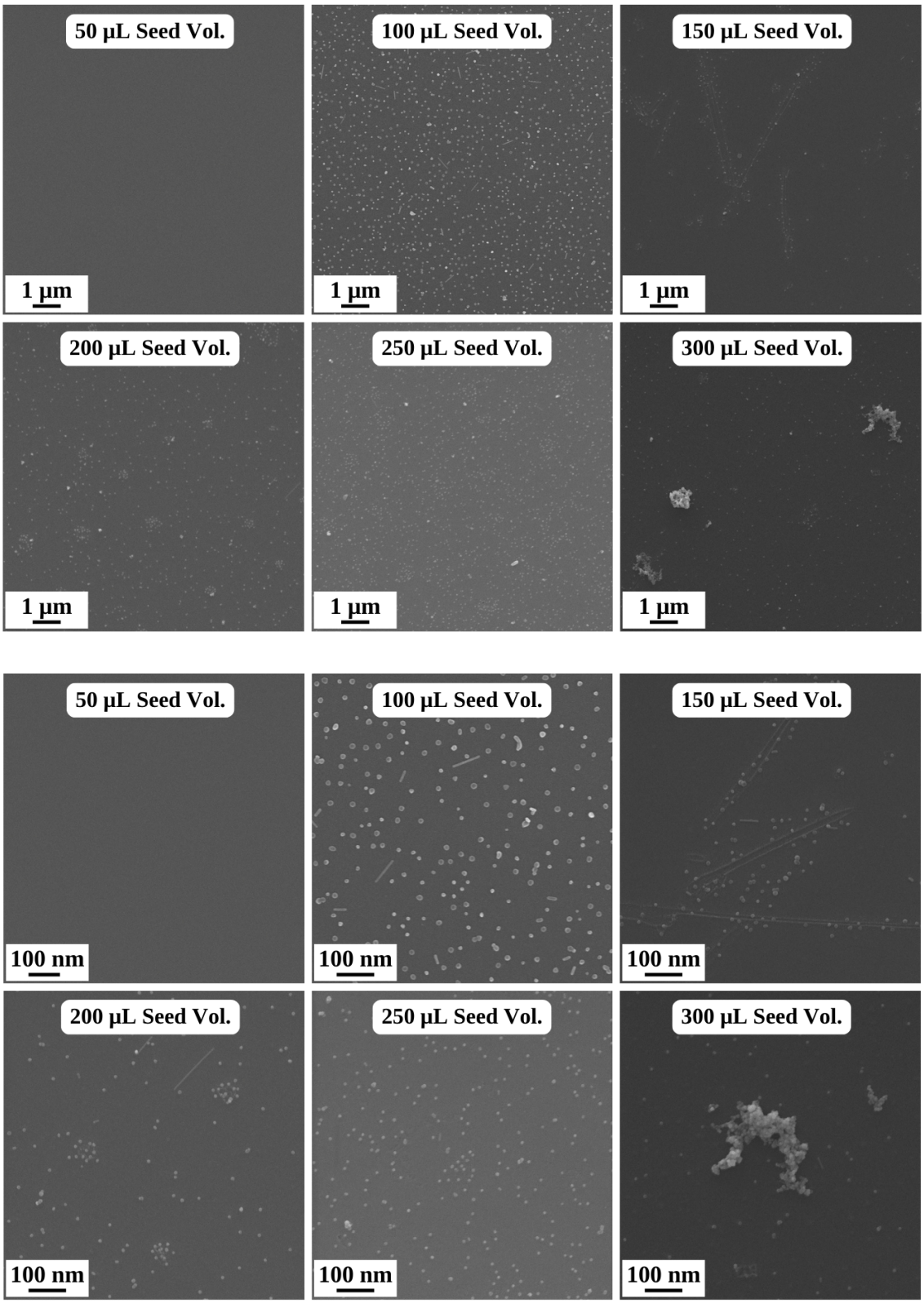


*Figure 127: SEM images of silver nanoparticle films fabricated using solutions with increasing 44K PVP-capped seeds from 50-300 µL in 50 µL increments. The glass substrates were piranha cleaned, and particles were redispersed in Type I water before fabrication*

ages confirmed that the particles adhered to the substrate are a combination of circular nanoplates and nanorods. Notably, no particles adhered to the substrate for the 50 µL seed volume film, as evidenced by the featureless extinction spectrum across the visible and NIR regions.

The remaining five films exhibit a distinct peak in the blue-green region and minimal optical response across the visible and NIR wavelengths, indicating a major blue-shift from solution to solid state. This shift is attributed to the dominance of small circular nanoplates in dictating the extinction profile of the films. The particle coverage across the films varies between solutions, with no discernible trend.

Clustering is observed in the film produced with the 300 µL seed volume solution but not in other film samples. The 100 and 250 µL seed volume films display uniform coverage and controlled particle proximity, while the 150 and 200 µL seed volume films show lower particle density and more sporadic arrangements.

#### 4.4.1.3 Particles Redispersed in Type I Water With and Without PVP in the Growth Solution

The following experiments investigate the impact of adding 10K PVP to the growth solution on the immobilisation of nanoparticles onto hydroxylated substrates. Each series consisted of three substrates that were immersed in nanoparticle solutions created using

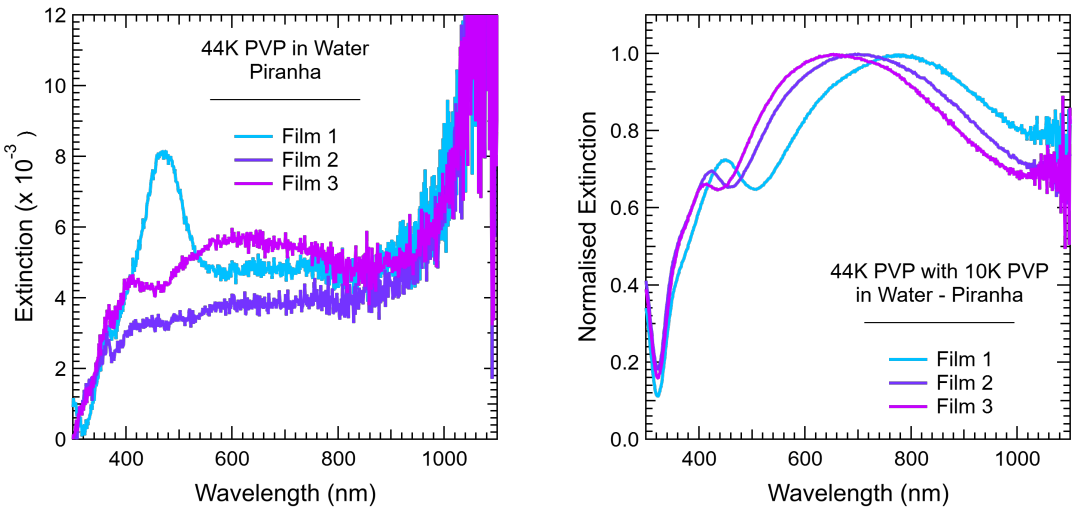


*(a) Without 10K PVP in growth*

*(b) With 10K PVP in growth*

*Figure 128: Extinction spectrum of silver nanoparticle films fabricated using 50 (Film 1), 100 (Film 2) or 150 µL (Film 3) 44K PVP-capped seed solutions, with or without 10K PVP added to the growth solution. The glass substrates were piranha cleaned, and the particles were redispersed in Type I water before fabrication*

increasing volumes of 44K PVP-capped seed volumes from 50-150 µL in 50 µL increments (Film 1-3). For comparison, one series had 10K PVP incorporated into the growth solution during the synthesis, and the other did not. The influence of introducing PVP on the resulting nanostructures is previously discussed in section 3.3.

The extinction spectra of the resulting films with and without the addition of 10K PVP are presented in Figure 128. In contrast to previous experiments, the spectra collected for these films exhibit more complex spectral features. Notably, the spectral features of the films without the 10K PVP vary with the seed volume in the nanoparticle solution. Film 1 exhibits a prominent, sharp peak in the blue-green region of the spectrum, followed by a tail that extends through the visible and into the NIR regions, with a significant increase in intensity. Films 2 and 3 also exhibit this tail in their spectra, with a broader peak in the yellow-red region than Film 1.

The spectral profile for the films produced from nanoparticle solutions containing 10K PVP differs significantly. A noticeable blue-shift in the maximum peak is evident as the seed volume increases and the particle size decreases. This peak appears broad, with an additional shoulder peak visible in the blue-green region.

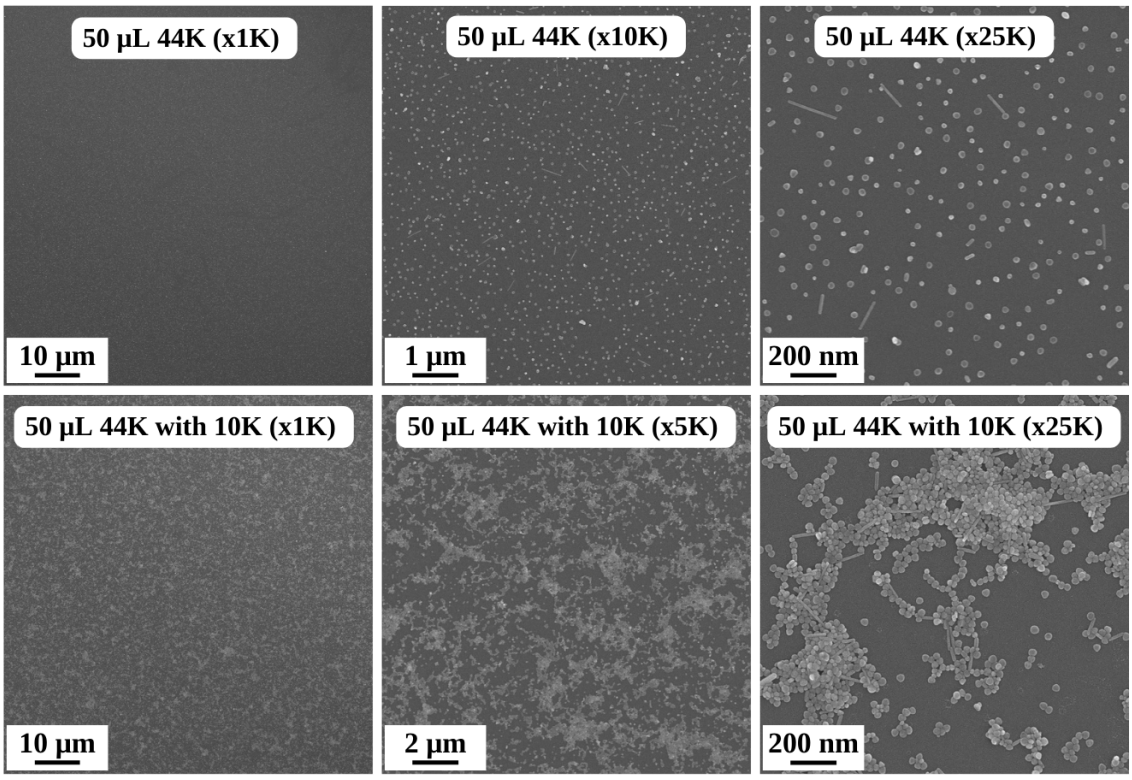


*Figure 129: SEM images of silver nanoparticle films fabricated using 50 µL 44K PVP-capped seed solutions, with or without 10K PVP added to the growth solution. The glass substrates were piranha cleaned, and the particles were redispersed in Type I water before fabrication*

The SEM images of the films produced using 50 µL seed volume solutions with and without the addition of 10K PVP are depicted in Figure 129. The analysis of these images revealed that the film created from a solution without the inclusion of PVP forms a consistent monolayer of particles with controlled proximity between the particles. This arrangement accounts for the distinct peak observed in the extinction spectrum.

This is in stark contrast to the film generated from a solution containing 10K PVP. In this case, the particles appear to be in closer proximity and begin to form islands in specific regions; however, the height and quantity of these formations are reduced compared to the films produced in previous experiments. The overall particle density in these films is heightened, explaining the increased intensity observed in the extinction spectrum.

### 4.4.2 Discussion

The findings from previous experiments have indicated that the most effective method for immobilising nanoparticles redispersed in CTAB (10 mM) involves the use of hydroxylated glass substrates with the incorporation of NaCl. This protocol ensures control over the ionic strength of the suspension by introducing NaCl to facilitate particle deposition. The rationale for introducing NaCl to support particle deposition was derived from a previously documented study by Ferhan et al.[109] In their research, Ferhan and coworkers introduced NaCl at a 1:1 ratio to the nanoparticle solution. Consequently, our initial trial replicated this introduction method. However, doubling the volume of the solution inadvertently halved the concentration of CTAB.

Our prior experiment concluded that at lower CTAB concentrations, the particles are more prone to experiencing desorption of the CTAB from their surface. This destabilises the particles and reduces their angularity, transforming them from triangular nanoplates to circular nanoplates. The implications of decreasing the CTAB concentration and reducing the particle angularity on the optical properties have been extensively discussed in section 3.5.1.1. A similar blue-shift in the SPR peak is observed in the solutions where NaCl was introduced in a 1:1 ratio, confirming the notable decrease in angularity and change in morphology. When solutions with a 1:1 100 mM NaCl introduction are used in the filming fabrication protocol, significant clustering is observed due to the decreased stability of the particles.

A notable improvement was observed when the volume of NaCl was reduced to 500 µL. The extinction spectra of the films created using a nanoparticle suspension with a 100 mM NaCl introduction at 500 µL display a distinct, singular peak in the blue-green

region of the spectrum. This single peak in the films and the observed blue-shift in the solution confirmed that introducing NaCl at a final concentration of 100 mM resulted in the triangular nanoplates being etched into a circular shape. This suggests that the high concentration of NaCl promotes the desorption of CTAB from the edges of the nanoparticles. This led to a similar change in morphology and decreased stability observed when the CTAB concentration in the suspension was reduced.

To minimise the etching of the triangular nanoplates, twelve solutions containing nanoparticles of the same size were synthesised and exposed to increasing concentrations of NaCl ranging from 10-120 mM. The blue-shift of the SPR peak observed after the NaCl introduction increased as the concentration increased, accompanied by a decrease in the zeta potential values. This confirmed that higher concentrations of NaCl led to increased etching, causing the observed blue-shift to be more significant. A high degree of aggregation was also observed in the nanoparticle suspensions with a NaCl concentration exceeding 80 mM; this is attributed to an increase in inter-particle attraction resulting from the change in ionic strength.

When the final NaCl concentration is reduced to 50 mM, a notable shift in the spectral profile of the nanoparticle films is observed. This contrasts the films created with a final concentration of 100 mM, which displayed a single sharp peak with varying intensity. In the case of the 50 mM final concentration, the films exhibit a peak in the green-yellow region of the spectrum, with a red-shift occurring as the nanoparticle size increases. Additionally, a tail extending across the remaining visible and NIR regions is observed, which is attributed to plasmon coupling between particles in near-field proximity. The relatively high intensity of the spectra indicates a good coverage of particles across the substrate. However, a blue-shift is still evident when comparing the extinction spectra of the particles suspended in solution to those immobilised on the substrate. This suggests that some etching and a decrease in angularity are still present under these conditions.

Previous experiments in this chapter investigated the immobilisation of nanoparticles in Type I water with the incorporation of NaCl. The experiments demonstrated that the reduced coverage of CTAB on the surface results in the destabilisation of the suspension and rapid aggregation of the particles when the ionic strength of the suspension is altered. Therefore, it was concluded that the most effective method for immobilising nanoparticles redispersed in Type I water occurs on hydroxylated substrates with no variations to the nanoparticle suspension. Our final experiment investigated the change in optical properties of films produced with particles in Type I water as the nanoparticle

size increased. The results have concluded that the extinction spectra of the particles redispersed in water are not susceptible to shifting when the nanoparticle size is altered, owing to the minimal size difference, approximately 10 nm, between the nanoplates.

Additionally, the high proximity between the particles on the film limits the occurrence of plasmon-plasmon coupling. This explains the limited optical activity observed across the green region and into the NIR regions of the spectrum. When comparing the etched nanoparticles in suspension to those immobilised on a substrate, the SPR peak shows a notable blue shift. When the size of the etched nanoparticle is altered, a change in intensity is noted. However, there does not appear to be a clear trend between particle size and particle density, which limits the control of this fabrication protocol.

The final experiment in this section confirmed that incorporating 10K PVP into the growth solution during nanoparticle synthesis significantly influences the configuration of the nanoparticle films. As discussed in Section 3.2, the presence of PVP binding synergistically with CTAB around the nanoparticles ensured that the angularity and stability of the nanoparticles were maintained when redispersed in Type I water. The SEM images for the films fabricated from nanoparticle solutions with 10K PVP illustrate that the inclusion of PVP significantly increases the particle density of the resulting films.

The films produced in this experiment without 10K PVP formed monolayer nanoparticle films with high particle density and uniform proximity. This suggests that the MPTMS functionalisation step was unnecessary, as hydroxylated glass substrates provided a sufficiently negatively charged surface for nanoparticle immobilisation. Additionally, it confirms that the CTAB concentration in these suspensions is low enough to ensure successful deposition and a high particle density. In contrast, the films created with the addition of 10K PVP exhibit a noticeable increase in particle density and clustering, similar to the observations made in Section 4.2.1.

Our findings align with those of Kawamura and colleagues, who explained that significant desorption would occur at low CTAB concentrations, particularly at the tips of the nanorods.[111] This explains the observed self-assembly of nanorods as connecting bridges between clusters of circular nanoplates. The increase in particle density when PVP is incorporated into the synthesis can be attributed to the formation of negatively charged regions around the nanoparticles. This increase in attractive force between the positively charged CTAB and negatively charged PVP encourages particle clustering.

The most significant outcome of this experiment is the controllable manipulation of the resonance peak of the film extinction with varying nanoparticle sizes. Three nanopar-

ticle suspensions with increasing particle sizes were used for each series. As discussed in the previous chapter, a distinct red-shift of the SPR peak is evident in the extinction spectra of the nanoparticle suspensions as the particle size increases. In the series that incorporated PVP, a similar red-shift is observed in the film extinction as the nanoparticle size increases. These spectra exhibit a significantly broader peak width when immobilised on a substrate compared to the suspension, owing to the decreased particle proximity and increased plasmon coupling.

These experiments have demonstrated that a hydroxylated glass substrate is the most suitable choice for the immobilisation of the nanoparticles synthesised in Section 3.2. The nanoparticles in these suspensions require a reintroduction of CTAB to maintain stability. However, a high concentration of excess CTAB in solution can hinder the deposition of the nanoparticles onto a hydroxylated substrate. Most significantly, these experiments have shown that a change in ionic strength can enhance the deposition of CTAB-capped nanoparticles. However, this adjustment in ionic strength must be carefully managed, as excessive shifts can lead to the destabilisation of the nanoparticles. Our findings demonstrate that incorporating NaCl at a final concentration of 50 mM effectively immobilises the CTAB-capped nanoparticles with minimal compromise to their stability. As a result, the optical properties of these nanoparticle films exhibited a successful tuning of the SPR peak across the spectrum as the size of the nanoparticles increased.

## 4.5 Gold-Core Nanorod Films

This experiment aimed to create films of gold-core silver nanorods by applying the insights gained from prior experiments. The films were fabricated on piranha-cleaned glass substrates immersed in nanoparticle solutions overnight. The gold-core nanorods were redispersed in Type I water, and NaCl (100 mM) was added before the fabrication process.

### 4.5.1 Results

The extinction spectra for the resulting nanoparticle films are presented in Figure 130 below.

The spectral data indicated a minimal optical response within the visible region of the spectrum. The presence of a high degree of relatively intense noise in the NIR region, coupled with the absence of spectral features, led to the conclusion that this method did not successfully produce monolayer nanoparticle films.

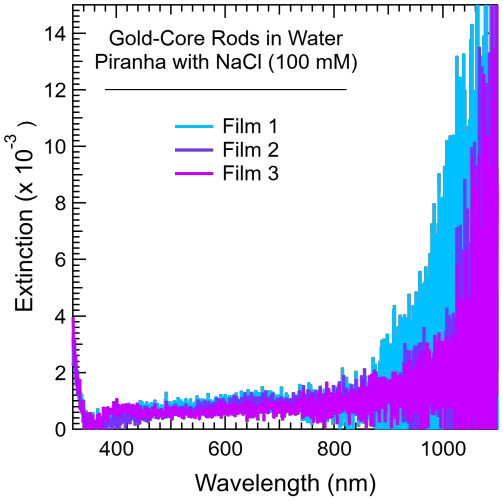


*Figure 130: Extinction spectrum of gold-core rod nanoparticle films. Glass substrates were piranha cleaned. Particles were redispersed in Type I water, and NaCl (100 mM) was introduced before fabrication*

### 4.5.2 Discussion

The initial attempt to create silver-gold-core nanorod films was not successful and will require additional effort. Similar to the nanoparticles in the previous experiment, these nanorods are stabilised by CTAB molecules and possess an overall positive surface charge. The assumption that these nanorods would immobilise onto hydroxylated glass substrates with an overall negative charge did not yield the expected results. Despite incorporating 100 mM of NaCl into the fabrication process to facilitate deposition and ensure a high particle density, the resulting films exhibited a very low particle density, as evidenced by the lack of optical response observed in the extinction spectrum.

Several future experiments will be necessary to identify the limiting factor of this fabrication method. It is essential to focus on testing other functionalised substrates, such as MPTMS or APTES/PSS, with a more negative surface charge. Furthermore, increasing the NaCl concentration may facilitate nanorod deposition. However, an initial study similar to the one conducted by Ferhan et al. should be carried out to determine the threshold of NaCl concentration on the stability of the nanorods.[109]

## 4.6 Triangular Nanoplate Films

The aim of this experiment was to produce nanoparticle films using triangular nanoplate solutions prepared through the chemical reduction method as described by Zhang et al.[12] To accommodate the negative net charge of the nanoparticles resulting from the TSC

addition during the synthesis, the glass substrates were functionalised with APTES.

### 4.6.1 Results

The normalised extinction spectra for the nanoparticle solutions are presented in Figure 131, alongside the extinction spectra of the resulting nanoparticle films. As previously discussed, the nanoplate edge lengths increase with the concentration of $NaBH_4$. Both the solutions and the films exhibit a red-shift in the SPR peak. This is attributed to the observed increase in particle size as evidenced by the SEM images of the films, as presented in Figure 132.

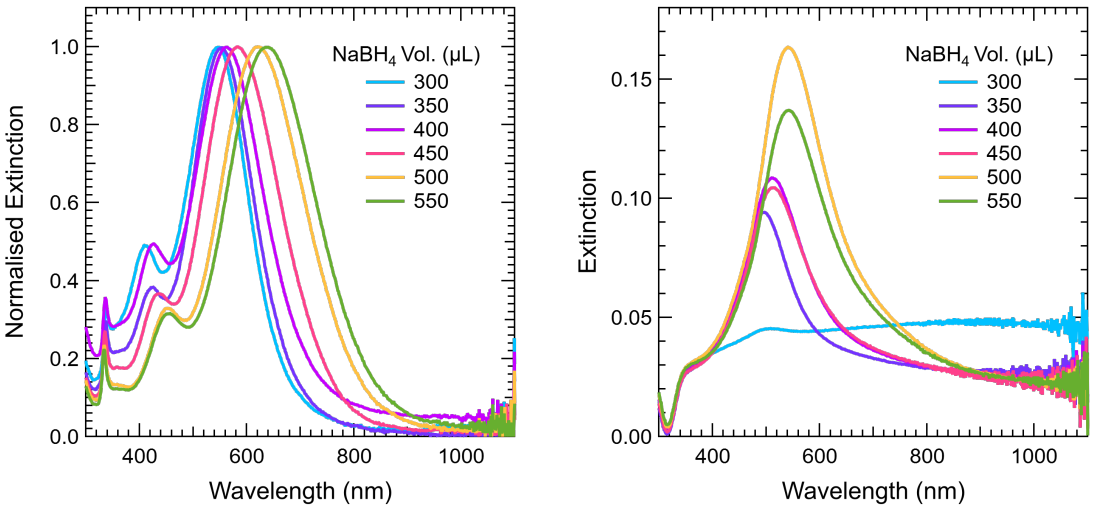


*(a) Solution Extinction*

*(b) Film Extinction*

*Figure 131: Comparison of the normalised extinction spectrum of the silver triangular nanoparticle solutions and the extinction spectrum of the resulting nanoparticle films. Each solution had an increased volume of $NaBH_4$ from 300-550 µL in 50 µL increments. The glass substrates were piranha cleaned and functionalised with APTES*

With the exception of the 300 µL $NaBH_4$ film, which displays significant clustering, the particle density remains consistent across all films. The observed clustering in the 300 µL $NaBH_4$ sample accounts for the broad and featureless extinction spectrum observed for the film. The remaining film extinction spectra exhibit a distinct peak in the blue-to-yellow region of the spectrum, which undergoes a red-shift as the particle size increases. The breadth of the resonance peak increases as the edge length of the particle grows, potentially attributed to an increase in plasmon coupling. It is worth noting that the extinction spectra of the films are blue-shifted compared to the identical particles in a colloidal solution. This could be explained by the truncation of the triangular plates.

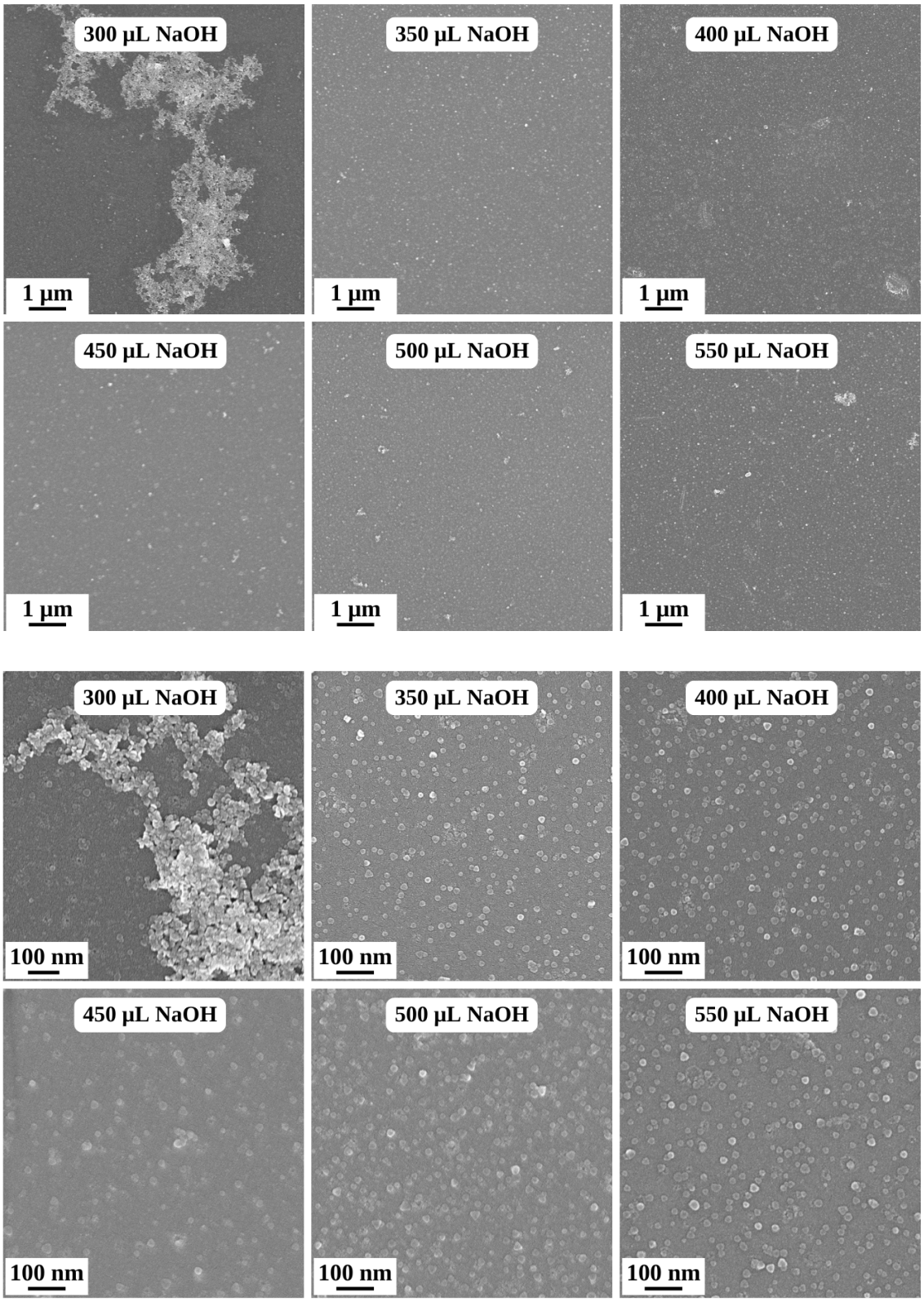


*Figure 132: SEM images of silver triangular nanoparticle films. Each filming solution had an increased volume of $NaBH_4$ from 50-300 µL in 50 µL increments. The glass substrates were piranha cleaned and functionalised with APTES*

### 4.6.2 Discussion

In contrast to the previous experiments in this chapter that used CTAB-capped nanoparticles, the TSC and PVP stabilising these nanoparticles provide an overall negative change for the particles. Therefore, a positively charged substrate was required for immobilisation. Previous studies have proven the functionalisation of glass substrates with APTES to be highly effective. The immobilisation of these triangular nanoplates on APTES functionalised substrates resulted in the fabrication of uniform nanoparticle films with high particle density. The only exception was the film produced with the smallest triangular nanoplates, which exhibited a high degree of clustering. This resulted in a flat, relatively featureless extinction spectral profile. In contrast, the other five films demonstrated controlled tuning of the defined SPR peak in the visible region of the spectrum. The SPR peak for each of the films shifted to longer wavelengths as the size of the nanoplates increased. This same shift was observed in the extinction spectra for the particles in suspension. However, similar to the extinction of all other films produced, the SPR peak of the film extinction was shifted to shorter wavelengths compared to the SPR peak of the suspended particles.

The SEM images confirmed a high degree of truncation when the particles were immobilised on the substrate. This explains the absence of the secondary shoulder peak typically observed in the extinction spectra of particles in solution. As previously discussed, the tips of the triangular nanoplates are a highly thermodynamically unstable feature of metal nanoparticles and will tend to truncate over time. Notably, the breadth of the SPR peak increased as the size of the nanoparticles immobilised on the substrate also increased. This increase in peak breadth is a common observation with increasing edge length due to the increase in plasmon modes.

As the size of the particles increased, the distance between the nanoparticles in the film decreased. However, no significant change in the spectral profile was observed. We suggest that the number of particles in close proximity was not high enough for effective plasmon-plasmon coupling to occur.

This experiment has demonstrated the successful fabrication of resonance-tunable triangular nanoplate films. In all but one occurrence, the SPR peak is red-shifted along the spectrum when the edge length of the nanoplates is increased; this same shift is observed to a similar degree in the nanoparticle suspension used to fabricate these films.

## 4.7 Conclusion

This chapter focuses on optimising an effective protocol for immobilising the nanoparticles synthesised in Chapter 3 onto glass substrates. To determine the optimal conditions for immobilisation, a variety of substrate modification options were investigated. These substrate modifications included hydroxylation or functionalisation by MPTMS, APTES, or APTES/PSS.

These experiments concluded that MPTMS functionalised substrates were the least effective for immobilising the synthesised nanoparticles. Most films fabricated on MPTMS functionalised substrates showed a low particle density and a high degree of clustering. The incorporation of NaCl to adjust the ionic strength of the suspension or NaOH to alter the pH had little effect on improving the particle density. These variations in suspension conditions also increased the degree of clustering observed in the films.

The use of APTES/PSS functionalised substrates demonstrated the highest particle density. The particle density was particularly increased when NaCl was incorporated into the nanoparticle suspension before fabrication. However, the increase in particle density did not warrant a significant increase in fabrication complexity. As a result, it was determined that the most favourable substrate for this immobilisation protocol was a hydroxylated glass substrate with no further modifications.

Chapter 3 highlighted the necessity of reintroducing CTAB into the particle suspension after purification to maintain the angularity and stability of the synthesised triangular nanoplates. However, this work has observed that this increase in CTAB concentration hinders the deposition of particles onto a substrate. In contrast, when the CTAB concentration is low, primarily when the nanoparticles are dispersed in Type I water, they readily deposit onto the hydroxylated substrate and form a monolayer film.

Numerous experiments were conducted to find a solution to improve the deposition of nanoparticles redispersed in CTAB solutions. These experiments concluded that incorporating NaCl into the nanoparticle suspension would facilitate the deposition. However, at high NaCl concentrations, the stability of the nanoparticles is compromised. The particles in these films appear significantly truncated and show a high degree of clustering. When the NaCl concentration is decreased to 50 mM, the CTAB-capped nanoparticles are effectively immobilised onto the hydroxylated glass substrate, but still show evidence of truncation.

These samples demonstrated the successful fabrication of nanoparticle films with tunable SPR peaks. The series fabricated with a 50 mM NaCl concentration observed a red-

shift in the SPR peak when the size of the nanoparticles was increased. This SPR peak tuning was also observed in the films fabricated using TSC-capped triangular nanoplates on APTES functionalised substrates.

Ultimately, the nanoparticle films fabricated in this chapter will be overlaid with rubrene to investigate the possibility of metal-enhanced absorption and fluorescence. The intent is that the tuning of the SPR peak will enable a correlation between the spectral overlap of the nanoparticle sublayer and the rubrene overlay.

# 5 Chapter 5 - Rubrene Film Fabrication and Characterisation

| Abbreviations | |
|---|---|
| PLE | Photoluminescence Excitation |
| PL | Photoluminescence |
| TRPL | Time-resolved Photoluminescence |
| AFM | Atomic Force Microscopy |
| SPR | Surface Plasmon Resonance |
| RPM | Revolutions Per Minute |
| nm | Nanometre |
| mL | Millilitre |
| mM | Millimole |
| K | Kelvin |

## 5.1 Introduction

This chapter focuses on the fabrication and characterisation of thin films of 5,6,11,12-tetraphenylnapthacene (rubrene). The film fabrication process was initially optimised using piranha-cleaned glass substrates to establish a correlation between the spin coater rotation rate during the fabrication and the resulting thickness of the rubrene films. Following this optimisation, the method was used to deposit a rubrene overlay onto various nanoparticle sublayers, including those discussed in Sections 4.6 and 4.7.

The photoluminescence excitation (PLE) and emission (PL) spectra for these samples were collected to explore any instances of metal-enhanced fluorescence within the rubrene film. Additionally, time-resolved photoluminescence (TRPL) data were gathered to assess whether any significant alterations in the fluorescence lifetime of the system were observed.

### 5.1.1 Organic Thin Film Fabrication

The fabrication of thin rubrene films involved the use of a spin coating deposition method. Reliable methods for producing thin films are crucial for cost-effective device fabrication. Previous studies have focused on identifying key parameters for controlled thin film fabrication, including adjustable thickness and uniform coverage.

Zhang et al. conducted a study outlining an effective approach for producing tunable ultra-thin organic semiconductor films. Their findings demonstrate that precise thickness control is achievable by adjusting the rotation speed or solution concentration.[115] Figure 133 below displays a reproduced image illustrating the relationship between the thickness of the organic semiconductor films and the rotation rate or concentration.

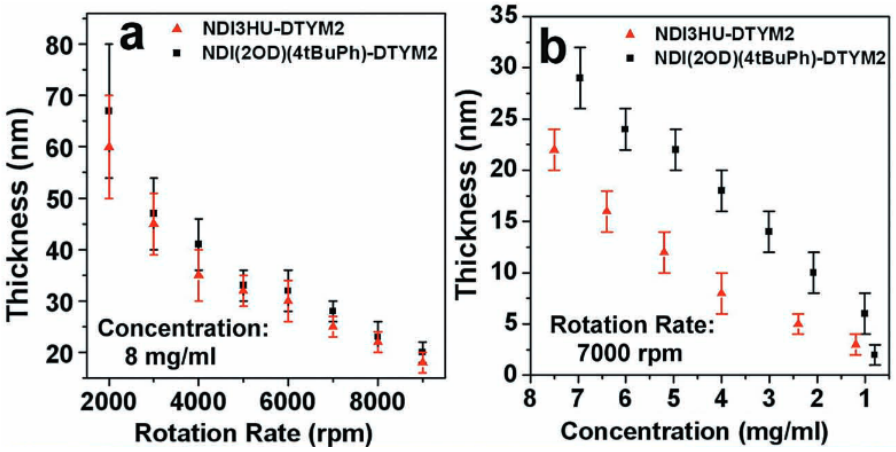


*Figure 133: Film thickness of organic semiconductor thin films, produced by spin coating, as a function of rotation rate (a) and concentration (b). As reported by Zhang et al.*[115]

Zhang and co-workers confirmed that the thickness of spin coated films decreases as the rotation rate increases. However, there are limitations to this parameter. As the rotation rate is further increased, the thin films become less uniform. This parameter is also influenced by the properties of the solution used, such as viscosity, which is determined by the solution concentration and solvent.

Zhang et al. found that thin organic films can be produced using low-concentration solutions and a high rotation rate of 7000 RPM. They discovered that high rotation speeds promote the formation of thin films; however, films under 10 nm cannot be effectively deposited from solutions with low viscosity. The hydrophobicity of the substrate also affects the uniformity of the resulting film. To address this issue, they developed a reproducible method for producing ultra-thin films (<10 nm) by dispensing the solution while the spin coater runs. Their method was successfully applied to a variety of organic semiconductor materials.[115]

### 5.1.2 Rubrene Thin Film Fluorescence

The organic semiconductor rubrene has been the subject of extensive research due to its versatile applications in organic electronic devices, such as field-effect transistors, photovoltaics, and light-emitting diodes. The high carrier charge mobility and almost 100% fluorescence quantum efficiency of rubrene in solution have contributed to its widespread exploration.[116]

The molecular structure of rubrene and its orthorhombic, monoclinic, and triclinic packing configurations are depicted in Figure 134. In prior research, rubrene thin films have been produced using various methods.[117–119] In a study by Chen et al., rubrene films

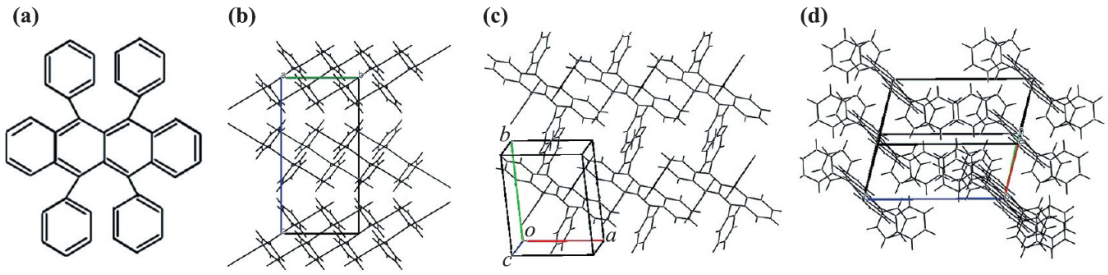


*Figure 134: Molecular structure of rubrene (a) and its orthorhombic (b), monoclinic (c), and triclinic (d) packing configurations. As reported by Liu et al.*[116]

with thicknesses ranging from 5 to 100 nm were successfully fabricated through thermal evaporation.

The authors delved into the exciton dynamics and singlet fission capabilities of these films. Chen et al. comprehensively analysed the PLE, PL and fluorescence lifetimes of the rubrene films at increasing temperatures. Figure 135 presents the reproduced PLE and PL data. Their findings demonstrated that the efficiency of singlet fission is significantly influenced by film thickness.[117]

Chen et al. found that as the film thickness increased, there was a slight red-shift in

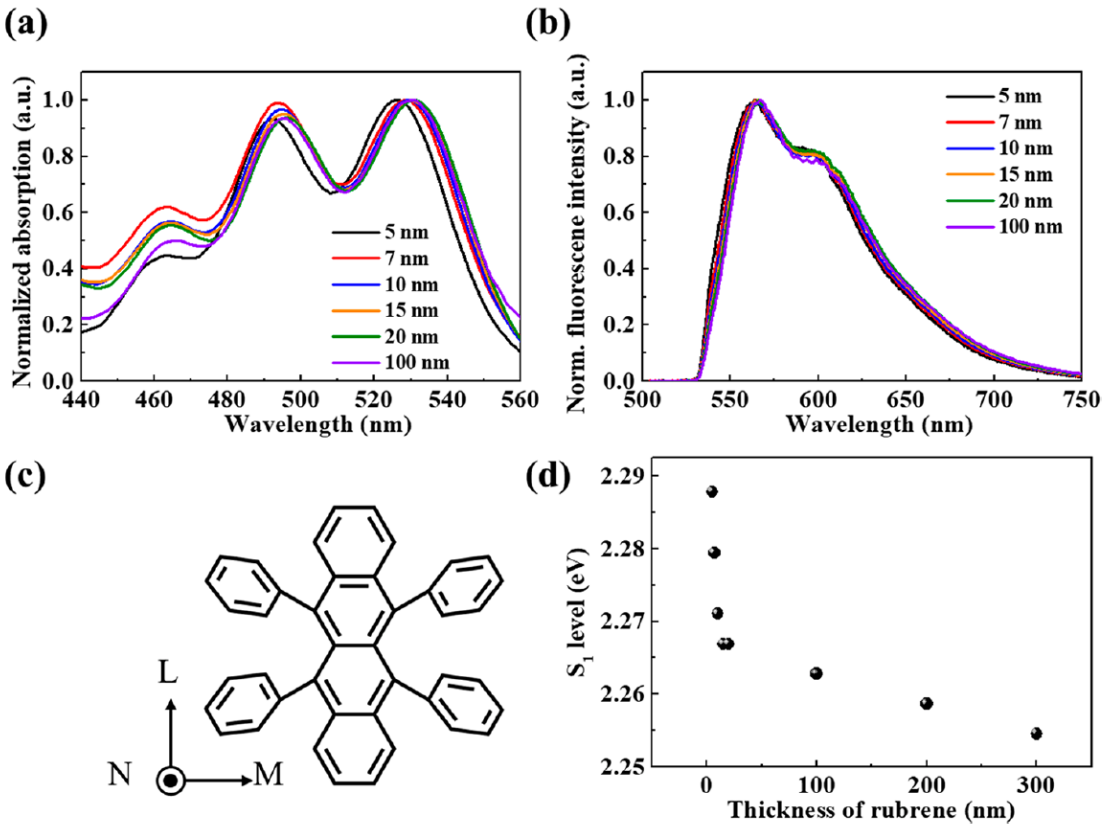


*Figure 135: PLE (a) and PL (b) spectra of rubrene (c) thin films of increasing thickness from 5-100 nm, produced through thermal evaporation. As reported by Chen et al.*[117]

the PLE and PL spectra, indicating a decrease in singlet energy due to enhanced molecular packing. Overall, the changes in the steady-state spectra were minimal, which is consistent with the expectation that molecular interactions on a sub-5 nm scale should determine the photophysical behaviour of a sample. Therefore, the film thickness should not significantly impact the excited state dynamics. However, they observed a notable difference in the time-resolved photoluminescence between the 5 nm and 100 nm films.[117] Figure 136 below presents the reproduced time-resolved photoluminescence data.

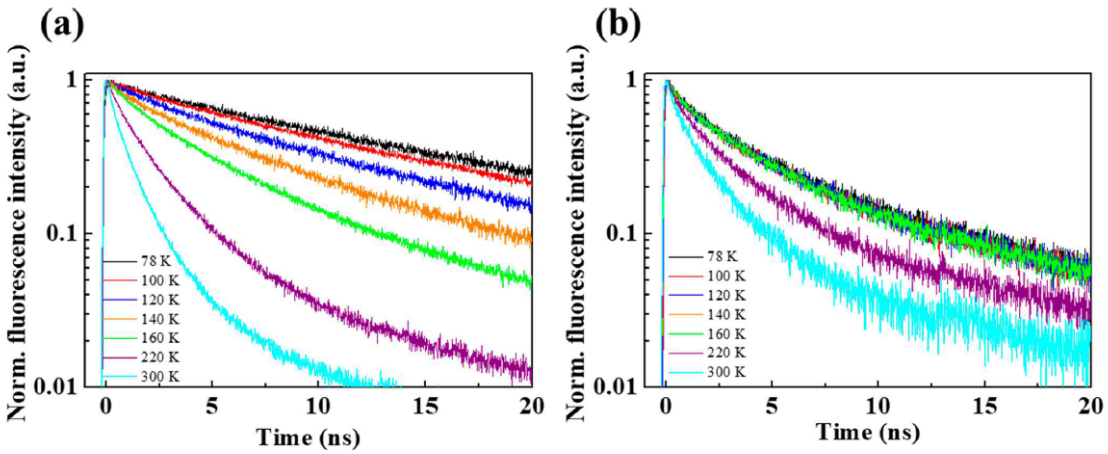


*Figure 136: TRPL of 100 nm (a) and 5 nm (b) thick rubrene films at increasing temperatures from 78-300K. As reported by Chen et al.*[117]

The authors observed a notable reduction in the fluorescence lifetime of the 100 nm film as the temperature was elevated to 300 K. In contrast, a significantly smaller decline was observed in the fluorescence lifetime of the 5 nm film under the same temperature increase. They attributed the significant difference in the 100 nm film to a phase transition from amorphous to polycrystalline upon thermal annealing. This resulted in a higher singlet fission rate in the 100 nm film through the formation of singlet fission "hotspots".[117]

## 5.2 Rubrene Film Fabrication and Characterisation

The initial section of this chapter focuses on the fabrication of rubrene thin films. To ensure the uniformity of the films, the glass substrates underwent piranha cleaning to remove any potential contaminants. These experiments aimed to establish an effective spin coating protocol for creating a uniform rubrene thin film that would serve as an appropriate overlay for the nanoparticle sublayers developed in Chapter 5.

### 5.2.1 Results

A solution of rubrene (11 mM) in toluene was used to fabricate the thin films. The normalised PLE and PL spectra of the rubrene solution are presented in Figure 137.

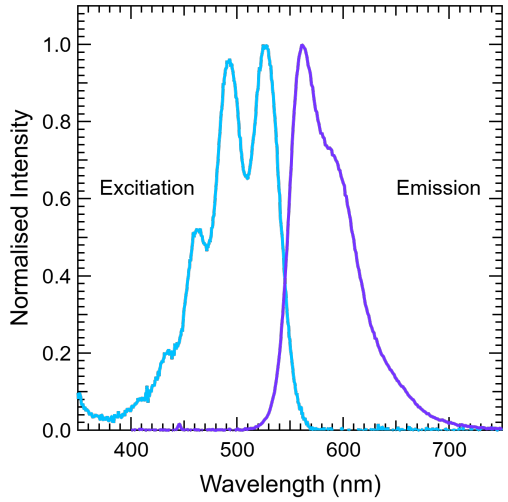


*Figure 137: PLE and PL spectra of rubrene (11 mM) in Toluene*

The PLE spectrum exhibits three distinct peaks at 463, 498, and 533 nm, characteristic of the vibrational band transitions in rubrene. The PL spectrum is also characteristic of rubrene, with a distinct peak at 560 nm and a red shoulder at 593 nm.

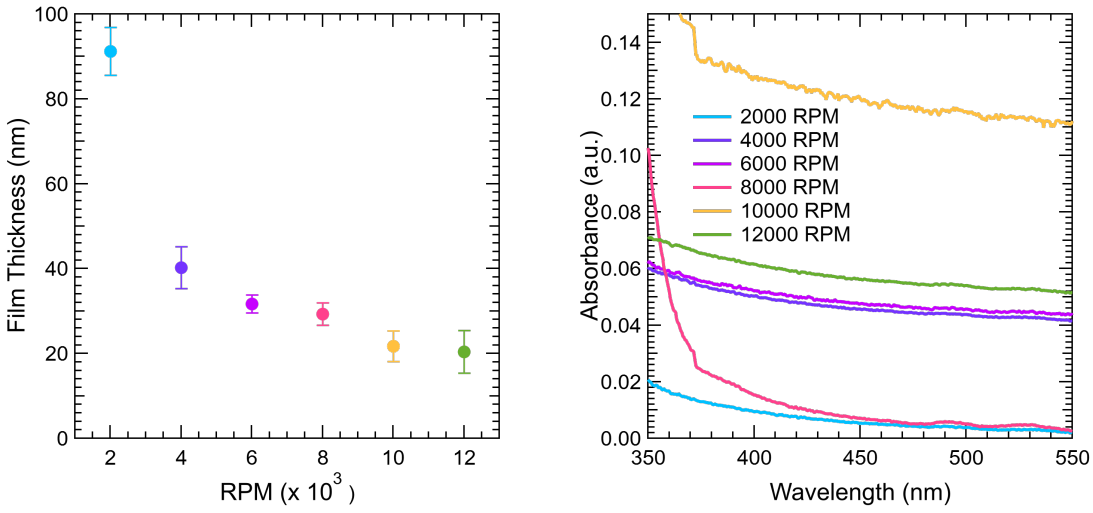


*(a) Thickness* *(b) Absorbance*

*Figure 138: Absorbance spectra of rubrene thin films fabricated with increasing rotation rates from 2000-12000 RPM*

A spin coater was used to fabricate a series of rubrene thin films. In this experiment,

the rotation rate was incrementally increased from 2000 to 12000 RPM in 2000 RPM intervals to observe how the thickness of the films changed. Theoretically, increasing the rotation rate would decrease the thickness of the thin film produced. To confirm this correlation, a series of atomic force microscopy (AFM) measurements were conducted to analyse the impact of rotation rate on the thickness of the films.

The AFM data confirmed that as the rotation rate increased from 2000-12000 RPM, the thickness of the rubrene film decreased from 91.2 $\pm$ 6 nm to 20.4 $\pm$ 5 nm. The absorbance data of the thin films produced at the increasing rotation rates are depicted in

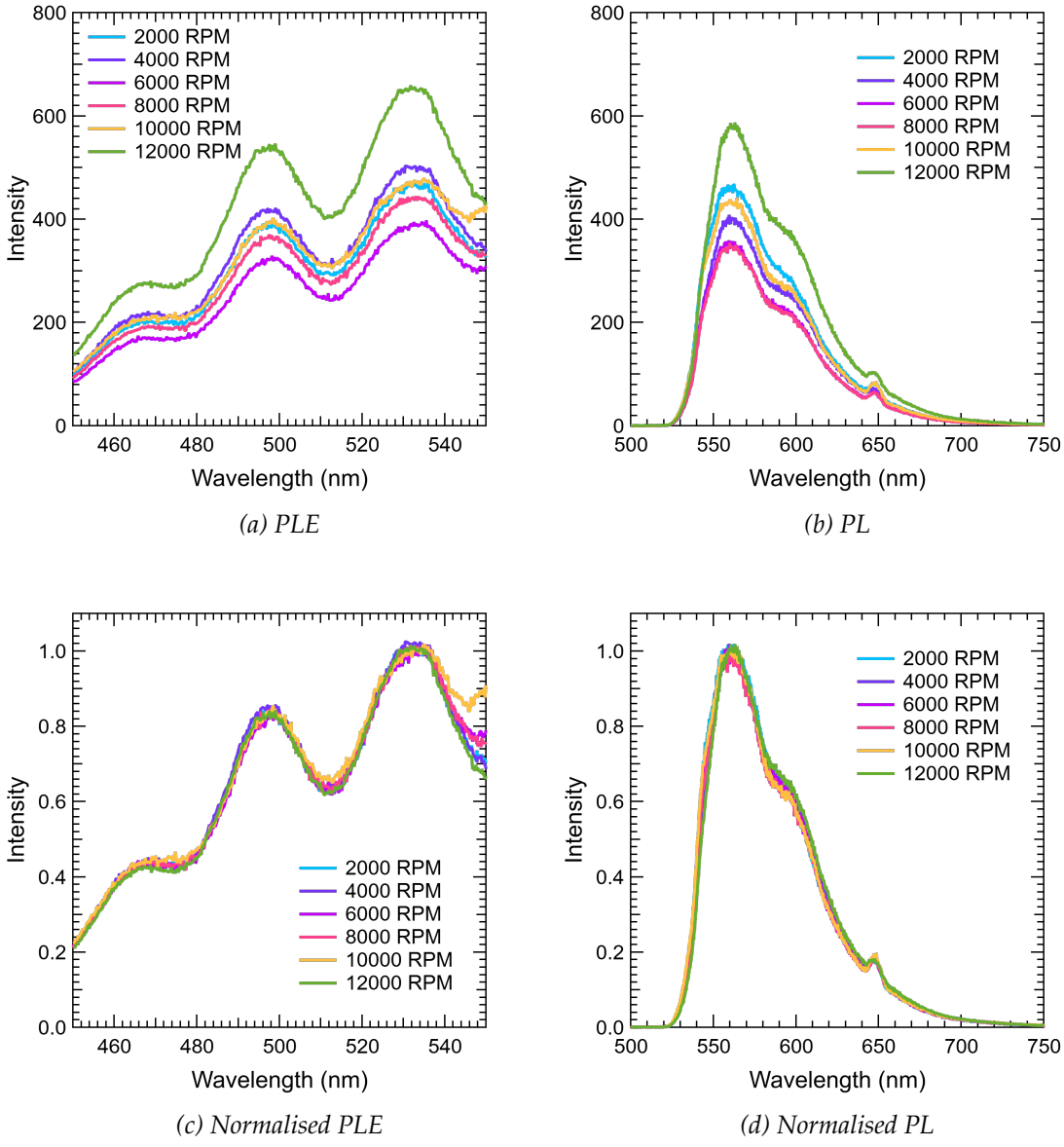


*Figure 139: PLE ($\lambda_{em} = 600nm$) (a) and PL ($\lambda_{ex} = 475nm$) (b) spectra of rubrene thin films fabricated with increasing rotation rates from 2000-12000 RPM, compared to the normalised PLE (c) and PL (d) spectra*

Figure 138. Notably, the specific peaks observed in the PLE spectra were not evident in these absorbance spectra, highlighting the limitations of the spectrophotometer setup for accurate analysis of thin films. As a result, absorbance data for any further fabricated films was not collected. However, PLE and PL spectra were obtained for comparison.

The PLE and PL spectra for the six thin films at increasing rotation rates are presented in Figure 139. Unfortunately, this analysis did not reveal a discernible trend or direct correlation between the film thickness and fluorescence intensity. The only significant observation is a minor blue-shift of 2 nm in the PLE peak at 533 nm as the rotation rate is increased over 10000 RPM, and consequently, the thickness of the film is decreased.

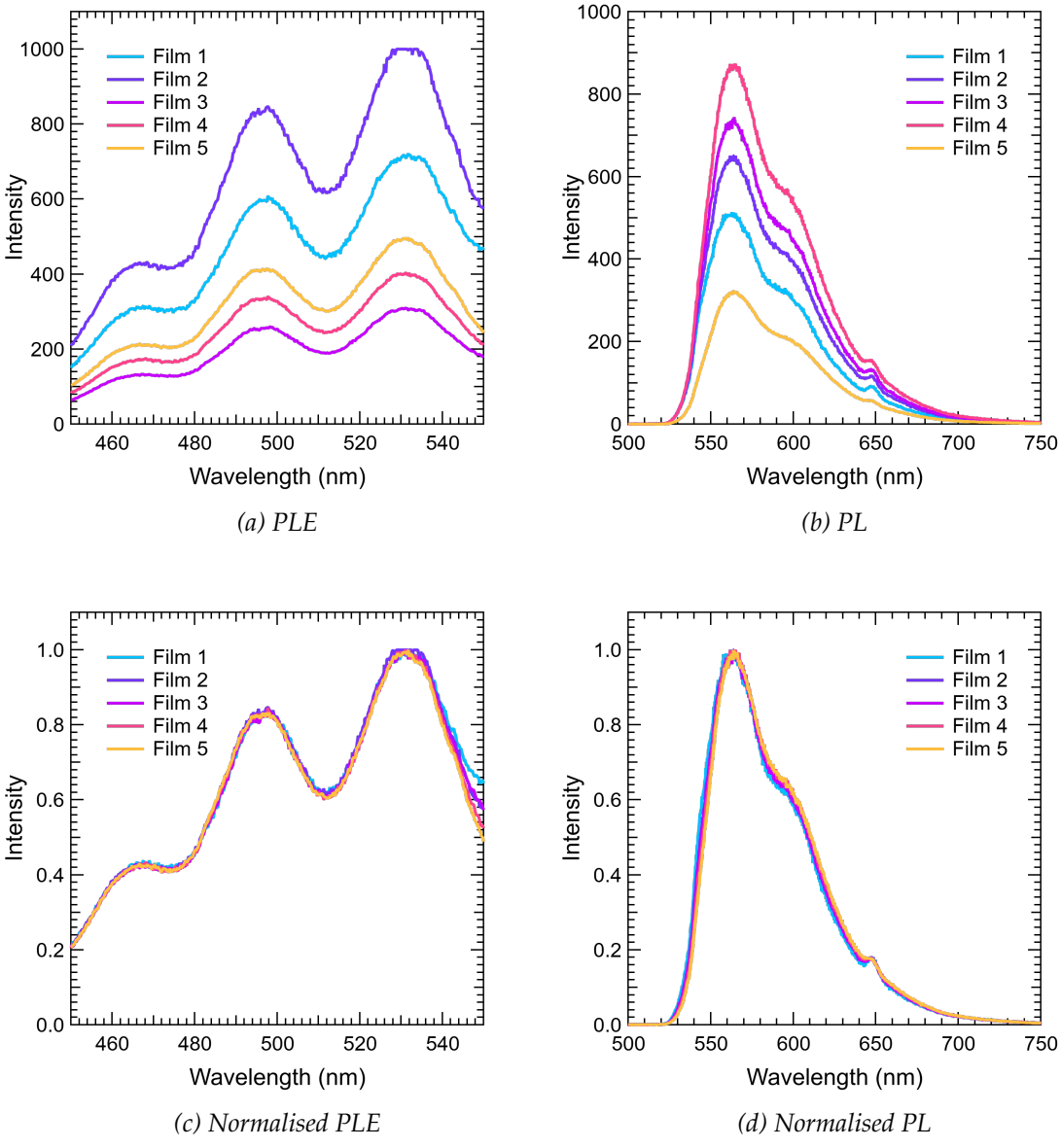


*(a) PLE*

*(b) PL*

*(c) Normalised PLE*

*(d) Normalised PL*

*Figure 140: PLE ($\lambda_{em} = 600nm$) (a) and PL ($\lambda_{ex} = 475nm$) (b) spectra of rubrene thin films spun at 6000 RPM, compared to the normalised PLE (c) and PL (d) spectra*

A second experiment was run to investigate the reproducibility of the spin coating protocol. This experiment included the fabrication of five rubrene thin films, all spun at 6000 RPM. The PLE and PL spectra for these five films can be found in Figure 140.

Significant variations in the intensity of the PLE and PL spectra were noted for each rubrene film. These intensity changes could arise from multiple factors, such as potential inhomogeneities within the films and differences in the data acquisition locations for each sample. Notably, no peak shifting was observed in the normalised spectra, indicating that the spin coating method successfully produced films with a consistent thickness. To further explore these variations in intensity, Film 1 underwent a cyclic PL data collection, and the spectra from this cycle are presented in Figure 141.

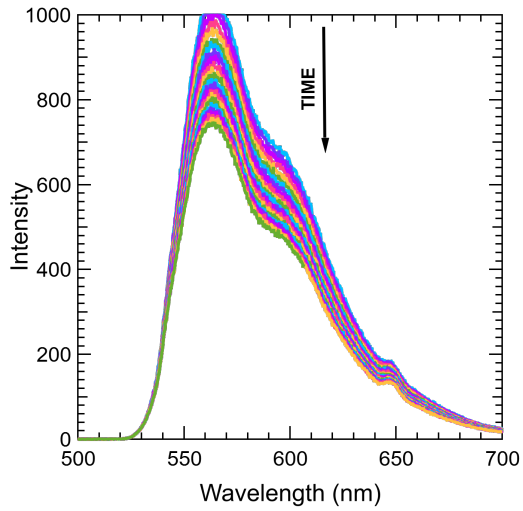


*Figure 141: Cycle PL ($\lambda_{ex} = 475nm$) spectra of a rubrene thin film spun at 6000 RPM*

Throughout the data collection cycle, the PL intensity decreased noticeably. This trend implies that the rubrene films degrade significantly over time. This could also explain the significant differences in intensity between films produced using the same fabrication method.

### 5.2.2 Discussion

The AFM data analysis of the rubrene film series revealed a reduction in film thickness from 55 nm to 14 nm with an increase in rotation rate from 2000 to 12000 RPM. This observation aligns with established literature, emphasising the pivotal role of rotation rate in governing film thickness.[115] Our findings corroborate that, under constant concentration and volume, the thickness of rubrene films decreases with increasing rotation rate.

The PLE data illustrated the anticipated peaks for vibration band transitions at 463,

497, and 533 nm across all rotation rates. A marginal red-shift in PLE and PL spectra was observed as the rotation rate decreased and film thickness increased. This phenomenon agrees with prior research by Chen et al., who reported comparable red-shift trends in the optical properties of thermally evaporated rubrene films with increasing thickness.[117] The maximum rotation rate of the spin coater constrained our film series, unlike Chen and co-workers, who achieved sub-10 nm thin films through thermal evaporation.

While enabling data collection, the use of a 3D-printed sample holder introduced variations in sample positioning, potentially contributing to the observed discrepancies in PLE and PL intensities. This was particularly noticeable among the rubrene films spun at a consistent rotation rate of 6000 RPM. However, the cyclic PL data suggests that these discrepancies can also be attributed to the ongoing photodegradation inherent in thin films.

Based on the outcomes of these experiments, it was determined that all subsequent rubrene films would be spun at a consistent rotation rate of 6000 RPM. This approach was adopted to maintain comparability among the plasmonic sublayers and avoid additional variables that could arise from variations in film thickness.

## 5.3 Silver Nanoparticle Sublayer with a Rubrene Overlay

This section examines the potential metal enhancement achieved by using nanoparticle sublayers fabricated with the nanoparticles described in Chapter 3. The fabrication of these films was previously detailed in Chapter 4. Each of these films was overlaid with rubrene to investigate the potential for metal-enhanced fluorescence.

### 5.3.1 Results

#### 5.3.1.1 Nanoseed Sublayers

Nanoparticle films fabricated with 44K PVP-capped seed particles on APTES functionalised substrates were used to investigate the impact of the rubrene film thickness on fluorescence intensity. Six nanoseed films were fabricated, and each film was overlaid with a rubrene layer spun at an increasing rotation rate from 2000 to 12000 RPM in 2000 RPM increments.

The extinction spectra for the six fabricated nanoseed films are presented in Figure 142. The maximum surface plasmon resonance (SPR) peak for all these films ranges between 404 and 415 nm. However, the extinction intensity varies significantly between

nanoparticle films, from 0.014 for the 2000-6000 RPM films to a maximum of 0.053 for the 10000 RPM film.

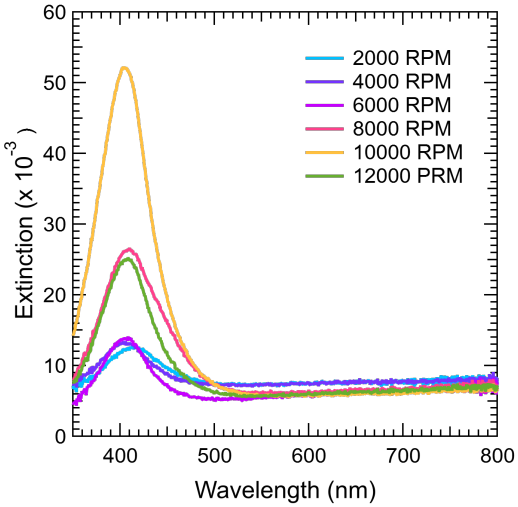


*Figure 142: Extinction spectrum of nanoparticle films fabricated with 44K PVP-capped nanoseeds*

Each nanoseed film was overlaid with a rubrene layer at an increasing rotation rate from 2000 to 12000 RPM in 2000 RPM increments. The PLE spectra ($\lambda_{em}$ = 600 nm) and the PL spectra ($\lambda_{ex}$ = 475 nm) for each film were collected and presented in Figure 143 below.

Notably, there was no discernible trend or direct correlation between the fluorescence intensity and the thickness of the rubrene films. To observe if the plasmon resonance influenced the excitation of the rubrene, each PLE spectrum is compared to the PLE spectrum of a rubrene-only film spun at the corresponding rotation rate. These spectra are compared in Figure 144.

The effects of plasmon-enhanced rubrene excitation would be expected to be observed as a relative increase in PLE intensity near the resonant plasmon wavelengths. Figure 144 shows that the nanoparticles cause no significant spectral differences for the rubrene films spun at 2000-8000 RPM (a-d). However, a 3 nm blue-shift of the 498 nm and 533 nm peaks in the PLE was observed on the thinnest films spun at 10000 and 12000 RPM. These blue-shifts might be due to increased photoabsorption induced by the tail of the plasmon peak centred around 400-420 nm.

The TRPL data were collected to observe the influence of the nanoseed sublayer on the fluorescence lifetimes of the rubrene films. The TRPL spectra for this nanoseed sublayer series are compared to the TRPL spectra of the rubrene films without a nanoparticle sublayer in Figure 145.

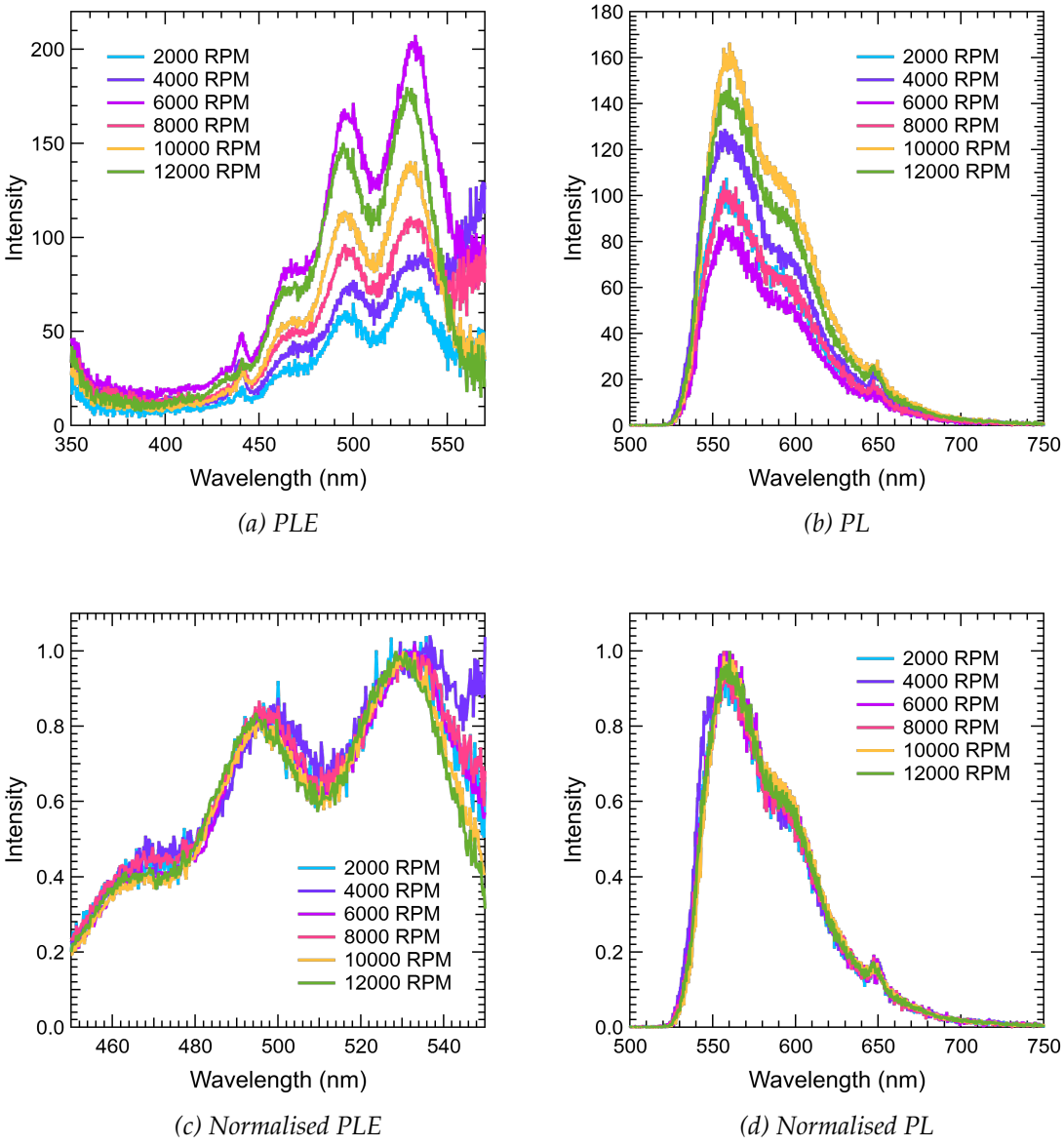


*(a) PLE*

*(b) PL*

*(c) Normalised PLE*

*(d) Normalised PL*

*Figure 143: PLE ($\lambda_{em} = 600nm$) and PL ($\lambda_{ex} = 475nm$) spectra of rubrene overlays at increasing spin rates, from 2000-12000 RPM, on 44K PVP-capped nanoseed films. Compared to the normalised PLE (c) and PL (d) spectra*

The decays of the films with a nanoseed sublayer all show a considerable drop in emission lifetime compared to the rubrene-only decays. This is likely due to fast energy transfer into the metal. The PL lifetimes for the films with and without a nanoseed sublayer are compared in Figure 146. The rubrene films have a slightly longer decay time, approximately 13-15 ns, compared to solution-phase rubrene at 10.6 ns, but there is little correlation with spin rate. The spectra of the rubrene films with a nanoseed sublayer exhibit a slight decay lengthening of approximately 0.7 ns with increasing spin rate, but the reason for this is unclear.

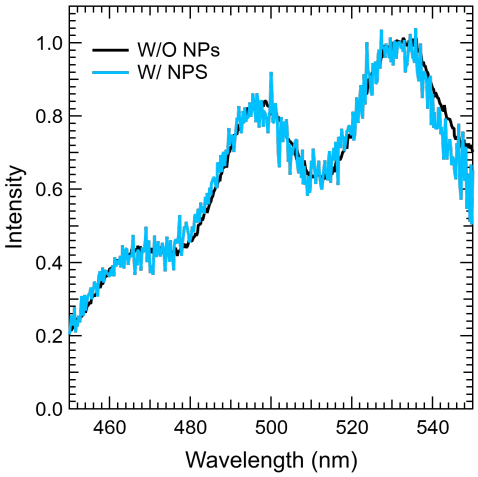


*(a) 2000 RPM*

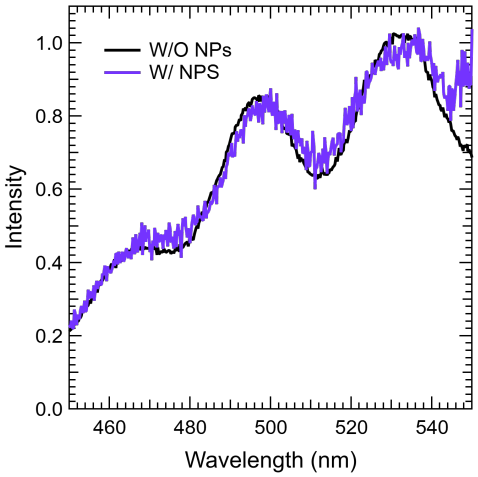


*(b) 4000 RPM*

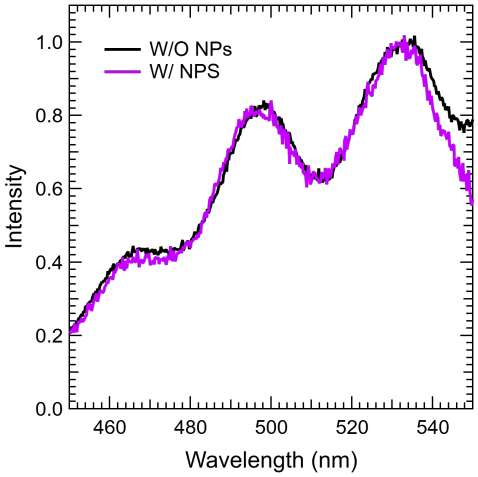


*(c) 6000 RPM*

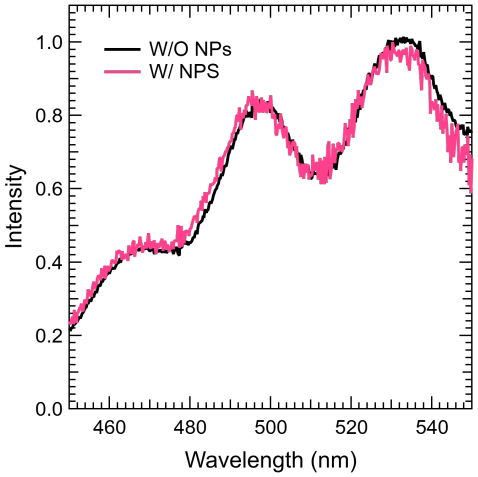


*(d) 8000 RPM*

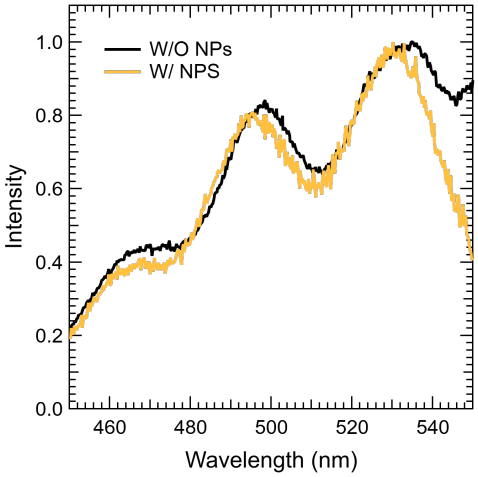


*(e) 10000 RPM*

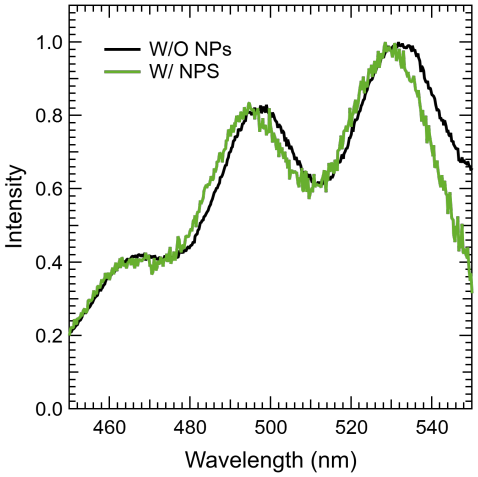


*(f) 12000 RPM*

*Figure 144: PLE ($\lambda_{em} = 600nm$) spectra of rubrene overlays at increasing spin rates, from 2000-12000 RPM, with and without a 44K PVP-capped nanoseed sublayer*

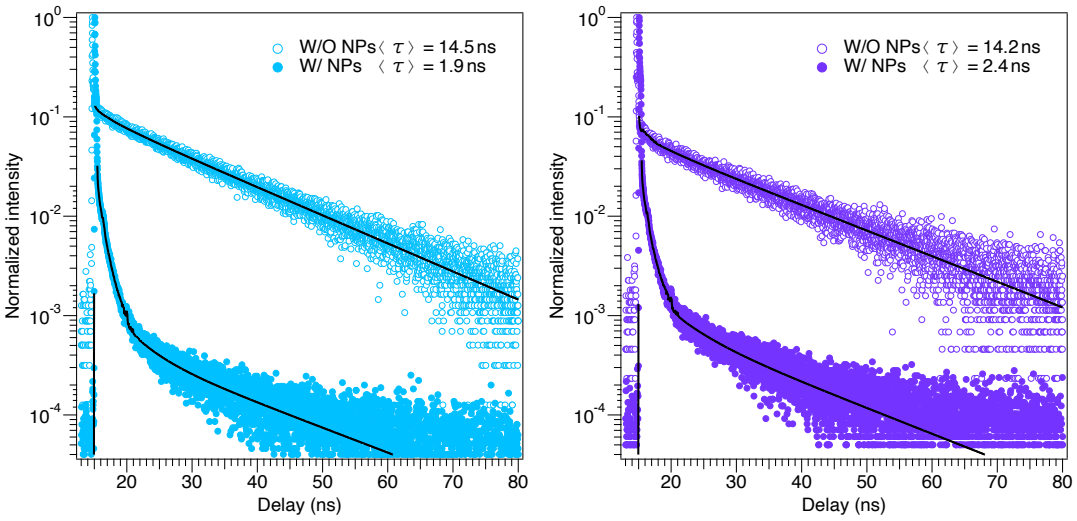


(a) 2000 RPM




(b) 4000 RPM

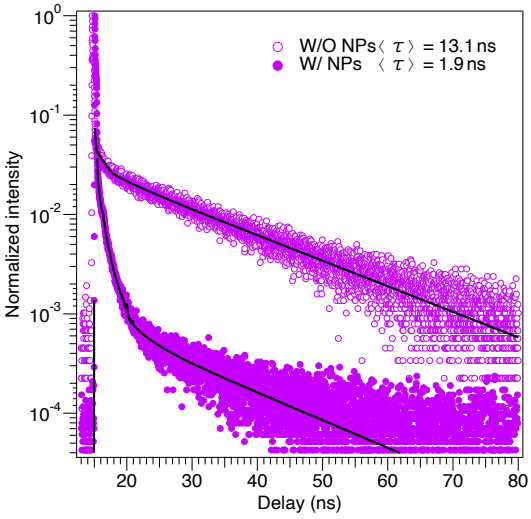


(c) 6000 RPM

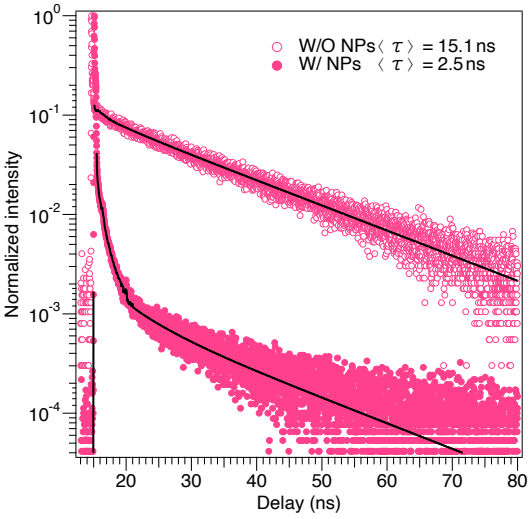


(d) 8000 RPM

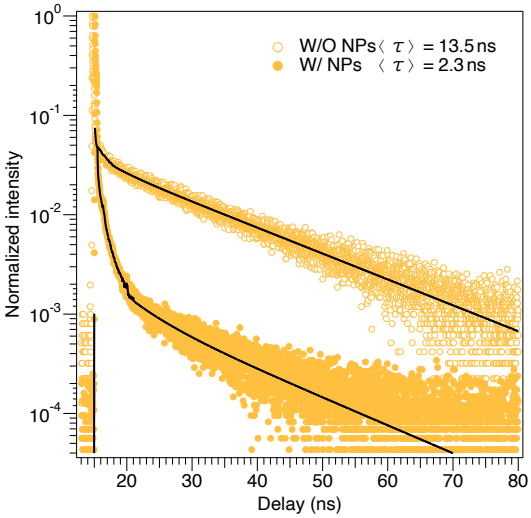


(e) 10000 RPM

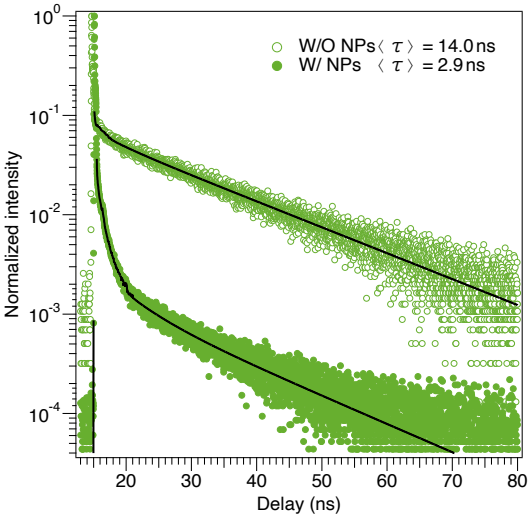


(f) 12000 RPM

*Figure 145: TRPL spectra of rubrene films with and without a 44K PVP capped nanoseed sublayer. The rubrene films were spun at an increasing rotation rate of 2000-12000 RPM in 2000 RPM increments*

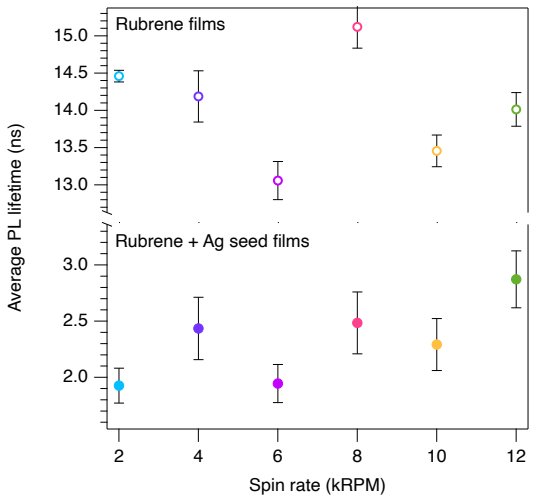


*Figure 146: PL lifetimes of rubrene films with and without a 44K PVP capped nanoseed sublayer. The rubrene films were spun at an increasing rotation rate of 2000-12000 RPM in 2000 RPM increments*

A second set of films was created to compare the potential for MEF in rubrene overlaid on a nanoparticle sublayer fabricated with 29K or 44K nanoseed particles. The absorbance spectrum of the rubrene-coated nanoparticle sublayer is compared to the extinction spectrum of the two nanoseed films, as illustrated in Figure 147 below.

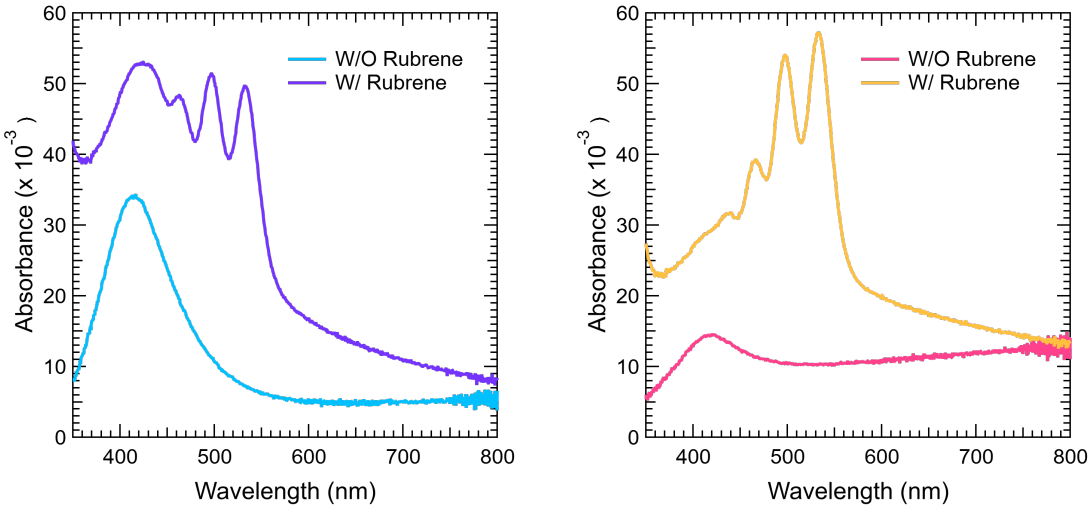


*(a) 29K PVP-capped Seed Film*

*(b) 44K PVP-capped Seed Film*

*Figure 147: Extinction spectra of 29K (a) and 44K (b) PVP-capped nanoseed films with and without a rubrene overlay spun at 6000 RPM*

Figure 147 shows that the extinction of the nanoparticle film can be observed in the absorbance spectra of the rubrene overlay if the extinction intensity is high enough. This is especially apparent in the sample featuring the 29K nanoseed sublayer, where the ab-

sorbance spectrum of the rubrene overlay exhibits a significant peak in the 400-450 nm range. This peak is not a spectral characteristic typically observed in a film composed solely of rubrene. The PL spectra for both films are presented in Figure 148 below.

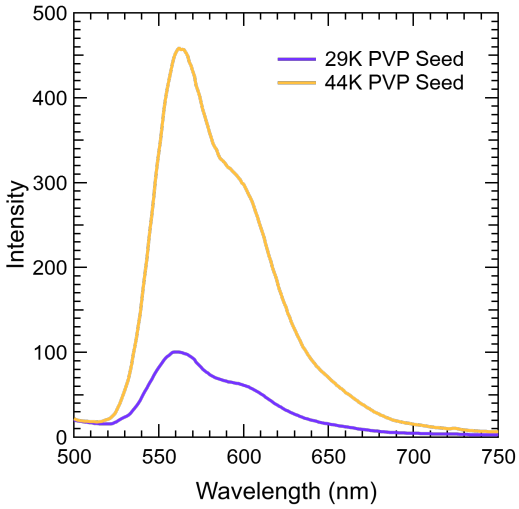


*Figure 148: PL ($\lambda_{ex} = 475nm$) spectrum of 29 and 44K PVP-capped seed films with a rubrene overlay, spun at 6000 RPM*

Interestingly, the intensity of the PL for the 29K PVP nanoseed film is significantly lower than the 44K PVP nanoseed film. This dynamic difference in intensity suggests that fluorescence quenching occurs in the 29K nanoseed sample due to the lack of distance between the metal nanoparticle sublayer and the rubrene overlay.

#### 5.3.1.2 Anisotropic Nanoparticle SubLayers - CTAB

The subsequent experiments aimed to increase the complexity of the nanoparticle structures used in the sublayers, from nanoseeds to anisotropic nanostructures with tunable SPR peaks. This was done to investigate the impact of spectral overlay on this system.

The first series investigated the PLE and PL spectra of the rubrene overlay of immobilised nanoparticles redispersed in CTAB, with a 1:1 ratio introduction of NaCl at a final concentration of 100 mM. The extinction of the nanoparticle films is depicted in Figure 149. This spectrum was thoroughly discussed in Section 4.4.1.1.

The PLE and PL spectra for these nanoparticle sublayers overlaid with rubrene spun at 6000 RPM are depicted in Figure 150. Similarly to previous experiments, there is no clear correlation between the extinction intensity and the PLE and PL spectra. Additionally, the extinction spectra do not exhibit distinctive SPR spectral features, which complicates the identification of a trend in the PLE and PL intensity with the SPR peaks of the

nanoparticle sublayer.

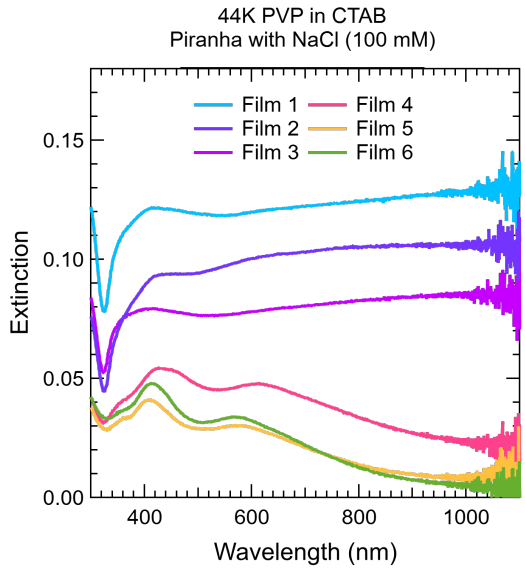


*Figure 149: Extinction spectrum of silver nanoparticle films fabricated using solutions with increasing 44K PVP-capped seeds from 50-300 µL in 50 µL increments (Film 1-6). The glass substrates were piranha cleaned. Particles were redispersed in CTAB (10 mM), and NaCl (100 mM) was introduced in a 1:1 volume ratio before fabrication*

The second series investigated the PLE and PL spectra of the rubrene overlay of immobilised nanoparticles redispersed in CTAB with a 500 µL addition of NaCl with a final concentration of 100 mM. The extinction of the nanoparticle films is illustrated in Figure 151. This spectrum was thoroughly discussed in Section 4.4.1.1.

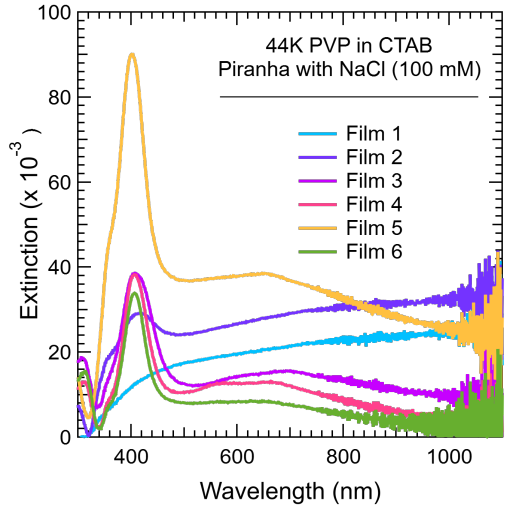


*Figure 151: Extinction spectrum of silver nanoparticle films fabricated using solutions with increasing 44K PVP-capped seeds from 50-300 µL in 50 µL increments (Film 1-6). The glass substrates were piranha cleaned. Particles were redispersed in CTAB (10 mM), and NaCl (100 mM) was introduced before fabrication*

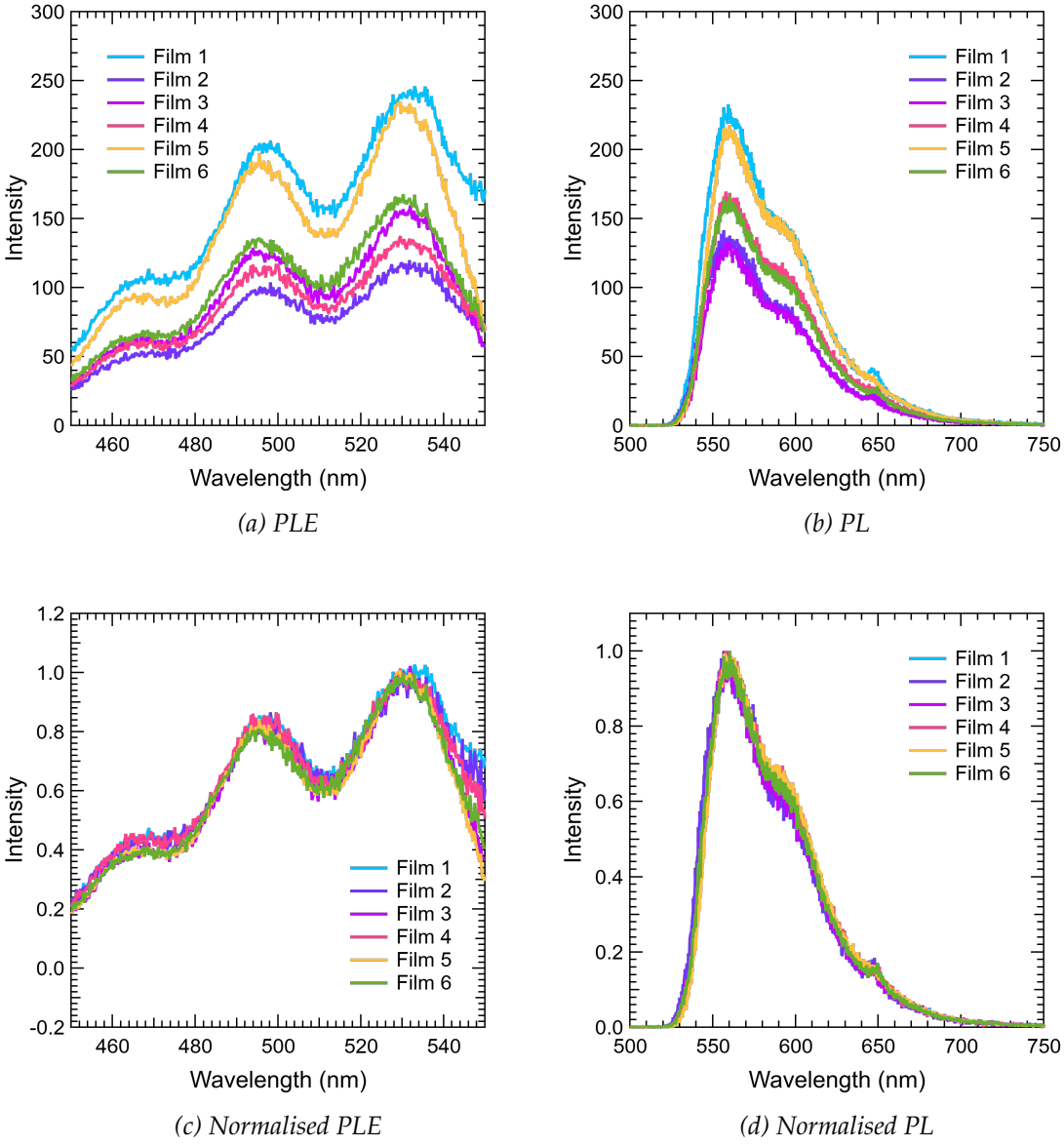


*(a) PLE*

*(b) PL*

*(c) Normalised PLE*

*(d) Normalised PL*

*Figure 150: PLE ($\lambda_{em} = 600nm$) and PL ($\lambda_{ex} = 475nm$) spectra of silver nanoparticle films with a rubrene overlay spun at 6000 RPM. Compared to the normalised PLE (c) and PL (d) spectra. Particles were redispersed in CTAB (10 mM), and NaCl (100 mM) was introduced in a 1:1 volume ratio before fabrication*

The PLE and PL spectra for these nanoparticle sublayers overlaid with rubrene spun at 6000 RPM are depicted in Figure 152 below. Similar to the previous film series, no distinct correlation is observed between extinction intensity and PLE and PL intensities. However, there is a noticeable increase in intensity for films 2, 3, and 5. Film 5, which displayed the highest intensity extinction, also exhibited the highest PLE and PL intensity. The maximum PLE intensity for this film rose from 230 to 970 compared to the previous series. Nevertheless, this rise in intensity is not mirrored in the PL intensity for this film. The inconclusive data underscore the need for further investigation and a more re-

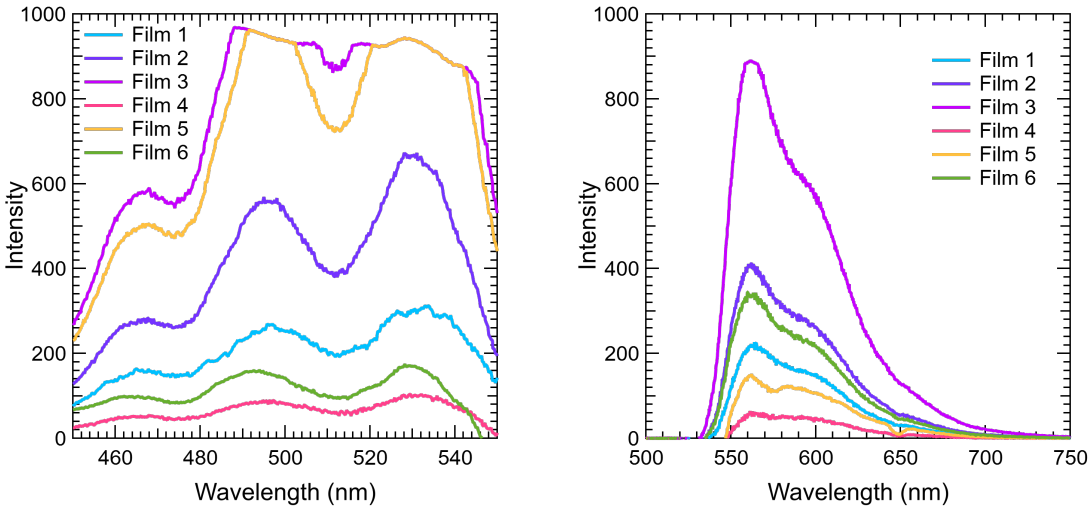


*(a) PLE* *(b) PL*

*Figure 152: PLE ($\lambda_{em} = 600nm$) and PL ($\lambda_{ex} = 475nm$) spectra of silver nanoparticle films with a rubrene overlay spun at 6000 RPM. Compared to the normalised PLE (c) and PL (d) spectra. Particles were redispersed in CTAB (10 mM), and NaCl (100 mM) was introduced as 500 µL before fabrication*

producible data collection method with greater control over critical parameters, such as sample positioning.

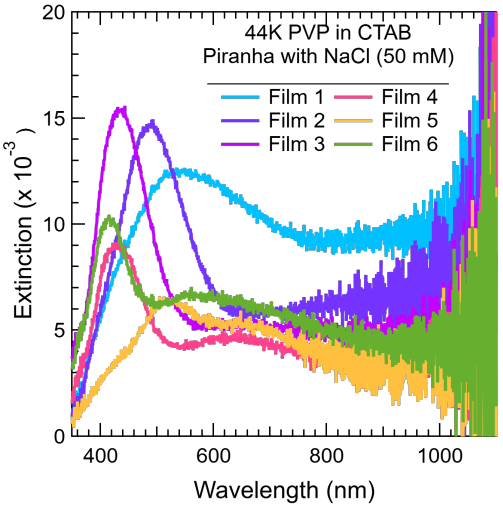


*Figure 153: Extinction spectrum of silver nanoparticle solutions and resulting films with increasing 44K PVP-capped seeds from 50-300 µL in 50 µL increments (Film 1-6). The glass substrates were piranha cleaned. Particles were redispersed in CTAB (10 mM), and NaCl (50 mM) was introduced before fabrication. In Figure (a), the detector was saturated at 500 nm*

The third series investigated the PLE and PL spectra of the rubrene overlay of immobilised nanoparticles redispersed in CTAB with the addition of 500 µL of NaCl with

a final concentration of 50 mM. The extinction of the nanoparticle films can be seen in Figure 153. This spectrum was thoroughly discussed in Section 4.4.1.1.

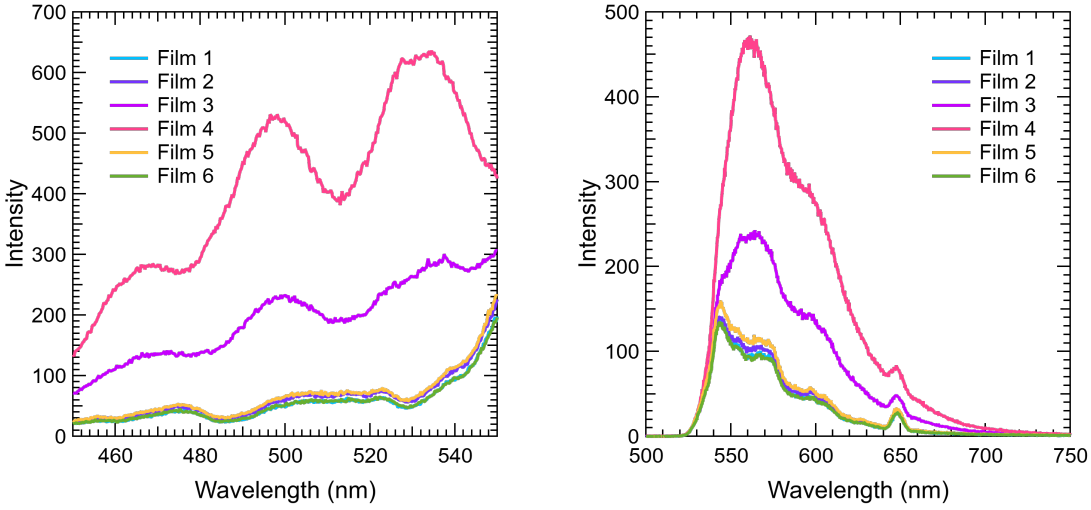


*(a) PLE* *(b) PL*

*Figure 154: PLE ($\lambda_{em} = 600nm$) and PL ($\lambda_{ex} = 475nm$) spectra of silver nanoparticle films with a rubrene overlay spun at 6000 RPM. Compared to the normalised PLE (c) and PL (d) spectra. Particles were redispersed in CTAB (10 mM), and NaCl (50 mM) was introduced as 500 µL before fabrication*

The PLE and PL spectra for these nanoparticle sublayers overlaid with rubrene spun at 6000 RPM are depicted in Figure 154. Notably, the typical spectral characteristics of rubrene are not observed in the PLE or PL spectra for films 1, 2, 5, and 6.

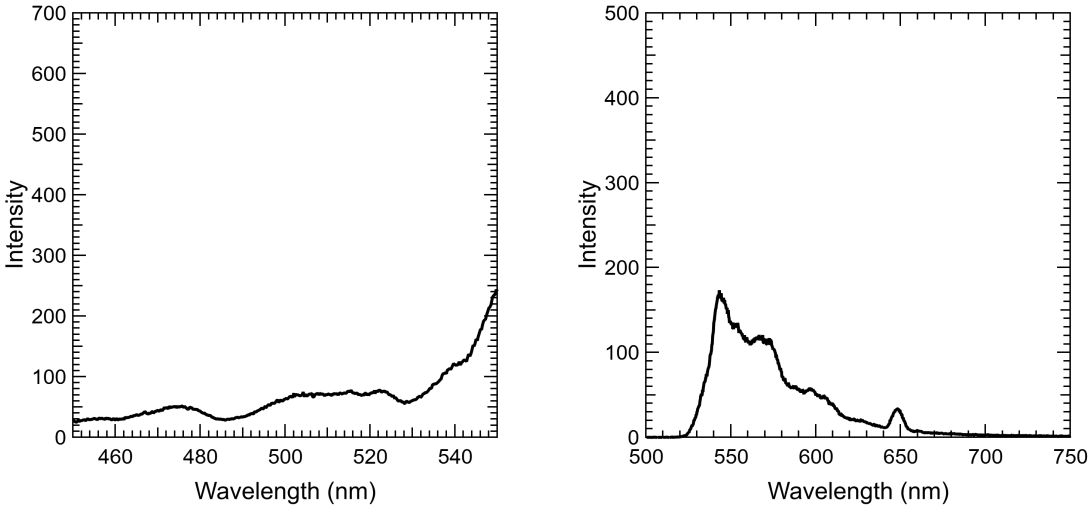


*(a) PLE* *(b) PL*

*Figure 155: PLE ($\lambda_{em} = 600nm$) and PL ($\lambda_{ex} = 475nm$) spectra blank of a piranha cleaned glass substrate in the 3D printed sample holder*

The spectra for these films resemble the blank used to account for the response from the sample holder material. The PLE and PL spectra collected for a blank piece of glass in the sample holder are presented in Figure 155.

The PLE and PL spectra for these films show none of the spectral characteristics typical of a rubrene film. This can be explained by the rubrene and nanoparticle layers not being separated by a spacer layer, which allows a considerable amount of quenching to occur into the metal sublayer. Alternatively, this could also highlight an issue in the fabrication protocol. The 6000 RPM rotation rate may be unsuitable to produce a uniform thin film over these nanoparticle sublayers.

#### 5.3.1.3 Anisotropic Nanoparticle SubLayers - Type I Water

The final series investigated the PLE and PL spectra of the rubrene overlay of immobilised nanoparticles redispersed in Type I water. The extinction of the nanoparticle films is depicted in Figure 156. This spectrum was thoroughly discussed in Section 4.4.1.1.

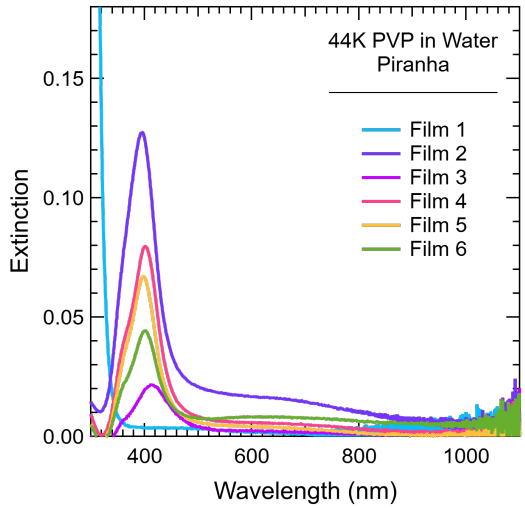


*Figure 156: Extinction spectrum of silver nanoparticle films fabricated with solutions using increasing 44K PVP-capped seed volumes from 50-300 µL in 50 µL increments (Film 1-6). Particles were redispersed in Type I water before fabrication*

The PLE and PL spectra for these nanoparticle films coated with a rubrene overlay spun at 6000 RPM are illustrated in Figure 157 below. Similar to the previous film series, there is no notable correlation between extinction intensity and the PLE and PL intensities. The PLE data of this series resemble the films produced using particles redispersed in CTAB with a 500 µL addition of NaCl (100 mM). Notably, the PLE and PL intensities are lower for this series than the CTAB series with a 500 µL addition of NaCl (50 mM).

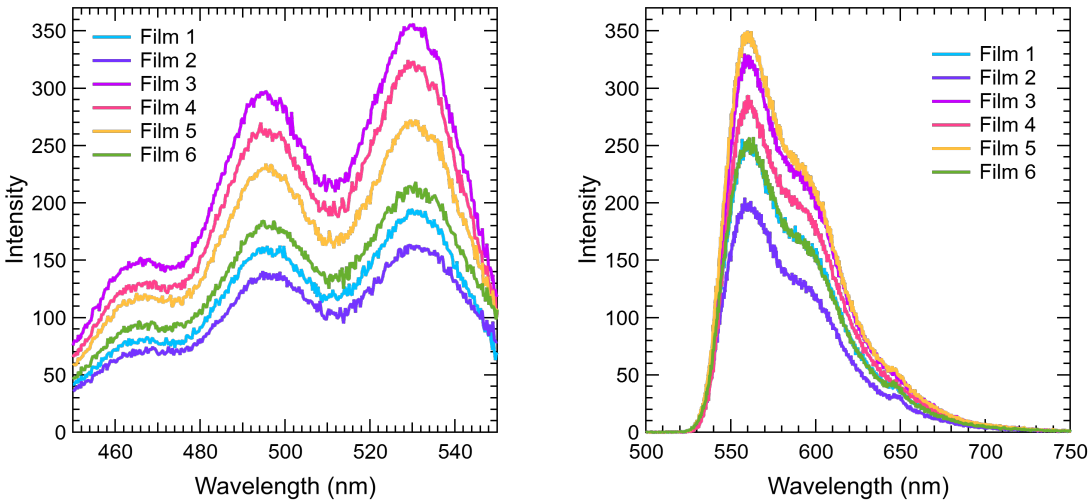


*(a) PLE* *(b) PL*

*Figure 157: PLE ($\lambda_{em} = 600nm$) and PL ($\lambda_{ex} = 475nm$) spectra of silver nanoparticle films with a rubrene overlay spun at 6000 RPM. Compared to the normalised PLE (c) and PL (d) spectra. Particles were redispersed in Type I water*

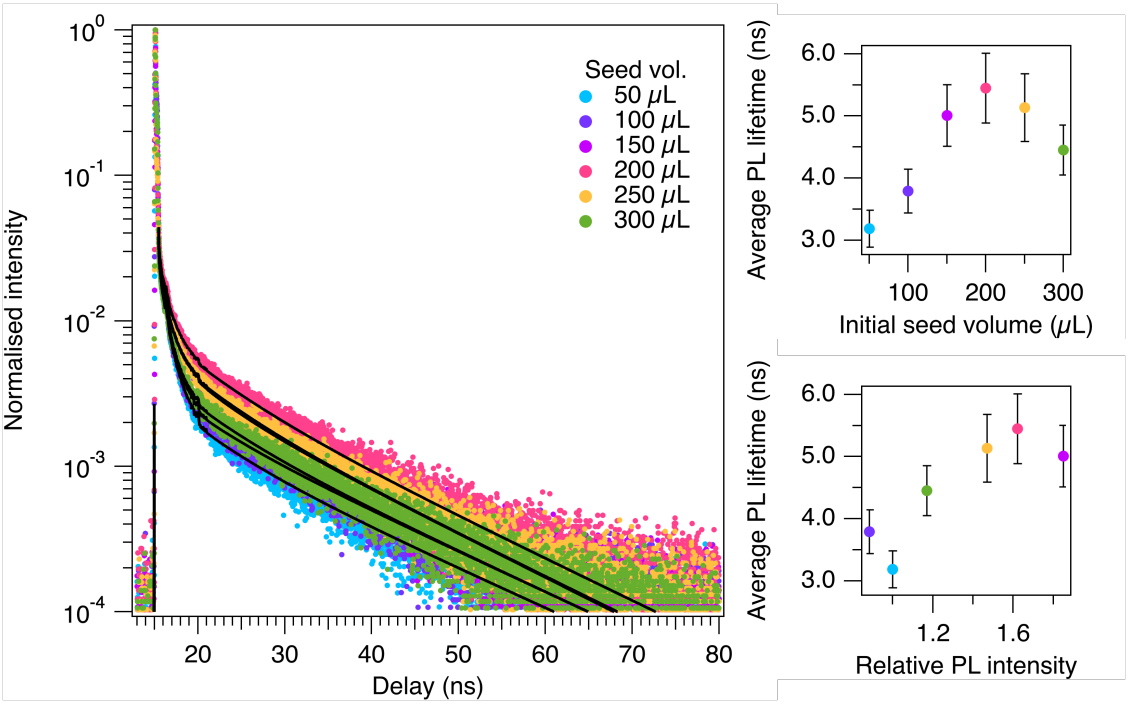


*Figure 158: TRPL spectra of silver nanoparticle films with a rubrene overlay spun at 6000 RPM. Nanoparticle films were produced using nanoparticle solutions with increasing 44K PVP-capped seed volumes from 50-300 µL in 50 µL increments (Film 1-6)*

The TRPL spectra for this series are compared in Figure 158. These nanoparticle sublayers show similarly short lifetimes as the samples with a nanoseed sublayer. However, a stronger correlation is observed between the PL lifetimes and the initial seed volumes

used in the Ag NP syntheses. Lifetimes peaked for the 200 µL NPs, which indicates that there may be some spectral dependence on the energy transfer rate. In the absence of plasmon-enhanced emission, shorter lifetimes should correspond to lower emission intensities, and this is what we observe in the plot of emission lifetime versus normalised steady-state PL intensity. There is no indication of plasmonic effects, and only evidence of quenching into the metal sublayer is observed.

### 5.3.2 Discussion

These experiments aimed to investigate any possible metal-enhanced fluorescence observed in rubrene films overlaid onto various nanoparticle sublayers with a range of plasmon resonance features.

When the rubrene film was overlaid onto a sublayer of 44K PVP seeds, a wavelength shift of the three signature peaks for rubrene was observed when the thickness of the rubrene film was decreased. In the previous experiment, without the nanoparticle sublayer, the peaks showed a blue-shift when the rotation rate increased, and the thickness of the films decreased.

A further blue-shift is observed in Figure 144 when the PLE spectra of the films at decreasing thicknesses were compared with and without a silver nanoparticle sublayer. The two thinnest films exhibited a significant blue-shift when the nanoparticle sublayer was introduced. These blue-shifts are likely due to increased photoabsorption induced by the tail of the plasmon peak centred around 400-420 nm. The TRPL decays of the films with a nanoseed sublayer all show a considerable drop in emission lifetime compared to the rubrene-only decays, likely due to fast energy transfer into the metal.

The second nanoseed experiment compared the PLE and PL spectra of rubrene films with a 29K or 44K nanoseed sublayer. Similar to the findings by Han et al., critical changes to the extinction spectral profile were observed when the rubrene thin film was overlaid on top of the nanoseed film.[81]

This is particularly noticeable in the extinction spectra that compare the 29K and 44K PVP-capped nanoseed films in Figure 147. The extinction intensity of the 29K film is significantly higher than the 44K film. This caused a significant increase in the 400-450 nm region of the absorbance spectra of the rubrene overlay. In contrast, this region has a significantly smaller increase for the 44K film. An opposing trend was observed in the fluorescence intensities in Figure 148, with the 29K seed film with a rubrene overlay showing a significantly lower fluorescence intensity than the 44K seed film.

The nanoseed sublayers, which exhibited an SPR peak in the 400-420 nm range, showed a reduction in PL intensity accompanied by a slight blue-shift in the characteristic rubrene PLE peaks. These observations indicate that incorporating the plasmonic layer results in a moderate enhancement of photoabsorption. However, the decreased PL intensity relative to the rubrene films without a plasmonic sublayer, in Figure 157, implies that the absence of a spacer layer leads to quenching of any potential fluorescence enhancement due to interactions with the metal.

The second series of experiments aimed to adjust the SPR closer to ($\lambda_{ex} = 475nm$) to explore potential plasmon enhancement. The fabrication of nanoparticle films with particles redispersed in CTAB posed a significant challenge to the device fabrication. As discussed previously in Chapter 4, incorporating NaCl was necessary to facilitate the immobilisation of these nanoparticles onto hydroxylated glass substrates. However, the presence of NaCl substantially impacted the shape and stability of the nanoparticles.

At a final concentration of 100 mM and a 1:1 volume ratio, NaCl caused the triangular nanoplates to truncate into circular nanoplates and decreased the colloidal stability of the suspension, resulting in a high degree of particle clustering on the film. This is evident in the extinction of these nanoparticle films in Figure 149, making it difficult to correlate the PLE and PL spectra of the rubrene film to the plasmon resonance features of these nanoparticle sublayers.

In contrast, reducing the volume of the NaCl introduction to 500 µL resulted in similar truncation of the nanoplates but significantly reduced the degree of particle clustering on the film. This is reflected in the extinction spectra in Figure 151, where a single sharp peak is observed in the 410 nm region of the spectrum for all of the film samples. The extinction spectra for this series of films are very similar to those for nanoparticle films produced with particles redispersed in Type I water in Figure 156. However, there is a notable difference in the optical response across the remaining visible and NIR regions of the spectrum for the CTAB particle series. There is little to no activity outside the 390-450 nm region for the Type I water series.

This difference is reflected in the PLE and PL spectra of these two series with a rubrene overlay. The Type I water series has PLE and PL intensities resembling those of the rubrene films with a 44K PVP seed sublayer. In comparison, the CTAB series exhibits a sharp rise in intensity, particularly for films 3 and 5, which show a secondary peak in the yellow-red region of the spectrum, suggesting that a red-shifted spectral overlap may enhance the PLE and PL intensities more effectively.

This observation is also prominent in the final CTAB particle series, where the NaCl concentration was reduced to 50 mM. The SEM images of these films discussed in Section 4.4.1.2 show that the particles still truncate at this concentration but maintain a higher degree of angularity than at higher concentrations. Again, this is reflected in the nanoparticle film extinction spectra in Figure 153. This is the only series that observes a tuning of the prominent SPR peak as the particle size is altered. This means that the predominant resonance peak from these films spans from 400 to 540 nm, with many of the films exhibiting a secondary peak or shoulder in the yellow-red and into the NIR regions of the spectrum.

In contrast to the previous series, most of these films had no PLE or PL intensity. Films 3 and 4 were the only two films to show PLE and PL. The lack of PLE and PL intensity for the remaining four films in the series suggests that quenching occurs within the metal sublayer due to the absence of a spacer layer between the nanoparticles and the rubrene overlay.

## 5.4 Conclusion

This chapter was a proof of concept for investigating the application of the nanoparticle films fabricated in Chapter 4 to enhance light-matter interactions in a rubrene overlay. The spectroscopic data collected for the rubrene films overlaid on nanoparticle sublayers showed no evidence of metal-enhanced fluorescence. One of the main observations in these experiments was a slight blue-shift in the PL peak wavelengths, primarily observed when the thickness of the rubrene film was the thinnest. These blue-shifts were attributed to increased photoabsorption induced by the tail of the SRP peak of the nanoparticle sublayer.

Another critical observation was a considerable drop in the fluorescence lifetimes of the rubrene decays when a nanoparticle sublayer was introduced. However, these shorter lifetimes corresponded to lower emission intensities in the absence of plasmon-enhanced emission. Therefore, there is no indication of plasmonic effects and only evidence of quenching into the metal sublayer

# 6 Chapter 6 - Conclusion and Future Work

## 6.1 Conclusion

The overall aim of this project is the fabrication of a plasmon-enhanced photon up-conversion device. The work in this thesis details a series of optimisation experiments that resulted in the fabrication of resonance-tune silver nanoparticle sublayers that will be incorporated into this device.

Chapter 3 focuses on the synthesis and characterisation of silver and silver-gold core nanoparticles. It presents an optimised method for producing a high yield of triangular nanoplates. Notably, the SPR frequencies of these nanoparticle suspensions can be tuned by varying the volume of seed solution added to the growth solution. Additionally, this chapter examines the effects of different seed-capping reagents on the size, shape, and stability of the resulting nanoparticles. Furthermore, it explores the stability of the morphological features of the nanoparticles. It demonstrates how thermodynamically unstable features can be effectively stabilised by reintroducing CTAB after purification or by incorporating excess PVP during the synthesis. The findings in this chapter formed the basis for the key considerations in developing an effective nanoparticle immobilisation protocol, explored in Chapter 4.

Chapter 4 focuses on optimising an effective protocol for immobilising the nanoparticles synthesised in Chapter 3 onto glass substrates. Various substrate modification protocols were investigated to determine the optimal conditions for immobilisation. The experiments concluded that a hydroxylated substrate, with no further modifications, was the most suitable for fabricating a monolayer nanoparticle film. Further functionalisation of the glass substrates using MPTMS or APTES/PSS did not improve the particle density in the films and often resulted in clustering.

The findings in the synthesis experiments emphasised the importance of reintroducing CTAB into the particle suspension after purification to maintain the stability and angularity of the synthesised triangular nanoplates. When the nanoparticles are redispersed in Type I water, they readily deposit onto the hydroxylated substrate, forming a monolayer film. In contrast, it was observed that high concentrations of CTAB hindered the deposition of particles onto the substrate. The experiments concluded that incorporating NaCl into the nanoparticle suspension would facilitate deposition; however, at high NaCl concentrations, the stability and angularity of the nanoparticles are compromised. This chapter outlined the optimised conditions for successfully fabricat-

ing nanoparticle films with a tunable SPR peak. These nanoparticle films were overlaid with rubrene in Chapter 5 to explore solid-state plasmonic enhancement.

Chapter 5 focuses on the spectroscopic analysis of rubrene films overlaid onto the nanoparticle sublayers discussed in Chapter 4. This chapter serves as a proof of concept to investigate any potential metal-enhanced absorption and fluorescence in this system. The spectroscopic data revealed no evidence of metal-enhanced fluorescence occurring in the films. However, a significant decrease in fluorescence lifetimes was noted when the nanoparticle sublayer was introduced. The confirmed absence of plasmon-enhanced emission suggests that these shorter lifetimes correspond to lower emission intensities. In conclusion, there was no indication of plasmonic enhancement; instead, evidence of quenching was observed in the metal sublayer.

## 6.2 Future Work

The schematic in Figure 1 highlighted the layers required to fabricate the proposed plasmon-enhanced up-conversion device. This work focused on optimising the plasmonic sublayer.

The optimised synthesis described in Chapter 3 demonstrates that the surface plasmon resonance (SPR) of the synthesised nanoparticle suspension can be effectively adjusted across the spectrum. However, the process still yields a mixture of morphologies. The instability of the triangular nanoplates at low concentrations of CTAB presents both advantages and disadvantages in addressing this issue. At low CTAB concentrations, these triangular nanoplates tend to truncate, resulting in an abundance of small circular nanoplates. The significant volume difference between these circular nanoplates and the nanorods in suspension could facilitate the purification of nanorods through centrifugation or size-exclusion chromatography. This purification process would lead to an effective method for synthesising size-tunable nanorods without the presence of excess nanostructures. Ultimately yielding a high quantity of silver nanorods, solving a challenge that has long been faced by researchers in nanoparticle synthesis.

The successful immobilisation of the nanoparticles redispersed in CTAB was described in Chapter 4. The incorporation of NaCl into the fabrication protocol was necessary to facilitate the deposition of nanoparticles on the substrate. However, this addition compromised the stability of the particles and reduced the range of accessible SPR wavelengths that is achieved when the nanoparticles are in solution. The next step is to explore other salts that can alter the ionic strength of the nanoparticle solution. Finding a salt that facil-

itates nanoparticle deposition without causing truncation would significantly expand the range of SPR wavelengths that can be achieved from the fabricated nanoparticle films.

To advance this investigation, it is essential to develop a fabrication protocol for the polyelectrolyte spacer layers with precisely controlled thickness. The spectroscopic data in this thesis highlight fluorescence quenching in the metal sublayer as a significant issue. Incorporating a spacer layer offers a practical solution to this issue. By utilising this device design in conjunction with a broader range of SPR-tuned nanoparticle films, we can expand the exploration of plasmon-enhanced light-matter interactions to an almost limitless variety of fluorophores. Ultimately, the optimised synthesis and fabrication protocols described in this thesis will be used to fabricate an effective plasmon-enhanced up-conversion device. This device will feature a resonance-tuned plasmonic sublayer, ensuring the highest possible up-conversion efficiency within the system.

## References


(1) Kelly, K. L.; Coronado, E.; Zhao, L. L.; Schatz, G. C. *J. Phys. Chem. B* **2003**, *107*, 668–677.

(2) Lee, K.-S.; El-Sayed, M. A. *J. Phys. Chem. B* **2006**, *110*, 19220–19225.

(3) Liu, Z.; Zhao, F.; Gao, S.; Shao, J.; Chang, H. *Nanoscale Res. Lett.* **2016**, *11*, 460.

(4) Jiménez-Solano, A.; Galisteo-López, J. F.; Míguez, H. *J. Phys. Chem. Lett.* **2018**, *9*, 2077–2084.

(5) Yu, R.; Lin, Q.; Leung, S.-F.; Fan, Z. *Nano Energy* **2012**, *1*, 57–72.

(6) Rycenga, M.; Cobley, C. M.; Zeng, J.; Li, W.; Moran, C. H.; Zhang, Q.; Qin, D.; Xia, Y. *Chem. Rev.* **2011**, *111*, 3669–3712.

(7) Calderón-Jiménez, B.; Johnson, M. E.; Montoro Bustos, A. R.; Murphy, K. E.; Winchester, M. R.; Vega Baudrit, J. R. *Front. Chem.* **2017**, *5*, 6.

(8) Xia, Y.; Xiong, Y.; Lim, B.; Skrabalak, S. E. *Angew. Chem. Int. Ed Engl.* **2009**, *48*, 60–103.

(9) Zhu, X.; Yip, H. K.; Zhuo, X.; Jiang, R.; Chen, J.; Zhu, X.-M.; Yang, Z.; Wang, J. *J. Am. Chem. Soc.* **2017**, *139*, 13837–13846.

(10) Roach, L.; Coletta, P. L.; Critchley, K.; Evans, S. D. *J. Phys. Chem. C Nanomater. Interfaces* **2022**, *126*, 3235–3243.

(11) Sánchez-Iglesias, A.; Zhuo, X.; Albrecht, W.; Bals, S.; Liz-Marzán, L. M. *ACS Mater. Lett.* **2020**, *2*, 1246–1250.

(12) Zhang, Q.; Li, N.; Goebl, J.; Lu, Z.; Yin, Y. *J. Am. Chem. Soc.* **2011**, *133*, 18931–18939.

(13) Zayats, A. V.; Smolyaninov, I. I. *J. Opt. Pure Appl. Opt.* **2003**, *5*, S16–S50.

(14) BioRender Accessed: 24-09-2024, `https://www.biorender.com/`.

(15) Li, K.; Jia, X.; Tang, A.; Zhu, X.; Meng, H.; Wang, Y. *Integr. Ferroelectr.* **2012**, *136*, 9–14.

(16) Oldenburg, S. J. *Doctoral dissertation, Rice University* **2000**.

(17) Chen, H.; Shao, L.; Li, Q.; Wang, J. *Chem. Soc. Rev.* **2013**, *42*, 2679–2724.

(18) Turkevich, J.; Stevenson, P. C.; Hillier, J. *Discuss. Faraday Soc.* **1951**, *11*, 55.

(19) Polte, J.; Ahner, T. T.; Delissen, F.; Sokolov, S.; Emmerling, F.; Thünemann, A. F.; Kraehnert, R. *J. Am. Chem. Soc.* **2010**, *132*, 1296–1301.

(20) Suchomel, P.; Kvitek, L.; Prucek, R.; Panacek, A.; Halder, A.; Vajda, S.; Zboril, R. *Sci. Rep.* **2018**, *8*, 1–11.

(21) Patil, T.; Gambhir, R.; Vibhute, A.; Tiwari, A. P. *J. Cluster Sci.* **2023**, *34*, 705–725.

(22) Baburin, A. S.; Merzlikin, A. M.; Baryshev, A. V.; Ryzhikov, I. A.; Panfilov, Y. V.; Rodionov, I. A. *Opt. Mater. Express* **2019**, *9*, 611.

(23) Zhang, X.-F.; Liu, Z.-G.; Shen, W.; Gurunathan, S. *Int. J. Mol. Sci.* **2016**, *17*, 1534.

(24) Habibullah, G.; Viktorova, J.; Ruml, T. *Nanoscale Res. Lett.* **2021**, *16*, 47.

(25) Roy, A.; Bulut, O.; Some, S.; Mandal, A. K.; Yilmaz, M. D. *RSC Adv.* **2019**, *9*, 2673–2702.

(26) Salabat, A.; Mirhoseini, F. *J. Mol. Liq.* **2018**, *268*, 849–853.

(27) Flores-Rojas, G. G.; López-Saucedo, F.; Bucio, E. *Radiat. Phys. Chem. Oxf. Engl. 1993* **2020**, *169*, 107962.

(28) Jeyaraj, M.; Gurunathan, S.; Qasim, M.; Kang, M.-H.; Kim, J.-H. *Nanomaterials (Basel)* **2019**, *9*, 1719.

(29) Iravani, S.; Korbekandi, H.; Mirmohammadi, S. V.; Zolfaghari, B. *Res. Pharm. Sci.* **2014**, *9*, 385–406.

(30) Pastoriza-Santos, I.; Liz-Marzán, L. M. *Langmuir* **1999**, *15*, 948–951.

(31) Mafuné, F.; Kohno, J.-Y.; Takeda, Y.; Kondow, T.; Sawabe, H. *J. Phys. Chem. B* **2000**, *104*, 8333–8337.

(32) Jung, J. H.; Cheol Oh, H.; Soo Noh, H.; Ji, J. H.; Soo Kim, S. *J. Aerosol Sci.* **2006**, *37*, 1662–1670.

(33) Ramnani, S. P.; Biswal, J.; Sabharwal, S. *Radiat. Phys. Chem. Oxf. Engl. 1993* **2007**, *76*, 1290–1294.

(34) Jana, N. R.; Gearheart, L.; Murphy, C. J. *Chem. Commun. (Camb.)* **2001**, 617–618.

(35) Wiley, B.; Sun, Y.; Mayers, B.; Xia, Y. *Chemistry* **2005**, *11*, 454–463.

(36) Xue, C.; Métraux, G. S.; Millstone, J. E.; Mirkin, C. A. *J. Am. Chem. Soc.* **2008**, *130*, 8337–8344.

(37) Personick, M. L.; Mirkin, C. A. *J. Am. Chem. Soc.* **2013**, *135*, 18238–18247.

(38) CSID:5989, `https://www.chemspider.com/Chemical-Structure.5989.html`, Accessed: 03-11-2024.

(39) CSID:16635, `https://www.chemspider.com/Chemical-Structure.16635.html`, Accessed: 03-11-2024.

(40) Hue, D. T.; Hiep, H. P. *Biomed. Phys. Eng. Express* **2024**, *10*.

(41) C, F. C.; T, K. *Heliyon* **2024**, *10*, e29773.

(42) Xia, X.; Zeng, J.; Oetjen, L. K.; Li, Q.; Xia, Y. *J. Am. Chem. Soc.* **2012**, *134*, 1793–1801.

(43) Wijaya, Y. N.; Kim, J.; Choi, W. M.; Park, S. H.; Kim, M. H. *Nanoscale* **2017**, *9*, 11705–11712.

(44) Gole, A.; Murphy, C. J. *Chem. Mater.* **2004**, *16*, 3633–3640.

(45) Fales, A. M.; Yuan, H.; Vo-Dinh, T. *J. Phys. Chem. C Nanomater. Interfaces* **2014**, *118*, 3708–3715.

(46) Atta, S.; Beetz, M.; Fabris, L. *Nanoscale* **2019**, *11*, 2946–2958.

(47) Cho, N. H.; Guerrero-Martínez, A.; Ma, J.; Bals, S.; Kotov, N. A.; Liz-Marzán, L. M.; Nam, K. T. *Nat Rev Bioeng* **2023**, *1*, 88–106.

(48) Jin, W.; Liang, G.; Zhong, Y.; Yuan, Y.; Jian, Z.; Wu, Z.; Zhang, W. *Nanoscale Res. Lett.* **2019**, *14*, 81.

(49) CSID:5754, `https://www.chemspider.com/Chemical-Structure.5754.html`, Accessed: 03-11-2024.

(50) CSID:7862, `https://www.chemspider.com/Chemical-Structure.7862.html`, Accessed: 03-11-2024.

(51) Rekha, C. R.; Nayar, V. U.; Gopchandran, K. G. *J. Sci. Adv. Mater. Devices* **2018**, *3*, 196–205.

(52) Li, C.; Sun, L.; Sun, Y.; Teranishi, T. *Chem. Mater.* **2013**, *25*, 2580–2590.

(53) Patarroyo, J.; Genç, A.; Arbiol, J.; Bastús, N. G.; Puntes, V. *Chem. Commun. (Camb.)* **2016**, *52*, 10960–10963.

(54) Dong, H.; Chen, Y.-C.; Feldmann, C. *Green Chem.* **2015**, *17*, 4107–4132.

(55) Kim, D.; Jeong, S.; Moon, J. *Nanotechnology* **2006**, *17*, 4019–4024.

(56) Chen, Z.; Balankura, T.; Fichthorn, K. A.; Rioux, R. M. *ACS Nano* **2019**, *13*, 1849–1860.

(57) Tsuji, M.; Hashimoto, M.; Nishizawa, Y.; Tsuji, T. *Mater. Lett.* **2004**, *58*, 2326–2330.

(58) Zhu, Y.-J.; Hu, X.-L. *Chem. Lett.* **2003**, *32*, 1140–1141.

(59) Zhuo, X.; Zhu, X.; Li, Q.; Yang, Z.; Wang, J. *ACS Nano* **2015**, *9*, 7523–7535.

(60) Jiang, R.; Chen, H.; Shao, L.; Li, Q.; Wang, J. *Adv. Mater.* **2012**, *24*, OP200–7.

(61) Rónavári, A.; Bélteky, P.; Boka, E.; Zakupszky, D.; Igaz, N.; Szerencsés, B.; Pfeiffer, I.; Kónya, Z.; Kiricsi, M. *Int. J. Mol. Sci.* **2021**, *22*, 8673.

(62) El Badawy, A. M.; Scheckel, K. G.; Suidan, M.; Tolaymat, T. *Sci. Total Environ.* **2012**, *429*, 325–331.

(63) Tsuji, M.; Nishizawa, Y.; Matsumoto, K.; Kubokawa, M.; Miyamae, N.; Tsuji, T. *Mater. Lett.* **2006**, *60*, 834–838.

(64) Xia, X.; Zeng, J.; Oetjen, L. K.; Li, Q.; Xia, Y. *J. Am. Chem. Soc.* **2012**, *134*, 1793–1801.

(65) Mizuno, A.; Ono, A. *Appl. Surf. Sci.* **2019**, *480*, 846–850.

(66) Tylkowski, B.; Trojanowska, A.; Nowak, M.; Marciniak, L.; Jastrzab, R. *Phys. Sci. Rev.* **2017**, *2*.

(67) Borah, R.; Ninakanti, R.; Bals, S.; Verbruggen, S. W. *Sci. Rep.* **2022**, *12*, 15738.

(68) Ueno, K.; Oshikiri, T.; Sun, Q.; Shi, X.; Misawa, H. *Chem. Rev.* **2018**, *118*, 2955–2993.

(69) Zia, R.; Schuller, J. A.; Chandran, A.; Brongersma, M. L. *Mater. Today (Kidlington)* **2006**, *9*, 20–27.

(70) Rechberger, W.; Hohenau, A.; Leitner, A.; Krenn, J. R.; Lamprecht, B.; Aussenegg, F. R. *Opt. Commun.* **2003**, *220*, 137–141.

(71) Gunnarsson, L.; Rindzevicius, T.; Prikulis, J.; Kasemo, B.; Käll, M.; Zou, S.; Schatz, G. C. *J. Phys. Chem. B* **2005**, *109*, 1079–1087.

(72) Jain, P. K.; El-Sayed, M. A. *Chem. Phys. Lett.* **2010**, *487*, 153–164.

(73) Jain, P. K.; Huang, W.; El-Sayed, M. A. *Nano Lett.* **2007**, *7*, 2080–2088.

(74) Lu, Y.; Liu, G. L.; Lee, L. P. *Nano Lett.* **2005**, *5*, 5–9.

(75) Jana, J.; Ganguly, M.; Pal, T. *RSC Adv.* **2016**, *6*, 86174–86211.

(76) Yu, H.; Peng, Y.; Yang, Y.; Li, Z.-Y. *Npj Comput. Mater.* **2019**, *5*, 1–14.

(77) Stiles, P. L.; Dieringer, J. A.; Shah, N. C.; Van Duyne, R. P. *Annu. Rev. Anal. Chem. (Palo Alto Calif.)* **2008**, *1*, 601–626.

(78) Willets, K. A.; Van Duyne, R. P. *Annu. Rev. Phys. Chem.* **2007**, *58*, 267–297.

(79) Geddes, C. D.; Lakowicz, J. R. *J. Fluoresc.* **2002**, *12*, 121–129.

(80) Jeong, Y.; Kook, Y.-M.; Lee, K.; Koh, W.-G. *Biosens. Bioelectron.* **2018**, *111*, 102–116.

(81) Han, Y. D.; Lee, J. W.; Park, D. H.; Yang, S. H.; Kim, B. K.; Kim, J.; Joo, J. *Synth. Met.* **2011**, *161*, 2103–2106.

(82) Wu, D. M.; García-Etxarri, A.; Salleo, A.; Dionne, J. A. *J. Phys. Chem. Lett.* **2014**, *5*, 4020–4031.

(83) Huang, L.; Kakadiaris, E.; Vaneckova, T.; Huang, K.; Vaculovicova, M.; Han, G. *Biomaterials* **2019**, *201*, 77–86.

(84) Zhou, H.; Wang, C.; Lai, Y.; Yu, J.; Cheng, S. *Appl. Phys. A Mater. Sci. Process.* **2021**, *127*.

(85) Huang, Z.; Li, X.; Mahboub, M.; Hanson, K. M.; Nichols, V. M.; Le, H.; Tang, M. L.; Bardeen, C. J. *Nano Lett.* **2015**, *15*, 5552–5557.

(86) Jin, S. et al. *ACS Photonics* **2018**, *5*, 5025–5037.

(87) Niihori, Y.; Kosaka, T.; Negishi, Y. *Mater. Horiz.* **2024**, *11*, 2304–2322.

(88) DuBose, J. T.; Szabó, G.; Chakkamalayath, J.; Kamat, P. V. *J. Phys. Chem. A* **2022**, *126*, 7147–7158.

(89) Alves, J.; Feng, J.; Nienhaus, L.; Schmidt, T. W. *J. Mater. Chem. C Mater. Opt. Electron. Devices* **2022**, *10*, 7783–7798.

(90) Enrichi, F.; Quandt, A.; Righini, G. C. *Renew. Sustain. Energy Rev.* **2018**, *82*, 2433–2439.

(91) Honda, J.; Sugawa, K.; Tahara, H.; Otsuki, J. *Nanomaterials (Basel)* **2023**, *13*.

(92) Bossanyi, D. G.; Sasaki, Y.; Wang, S.; Chekulaev, D.; Kimizuka, N.; Yanai, N.; Clark, J. *JACS Au* **2021**, *1*, 2188–2201.

(93) CSID:12933, https://www.chemspider.com/Chemical-Structure.12933.html, Accessed: 03-11-2024.

(94) CSID:19280, https://www.chemspider.com/Chemical-Structure.19280.html, Accessed: 03-11-2024.

(95) Mooney, J.; Kambhampati, P. *J. Phys. Chem. Lett.* **2013**, *4*, 3316–3318.

(96) Chen, S.; Carroll, D. L. *Nano Lett.* **2002**, *2*, 1003–1007.

(97) Davis, T. J.; Vernon, K. C.; Gómez, D. E. *Opt. Express* **2009**, *17*, 23655–23663.

(98) He, Y.; Shi, G. *J. Phys. Chem. B* **2005**, *109*, 17503–17511.

(99) Tang, J.; Gao, K.; Ou, Q.; Fu, X.; Man, S.-Q.; Guo, J.; Liu, Y. *Spectrochim. Acta A Mol. Biomol. Spectrosc.* **2018**, *191*, 513–520.

(100) Near, R. D.; Hayden, S. C.; Hunter Jr, R. E.; Thackston, D.; El-Sayed, M. A. *J. Phys. Chem. C Nanomater. Interfaces* **2013**, *117*, 23950–23955.

(101) Phan, H. T.; Haes, A. J. *J. Phys. Chem. C Nanomater. Interfaces* **2019**, *123*, 16495–16507.

(102) Zheng, Y.; Zeng, J.; Ruditskiy, A.; Liu, M.; Xia, Y. *Chem. Mater.* **2014**, *26*, 22–33.

(103) Marques, M. E.; Mansur, A. A. P.; Mansur, H. S. *Appl. Surf. Sci.* **2013**, *275*, 347–360.

(104) Gomes, O. P.; Kim, S.; Lisboa-Filho, P. N.; Batagin-Neto, A.; De Koninck, Y.; Messaddeq, Y. *J. Mater. Chem. C Mater. Opt. Electron. Devices* **2024**, *12*, 6816–6825.

(105) Woeppel, K. M.; Zheng, X. S.; Cui, X. T. *J. Mater. Chem. B Mater. Biol. Med.* **2018**, *6*, 3058–3067.

(106) Cras, J. J.; Rowe-Taitt, C. A.; Nivens, D. A.; Ligler, F. S. *Biosens. Bioelectron.* **1999**, *14*, 683–688.

(107) Chen, X.; Li, G.; Głodek, M.; Knozowska, K.; Kujawa, J.; Zhang, P.; Kujawski, W. *Surf. Interfaces* **2023**, *43*, 103566.

(108) Marques, M. E.; Mansur, A. A. P.; Mansur, H. S. *Appl. Surf. Sci.* **2013**, *275*, 347–360.

(109) Ferhan, A. R.; Guo, L.; Kim, D.-H. *Langmuir* **2010**, *26*, 12433–12442.

(110) Ben Haddada, M.; Blanchard, J.; Casale, S.; Krafft, J.-M.; Vallée, A.; Méthivier, C.; Boujday, S. *Gold Bull.* **2013**, *46*, 335–341.

(111) Kawamura, G.; Yang, Y.; Nogami, M. *Appl. Phys. Lett.* **2007**, *90*, 261908.

(112) Huang, Y.; Kim, D.-H. *Langmuir* **2011**, *27*, 13861–13867.

(113) Guo, L.; Zhou, X.; Kim, D.-H. *Biosens. Bioelectron.* **2011**, *26*, 2246–2251.

(114) Matsumoto, M.; Kaneko, K.; Hara, M.; Matsui, M.; Morita, K.; Maruyama, T. *RSC Adv.* **2021**, *11*, 23409–23417.

(115) Zhang, F.; Di, C.-A.; Berdunov, N.; Hu, Y.; Hu, Y.; Gao, X.; Meng, Q.; Sirringhaus, H.; Zhu, D. *Adv. Mater.* **2013**, *25*, 1401–1407.

(116) Liu, S.; Wu, H.; Zhang, X.; Hu, W. *Front. Phys.* **2021**, *16*.

(117) Chen, C.-H.; Sher, P.-H.; Chen, C.-P.; Choi, W.-K.; Bardeen, C. J.; Chiu, T. L.; Wang, J.-K.; Lee, J.-H. *J. Phys. Chem. C Nanomater. Interfaces* **2020**, *124*, 25729–25737.

(118) Dhakal, K. P.; Joo, J.; Kim, J. *Curr. Appl. Phys.* **2022**, *39*, 304–310.

(119) Guang, Y.; Su-Ling, Z.; Zheng, X.; Fu-Jun, Z.; Chao, K.; Hai-Na, Z.; Dan-Dan, S.; Xu-Rong, X. *Chin. Physics B* **2010**, *19*, 037804.